

**Exploring the Use of Remote Sensing CO₂ Data to Measure the
CO₂ Concentration Enhancements Caused by Coal-fired
Power Plants**

by

Xiao Xu

A thesis
presented to the University of Waterloo
in fulfillment of the
thesis requirements for the degree of
Doctor of Philosophy
in
Geography

Waterloo, Ontario, Canada, 2014

©Xiao Xu 2014

Author's Declaration

I hereby declare that I am the sole author of this thesis. This is a true copy of the thesis, including any required final revisions, as accepted by my examiners.

I understand that my thesis may be made electronically available to the public.

Abstract

Ontario's power generation system is undergoing significant changes towards a modern and sustainable electricity system. One significant objective for the planned system transition is to reduce CO₂ emissions. CO₂ emissions from Ontario's power generation are expected to be cut significantly as coal is phased out and more renewables and natural gas capacity are incorporated into the provincial electricity supply. This restructuring of Ontario's electricity system and associated reduction of CO₂ emissions need to be monitored.

Equally, the dynamics of CO₂ in the atmosphere are also a major issue of interest in the scientific world and how the reduced CO₂ emissions from power plants can influence the distribution of CO₂ concentration remains an important question. In this regard, remote sensing which provides global-coverage, near real-time and 3-D information on atmospheric CO₂ is proposed as a useful tool for monitoring the processes and phenomena of interest. The ongoing space-based instruments such as GOSAT TANSO provide accurate CO₂ concentration information at different altitudes especially near the Earth's surface where interactions between power-generation CO₂ emissions and the atmosphere are intensive. These data can be used for both long-term CO₂ monitoring and short-term CO₂ detection by measuring the emitting activities of power plants. Therefore, this project examines the use of remote sensing to estimate the change of CO₂ enhancements due to the variation of coal-fired power generation intensity and to evaluate the effect of Ontario's energy decision/policy.

Partial column CO₂ data are more capable of presenting the surface CO₂ fluxes compared to column CO₂ data. By introducing the 'background' observations, the fossil fuel CO₂ flux in the Nanticoke area can be clearly detected and identified. The reduction of coal-fired power generation by Nanticoke Generating Station leads to decreased enhancement of local atmospheric CO₂ concentrations. It is shown that Ontario's decision to shut down coal-fired power plants is an effective measure to reduce atmospheric CO₂ and to mitigate climate change. More policies and actions are encouraged along with new monitoring techniques that include remote sensing tools.

Keywords:

Climate change, Nanticoke coal-fired power plants, CO₂ emissions, remote sensing CO₂ retrieval, CO₂ surface flux, CO₂ seasonality

Acknowledgements

First and foremost I offer my sincerest gratitude to my supervisor, Dr. Paul Parker. It has been my dream to study at a prestigious University in Canada. Thanks to Paul, my dream came true. Throughout the whole process of my dissertation, he has supported me with his patience and knowledge whilst allowing me to work in my own way. Paul is more than a supervisor. He cares about the wellbeing of this students and he appreciates what works best for the students. Without him, I could not have completed this dissertation. One could not expect a better supervisor than Paul.

I would also like to show my great gratitude to my co-supervisor, Dr. Richard Kelly. He provided me with the valuable data analysis and interpretation skills and delivered the insight into how to improve document writing under pragmatic context. I have been blessed with a supportive and cheerful PhD committee. Thanks for the inspiration by my committee members, Dr. Peter Deadman and Dr. Geoffrey Lewis, and their contributions to my dissertation writing. Dr. Christopher Fletcher helped me with the climate science and his input has been important and cannot be forgotten.

My research involves a variety of data sources which I was not perfectly familiar with and I have been haunted with the conceptual and technical questions throughout the data processing. All these problems could not have been solved without the help from those friendly people out there: Karla Mann from Independent Electricity System Operator (IESO), Andy Jacobson from CarbonTracker Team-NOAA ESRL, Christopher O'Dell from Colorado State University, Annmarie Eldering from JPL NASA and Ray Nassar from Environment Canada, etc.

Finally, I thank my parents and grandma for supporting me throughout my study overseas for these four years, making me feel loved, missed and warmed, with which I have been standing strong and determined.

Table of Contents

Author’s Declaration	ii
Abstract	iii
Acknowledgements	iv
Table of Contents	v
List of Figures	ix
List of Tables	xii
Chapter 1: Introduction.....	1
1.1 Background	2
1.1.1 Climate Change, Energy Consumption and GHG.....	2
1.1.2 CO ₂ Measurements	4
1.1.3 CO ₂ Concentration Factors	7
1.2 Statement of Problem	9
1.3 Primary Research Questions.....	9
1.4 Research Approach.....	10
1.5 Significance	10
1.6 Definition of Terms	11
1.7 Dissertation Outline.....	12
1.8 Summary	13
Chapter 2: Literature Review	14
2.1 Introduction	14
2.2 Climate Change, Energy Use and GHG Emissions.....	14
2.2.1 Climate Change	14

2.2.2 Electricity System of Ontario	22
2.3 Remote Sensing CO ₂ Observations	30
2.3.1 Overview	31
2.3.2 Measuring CO ₂ from Space	32
2.3.3 GOSAT CO ₂ Retrievals.....	41
2.3.4 Reliability in Practice-GOSAT.....	48
2.4 Influential Factors.....	52
2.4.1 CO ₂ Atmospheric Transport	52
2.4.2 State Vector	60
2.5 Summary	69
Chapter 3: Methods	71
3.1 Introduction	71
3.2 Research Planning	71
3.2.1 Method.....	74
3.2.2 Assumptions and Reliability Issues.....	84
3.3 Data Collection.....	86
3.4 Importance and Limitations.....	88
3.5 Hypotheses and Proposed Analysis.....	89
3.5.1 Nonlinear Regression	90
3.5.2 Meteorological Condition.....	92
3.6 Summary	93
Chapter 4: Results	94
4.1 Introduction	94
4.2 Target Column XCO ₂ and CO ₂ Abundance	94
4.3 Background Area Pre-analysis	99

4.3.1. Flux Heterogeneity	100
4.3.2 Column and Partial Column XCO ₂	100
4.4 Estimate of Number of Layers.....	102
4.5 Data Fitting.....	103
4.6 Regression Results.....	105
4.6.1 Linear Correlation	106
4.6.2 Power Regression	107
4.6.3 Polynomial Regression.....	108
4.6.4 Rational Regression.....	109
4.6.5 Sum of Sine	111
4.6.6 Summary	112
4.7 Partial Column XCO ₂ Statistics.....	114
4.8 Weather Indicators and Station Comparison	117
4.8.1 Wind Speed and Direction.....	117
4.8.2 Temperature.....	118
4.8.3 Humidity.....	118
4.8.4 Pressure	119
4.8.5 Weather Description.....	119
4.9 Influence of Weather Conditions.....	119
4.9.1 Meteorological Parameters Scaling	120
4.9.2 Influence Evaluation: 10-Layer Partial Column.....	120
4.9.3 Influence Evaluation: 3-Layer Partial Column.....	127
4.9.4 Simplified Regression and Modified Parameter Scaling.....	129
4.9.5 Influence of Categorical Meteorological Parameters	134
4.10 Monthly and Seasonal Variations in CO ₂ in Hamilton	140

4.10.1 Target Soundings in Hamilton.....	141
4.10.2 Partial Column XCO ₂	141
4.11 Summary	145
Chapter 5: Discussion.....	147
5.1 CO ₂ Concentrations and Surface Emissions.....	147
5.2 Background Selection and CO ₂ Profiles.....	148
5.3 Data Fitting.....	150
5.4 Surface and Atmospheric Parameters.....	152
5.5 Seasonal CO ₂ Variation in Hamilton.....	155
5.6 Comparisons with Other Studies	156
5.7 Summary	159
Chapter 6: Conclusion.....	161
6.1 Introduction	161
6.2 Research design.....	161
6.3 Key Findings	162
6.4 Contributions and Implications	163
6.5 Limitations and Future Research.....	165
Appendix A: Tables.....	168
Appendix B: Figures	221
Bibliography.....	231

List of Figures

Figure 2.1 Observed Globally Averaged Combined Land and Ocean Surface Temperature Anomaly 1850-2012.....	16
Figure 2.2 National Emission Trends for 2005-2011 by Major Sector	28
Figure 2.3 CO₂ Absorption Spectrum.....	31
Figure 2.4 ACOS B3.3 Data Processing Flow	45
Figure 2.5 Height Dependences of Pressure (Blue) and Temperature (Red)	61
Figure 3.1 The Workflow for Partial-Column CO₂ and XCO₂ Retrieval	72
Figure 3.2 Location of Target and Background Areas	73
Figure 3.3 ACOS B2.9 Pressure System	78
Figure 3.4 Different Pressure Systems of Target Sounding and Two Background Soundings	81
Figure 4.1 Target and Background Column XCO₂ and One-Hour Output.....	95
Figure 4.2 Smoothing Spline of XCO₂ and Daily Generating Outputs.....	96
Figure 4.3 Target XCO₂ against One-Hour Output	96
Figure 4.4 Histogram of XCO₂ Data	97
Figure 4.5 CO₂ Concentration Seasonality and CO₂ Emission Seasonality	98
Figure 4.6 Generating Output and CO₂ Concentrations of Individual Month and Individual Season	99
Figure 4.7 Shape of Target CO₂ Profiles	102
Figure 4.8 Shape of Background CO₂ Profiles-150 Samples Randomly Selected.....	102
Figure 4.9 Column dXCO₂ against Generating Output.....	104
Figure 4.10 10-Layer Partial Column dXCO₂ against Generating Output.....	104
Figure 4.11 Column dXCO₂ Smoothing Spline.....	104

Figure 4.12 Histograms of Wind Speed (a), Wind Direction Deviation (b), Temperature (c), Humidity (d), Pressure (e) and Weather Event (f)	120
Figure 4.13 Residual Plot of 10-Layer Rational Regression	121
Figure 4.14 Histogram of Original Residuals	121
Figure 4.15 Residual Plot of 3_Layer Polynomial Regression	127
Figure 4.16 Histograms of Scaled Meteorological Parameters (Adjusted)	129
Figure 4.17 Interactions Regression for 10-Layer Model Residuals	136
Figure 4.18 Full Quadratic Regression for 10-Layer Model Residuals	136
Figure 4.19 Interactions Regression for 3-Layer Model Residuals	137
Figure 4.20 Full Quadratic Regression for 3-Layer Model Residuals	138
Figure 4.21 Monthly Average Column XCO₂ for Year 2010, 2011 and 2012	141
Figure 4.22 Monthly Average 4-Layer Partial Column XCO₂ for Year 2010, 2011 and 2012	142
Figure 4.23 Monthly Average 6-Layer Partial Column XCO₂ for Year 2010, 2011 and 2012	142
Figure 4.24 Monthly Average 8-Layer Partial Column XCO₂ for Year 2010, 2011 and 2012	142
Figure 4.25 Monthly Average 10-Layer Partial Column XCO₂ for Year 2010, 2011 and 2012	143
Figure 4.26 Column and Partial Column XCO₂ for 2010	143
Figure 4.27 Column and Partial Column XCO₂ for 2011	144
Figure 4.28 Column and Partial Column XCO₂ for 2012	144
Figure B.1 Linear Regression for Column dXCO₂	221
Figure B.2 Linear Regression for 3-Layer Partial Column dXCO₂	221
Figure B.3 Linear Regression for 8-Layer Partial Column dXCO₂	221
Figure B.4 Linear Regression for 9-Layer Partial Column dXCO₂	222
Figure B.5 Linear Regression for 10-Layer Partial Column dXCO₂	222

Figure B.6 Linear Regression for 11-Layer Partial Column dXCO₂	222
Figure B.7 Power Regression for Column dXCO₂	223
Figure B.8 Power Regression for 3-Layer Partial Column dXCO₂	223
Figure B.9 Power Regression for 8-Layer Partial Column dXCO₂	223
Figure B.10 Power Regression for 9-Layer Partial Column dXCO₂	224
Figure B.11 Power Regression for 10-Layer Partial Column dXCO₂	224
Figure B.12 Power Regression for 11-Layer Partial Column dXCO₂	224
Figure B.13 2-Degree Polynomial Regression for Column dXCO₂	225
Figure B.14 2-Degree Polynomial Regression for 3-Layer Partial Column dXCO₂ ...	225
Figure B.15 2-Degree Polynomial Regression for 8-Layer Partial Column dXCO₂ ...	225
Figure B.16 2-Degree Polynomial Regression for 9-Layer Partial Column dXCO₂ ...	226
Figure B.17 2-Degree Polynomial Regression for 10-Layer Partial Column dXCO₂ ..	226
Figure B.18 2-Degree Polynomial Regression for 11-Layer Partial Column dXCO₂ ..	226
Figure B.19 Rational Regression for Column dXCO₂	227
Figure B.20 Rational Regression for 3-Layer Partial Column dXCO₂	227
Figure B.21 Rational Regression for 8-Layer Partial Column dXCO₂	227
Figure B.22 Rational Regression for 9-Layer Partial Column dXCO₂	228
Figure B.23 Rational Regression for 10-Layer Partial Column dXCO₂	228
Figure B.24 Rational Regression for 11-Layer Partial Column dXCO₂	228
Figure B.25 Sum of Sine Regression for Column dXCO₂	229
Figure B.26 Sum of Sine Regression for 3-Layer Partial Column dXCO₂	229
Figure B.27 Sum of Sine Regression for 8-Layer Partial Column dXCO₂	229
Figure B.28 Sum of Sine Regression for 9-Layer Partial Column dXCO₂	230
Figure B.29 Sum of Sine Regression for 10-Layer Partial Column dXCO₂	230
Figure B.30 Sum of Sine Regression for 11-Layer Partial Column dXCO₂	230

List of Tables

Table 2.1 Ontario Annual Energy Demand	23
Table 2.2 Ontario Electricity Supply Mix Change from 2003 to 2013: IESP Participants. (in MW)	24
Table 2.3 Ontario’s GHG Emissions by Sector (in kt CO_{2e})	29
Table 2.4 Specifications of AIRS	36
Table 2.5 SCIAMACHY Optical Performance	37
Table 2.6 Specifications of TANSO-FTS	40
Table 2.7 Basic Specifications of Different Algorithms	49
Table 2.8 GOSAT CO₂ Retrieval Algorithm Validation against TCCON	51
Table 2.9 Major Water Vapor and CO₂ Absorption Bands in NIR	66
Table 3.1 Change of Pressure and Temperature with Altitude (ICAO, 1964)	77
Table 3.2 Data Sources and Data Description	87
Table 3.3 Forms of Nonlinear Regression	91
Table 4.1 Number of Soundings by Year	95
Table 4.2 Pearson’s Correlation between XCO₂ and Output	97
Table 4.3 Statistics of XCO₂ Difference between Two Areas	101
Table 4.4 Statistics of XCO₂ Difference with Number of Soundings Larger than Three	101
Table 4.5 Potential Functions for Linear and Nonlinear Regression	105
Table 4.6 Summary of Linear Correlation	107
Table 4.7 Summary of Power Regression	108
Table 4.8 Summary of Polynomial Regression	109
Table 4.9 Summary of Rational Regression	110

Table 4.10 Summary of Sum of Sine Regression	111
Table 4.11 Summary of R² for Linear and Nonlinear Regressions.....	112
Table 4.12 Summary of Intercept on Y-Axis for Linear and Nonlinear Regressions .	113
Table 4.13 Summary of Output Averaging for Linear and Nonlinear Regressions....	114
Table 4.14 Statistics of XCO₂ on Each Level of Target Soundings.....	115
Table 4.15 Statistics of XCO₂ Uncertainty on Each Level of Target Soundings	116
Table 4.16 Statistics on Wind Speed Difference	117
Table 4.17 Statistics on Temperature Difference	118
Table 4.18 Statistics on Humidity Difference.....	118
Table 4.19 Statistics on Pressure Difference	119
Table 4.20 Correlations between Regression Residual Scale and Meteorological Parameter Scale	121
Table 4.21 The Statistics of Potential Influential Factors on Residuals	122
Table 4.22 The Statistics of Potential Influential Factors on Residuals: Alternative Criteria	123
Table 4.23 The Statistics of Potential Influential Factors on Surface XCO₂ Uncertainty	124
Table 4.24 Frequency of Association between High/High Scale Variables (%).....	125
Table 4.25 Frequency of Association between High/Low Scale Variables (%)	125
Table 4.26 Frequency of Association between Low/Low Scale Variables (%)	125
Table 4.27 A Summary of Frequency of Association between Variables (%)	125
Table 4.28 A Summary of Frequency of Association between Variables in Summer (%)	126
Table 4.29 Statistics of Potential Influential Factors on Residuals	128
Table 4.30 Influence of Adjusted Meteorological Parameters on 10-Layer Model Residuals.....	130
Table 4.31 Regression Equations and Goodness of Fit: 10-Layer dXCO₂, Adjusted Meteorology	131

Table 4.32 Influence of Adjusted Meteorological Parameters on 3-Layer Model Residuals.....	132
Table 4.33 Regression Equations and Goodness of Fit: 3-Layer dXCO₂, Adjusted Meteorology	133
Table 4.34 The Influence of Adjusted Meteorology on Surface XCO₂ Uncertainty....	134
Table 4.35 Power Regression Results for Shallow and Deep Groups.....	139
Table 4.36 Goodness of Fit: CO₂ Seasonality by Full Column and Partial Columns..	144
Table A.1 CO₂ Dry Air Mole Fractions and Nanticoke Generating Outputs	168
Table A.2 Difference of Column and Partial Column XCO₂ and CO₂.....	170
Table A.3 Linear Correlation for Column dXCO₂ and dCO₂.....	172
Table A.4 Linear Correlation for 3-Layer Partial Column dXCO₂ and dCO₂.....	172
Table A.5 Linear Correlation for 4-Layer Partial Column dXCO₂ and dCO₂.....	172
Table A.6 Linear Correlation for 5-Layer Partial Column dXCO₂ and dCO₂.....	173
Table A.7 Linear Correlation for 6-Layer Partial Column dXCO₂ and dCO₂.....	173
Table A.8 Linear Correlation for 7-Layer Partial Column dXCO₂ and dCO₂.....	173
Table A.9 Linear Correlation for 8-Layer Partial Column dXCO₂ and dCO₂.....	174
Table A.10 Linear Correlation for 9-Layer Partial Column dXCO₂ and dCO₂.....	174
Table A.11 Linear Correlation for 10-Layer Partial Column dXCO₂ and dCO₂.....	174
Table A.12 Linear Correlation for 11-Layer Partial Column dXCO₂ and dCO₂.....	175
Table A.13 Power Regression R² Statistics for Column dXCO₂ and dCO₂	175
Table A.14 Power Regression R² Statistics for 3-Layer Partial Column dXCO₂ and dCO₂	175
Table A.15 Power Regression R² Statistics for 4-Layer Partial Column dXCO₂ and dCO₂	175
Table A.16 Power Regression R² Statistics for 5-Layer Partial Column dXCO₂ and dCO₂	176
Table A.17 Power Regression R² Statistics for 6-Layer Partial Column dXCO₂ and dCO₂	176

Table A.18 Power Regression R^2 Statistics for 7-Layer Partial Column $dXCO_2$ and dCO_2	176
Table A.19 Power Regression R^2 Statistics for 8-Layer Partial Column $dXCO_2$ and dCO_2	176
Table A.20 Power Regression R^2 Statistics for 9-Layer Partial Column $dXCO_2$ and dCO_2	177
Table A.21 Power Regression R^2 Statistics for 10-Layer Partial Column $dXCO_2$ and dCO_2	177
Table A.22 Power Regression R^2 Statistics for 11-Layer Partial Column $dXCO_2$ and dCO_2	177
Table A.23 2-Degree Polynomial Regression R^2 Statistics for Column $dXCO_2$ and dCO_2	177
Table A.24 2-Degree Polynomial Regression R^2 Statistics for 3-Layer Partial Column $dXCO_2$ and dCO_2.....	178
Table A.25 2-Degree Polynomial Regression R^2 Statistics for 4-Layer Partial Column $dXCO_2$ and dCO_2.....	178
Table A.26 2-Degree Polynomial Regression R^2 Statistics for 5-Layer Partial Column $dXCO_2$ and dCO_2.....	178
Table A.27 2-Degree Polynomial Regression R^2 Statistics for 6-Layer Partial Column $dXCO_2$ and dCO_2.....	178
Table A.28 2-Degree Polynomial Regression R^2 Statistics for 7-Layer Partial Column $dXCO_2$ and dCO_2.....	179
Table A.29 2-Degree Polynomial Regression R^2 Statistics for 8-Layer Partial Column $dXCO_2$ and dCO_2.....	179
Table A.30 2-Degree Polynomial Regression R^2 Statistics for 9-Layer Partial Column $dXCO_2$ and dCO_2.....	179
Table A.31 2-Degree Polynomial Regression R^2 Statistics for 10-Layer Partial Column $dXCO_2$ and dCO_2.....	179
Table A.32 2-Degree Polynomial Regression R^2 Statistics for 11-Layer Partial Column $dXCO_2$ and dCO_2.....	180
Table A.33 1-Degree Rational R^2 Statistics for Column $dXCO_2$ and dCO_2.....	180

Table A.34 1-Degree Rational R^2 Statistics for 3-Layer Partial Column $dXCO_2$ and dCO_2	180
Table A.35 1-Degree Rational R^2 Statistics for 4-Layer Partial Column $dXCO_2$ and dCO_2	180
Table A.36 1-Degree Rational R^2 Statistics for 5-Layer Partial Column $dXCO_2$ and dCO_2	181
Table A.37 1-Degree Rational R^2 Statistics for 6-Layer Partial Column $dXCO_2$ and dCO_2	181
Table A.38 1-Degree Rational R^2 Statistics for 7-Layer Partial Column $dXCO_2$ and dCO_2	181
Table A.39 1-Degree Rational R^2 Statistics for 8-Layer Partial Column $dXCO_2$ and dCO_2	181
Table A.40 1-Degree Rational R^2 Statistics for 9-Layer Partial Column $dXCO_2$ and dCO_2	182
Table A.41 1-Degree Rational R^2 Statistics for 10-Layer Partial Column $dXCO_2$ and dCO_2	182
Table A.42 1-Degree Rational R^2 Statistics for 11-Layer Partial Column $dXCO_2$ and dCO_2	182
Table A.43 Sum of Sine R^2 Statistics for Column $dXCO_2$ and dCO_2.....	182
Table A.44 Sum of Sine R^2 Statistics for 3-Layer Partial Column $dXCO_2$ and dCO_2	183
Table A.45 Sum of Sine R^2 Statistics for 4-Layer Partial Column $dXCO_2$ and dCO_2	183
Table A.46 Sum of Sine R^2 Statistics for 5-Layer Partial Column $dXCO_2$ and dCO_2	183
Table A.47 Sum of Sine R^2 Statistics for 6-Layer Partial Column $dXCO_2$ and dCO_2	183
Table A.48 Sum of Sine R^2 Statistics for 7-Layer Partial Column $dXCO_2$ and dCO_2	184
Table A.49 Sum of Sine R^2 Statistics for 8-Layer Partial Column $dXCO_2$ and dCO_2	184
Table A.50 Sum of Sine R^2 Statistics for 9-Layer Partial Column $dXCO_2$ and dCO_2	184
Table A.51 Sum of Sine R^2 Statistics for 10-Layer Partial Column $dXCO_2$ and dCO_2	184
Table A.52 Sum of Sine R^2 Statistics for 11-Layer Partial Column $dXCO_2$ and dCO_2	185

Table A.53 XCO₂ on the 10 Levels of Targeted Soundings (ppm)	186
Table A.54 XCO₂ Uncertainty of the 10 Levels of Targeted Soundings (ppm)	188
Table A.55 Wind Speed and Direction (One-hour) at Hamilton Station and London Station	190
Table A.56 Temperature at Hamilton Station and London Station	192
Table A.57 Humidity at Hamilton Station and London Station	194
Table A.58 Pressure at Hamilton Station and London Station	196
Table A.59 Weather Event/Description at Hamilton Station and London Station	198
Table A.60 Scale of Wind Speed and Wind Direction Deviation	202
Table A.61 Scale of Temperature	204
Table A.62 Scale of Humidity	206
Table A.63 Scale of Surface Pressure	208
Table A.64 Scale of Weather Event/Description	210
Table A.65 The Scale of 10-Layer Absolute Residuals in dXCO₂	212
Table A.66 Two Residual Groups and Relevant Statistics	214
Table A.67 Targeted Soundings in Hamilton	216
Table A.68 XCO₂ Uncertainty of the Column and 10 levels	218
Table A.69 Scales of Weather Factors (Hamilton)	220

Chapter 1: Introduction

'CO₂ can be considered the mobile component of the carbon cycle' since it determines most carbon exchange processes among the soil, ocean, and atmosphere (Houweling *et al.*,2004). As a primary and long-lived greenhouse gas (GHG), CO₂ has always influenced the global climate, but attention has focused on its increasing concentration since the industrial age (CO₂ and CH₄ account for 80% of the global warming effect). According to the Intergovernmental Panel on Climate Change (IPCC) 2013, the atmospheric CO₂ concentration has increased since 1750 due to human activity. This mainly results from increasing combustion of fossil fuel, but includes other anthropogenic factors such as land use change and cement production.

It has been a primary political and scientific concern to better estimate CO₂ sources and sinks at various spatial and temporal scales. Traditionally, measurements of CO₂ are obtained from surface network, aircraft and ship sampling; however representations of CO₂ are vulnerable to the sparsity of spatial coverage. In addition, the surface network is limited in its capability of representing the complex atmospheric mixing in mid-high troposphere where the surface signal is diluted. In this regard, an increasing attention is devoted to the application of remote sensing observations in estimating CO₂ fluxes. Particularly, the increased spatiotemporal resolution and accuracy of satellite instrument measurements makes remote sensing a practical tool for monitoring CO₂ emissions at regional scales, thereby enhancing our understanding of the dynamic processes that influence the atmospheric CO₂ concentrations.

This research is conducted in the context of Ontario and its government's decisions. Ontario's electricity system has evolved quickly in the 21st century as the province endeavored to reduce GHG emissions. As more clean and renewable sources are incorporated into the electricity system, the province is committed to phasing out coal for electricity generation by the end of 2014 [Ontario Power Authority (OPA), 2010]. Nanticoke power generating station (GS) is the largest coal-fired GS operated by Ontario Power Generation (OPG). It is located on the north shore of Lake Erie (location coordinates: 42.80 N, 80.05 W). As generating units have been shut down or put on stand-by, the emissions of CO₂ and air pollutants have decreased.

In this research, remote sensing CO₂ retrieval data are used to examine whether the change of atmospheric CO₂ concentration is observable as Nanticoke GS's electricity output changes over

time. The reliability of using remote sensed CO₂ data to monitor ground CO₂ emissions is also investigated.

1.1 Background

In order to set the background for this research, this section briefly introduces the significant conclusions/findings, unresolved issues, and national/international concerns in relevant research fields, including: climate change, energy consumption, GHG emissions, CO₂ measurements, and influential factors on CO₂ concentrations. More details are discussed in the ‘Literature Review’ chapter.

1.1.1 Climate Change, Energy Consumption and GHG

GHG emissions from the consumption of energy are considered to be a major contributor to climate change. The global consumption of primary energy increased at an average annual rate of 2.0% (Jovanovic *et al.*,2010). The annual CO₂ emissions from fossil fuel combustion and cement production were 8.3 [7.6 to 9.0] GtC¹²/year¹ averaged over 2002-2011. In 2011, the emissions were 9.5 [8.7 to 10.3] GtC¹²/year which is 54% above the 1990 level. Annual CO₂ emission from anthropogenic land use changes are 0.9 GtC¹²/year averaged over 2002-2011 (Stocker *et al.*,2013b). An excess of fossil fuels exploitation and combustion not only result in negative impacts environmentally, but also seriously challenge the security of energy supply.

An extensive literature has focused on GHG emissions from energy consumption and their role in causing climate change (Hohmeyer,1988, Kim and Dale,2005, Norman *et al.*,2006, Soyta *et al.*,2007, Ou *et al.*,2009), as well as policies towards mitigating climate change (Wigley *et al.*,1996, Zhang,1998, Nakicenovic and Swart,2000, Jean-Baptiste and Ducroux,2003, Blyth and Lefevre-Marton,2005, Leiserowitz,2006, Mattoo *et al.*,2009).

The mitigation of climate change requires urgent attention from both policy makers and the general public and calls for a collective effort internationally. The fourth assessment report by the IPCC suggested significant reductions in GHG emissions with a great potential of outcomes from energy and industrial processes. The fifth IPCC report enhances the understanding of climate

¹ 1 GtC (1 Gigatonne of carbon) = 10¹⁵ grams of carbon, which equals to 3.667 GtCO₂

change and the negative role of GHG with a series of clear and robust conclusions in a global assessment of climate change science.

As of 2007, eighteen EU members had set national targets for GHG emissions reduction. Particularly, the EU Greenhouse Gas Emission Trading Scheme (EUETS) launched in 2005 allowed for trading carbon credits among countries (Ellerman and Buchner,2007). A number of developing countries had also proposed GHG emission reduction targets to fight climate change. Most climate/energy policies emphasize cost-effective CO₂ reduction measures, energy conservation and development of sustainable energy systems. These policies have experienced modifications and adjustments during the transition of the energy system (Kern and Smith,2008).

Canada is the 5th largest producer of energy in the world. Even though for domestic use Canada consumes a small fraction of energy in terms of global consumption, its per capita energy use is among the highest across the world (Hofman and Li,2009). Canada has high potentials to curtail its energy consumption and associated GHG emissions while securing its energy supply and maintaining its overall competitiveness. The Government of Canada specifically Natural Resources Canada (NRCan) identifies adaptations to climate change as a top priority, and aims to reduce GHG emission levels to mitigate the severity and impacts of climate change. However, energy jurisdictions of the federal and provincial governments are separated. Though the federal government has the authority to sign international treaties, regulate international and inter-provincial trade and set national product and environmental standards, the provincial governments have the constitutional responsibility over energy and natural resources management. Therefore, the mitigation of climate change requires close and concerted collaborations among provincial and federal governments.

The electricity sector contributes a large share of GHG emissions in Canada. The supply mix of the electricity system varies among provinces and changes over time. In Ontario, the electricity system has undergone a significant transition since the 1950s when the province was highly dependent on hydroelectric power and coal (Planning,1980). Nuclear generating facilities were brought into service between early 1970s and early 1990s. Prior to 2003, there was no long-term energy plan in Ontario (Ministry of Energy Ontario, 2010). At that time, 25% of the provincial electricity supply came from coal-fired power generation. As the demand for electricity grew and the infrastructures aged, new renewables sources were incorporated into the electricity system. In the past decade, Ontario made progress on building and maintaining a clean, reliable and affordable electricity system (OPA, 2014). Most importantly, Ontario's phasing out coal for

power generation is the largest climate change initiative in North America (OPA, 2013). Ontario had virtually eliminated coal from the electricity system by 2013, when coal accounted for 2% of total power generation and the GHG emissions were reduced by 90% compared to 2003 (OPA, 2014). At the same time, the supply changed from net deficit to net surplus as the demand remained nearly flat. Moreover, Ontario is devoted to creating a less energy-intensive future when the demand for energy is not closely linked to economic growth (OPA, 2013).

1.1.2 CO₂ Measurements

CO₂ is a primary concern for climate change. In order to estimate the sources and sinks of CO₂ and evaluate the performance of CO₂ emissions reduction, the atmospheric CO₂ concentrations need to be measured with high accuracy.

In situ measurements have been a major tool to estimate and understand CO₂ spatial and temporal variability. A long history of research and applications demonstrate the reliability and accuracy of *in situ* measurements using various types of instruments (Webster and May, 1987, Vourlitis *et al.*, 1993, Ray *et al.*, 1999, Gibert *et al.*, 2007, Machida *et al.*, 2008, Deutscher *et al.*, 2010, Chevallier *et al.*, 2011, Fang *et al.*, 2014). Ground-based instruments are very insensitive to aerosols which can change the optical depth of signals (sunlight). The bias of CO₂ concentration retrieval due to aerosols can thus be mostly eliminated and the accuracy of the results is usually very high. In particular, the Fourier Transform Infrared Spectrometry (FTIR) measurement, which is normally used from ground-based platforms, has been demonstrated as capable of detecting particular materials (e.g. CO₂, CO, CH₄, N₂O, and H₂O) and their scattering effects in the atmosphere to enable the estimation of their abundances.

However, *in situ* networks are challenged by the stringent requirements for the identification of CO₂ sources and sinks at global and regional scales. In general, the sparse spatial coverage of surface network is the foremost problem for geographical and political reasons. This creates a great need and opportunity for developing and applying remote sensing techniques in CO₂ studies.

The first application of space-based measurements for CO₂ concentration was in 1979 using NOAA-TOVS data after the NOAA polar orbiting meteorological satellite was launched to provide constant observation of the earth surface and the atmosphere (Smith *et al.*, 1979). The results showed a high agreement with surface observations and aircraft measurements (Chédin *et al.*, 2002a).

Considering the absorption characteristics of atmospheric CO₂, two main spectral ranges [thermal infrared (TIR) and near infrared (NIR)] are used by space-based instruments for retrieving atmospheric CO₂ information. The Atmospheric Infrared Sounder (AIRS) onboard Aqua spacecraft is the first TIR instrument measuring clouds, abundances of trace components in the atmosphere such as CO₂, CH₄, CO, SO₂, and O₃ etc. Prior to wide use of TIR soundings, feasibility studies showed that although uncertainties in atmospheric conditions such as water vapor and temperature can dominate, a careful averaging of retrieved CO₂ data is able to capture the change of column CO₂ abundance at an acceptable level (1% or less). Additionally, it has been suggested that 50 TIR channels are adequate for resolving the tropospheric CO₂ abundances (Chédin *et al.*,2003a).

However, TIR is not sensitive to lower atmosphere where the dispersion of CO₂ is very complex. In contrast, NIR is expected to be capable of inferring the CO₂ concentrations near the surface especially within the boundary layer.

The Scanning Imaging Absorption spectrometer for Atmospheric Chartography (SCIAMACHY) onboard the ENVISAT satellite is the first instrument measuring CO₂ (along with other trace gases) column abundances through NIR channels on a long-term basis (Bovensmann *et al.*,1999). For the first time the regional CO₂ sources and sinks have been estimated using space-based measurements. However, the transmission of SCIAMACHY is affected by two factors: the degradation of optical components and the varying ice-layer on channel 7 and 8 detectors (Lichtenberg *et al.*,2006). Using the version 0.4 of Weighting Function Modified (WFM) DOAS retrieval algorithm, the spatiotemporal patterns of measured CO₂ dry air mole fraction (indicated as XCO₂ hereafter) and modelled XCO₂ are in reasonable agreement, but the amplitude of measurements are much higher than the variability of model data (Buchwitz *et al.*,2005). This discrepancy is mainly attributable to the ice-layer on channel 8 detector and partially because of the retrieval algorithm. Since the ice-layer problem was solved and the algorithm was improved from the older version, the quality of retrieved CO₂ data could be significantly higher than previous studies that used the same set of spectral data (Buchwitz *et al.*,2006).

In general, after the launch of SCIAMACHY, an improved accuracy (less than 1%) can be consistently achieved compared to previous instruments (Buchwitz and Burrows,2003, Bramstedt,2008, Bergamaschi *et al.*,2009, Bramstedt *et al.*,2009, Reuter *et al.*,2010). However, SCIAMACHY cannot provide accurate trace gases information over water due to lack of a targeted glint mode. In addition, key surface and atmospheric parameters cannot be retrieved such

as the vertical profile of trace gas, pressure and temperature profiles, aerosols and surface albedo. The uncertainties in these parameters that are not retrieved contribute to the systematic errors and need to be quantified (Buchwitz *et al.*,2000). .

The project Greenhouse Gases Observing Satellite (GOSAT, or 'IBUKI') was started early in 2009 with two sensors onboard: the Thermal and Near-infrared Sensor for Carbon Observation Fourier Transform Spectrometer (TANSO-FTS) and the Cloud and Aerosol Imager (TANSO-CAI). GOSAT is the world's first spacecraft specifically dedicated to measuring the concentrations of CO₂ and CH₄. By measuring both TIR and NIR radiances, GOSAT is able to observe both column amounts and vertical profiles of the trace gases. Estimates of the global distribution of CO₂ and CH₄ can be obtained as well as the spatiotemporal variability of their sources and sinks (Fraser *et al.*,2011, Houweling *et al.*,2012, Basu *et al.*,2013, Byckling *et al.*,2013, Maksyutov *et al.*,2013, Basu *et al.*,2014a).

The quality of GOSAT retrieval is highly dependent on calibration. An early study on CO₂ and CH₄ retrieval indicated that the measured latitudinal differences agreed with ground-based measurements and other space-based observations whereas the absolute gas concentrations were underestimated (Yokota *et al.*,2009). Preliminary validation studies also inferred that the first year retrievals were biased low by -0.05% compared to ground-based high-resolution FTS (Butz *et al.*,2011, Morino *et al.*,2011). As the calibration and validation are improved in recent years, the agreement of GOSAT retrievals with accurate *in situ* measurements is improved correspondingly. A recent validation study showed that the GOSAT XCO₂ agreed with aircraft-based measurements with a negative bias of 0.68ppm (1.82ppm over ocean) and a standard deviation of 2.56ppm (1.04ppm over ocean) (Inoue *et al.*,2013).

Currently, there are five XCO₂ retrieval algorithms developed by four research groups/institutes . Each algorithm has gone through continuous modifications and upgrades. CO₂ data retrieved by each algorithm are in reasonable agreement with ground-based measurements at reference sites. It is crucial to note, however, that the inter-comparison among different retrievals in the regions away from the reference sites showed variable inter-product consistency (Takagi *et al.*,2013).

The utility of GOSAT CO₂ observations have gone beyond the original focus of studying natural CO₂ sources and sinks. Attempts have been made to use GOSAT observations for detecting large point sources (LPS). A JPL team conducted a megacity CO₂ study in which robust and statistically significant XCO₂ enhancements were observed for Los Angeles and Mumbai. It was

estimated that a small change in XCO₂ (0.7ppm) in Los Angeles can be captured by GOSAT observations at a 95% confidence level (Kort *et al.*,2012).

To summarize, space-based observations have provided extensive opportunities for studying natural GHG concentrations and fluxes and anthropogenic GHG emissions. As the instruments are improved and getting more specialized in a specific type of GHG e.g. CO₂ or CH₄, the understanding of trace gas dynamics and relationship with human activity are enhanced. Further efforts are needed to obtain higher accuracy and to estimate CO₂ at various spatiotemporal scales.

1.1.3 CO₂ Concentration Factors

Despite the considerable successful studies on CO₂ concentration and the inspiring potentials of space-based observations, it is crucial to understand the influential factors on the observed CO₂ concentration. A number of factors are introduced in this section and discussed in more detail in Chapter 2, including the atmospheric transport of CO₂, temperature, pressure and relative humidity.

The motion of CO₂ in the atmosphere is driven by three principle forces: gravity, pressure gradients and the Coriolis effect². The transport of CO₂ partially determines the pattern of CO₂ concentration given the spatial distribution of CO₂ fluxes (Rayner *et al.*,1999). However, this process shows variations at different spatiotemporal scales, including spatial scales such as local plume spread, regional mesoscale transport and global scale, and temporal scales such as hourly, diurnal, synoptic, seasonal and interannual cycles (Maksyutov *et al.*,2008). For example, from a global perspective, it was discovered in an intercontinental study that the fastest vertical transport occurs to the emissions from Asia while the emissions from Europe are most likely to stay in the lower troposphere; the emission tends to transport via the upper troposphere from the upwind continent to a receptor continent with an approximate period of 4 days, followed by the arrival of foreign tracers transported through the lower troposphere. Assuming a life time of 2 days, all continents are dominated by domestic tracers except Australia; however, when assuming a 20-day life time, all the continents are ‘contaminated’ by foreign emissions even in an emission-intensive continent (Stohl *et al.*,2002).

² ‘In physics, the Coriolis effect is a deflection of moving objects when they are viewed in a rotating reference frame’. http://en.wikipedia.org/wiki/Coriolis_effect. For example, affected by Coriolis, the surface air in the two Hadley cells flows towards the equator with a slant to the west.

When CO₂ is emitted from a surface source, there is a boundary between when CO₂ is influenced by its characteristics or thermodynamics (e.g. pressure, gas temperature, etc.) and when it is influenced by meteorological conditions such as wind speed and direction, ambient air temperature and terrain (Heino and Kakko,1998). It is extremely complicated to measure or assess the dispersion of CO₂ in the atmosphere especially in the atmospheric boundary layer (ABL) or planetary boundary layer (PBL). It is also known as the mixing layer where most dispersion and transport of gases occur. The dispersion of CO₂ cannot be simply based on gas density. It is possible that CO₂ is displaced on calm days when the average wind speed is 10km/h which can hardly be felt (Heino and Kakko,1998).

Temperature (ambient air temperature) is a significant factor that influences CO₂ concentration since it determines the dispersion of CO₂ in the atmosphere. In a CO₂ dispersion study (Lac *et al.*,2013), it was discovered that an underestimated near-ground temperature could induce incorrect vertical transport scenario and lead to overestimated CO₂ mixing ratio. This implies that the dispersion of CO₂ (as well as other comparable gases) is relatively inactive at low temperature and leads to a high CO₂ concentration near the surface, and vice versa.

Atmospheric temperature and pressure are the input parameters for remote sensing CO₂ retrieval algorithms as indispensable elements of the 'state vector' for building a forward model. XCO₂ is retrieved by surface pressure from O₂ A band and CO₂ profile from CO₂ bands, and both the O₂ and CO₂ absorption bands are dependent on temperature and surface pressure (B ösch *et al.*,2006). For NIR absorption, the temperature and pressure dependence is very strong (Frankenberg *et al.*,2005). Therefore, an error in temperature would result in inaccurate CO₂ retrievals. Water vapor is another crucial factor for CO₂ retrieval. Generally, a more severe problem arises from water vapor than temperature and pressure because it highly enhances the temperature dependence of absorption. Moreover, it makes it a challenge for yielding unbiased results for the state vector since a strong deviation is highly likely to exist between the actual state and the a priori assumptions (Frankenberg *et al.*,2005, Houweling *et al.*,2005).

There are a number of other factors that could be taken into account for analyzing the observed CO₂ concentrations. Considering the availability of weather/meteorological information from the weather stations and the access to physical parameters in the CO₂ retrieval dataset, these three factors (i.e. temperature, pressure and humidity) are of special interest in this study. The influence of these factors and their uncertainties (if available) on XCO₂ (or XCO₂ derivatives) are analyzed in later chapters.

1.2 Statement of Problem

Although space-based CO₂ observations have been successfully used for various purposes, gaps exist in the body of knowledge. Some interesting questions still remain unanswered and the potential of space-based measurements is not fully exploited.

The CO₂ concentration near the surface rather than at mid-upper troposphere is expected to be mostly related to ground emissions. However, quite a few articles only use column XCO₂ measures, despite the strong signals of emissions from the surface being weakened with increasing height. Exploration of the potential of partial column CO₂ information has not drawn close attention.

Most studies using space-based observations are conducted at relatively large scales by averaging the retrievals within a large region and over a period of time. CO₂ emissions at small scales such as LPS can be intense and easily captured by space-based instruments with mid-high spatial resolutions. However, this has not been a popular interest since currently the preference is to collect observations at reference sites where peer studies are available so that the reliability of CO₂ retrievals can be estimated.

Even though large facilities are required by certain jurisdictions to report CO₂ emissions, e.g. Ontario's CO₂ reporting system, remote sensing CO₂ instruments have not been used on management and policy-making levels as a direct tool for monitoring CO₂ emissions from the large-size facilities.

Considering the development of specialized remote sensing CO₂ observations and common research interests, very few studies are on a long-term basis. CO₂ seasonality studies are mostly extended to one year only. The advantages of constant and real-time observations by remote sensing instruments have been largely ignored possibly due to the lack of reference data.

1.3 Primary Research Questions

This dissertation will address several research questions:

1. How can remote sensing CO₂ observations be used to estimate surface CO₂ fluxes?
2. How can remote sensing CO₂ observations be used in a scientifically innovative way?

3. How can partial column CO₂ information be retrieved from existing observation datasets?
4. What is the relationship of full/partial column CO₂ information with the surface emissions from Nanticoke GS and what is the CO₂ natural seasonality in Hamilton?
5. How is Ontario's 'phasing out coal for power generation' influencing the local CO₂ concentration in Nanticoke area?

1.4 Research Approach

This research is designed to answer the questions identified in the previous section. The main aspects of the proposed approach are as follows (see Chapter 3 for details):

1. Space-based observations over the target site are collected from dataset distributed by the Atmospheric CO₂ Observations from Space Task (ACOS).
2. Background areas are identified using fossil fuel flux and biosphere flux distributed by CarbonTracker.
3. Partial column CO₂ amounts and concentrations are calculated based on ACOS retrieval algorithm Build3.3 and the enhancement of CO₂ concentrations/abundances are calculated.
4. The CO₂ emissions from Nanticoke GS are represented by hourly generating output.
5. The relationship between the enhancement of CO₂ concentrations/abundances and GS output is analyzed by linear and nonlinear regressions.
6. The influence of surface and meteorological parameters on surface XCO₂ uncertainties and the model residuals are estimated using weather information collected from Hamilton Station and London Station.
7. Column and partial column XCO₂ are compared by presenting CO₂ monthly/season variation in Hamilton.

1.5 Significance

The purpose of this research is to examine the feasibility of using partial column CO₂ information to monitor and estimate fine-scale CO₂ emissions from a LSP which is not limited to fossil-fueled

power plants. Few studies are focused on this topic. This research serves as a pilot study and it is expected to enlighten future studies on relevant topics.

On the one hand, this research is significant because it strengthens the confidence in using space-based CO₂ observations: the space-based instruments provide measurements within reasonable accuracy and are less vulnerable to the limitation in spatial coverage than ground-based platforms; on the other hand, it fills the gap in knowledge and practice: the vertical structure of the atmosphere is considered and detailed information about the CO₂ vertical profiles is analyzed to explore its relationship with surface fluxes. Moreover, this research not only benefits CO₂ researchers in generating innovative areas for CO₂ studies, but also provides assistance in decision-making on CO₂ reduction and management by advancing the development of remote sensing monitoring techniques.

In this research a derived type of data (i.e. partial column CO₂ amounts and concentrations) are retrieved based on available profiles of relevant parameters. Theoretically, partial column CO₂ amounts and concentrations are the optimal type of data for monitoring near-surface CO₂ concentrations and estimating surface CO₂ flux. However, they are rarely seen in previous studies because not all algorithms retrieve or disclose relevant parameters that are necessary for making partial column CO₂ products. Furthermore, LSP study is expected to become a popular research interest especially considering that a mission on CO₂ observation with very high spatial resolution (1km by 1km) has been successfully launched by the Orbiting Carbon Observatory-2 (OCO-2) Team in NASA.

In addition to the contribution to CO₂ studies, this research also explores the possibility of estimating the performance of Ontario's energy plans. The results explore the question of whether phasing out CO₂-intensive power generation could lead to decreased local atmospheric CO₂ concentration. With desirable outcomes from this research, further CO₂ reduction policies and actions are encouraged to improve the environment and mitigate climate change.

1.6 Definition of Terms

Normally CO₂ concentration refers to the volume mixing ratio of CO₂ in the atmosphere; however, in literature on the study of CO₂ as well as in this dissertation, CO₂ concentration and CO₂ dry air mole fraction are interchangeable. Another widely used term in CO₂ study is CO₂ abundance which refers to the amount of CO₂ particles.

Column CO₂ concentration is most often used in previous literatures and is denoted as XCO₂. In this dissertation, XCO₂ is not exclusive for column CO₂ concentration but used for both column and partial column. Especially in Chapter 3 and Chapter 4, XCO₂ refers to the CO₂ concentration within the field of view (FOV) of the space-based instrument.

The infrared absorption bands are used by remote sensing techniques to detect CO₂ in the atmosphere. The criteria for dividing and differentiating the infrared radiation vary among different research groups, institutions and individual articles. This study does not provide a standard for the division of infrared spectrum. Instead, the established, though sometimes overlapping, terminology such as ‘thermal infrared’, ‘near infrared’ and ‘short-wavelength infrared’ are used to match the research or literatures that are reviewed or cited.

Ground-based CO₂ observation networks specifically those using Fourier Transform Spectrometer (FTS) are different from conventional *in situ* measurements such as tower flask sampling. In this dissertation, the term ‘*in situ* measurement’ does not exclude ground-based FTS observations as in many literatures. However, when quoting the ‘ground-based observation’ such as the Total Carbon Column Observing Network (TCCON), it is differentiated from the conventional *in situ* network.

1.7 Dissertation Outline

In the next Chapter, the literatures on relevant research and practical fields to this study are reviewed, including climate change and GHG, energy planning and GHG emissions reduction, CO₂ measurements particularly space-based observations, and the factors that influence CO₂ atmospheric concentration.

Chapter 3 introduces the methods used to answer the research questions.

Chapter 4 presents the results from the proposed methods.

Chapter 5 interprets and discusses the results based on both Chapter 4 and the significant conclusions/findings in Chapter 2.

Chapter 6 makes final conclusions on this study.

1.8 Summary

This chapter introduces the fundamental background and motivations for designing and conducting this research.

The purpose of this research is to fill the gaps in knowledge and practice that are described in Section 1.2. A number of research questions are put forward in Section 1.3. A research design is described in Section 1.4 to answer these questions and fulfill the purpose of this research.

This research is expected to serve as a pilot study that provides insights for future studies. It is also expected to benefit not only CO₂ research but also decision making on CO₂ reduction as a tool for evaluating the performance of GHG reduction plans/actions.

Chapter 2: Literature Review

2.1 Introduction

As the concern for climate change rises, people are paying more attention to GHG emissions. The energy sector is a major source of GHG emissions and various types of measures are taken for reducing GHG emissions and mitigating climate change. It is expected that the effects of GHG emissions reduction (e.g. reducing local CO₂ concentrations) can be measured and evaluated by means of advanced CO₂ observation techniques.

This chapter provides an overview of the literature on three dominant themes:

1. Climate change, energy consumption and GHG emissions
2. Remote sensing CO₂ observations
3. Influential factors on CO₂ concentrations and CO₂ observations

This literature review enhances the understanding of the context of this research (in Section 2.2). It also introduces the key concepts and data sources for this research (in Section 2.3). In addition, this chapter summarizes several primary factors/issues that are necessary for interpreting the research results (in Section 2.4).

2.2 Climate Change, Energy Use and GHG Emissions

This section reviews the science of climate change and its relationship with GHG especially CO₂. Ontario's energy (electricity) system is taken as an example to introduce the measures that are taken to reduce GHG emissions and mitigate climate change.

2.2.1 Climate Change

The climate system is a complex and interactive system. It consists of five components: atmosphere, hydrosphere (oceans and other bodies of water), cryosphere (snow and ice), land surface, and biosphere (living things) (Team,2008). Climate is often defined as 'average weather'

regionally which is measured by major meteorological variables such as temperature, precipitation and wind over a period of time. Climate is differentiated from weather since the latter emphasizes short term meteorological variability. However, the change in weather over time identifies climate change (Change,2007).

2.2.1.1 Effects of Climate Change

Climate change is mainly caused by the GHGs in the atmosphere that absorb and emit radiations within thermal infrared (TIR). This process results in change of temperature, precipitation, snow and ice on the earth, sea level, and the occurrence of extreme events.

Temperature is an important topic for climate change studies (accounting for 40% of these publications) (Andrew *et al.*,2013). Surface temperature has been rising globally since 1880 based on various independent temperature datasets, e.g. historical direct instrumental measurements and recent remote sensing observations. A warming of 0.85 [0.65-1.06] °C is observed over this period (Stocker *et al.*,2013b). This conclusion on the rising temperature is in line with previous studies that explores the effects of climate change (Houghton *et al.*,2001, Walther *et al.*,2002, Berrang-Ford *et al.*,2011, Hansen *et al.*,2012).

The rise of temperature is spatially and temporally variable. Since the late 1950s, the temperature of the troposphere has been rising slightly faster than surface temperature, while the stratosphere has cooled since 1979 (Change,2007). As for the oceans from a global perspective, the warming is largest near the surface (Stocker *et al.*,2013b). In addition, substantial decadal and interannual variability is observed using a single longest dataset available (IPCC 2013), as shown in Figure 2.1.

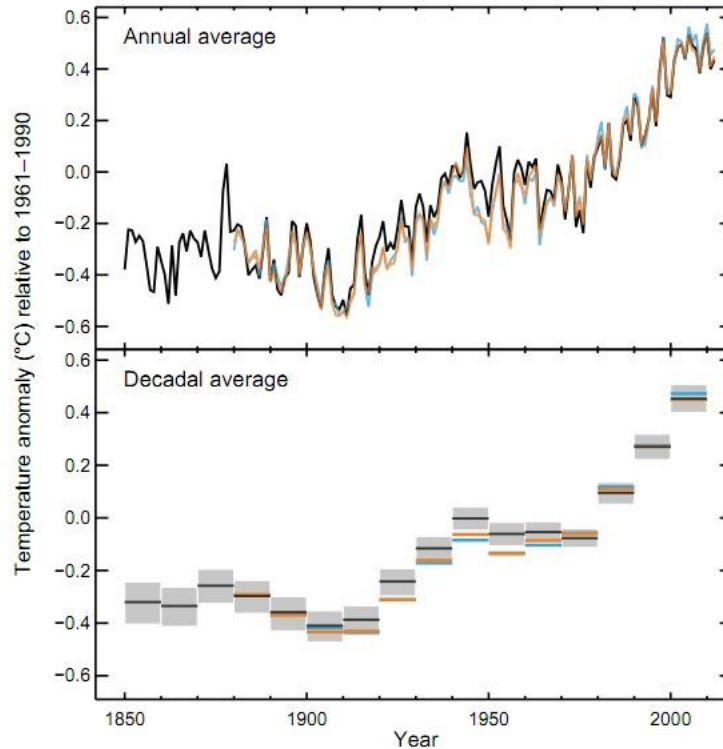


Figure 2.1 Observed Globally Averaged Combined Land and Ocean Surface Temperature Anomaly 1850-2012

Source: Climate Change 2013, Working Group I Contribution to the Fifth Assessment Report of the IPCC: the Physical Science Basis

The change of precipitation pattern is another main focus of climate change studies. Among these studies the consistency is very high with respect to the impact of climate change on precipitation, e.g. wet areas get wetter especially in mid to high latitudes, dry and arid areas get more so generally throughout the subtropics; precipitation in high latitudes (Northern Hemisphere) increases and decreases in China, Australia and the Small Island States in the Pacific; more precipitation occurs in the form of rain instead of snow, etc. (Dore,2005, Jones *et al.*,2007, Bhutiyani *et al.*,2010, Berrang-Ford *et al.*,2011, Trenberth,2011).

As global precipitation is affected by climate change, the risk of hydrological extreme events increases correspondingly. The intensity and frequency of floods increase (normally in spring when precipitation occurs as rain and the snow melts simultaneously) usually at short time scales associated with thunderstorms, orographic rainfalls, extratropical cyclones, etc. On the other hand, the risk of droughts is increased (normally occurs in summer and lasts from months to years), which often lead to devastating wildfires and heat waves (Trenberth,2011).

The loss of ice and the rise of sea level can be observed globally with high confidence. According to the fifth Assessment Report of the IPCC, ‘the average rate of ice loss from glaciers around the world excluding glaciers on the periphery on the ice sheets was very likely 226 [91 to 361] Gt yr⁻¹ over the period 1971 to 2009, and very likely 275 [140 to 410] Gt yr⁻¹ over the period 1993 to 2009’. The average of sea level rise was 2.0 [1.7 to 2.3] mm yr⁻¹ over the period 1971 to 2010 and 3.2 [2.8-3.6] mm yr⁻¹ for 1993 to 2010 (Church and White,2011, Gregory *et al.*,2013).

In summary, all the above-mentioned changes provide strong evidence of climate change. Moreover, these changes became more obvious since the mid-20th century.

2.2.1.2 Forcings for Climate Change

Climate change is driven by internal dynamics and external factors (called forcings). The external forcings consist of natural phenomena and anthropogenic change in atmospheric composition especially the GHGs (Change,2007).

The earth surface temperature depends on the incoming energy from the sun and outgoing energy from the earth. A shift of this energy balance could make the earth surface warmer or cooler resulting in a variety of climate changes [United States Environmental Protection Agency (EPA), 2012]. GHGs in the atmosphere absorb and re-emit the energy radiated from the earth, and ‘trap’ the energy in the lower atmosphere (EPA, 2012).

The primary GHGs are water vapor, carbon dioxide, methane, nitrous oxide, and ozone. These GHGs are major causes for the increased temperature. Without these GHGs, the surface temperature would be approximately 33 °C lower (Karl and Trenberth,2003, Solomon,2007).

Since the start of the Industrial Revolution, combustion of fossil fuel (carbon based fuels such as coal, oil, and natural gas) and exploitation of forest have contributed to 40% increase of CO₂ concentration from 280ppm in 1750 (Prentice *et al.*,2001) to 392.6ppm in 2012 (NOAA/ESRL, 2012). As stated before, the annual CO₂ emissions from fossil fuel combustion and cement production in 2011 is 14.5% higher than the average annual emissions over 2002 to 2011 and 54% above the 1990 level.

This occurred regardless of the large uptake capacity of natural CO₂ sinks (Yadav and Mishra,2013). From 1750 to 2011, fossil fuel combustion, cement production, deforestation and other land use changes have released 555 [470 to 640] GtC into the atmosphere. Of these

anthropogenic CO₂ emissions, 240 [230 to 250] GtC (43.2%) have accumulated in the atmosphere and the remaining are taken up by the ocean and land ecosystems (Stocker *et al.*,2013a). A majority of peer studies made a consistent conclusion that human activity is the main cause of increased atmospheric CO₂ concentration and the dominant forcing for the observed warming since the mid-20th century (Houghton and Woodwell,1989, Houghton,1996, Vitousek *et al.*,1997, Watson,2000, Oreskes,2004, Pielke,2005, Min *et al.*,2011, Montzka *et al.*,2011, Goudie,2013, Wang *et al.*,2013).

2.2.1.3 Climate Change Mitigation

Taking into account the considerable GHG emissions generated by human activity, there is an urgent need to take measures to reduce GHG emissions and mitigate climate change. Climate change mitigation has been studied from diverse perspectives (politically, technologically and socially) in terms of evaluating mitigation potentials, contribution to sustainable development, risk, cost, etc.

The major focus of climate policies and technologies is on reducing GHG emissions from the regional or national energy system. Possible options include, but are not limited to energy efficiency and conservation, renewable energy (RE), fossil fuel reduction/switching, nuclear power, carbon capture and sequestration (CCS) (Mitigation,2011). Each option has been investigated in depth in previous studies (Sutherland,1991, Grubb *et al.*,1993, Patterson,1996, Parker *et al.*,2003, Sims *et al.*,2003, St Denis and Parker,2009, Marv ão Pereira and Marv ão Pereira,2010, Zhou *et al.*,2010, Corner *et al.*,2011, Mitigation,2011, Edenhofer *et al.*,2012, Poortinga,2012, Suter and Shammin,2013, Levitan *et al.*,2014). Michel den Elzen *et al.* presented a set of technically feasible multi-gas emission pathways (envelopes) for stabilising greenhouse gas concentration at 450, 550 and 650 ppm CO₂ equivalent (CO_{2e}) and their trade-offs between direct abatement costs and probabilities to meet temperature targets (den Elzen *et al.*,2007). Based on an integrated assessment model, Keigo Akimoto *et al.* discovered that the optimal climate change mitigation should take into account various options among which energy saving is important throughout the 21st century and CO₂ sequestration is after the middle of the century (Akimoto *et al.*,2004). Using the ETSAP TIAM global energy systems model, Sanna Syri *et al.* discovered that the significant progress towards emission-free sources occur in the 21st century; CCS, nuclear power, wind power, biotechnologies and energy efficiency measures are major contributors (Syri *et al.*,2008).

In particular, as the demand for energy and associated services are increasing, RE is expected to make a considerable contribution to the development of reliable and healthy energy system. If implemented properly, RE could enhance social and economic development, reduce negative environmental impacts and improve human well-beings (Mitigation,2011). As the conventional energy specifically fossil fuel is expected to be reduced or eliminated in specific regions, the challenge for securing the energy supply rises, but could be overcome as the RE technologies are becoming more mature. In the meanwhile, fossil fuel switching can be a ‘no-regrets’ environmental policy for reducing CO₂ emissions without jeopardizing economic development as long as ‘the overall economic costs of reducing carbon dioxide emissions are considered’ (Marvão Pereira and Marvão Pereira,2010).

The primary international treaty on climate change is the United Nations Framework Convention on Climate Change (UNFCCC). As an amendment to the UNFCCC and an international agreement on combating climate change, the Kyoto Protocol came into force in early 2005 and ended at the end of 2012. At present, most climate policies are centered to the post-Kyoto climate change mitigation regimes. The mitigation architectures have different impacts on different groups of countries. Dalia Streimikiene and Stasys Girdzijauskas carried out an analysis on the post-Kyoto mitigation regimes and their impacts on sustainable development. They concluded that most assessments of climate change measures (as of 2009) are partial and incomplete. More holistic assessments were encouraged against economic, social and environmental dimensions of sustainable development, i.e. acceptability, availability and accessibility (Streimikiene and Girdzijauskas,2009).

The mitigation against climate change needs efforts from all sectors. Not only government actions, but also spontaneous mitigations of energy consumers are needed in this course. Semenza *et al.* identified a number of cognitive, behavioral and structural obstacles to voluntary mitigation. The study also suggested government policy eliminate economic, structural and social barriers to change and advance accessible and economical alternatives (Semenza *et al.*,2008). Attention needs to be given to the social and psychological motivations regarding why these barriers to individual commitment exist even though the public are concerned about climate change (Stoll-Kleemann *et al.*,2001).

Coordination and cooperation among nations are also crucial to the success of mitigation against climate change. A major focus of debates over climate policy is on the design of instruments that impose a price on the emission of CO₂ and/or other GHGs such as cap-and-trade and emission

taxes. However, it was found that these policy instruments could cause adverse competitiveness effects for the energy-intensive firms in developed countries when they make continuous efforts on combating climate change while major developing countries do not move forward (Aldy and Pizer,2011).

By taking effective mitigation measures, the GHGs' concentrations are expected to decrease and the negative impacts of climate change on the environment (rising temperature and sea level, etc.) could be alleviated. In this regard, an interesting question rises in terms of how long it takes for the mitigation measures to take effect.

Mitigation against climate change is a long-term process since the severity of human-induced climate change is determined by not only the magnitude of the change but also the potential for irreversibility. No climate policies or actions are capable of yielding immediate outcomes on reversing climate change. The irreversibility of climate change was first highlighted by Matthews and Caldeira in 2008. Their study showed that global average temperature stabilized and remained at a nearly constant level following CO₂ emissions (Matthews and Caldeira,2008). A comparison of 8 climate model simulations showed persistence of high global temperature for at least several centuries across all models even though CO₂ emissions were eliminated (Plattner *et al.*,2008). Solomon *et al.* found that the atmospheric CO₂ concentration was irreversible for 1000 years after the cessation of CO₂ emissions; global average temperature increased as CO₂ concentration increased and then remained approximately constant (within ± 0.5 °C) until the end of the millennium; the rise of sea level was also irreversible (Solomon *et al.*,2009). A recent study discovered that global temperature could be stabilized with aggressive mitigations, but the rise of sea level cannot be stopped over the next several centuries (Meehl *et al.*,2012). One major reason for the irreversibility of climate change is that the long-term warming legacy of anthropogenic GHGs is primarily determined by the CO₂-induced warming while CO₂ has a long life time in the atmosphere (Solomon *et al.*,2013).

2.2.1.4 Skepticism about Climate Change

Although scientific evidences are becoming more certain and political and media messages appear to be increasingly confident, skepticism about climate change exists and public attitudes and actions on climate change do not follow the scientific evidence closely. Skepticism in public attitudes is seen as a significant barrier to public engagement (Corner *et al.*,2012).

Some studies implied that this is because of ignorance and misunderstanding on the part of the public (Whitmarsh,2011) while others suggested that climate skepticism is rooted in people's core values and worldviews (Poortinga *et al.*,2011). Public attitudes seem to be distinguished among different groups of peoples by considering their ages and socio-economic backgrounds. Based on a study in Britain, climate skepticism is particularly common among older individuals from lower socio-economic backgrounds who are politically conservative and hold traditional values; while it is less common among younger people from higher socio-economic backgrounds who hold self-transcendence and environmental values (Poortinga,2012).

Skepticism can be beneficial to improving the existing knowledge and overcoming scientific uncertainty. However, skeptics on climate change simply ignore or vigorously criticize the strong evidences that support human-induced climate change; while on the other hand, any untenable argument, blog, or internet message that purports to refute climate change is embraced. 'Denial' and 'denier' are introduced as more accurate terms than 'skepticism' and 'skeptic' to define those who are against climate change and associated policies or regulations. The motivations vary considerably among the deniers from economics (e.g. fossil fuel industry) to individuals, but they share the common opposition to governmental regulatory efforts to ameliorate climate change (Dunlap and McCright,2011). Although the skeptical claims differ sometimes and evolve over time (such as 'there is no warming and the unstable temperature is natural', 'the change is not caused by humans' and 'the change is no harm'), the themes of 'no need for regulations' remain unchanged (McCright and Dunlap,2000, Oreskes and Conway,2010, Dunlap and McCright,2011). By attacking climate science and individual scientists, the deniers seek to influence climate policy making by removing the scientific basis from such policies.

Public reluctance on adaption to climate change or postponed actions can be highly detrimental to the effectiveness of existing climate policies and seriously jeopardize the policy making for the future. The need is urgent to enhance public awareness of the severe consequences of climate change. It is also crucial to weaken or eliminate the negative influence of public denial on climate policy implementation and policy making process by eliminating economic, structural and social barriers to change and advancing accessible and economical alternatives.

Although there is a long way to go for mitigating climate change, it is encouraging and inspiring to see successful climate/energy policies and actions all over the world. The next sub-section introduces the electricity system of Ontario and how Ontario's electricity system evolved in response to climate change policy.

2.2.2 Electricity System of Ontario

Electricity is a major driver of the economy of Canada. The electricity system has undergone a significant change over the past two decades as Canada's economy is prospering and population keeps growing (EIA,2011). A reliable and cost-effective electricity system is crucial to the prosperity of Canada and Canadians' well-being.

The supply mix of the electricity system varies among provinces and changes over time. A series of major changes to Ontario's electricity system started from the mid 20th century when coal-fired GS were established to supplement hydro-electric capacity and were followed by nuclear generating facilities in the 1970s and 1980s to meet the increasing demand for electricity. Ontario's electricity system went through another significant change after 2002. Considering the aging of large generating infrastructures and the impacts of dirty power generation on human well-being, an increasing amount of clean and renewable sources were desired for power generation. A variety of policies were made and actions were taken to advance and adjust to this change. Some landmark programs (e.g. feed-in-tariff program) received positive feedbacks from the public and scholars and were regarded as beneficial to modernizing the electricity system while achieving the goal of GHG emissions reduction (Stokes,2013, Pal,2014).

2.2.2.1 Electricity Demand and Supply

By 2010, Ontario achieved a net surplus supply situation. The demand was declining and the supply growing. The demand for electricity is expected to remain approximately flat for the next decade (OPA, 2013).

As of 2005, the provincial demand for electricity had been increasing at an annual rate of approximately 0.5% over the past decade (OPA, 2005). This was mainly because of population growth, economic growth and climate variability (Statistics Canada, 2007; Ontario Ministry of Finance, 2006; Energy Information Administration, 2004). As the total electricity demand was forecast to rise continuously, the supply was proposed to grow to meet such demand. As of June 2012, Ontario's electricity generation capacity had increased by 13% since September 2003 (Ontario Clean Air Alliance, 2012).

However, in recent years (2011-2013), Ontario's electricity demand has been falling and is expected to remain no higher than the current levels for the next few years (Zahedi *et al.*,2013).

The falling demand for electricity does not necessarily imply an economic downturn or low economic growth; on the contrary, Ontario was recovering from the economic recession in 2008 and the GDP increased steadily over the period of 2009-2012 (there was a decrease of GDP in 2009 compared to 2008, i.e. 1.46%) (Statistics Canada, 2013). The reduced demand is mainly attributable to effective energy conservation, increased energy efficiency and the transition of Ontario's economy to be more efficient and less energy intensive (OPA, 2014). Ontario's annual energy demand over the 2000-2013 period is shown in Table 2.1.

Table 2.1 Ontario Annual Energy Demand

Year	Total Demand (TWh)	Increase over Previous Year (%)
2000	147	2.1
2001	147	0
2002	153	4.1
2003	152	-0.70
2004	153	1.10
2005	157	2.30
2006	151	-3.80
2007	152	0.70
2008	148	-2.30
2009	139	-6.10
2010	142	2.20
2011	141.5	-0.35
2012	141.3	-0.14
2013	140.7	-0.42

Source: IESO, 2014 (<http://www.ieso.ca/Pages/Power-Data/Demand.aspx>)

A significant change is also seen on the supply side especially since 2003. In 2003, nuclear, hydroelectric and coal power generation supplied the majority of electricity in Ontario. Concerns arose with respect to the adequacy and reliability of the generation facilities as the infrastructures were aging and the electricity demand continued to increase. Ontario encountered a shortfall in supply in 2003 as the provincial generating capacity dropped by 6% while the demand increased by 8.5% compared to 1996. On the other hand, Ontario was dependent on coal-fired power generation. Coal provided 25% of the Ontario's electricity supply in 2003. Combustion of coal not only accounted for approximately 90% of provincial GHG emissions in the electricity sector but also produced detrimental air pollutants. The average annual financial, health and environmental cost of coal was calculated to be \$4.4 billion (OPA, 2014).

In this regard, Ontario endeavored to achieve a reliable, clean and cost-effective electricity system mainly through incorporating more renewable sources for electricity generation, reducing the use of coal, and fossil fuel switching from coal to natural gas. Taking participating utilities in the IESO-administered market for example, the change of supply mix over the period 2003-2013 is summarized in Table 2.2. The figures indicated newly installed or refurbished in the case of nuclear (positive) or retired (negative) capacity in that year.

Table 2.2 Ontario Electricity Supply Mix Change from 2003 to 2013: IESP Participants. (in MW)

Year	Nuclear	Natural Gas	Coal	Hydro	Wind	Others (Wood Waste, Bio-Gas, etc.)	Total
2003	1285						1285
2004	782	612		80			1474
2005	515		-1130				-615
2006		117			396		513
2007				20	76		96
2008		1547		24	233		1804
2009		1966		137	380		2483
2010		992	-2000		101	47	-860
2011			-980		248		-732
2012	1552	438	-221		99		1868
2013			-3001		372	40	-2589
Total	4134	5672	-7332	261	1905	87	4727

Source: IESO, 2014 (<http://www.ieso.ca/Pages/Power-Data/Supply.aspx>)

Most increased renewable sources, excluding hydro, across the province are not reflected in the IESO database. Presently, Ontario has more than 18500 MW of renewables online or announced consisting of more than 9000MW of hydroelectric capacity and more than 9500MW of wind, solar and bioenergy capacity, etc. The target capacity is 9300MW for hydro by 2025 and 10700MW for wind, solar and bioenergy by 2021 which together account for about half of the installed capacity (OPA, 2013). Coal-fired power generation was dramatically reduced, i.e. less than 3% (2013) vs 25% (2003) of total supply.

New electricity sources were cleaner and less GHG-intensive than coal. As of 2013, SO₂ emissions due to coal-fired power generation were reduced by 93%; NO emissions dropped by 90%; mercury level was at its lowest over the past 45 years; and there was a reduction in GHG emissions by almost 90%, compared to the 2003 level (OPA, 2014).

As a consequence of rising supply and falling demand, the market price of electricity in 2013 (2.65 cents/kWh) has dropped by 54% since 2003 (5.76 cents/Kwh) (IESO, 2014). However, the consumers have not benefited from the reduced market price since the Global Adjustment Charge is imposed in order to compensate the rate paid to electricity generator and conservation and demand management programs. Moreover, considering the limited capability of nuclear GS to lower the output when demand declines (Caldicott,2013), it is highly likely that there is an excessive surplus of supply for numerous hours. In this case, Ontario pays consumers in Manitoba, Quebec and the U.S. to take away the excess electricity (OEB, 2012). As a result, this further increases the cost of Ontario's electricity system.

Considering the projected electricity demand and the cost for maintaining existing large generating facilities, the government proposed a series of plans while securing a reliable electricity supply: deferring the construction of nuclear capacity at Darlington, early retiring Pickering GS (the cost of Pickering GS is among the highest in the North America), and shutting down the coal-fired units (OPA, 2014). More flexible, dispatchable and cost-effective options such as renewable sources and combined heat and power natural gas-fired power generation are expected to play more important roles in securing the electricity supply. None of these can be achieved without efficient, reasonable and Ontario-suitable policies and plans.

2.2.2.2 Clean Electricity Generation

Ontario has a series of policies on improving the province's electricity system and reducing GHG emissions. Ontario is making progress on its journey to achieve the long-term goal—a reliable, modern, clean and sustainable electricity system that emphasizes economic, environment and social benefits.

Clean energy is a major principle for policy making and policy instruments especially since 2003 when the McGuinty Government and the Liberal Party came into power. In Canada, many jurisdictions are reforming their electricity sector with policies to promote the use of clean energy

as an effort to reduce GHG emissions and boost economic development(Jaccard *et al.*,2011, Holburn,2012). Ontario is one of the two most active jurisdictions (the other is British Columbia).

In Ontario, there was no long-term energy plan before 2003. In 2004, OPA was established as the province's long-term planner. OPA is a part of Ontario's electricity system associated with the Ministry of Energy and a variety of other organizations including OEB, IESO, OPG and Ontario's non-utilities generators (NUGs), Hydro One and other electricity distributors, and a number of electricity retailers. These organizations play different roles in ensuring the reliability, cost-effectiveness and sustainability of Ontario's electricity system in a collaborative manner. The Ministry of Energy is responsible for proposing the provincial energy policy framework to direct Ontario's electricity system development and regulate the electricity market; OPA endeavors to 'procure new generation, initiate conservation measures and craft a long-term plan for the electricity sector'; OEB regulates the electricity and natural gas sectors; IESO is responsible for monitoring and managing daily operations; OPG and NUGs generate electricity using various sources of fuel; Hydro One and other distributors deliver the electricity to the consumers (OPA, 2011).

The motivation to promote renewable energy through political influence rather than market mechanism originated when the Liberal Party were in office in 2003 (Hoberg and Rowlands,2012). At that time, the government was committed to shutting down the coal-fired power stations by the end of 2007. It was expected that the renewable sources would be capable of offsetting the supply shortfall. A significant practice in using renewable energy for electricity generation was carried out in March 2006. The McGuinty Government announced the first feed-in-tariff program in North America, i.e. the Renewable Energy Standard Offer Programme (RESOP). However, this program was suspended in May 2008. The RESOP was argued as a failure in attracting its target audience of small developers (Holburn,2012). Major causes for its failure were discussed such as unanticipated transmission constraints and program design problems (Mabee *et al.*,2012, Nishimura,2012). Despite the demise of this program, the innovation (in North America) was remarkable and it provided valuable lessons for further steps in renewable energy policy.

The Green Energy and Green Economy Act was created to expand renewable energy generation, encourage energy conservation and promote the creation of clean energy jobs (Ontario Ministry of Energy, 2013). This Act passed into law in May 2009 and enacted the FIT and microFIT program which considered wind, solar, bioenergy and waterpower as qualified energy sources.

The FIT program was intended for projects larger than 10kW while the microFIT projects that were 10kW or smaller focused on the residential sector. Within the first year, applications totaled over 15000MW. For the first phase of FIT and microFIT programs, about 2000 contracts were executed with approximately 4662MW of capacity as of August 7th 2012 (not all of them were online or proceeded). As of September 10th 2013, the total supply of OPA contracted capacity in service was 4541MW consisting of 185MW of waterpower (4.08%), 1224MW of solar (26.94%), 60.4MW of bioenergy (1.33%) and 3072MW of wind (67.64%). The clean energy capacity is still rising. The total capacity of solar, waterpower and bioenergy is expected to reach 10700MW across the province (OPA, 2014).

Despite implementation challenges and political resistance to the FIT program, e.g. argument on the cost of the FIT program, local resistance to wind farms and criticism about the transparency of program implementation, promoting renewable energy for electricity generation is beneficial to Ontario from a holistic and long-term perspective. The electricity supply can be secured by incorporating various types of energy sources. The diverse supply mix makes the province less dependent on specific energy sources that may confront temporary shortages such as nuclear power. Motivations and/or measures on cutting down the cost of renewable energy deployment specifically the FIT program (e.g. reduce the rate paid to the generators) are expected to stimulate innovation of renewable energy technology considering that currently the renewable sources are mainly wind and solar. This further encourages Ontario to pursue a leader position in green energy in North America. The proportion of renewable energy in total electricity production in Ontario is higher than that in Ontario's major competitor New York (27% vs 23% in 2013), though the proportions of non-hydro renewables in both jurisdictions are very close and the use of coal for power generation by New York is also decreasing, i.e. less than 10% in recent years [OPA, 2014; The U.S. Energy Information Administration (EIA), 2014].

2.2.2.3 GHG Emissions Reduction

Canada is committed to tackling climate change through sustained action to build a low-carbon economy that includes reaching a post 2020 global climate change agreement (Environment Canada, 2013), which requires the total GHG emissions to be reduced by 17% by 2020 relative to 2005 emission levels (737Mt CO_{2e}). In 2011, CO₂ and CH₄ accounted for 92% of total GHG emissions in Canada, 79% and 13% respectively. The energy sector was responsible for the majority of Canada's GHG emissions, i.e. 81% or 572Mt CO_{2e}, resulting from stationary

combustions, transportation and fugitive sources. The remaining 19% came from the agriculture sector (8%), industrial sector (8%) and waste sector etc. (3%).

Canada is only half way to meeting the target of ‘17% reduction’. Figure 2.2 shows Canada’s emission trends for 2005-2011 by sector. The electricity sector is a major contributor, as in 2011 ‘emissions from electricity and heat generation have been the largest driver of the overall downward trend, dropping by 30Mt since 2005, primarily the result of reduced generation by coal, switching to renewable resources and improved efficiencies in combustion generation’ (Environment Canada, 2014). In 2011, the emissions from manufacturing decreased by 12.1Mt (11%), but transportation emissions rose by 10.6Mt (5.8%) mainly due to diesel transport. As published in October 2013, the national emissions trend indicates that the national gross GHG emissions would be 734Mt in 2020 as a result of joint efforts across the country (Environment Canada, 2014). This is 128Mt lower than the emissions if no actions were taken since 2005. The gap between the projected emissions and the target is estimated to be 122Mt.

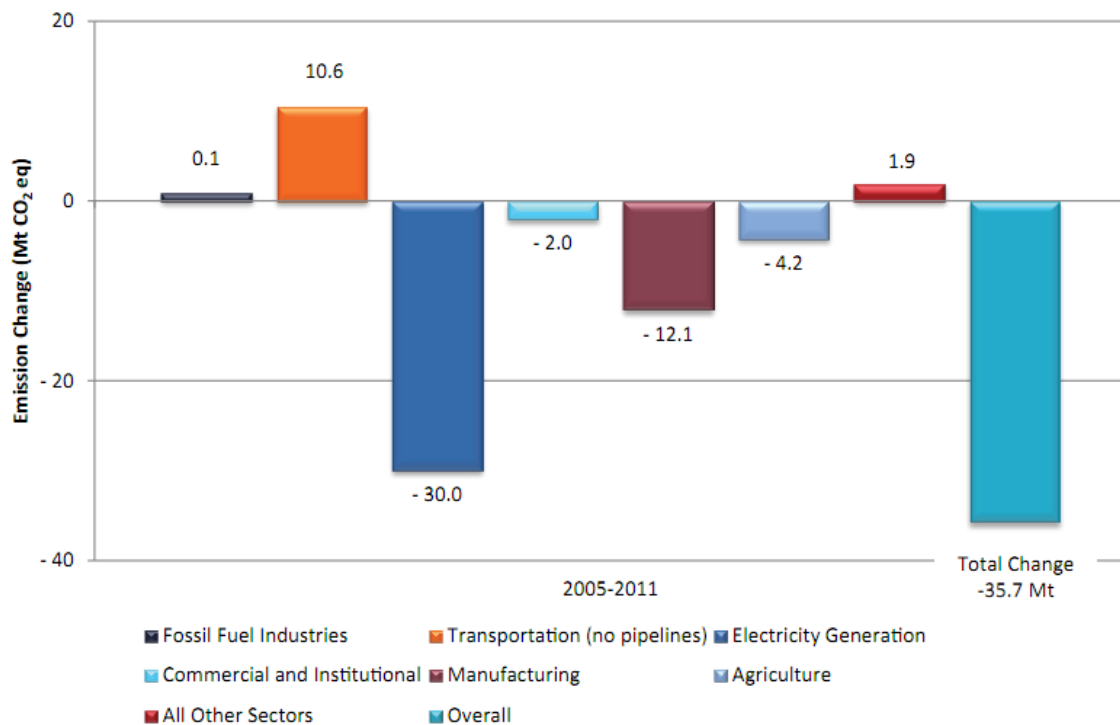


Figure 2.2 National Emission Trends for 2005-2011 by Major Sector

Source: Canada’s National Inventory Report Submitted to the UNFCCC in 2013

In Ontario, the total GHG emissions are decreasing. Table 2.3 presents Ontario’s GHG emissions by sector in 1990, 2000 and over the period 2005-2011 excluding 2006. Based on the GHG

emissions from most sectors and/or subsectors, the emissions in 2009 are exceptionally lower than the others most likely due to the impacts of the recession of global economy, e.g. the energy sector ‘shrank’ and the industrial processes ‘slowed down’. Since energy and industrial processes are two primary sectors that contribute to provincial GHG emissions, the total emissions in 2009 are the lowest observed.

Table 2.3 Ontario’s GHG Emissions by Sector (in kt CO_{2e})

Sector	1990	2000	2005	2007	2008	2009	2010	2011
Energy	131000	165000	161000	156000	148000	129000	135000	132000
<i>Stationary Combustion</i>	81700	104000	95600	93600	87000	69000	72700	70900
<i>Electricity and Heat Generation</i>	25500	43100	34100	32600	27100	14800	19600	14800
<i>Transport</i>	47800	60300	64200	60500	59000	58400	60700	59000
<i>Fugitive Sources</i>	1210	1540	1610	1640	1630	1610	1660	1650
Industrial Processes	29900	23400	27400	27400	26800	20400	21900	22600
Agriculture	10000	9600	9700	10000	9700	10000	10000	9600
Waste	6000	6000	6700	6800	6700	6700	6700	6800
Solvent & Other Product Use	66	170	150	130	130	100	94	96
Total	177000	205000	205000	200000	191000	166000	174000	171000

Source: Canada’s National Inventory Report Submitted to the UNFCCC in 2013

Note: Based on sector categorization by the IPCC, ‘stationary combustion’, ‘transport’ and ‘fugitive sources’ are three subsectors of ‘Energy’, and ‘electricity and heat generation’ (the so-called electricity sector) is a subsector of ‘Stationary Combustion’.

Ontario’s decision to shut down its coal-fired power plants is the largest climate change initiative in North America. From 2010 to 2011, the emissions from the electricity sector decreased by 4.8Mt (24%). Overall, Ontario’s electricity sector experienced a decrease of 19Mt (56%) compared to the 2005 level mostly attributable to the closures of coal-fired power plants.

By making intensive efforts on reducing GHG emissions and ‘greening’ the electricity system, Ontario acts as a significant role model in meeting the federal target on the reduction of GHG emissions. Notably, there are still great potentials for Ontario to reduce GHG emissions from

other sectors such as transport and waste disposal. Technological innovations are expected to play significant roles in achieving the long-term goal (Bahn *et al.*,2013, Schneider *et al.*,2013, Streimikiene *et al.*,2013, Takata *et al.*,2013). Moreover, policies are indispensable for promoting specific types of advanced low-carbon technologies while emphasizing the cost-effectiveness taking into account environmental, economic and social benefits from a holistic perspective.

Given the high political priority to advance policies that reduce GHG emissions, an important need is to be able to systematically measure and monitor GHG emissions. One approach to meet this need is to use remote sensing technologies and modelling techniques.

2.3 Remote Sensing CO₂ Observations

The atmospheric GHG concentrations are determined by a series of factors in addition to the surface emissions, e.g. meteorological conditions, atmospheric transport and distribution of sources and sinks. Though GHG emissions are monitored and reported regularly under particular regulations in some regions (e.g. the UNFCCC requires Parties³ to report their national emissions and removals of GHGs, and Ontario requires large emitting facilities to report their annual GHG emissions to the Ministry of Environment), direct observations of global or regional GHG concentrations are currently limited to the research domain and rarely involved in political practice such as evaluation of policy instruments and GHG management. A better understanding of the GHG concentrations and their distribution associated with the physical processes or factors that determine the concentrations can provide insights into a broader and more comprehensive policy framework for climate mitigation. In this regard, remote sensing is a valuable and promising tool for providing sufficient accurate measurements of GHG concentrations globally and locally.

This section introduces the basic spectral properties of CO₂ and provides a brief description of major satellite-borne infrared sounders for CO₂ observation. The GOSAT CO₂ observations are then discussed including the instrument specifications and a comparison of different retrieval

³ The UNFCCC divides countries into three main groups: Annex I Parties, Annex II Parties and Non-Annex I Parties. Annex I Parties include the industrialized countries that were members of the OECD (Organisation for Economic Co-operation and Development) in 1992, plus countries with economies in transition (the EIT Parties). Annex II Parties consist of the OECD members of Annex I, but not the EIT Parties. Non-Annex I Parties are mostly developing countries (UNFCCC, 2014).

algorithms based on GOSAT spectral data. In addition, the reliability of GOSAT CO₂ observations is examined based on the calibration and validation work in the literature.

2.3.1 Overview

CO₂ absorbs the radiation from the earth and reemits part of the energy back to the surface. This is the primary process that keeps the heat in the lower atmosphere and results in increasing temperatures. The spectral absorption characteristics of CO₂ are distinguished from other GHGs. Therefore, it provides an opportunity to measure the abundance or concentration of CO₂ using a particular range of spectrum.

The electromagnetic spectrum is divided into 7 segments: Gamma Ray (less than 0.01nm), X-Ray [0.01-10nm], Ultraviolet [10-380nm], Visible [380-700nm], Infrared [700nm-1mm], Microwave [1mm-1m] and Radio [1mm-100000km]. The radiation by the earth is in the range between 5 μm and 60 μm. The primary spectrums absorbed by CO₂ are three narrow bands in the infrared wavelength range, i.e. 2.7 μm, 4.3 μm and 15 μm (Horvath,1993), as shown in Figure 2.3.

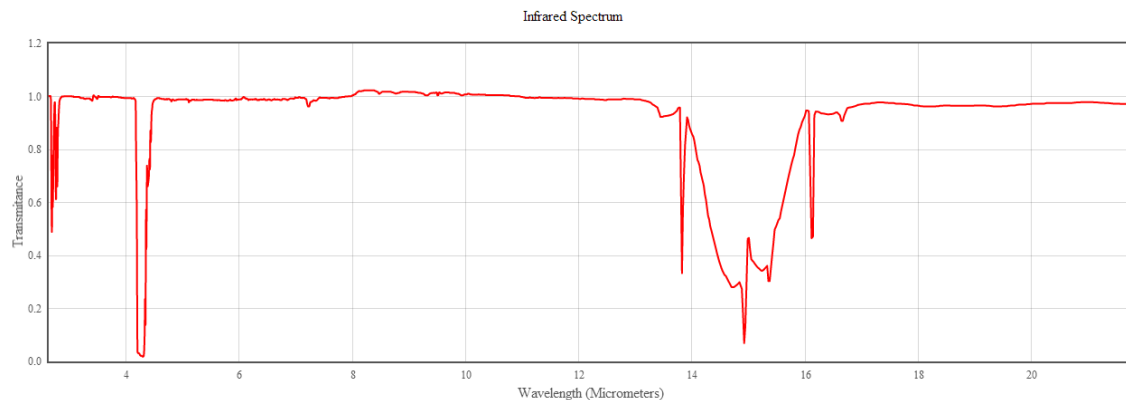


Figure 2.3 CO₂ Absorption Spectrum

Source: Data compiled by: Coblenz Society, Inc. Data compilation copyright by the U.S. Secretary of Commerce on behalf of the U.S.A.

Note: CO₂ absorption spectrum varies in the weak absorption bands among different articles and studies but there is a consistency with the three strong bands.

As for the division of infrared radiation, there are a number of criteria. The International Commission on Illumination (CIE) recommends the division of infrared radiation into three bands: IR-A [0.7 μm -1.4 μm], IR-B [1.4 μm-3 μm] and IR-C [3 μm-1000 μm]. The ISO20473 specifies three schemes: near-infrared (NIR) [0.78 μm-3 μm], mid-infrared (MIR) [3 μm-50 μm] and far-

infrared (FIR) [50 μm -1000 μm]. Astronomers typically divide the infrared spectrum as NIR [(0.7-1) μm to 5 μm], MIR [5 μm to (25-40) μm] and FIR [(25-40) μm to (200-350) μm] (NASA, 2007). Another commonly used scheme is NIR [0.75 μm -1.4 μm], short-wavelength infrared (SWIR) [1.4 μm -3 μm], mid-wavelength infrared (MWIR) [3 μm -8 μm], long-wavelength infrared (LWIR) [8 μm -15 μm] and FIR [20 μm -1000 μm] (Byrnes,2009). In addition, thermal infrared is a widely used term in remote sensing specifying the range between 3.5 μm and 20 μm or 5.6 μm and 1mm. Most remote sensing applications make use of the 8 μm to 13 μm range. The main NIR absorption bands of CO₂ are 1.4 μm , 1.6 μm , 2.0 μm , 2.7 μm and 4.3 μm (Rothman *et al.*,2009). Particularly, the 1.6 μm (the CO₂ weak absorption band) is mostly exclusive to CO₂ among the GHGs.

Considering the possibility that the literature on remote sensing CO₂ observations and measurements adopts different schemes, e.g. the SCIAMACHY channel 7 [1.94 μm -2.04 μm] was referred as NIR (Buchwitz *et al.*,2004), SWIR (Hoogeveen *et al.*,2007) or NIR/SWIR (Buchwitz *et al.*,2010), this study does not provide a standard for the subdivision of infrared spectrum. Instead, the established, though sometimes overlapping, terminology such as NIR or SWIR are used to match the research or literatures that are reviewed or cited.

2.3.2 Measuring CO₂ from Space

CO₂ concentrations are measured by both *in situ* and satellite-borne instruments. For *in situ* measurements, ground-based CO₂ observations using flask sampling are widely used by NOAA to provide long-term records of CO₂ concentrations, e.g. Climate Monitoring and Diagnostics Laboratory (Saitoh *et al.*,2009). Instruments onboard aircrafts are mainly used for obtaining CO₂ concentrations in upper troposphere (Matsueda *et al.*,2002). Ground-based CO₂ measurements served as the primary data source for estimating the strength of CO₂ sources and sinks until recent years when space-based instruments were developed to make up for the limitations of ground-based measurements (Saitoh *et al.*,2009), i.e. spatiotemporal sparsity for CO₂ sources and sinks estimation (Rayner and O'Brien,2001, Houweling *et al.*,2004). Measuring atmospheric components from space are challenging. The target signal must be separated from radiative interference from temperature, surface and cloud parameters, water, and other trace gases (Kulawik *et al.*,2012). However, remote sensing instruments provide a unique perspective on the state of the environment from short term to long term and on a local to global scale (Clerbaux *et al.*,2009). By using Earth's or atmosphere's thermal radiation, reflected solar radiation or solar radiation itself, remote sensing sounders are demonstrated capable of valuable information on air

quality (Richter *et al.*,2005), emission sources (Frankenberg *et al.*,2008) and climate change issues (Worden *et al.*,2008).

2.3.2.1 HIRS

The High-Resolution Infrared Radiation Sounder (HIRS) is one of the three instruments installed on the TIROS Operational Vertical Sounder (TOVS) onboard NOAA's series of polar orbiting satellites. These series of satellites have been providing continuous measurements of the earth's surface and atmosphere since 1979. The HIRS observes the earth-emitted radiation in the infrared with 19 infrared channels covering 3.8 μm to 15 μm (there is another channel in the visible).

HIRS radiances have been used for estimating the temporal variations of CO₂ concentration at different scales by analyzing the 4.3 μm and 15 μm bands. The signatures of annual and seasonal variations of CO₂ along with other GHGs were captured using the 19 channels of HIRS on TOVS and the results showed a high agreement with the knowledge of atmospheric cycle of trace gases that was known to that date (Chédin *et al.*,2002a, Chédin *et al.*,2002b, Chédin *et al.*,2003b). At finer temporal scales, 48 maps of monthly mean mid-tropospheric CO₂ concentration were produced at a resolution of 15°x15°. The method-induced standard deviation of the CO₂ retrievals was estimated to be of the order of 3ppm (less than 1%). In particular, the impact of El Nino Southern Oscillation (ENSO) events was clearly seen and confirmed by *in situ* observations and model simulations (Chédin *et al.*,2003c). By analyzing the night-minus-day difference of CO₂ concentration, the diurnal variations of CO₂ caused by biomass burning was well detected which was in accordance with the recorded activities of diurnal and seasonal biomass burning (Chédin *et al.*,2005).

2.3.2.2 IASI

The Infrared Atmospheric Sounding Interferometer (IASI) is a passive IR remote sensing instrument onboard the European MetOp-A platform. It uses an accurately calibrated Fourier Transform Spectrometer operating in the 3.7 μm -15.5 μm spectral range and an associated infrared imager operating in the 10.3 μm -12.5 μm spectral range [National Centre for Space Studies (CNES), 2014].

The major goal of IASI mission is to provide temperature and humidity profiles for use in the understanding and making atmospheric forecasts. It also provides the quantification of

atmospheric components such as CO₂, CH₄ and O₃ (EUMETSAT, 2014). Studies on using IASI to measure CO₂ alone are very few. A pre-launch feasibility analysis indicated that for CO₂ retrieval using IASA data, a careful averaging over area of 500 by 500 km² and 2 weeks should be able to extract change at the level of 1% or less in the total column CO₂ amount (Chédin *et al.*,2003a). In 2009, the IASI CO₂ data for the first operation year of MetOp (2008) were used to retrieve the upper tropospheric CO₂ from 11 to 15km, in clear-sky conditions, in the tropic and over the ocean (Crevoisier *et al.*,2009). The precision was estimated to be 2ppm (~0.5%) over an area of 5 °×5 ° on a monthly temporal scale. The study identified ‘a strong seasonal cycle of 4ppm in the northern tropics’; ‘a more complex seasonal cycle in the southern tropics, in agreement with *in situ* measurements’; ‘a latitudinal variation of CO₂ shifting from a South-to-North increase of 3.5ppm in boreal spring to a South-to-North decrease of 1.5ppm in the fall, in excellent agreement with tropospheric aircraft measurements’; and ‘signatures of CO₂ emissions transported to the upper troposphere’.

2.3.2.3 TES

The Tropospheric Emission Spectrometer(TES) is onboard NASA’s Aura satellite focused on the troposphere, the layer of atmosphere that stretches from the ground to the altitude at which airplanes fly (JPL, 2014). TES is an infrared, high-resolution, Fourier transform spectrometer covering the spectral range from 3.3 μm to 15.4 μm (Beer,2006).

The satellite was launched in 2004 and the instrument TES is mainly targeted on O₃. Studies on CO₂ estimates with improved TES did not arise until recent years. A pilot study for the area between 40 °S and 45 °N found about one degree of freedom with peak sensitivity at 511 hPa. The estimated error is ~10ppm for a single target and 1.3-2.3 ppm for monthly averages on spatial scales of 20 °×30 °. The TES CO₂ estimates were compared to different sources of data and the highest correlation was found with the Mauna Loa surface data (Kulawik *et al.*,2010). If the biases in the data and model are well characterised, the uncertainty on annual estimates of CO₂ sources and sinks can be significantly reduced using the averaged data. A more recent study achieved better results by characterising the TES CO₂ biases and errors through comparisons to ocean and land-based aircraft profiles and to the CarbonTracker assimilation system (Kulawik *et al.*,2012). The actual errors ranged from 0.8-1.8ppm depending on the campaign that the TES data were compared to and the pressure level. The best result was generated from the comparison with the United States Southern Great Plains (SGP) Atmospheric Radiation Measurement (ARM)

between 2005 and 2011 measured from surface to 5km. The overall bias was -0.3ppm to 0.1ppm and standard deviations of 0.8ppm to 1.0ppm at different pressure levels.

2.3.2.4 AIRS

The Atmospheric Infrared Sounder (AIRS) has been widely used for middle-upper tropospheric CO₂ columns retrieval (Crevoisier *et al.*,2004, Chevallier *et al.*,2005, Chahine *et al.*,2008, Olsen *et al.*,2011, Pagano *et al.*,2012, Pagano and Olsen,2012). It began to serve in orbit on May 4th 2002 (aboard the NASA's Aqua spacecraft) and is still in operation. The purpose of AIRS is to promote researches on climate change and improve the ability of weather forecasting. This was one of the most developed atmospheric sounding system along with its partner microwave instrument AMSU-A. The 3D maps of air and surface temperature, water vapor, and cloud properties can be created by AIRS using a so-called cutting-edge infrared technology.

AIRS is a sun-synchronous cross-track scanning instrument orbiting at 705km above polar with an inclination of 98.2+/-0.1 degrees. The full swath width is 1650km, i.e., ground coverage of +/- 49.5 degrees, more than 95% of global daily coverage. Other than the thermal infrared sensor, a visible/near-infrared sensor is also onboard AIRS instrument providing Level 1b products. Table 2.4 describes the specifications of AIRS instrument suite and performance characteristics of AIRS.

Table 2.4 Specifications of AIRS

Parameter	AIRS Infrared radiances	AIRS Visible/NIR Radiances
Spatial resolution	13.5 km at nadir; 41 km x 21.4 km at the scan extremes	2.3 x 1.8 km (across-track, along-track)
Spatial sampling	90 1.1° footprints per scan (2.67 seconds)	8 x 9 pixels per AIRS 13.5 km footprint
Spectral range	2378 channels, 3.75-15.4 μm (650-2665 cm ⁻¹)	4 channels from 0.4-1.0 μm: Channel 1: 0.40-0.44 μm Channel 2: 0.58-0.68 μm Channel 3: 0.71-0.92 μm Channel 4: 0.49-0.94 μm
Spectral resolution	~1200 nominal (0.5-2cm ⁻¹)	N/A
Spectral accuracy	1ppm	N/A
Radiometric accuracy	< 0.2 K 3 sigma at 256 K	10%
Signal-to-noise	N/A	(ratio at albedo of 0.4) > 100
Data volume	56 MB per granule, 13.4 GB/day	11 MB per granule, 2.6 GB/day

Source: AIRS, JPL-NASA: <http://airs.jpl.nasa.gov/instrument/specs/>

As a hyperspectral instrument, AIRS has 2378 spectral channels. Its spectral resolution is more than 100 times greater than previous IR sounders. This guarantees accurate information on the vertical profiles of atmospheric temperature and moisture. By using the cloud-free TIR radiance spectra in the 15 μm band, AIRS distributes CO₂ retrievals continuously on a global daily basis with accuracy better than 2ppm (Chahine *et al.*, 2008). The infrared radiation from Earth's surface and atmosphere are measured and split into constituent 'colors' (wavelengths) by the optical system. Every single color is sensitive to the temperature and water vapor over certain height range. Temperature and water vapor are then measured as functions of height. Through this technique, a temperature profile, or sounding of the atmosphere can be created using multiple infrared detectors that are sensitive to specific wavelengths.

Remarkably, AIRS has provided the first space-based retrieval of mid-tropospheric CO₂ under cloudy conditions without using the a priori modelled information (JPL, 2014). A number of significant findings have been achieved by using AIRS CO₂ data (AIRS, 2014):

'Carbon dioxide is not homogeneous in the mid-troposphere; previously it was thought to be well-mixed; the distribution of carbon dioxide in the mid-troposphere is strongly influenced by large-scale circulations such as the mid-latitude jet streams and by synoptic weather systems, most notably in the summer hemisphere; there are significant

differences between simulated and observed CO₂ abundance outside of the tropics, raising questions about the transport pathways between the lower and upper troposphere in current models; zonal transport in the southern hemisphere shows the complexity of its carbon cycle and needs further study'.

2.3.2.5 SCIAMACHY

The Scanning Imaging Absorption Spectrometer for Atmospheric Chartography (SCIAMACHY) onboard ENVISAT was launched on March 1st 2002. It is a multichannel diode array spectrometer which passively observes the backscattered, reflected, transmitted and/or emitted radiations from the Earth's surface and the atmosphere. The instrument has a spectral resolution of 0.2-1.5 μm in the spectral range between 0.24 μm and 2.38 μm . SCIAMACHY is the first satellite instrument using NIR spectra that are sensitive to CO₂ concentration changes in the lowest atmospheric layers (Schneising *et al.*,2011). The purpose of SCIAMACHY is to retrieve various trace GHGs in the troposphere and stratosphere by measuring the solar irradiance and Earth radiance spectra. A polarization measurements device (PMD) is also installed on SCIAMACHY with a spectral coverage of 310-2405 nm. The optical performance of SCIAMACHY high resolution channels is described in Table 2.5.

Table 2.5 SCIAMACHY Optical Performance

	Channel spectral range(nm)	Spectral resolution(nm)	Spectral stability(nm)
Channel 1	240-314	0.24	0.003
Channel 2	309-405	0.26	0.003
Channel 3	394-620	0.44	0.004
Channel 4	604-805	0.48	0.005
Channel 5	785-1050	0.54	0.005
Channel 6	1000-1750	1.48	0.015
Channel 7	1940-2040	0.22	0.003
Channel 8	2265-2380	0.26	0.003

Source: <http://www.iup.uni-bremen.de/sciamachy/instrument/performance/index.html>

The spatial characteristics of SCIAMACHY vary with the viewing modes. The swath in nadir geometry is up to 960km across track with the finest resolution of 26km \times 15 km. The FOV is 25km along track and 0.6km across track; for limb geometry when the instrument observe the edge of the atmosphere, a vertical resolution of 2.6km can be implemented when the instrument scans at different tangent altitudes; the occutation measurements are performed in a similar way with limb mode with the sun/moon in the FOV during the time of sunrise/moonrise. In particular

the nadir measurements can be performed 7mins after the limb measurement. By applying these 2 modes, 3D atmospheric information can be obtained. With the orbiting period of about 100 minutes, the spacecraft is able to observe the whole Earth every 6 days in the standard alternating limb/nadir scan mechanism. With nadir or limb mode alone, the global coverage is achieved within 3 days (for 960 km swath). The vertical profiles of temperature and a series of long-lived trace constituents are measured at high spatial resolution. The limitation of SCIAMACHY is that it can hardly provide useful trace gases information over water due to lack of a targeted glint mode.

SCIAMACHY CO₂ retrievals have been widely studied and used for accurately monitoring the CO₂ emissions in lower atmosphere (Buchwitz *et al.*,2005, Bösch *et al.*,2006, Buchwitz *et al.*,2006, Schneising *et al.*,2011, Wang *et al.*,2011, Tan *et al.*,2012, Zhang *et al.*,2014). A comparison study between AIRS and SCIAMACHY CO₂ retrievals showed that there was a general consistency between the two instruments when considering the different vertical sensitivities of the instruments; and SCIAMACHY has the ability of presenting the seasonal cycle signal of CO₂ (Barkley *et al.*,2006). Using the WFM-DOAS v2 retrieval algorithm, CO₂ concentrations were obtained and compared to global model simulations (CarbonTracker XCO₂) focusing on large-scale features (i.e. seasonal variations over 2003-2009) (Schneising *et al.*,2011). The steady increase of CO₂ concentration caused by fossil fuel combustion was well capture by SCIAMACHY retrieved XCO₂ based on comparison with CarbonTracker [1.80 ± 0.13 ppm yr⁻¹ compared to 1.81 ± 0.09 ppm yr⁻¹].

The accuracy of SCIAMACHY CO₂ retrievals are challenged by the uncertainty caused by aerosols. Over the continents, aerosols are highly likely to result in overestimated CO₂ abundances except for biomass burning plume and dark coniferous forests (Houweling *et al.*,2005). A study over the Sahara desert (Houweling *et al.*,2005) discovered a large variability in total CO₂ column abundances of up to 10%. Aerosol optical depth was responsible for half of the variance and a sensitivity test showed that the vertical distribution of dust mostly accounted for the rest. More accurate CO₂ retrievals were encouraged by means of developing advanced retrieval algorithms that account for the aerosol and thin cirrus cloud. For example, an improved cloud filtering method was applied to WFM-DOAS v2.2 and greatly improved the quality of WFM-DOAS dataset. The filter was based on a threshold technique using radiances from the saturated water vapour absorption band at 1.4 μ m that is mostly sensitive to thin clouds (Heymann *et al.*,2012b). Another approach was to simultaneously analyze the CO₂ absorption band at 1.58 μ m and O₂ A-band at 0.76 μ m. The information on the scattering caused by aerosols and thin

cirrus cloud was obtained by the O₂ A-band. A merged fit window approach allowed the information to transfer between the two bands. For cirrus clouds with optical thickness up to 1.0, this method was presented capable of constraining the systematic errors to below 4ppm which was better than peer approaches (Reuter *et al.*,2010).

Space-based observations not only improve the estimation of CO₂ atmospheric distributions but also enhance the understanding of the CO₂ dynamics in the terrestrial ecosystem and their interactions. A recent study using SCIAMACHY CO₂ retrievals over 2003-2009 discovered that the variation of CO₂ spatial distribution was estimated to be 6-8% at global scale. This challenged the traditional view that the spatial heterogeneity of CO₂ (perceived below the 4% level) was not significant enough to influence terrestrial ecosystem carbon cycles (Zhang *et al.*,2014). By analyzing the growth rate of CO₂ concentration, it was further found that the increase of CO₂ concentration was dominated by temperature in the NH and by precipitation in the SH.

2.3.2.6 TANSO-GOSAT

The GOSAT Project is a joint effort of the Ministry of the Environment (MOE), the National Institute for Environmental Studies (NIES), and the Japan Aerospace Exploration Agency (JAXA). The spacecraft was launched successfully on January 23rd, 2009. GOSAT is the world's first spacecraft designed to specifically measure the concentrations of CO₂ and CH₄ from space. The global distribution of CO₂ and CH₄ can be obtained by analyzing the observational data from GOSAT, as well as the spatiotemporal variability of the sources and sinks (Baker *et al.*,2006b, Chevallier *et al.*,2007). By measuring both TIR and NIR radiances, GOSAT is able to observe both column amounts and vertical profiles of the trace gases. Therefore, the fundamental information is available for enhancing the prediction of climate change and weather forecasting and for policy making on climate change mitigation.

The instrument TANSO is composed of two sensors FTS and CAI. The spacecraft is orbiting at an altitude of approximately 666 km. FTS takes 56 thousand measurements during the revolution period of 3 days with a global coverage. Only two to five percent of these data are applicable for CO₂ retrieval due to persistent cloud cover. However, the huge volumes of data collected are still sufficient for filling out the blanks in the ground-based network especially in tropical areas.

FTS measures the absorptions at O₂-A band at 0.76μm, weak CO₂ band and strong CO₂ band at the wavelength of 1.61μm and 2.06μm respectively. Since the energy within the weak CO₂ band

is almost taken by CO₂, this band is regarded highly sensitive to CO₂ abundances near the Earth's surface. Table 2.6 shows the specifications of FTS.

Table 2.6 Specifications of TANSO-FTS

	Band 1	Band 2	Band 3	Band 4
Spectral Coverage(μm)	0.758-0.775	1.56-1.72	1.92-2.08	5.56-14.3
Spectral Resolution(cm^{-1})	0.2	0.2	0.2	0.2
Spatial Resolution	10km by 10km			
Polarized Light Observation	Performed	Performed	Performed	Not Performed
Targeted Gases	O ₂	CO ₂ , CH ₄	CO ₂ , H ₂ O	CO ₂ , CH ₄
Angle of Instantaneous FOV	15.8 mrad. (corresponds to 10.5Km spatial resolution when projected on the surface of earth)			
Time Necessary for a Single Scanning (sec)	4.0, 2.0, or 1.1 (depending on the scanning mode being used)			

Source: GOSAT 2010, <http://www.gosat.nies.go.jp/eng/gosat/page2.htm>

FTS measures the incoming brightness from both the Earth's surface and the atmosphere. The sunlight reflected from the Earth's surface is measured in band 1, 2 and 3 during daytime and the light emitted by both the atmosphere and the surface is obtained by band 4 all through the day. The brightness obtained by band 1, 2, and 3, before reaching the sensors, is split into two orthogonally-polarized beams (P and S components) with different optical paths. An interference is then created by recombining the two beams and its intensity is measured by changing the optical path difference. At last, Fourier transform is performed to obtain the spectral information.

CAI is designed not only to determine whether the images are cloud/aerosol free but also to estimate and correct the effects of clouds and aerosols on the spectra obtained by FTS. This is achieved by calculating the cloud characteristics and aerosol amounts and identifying their optical depth and scattering effects. CAI is a great tool to map the state of the Earth's surface and the atmosphere during daytime. The sensor is also designed with 4 bands at the wavelength of 0.37-0.39 μm , 0.664-0.684 μm , 0.86-0.88 μm and 1.56-1.65 μm respectively. The spatial resolution of CAI is up to 0.5km for the first 3 bands and 1.5km for band 4.

2.3.2.7 OCO-2

The Orbiting Carbon Observatory-2 (OCO-2) is based on the original OCO mission that was developed under the NASA Earth System Science Pathfinder (ESSP) Program Office and launched from Vandenberg Air Force Base on February 24, 2009. The launch of OCO failed and

the OCO-2 mission is intended to ‘duplicate the original OCO design using identical hardware, drawings, documents, procedures, and software wherever possible and practical’ to minimize cost risk, schedule risk, and performance risk’ (NASA, 2014). The spacecraft was successfully launched in July 2014.

OCO-2 is the first instrument targeted at CO₂ concentration only. OCO-2 is a sun-synchronized orbiting spacecraft at an altitude of 705km and provides global coverage with a 16-day repeat cycle. The spectral range of O₂ band covers 0.757-0.772 μm (13210-12953 cm⁻¹) using the detector of Si, and the weak CO₂ band and strong CO₂ band cover 1.59-1.621 μm (6289-6169cm⁻¹) and 2.041-2.081 μm (4899-4805 cm⁻¹) respectively. The spatial resolution of OCO-2 is considerably enhanced compared to previous instruments, i.e., FOV of 1.25km cross track and 2.2km along track. This facilitates studies on CO₂ sources and sinks at much smaller scale. More specifications of the OCO-2 instrument are described in (Sakuma *et al.*,2010).

Similar to GOSAT, the OCO-2 mission also applies target mode for measurements in addition to nadir and glint modes. A target track pass can last up to 9 minutes and acquire 12960 samples at local zenith angles that vary between 0 ° and 85 °. The target mode is planned to be played on the OCO-2 calibration sites where ground-based solar FTS are located. Comparison between space-based and ground-based measurements will be conducted to identify and correct the systematic and random errors (NASA, 2014).

2.3.3 GOSAT CO₂ Retrievals

The GOSAT L1B (radiance spectra) data are distributed among collaborating institutions and research groups who have developed different algorithms for retrieving column CO₂ and XCO₂. The various algorithms are likely to yield different retrieval results since these algorithms have different concerns and strategies for data processing, aerosol and cloud scattering and post-processing filtering etc. (Oshchepkov *et al.*,2013).

As of 2013, there are mainly 5 algorithms developed for GOSAT CO₂ retrieval: NIES algorithm, ACOS algorithm, UoL-FP (University of Leicester Full Physics), RemoTeC [Remote sensing of greenhouse gases for carbon cycle modeling by the Netherlands Institute for Space Research (SRON)/the Karlsruhe Institute of Technology (KIT)] and NIES (PPDF-D). All these algorithms are based on optimal estimation or maximum a posteriori rule by minimizing a cost function in terms of the weighed least squares deviation between the observed and modeled radiance spectra

for the GOSAT SWIR bands under constraints on the state vector of desired parameters (Oshchepkov *et al.*,2013). Each algorithm has experienced continuous updates and improvements. In particular, the NIES and ACOS projects routinely provide to the public the standard data products using their own operational algorithms (Crisp *et al.*,2012, Yoshida *et al.*,2012). The rest are research project-based. The ACOS algorithm and UoL-FP algorithms are two parallel developments that are based on the original algorithm developed for the OCO mission. In this regard, these two algorithms follow a similar strategy while the UoL-FP utilizes the OCO algorithm and the ACOS is a re-development prepared for OCO-2 (Cogan *et al.*,2012).

2.3.3.1 ACOS Retrieval Algorithm

Among other retrieval algorithms, the ACOS retrievals (specifically since Build3.3) provide more complete information about the physical parameters (full physics) such as vertical profiles of CO₂ dry air mole fraction and associated uncertainties. The ACOS algorithm differs from the UoL-FP method in the definition of the state vector, a priori values, and a priori covariances, especially in the treatment of aerosols and cirrus clouds. ‘There are also differences in spectroscopy, sounding selection methods, and post-screening criteria. All of these aspects can lead to differences in algorithm performance and XCO₂’ (Cogan *et al.*,2012).

The ACOS team produces two versions of CO₂ retrievals and provide data access to the general public: B2.9 with temporal coverage from April 2009 to September 2012, and B3.3 covering from April 2009 to May 2013. The original ACOS algorithm developed for the OCO-2 mission and the B2.9 algorithm have been discussed in full detail (Crisp *et al.*,2010, Boesch *et al.*,2011, Crisp *et al.*,2012, O'Dell *et al.*,2012).

The original retrieval method designed for the OCO-2 mission consists of 5 main components: forward model, state vector, radiance Jacobians, inverse method and error analysis (Crisp *et al.*,2010). The forward model is composed of a solar model, radiative transfer model and an instrumental model. The optical properties of trace gases are considered and handled by the forward model such as calculating the gas absorption cross-section, calculating the gas absorption optical depth in each atmospheric layer and accounting for the scattering effects of cloud and aerosol. By constructing a sophisticated state structure⁴, the forward model is capable of

⁴ A state structure is to indicate the complete set of parameters required by the forward model to simulate a measurement to the necessary accuracy; a state vector is to indicate the set of parameters being retrieved. A state vector can be a simple subset of a state structure.

accommodating all the physics of the atmospheric and surface processes that contribute to the absorption and scattering of solar radiation as well as others that may affect the radiation received by the instrument (e.g. some aspects of the instrument throughput such as dispersion and instrument line shape). However the computational expense increases with the complexity of the state vector. In this algorithm, the state vector involves 8 factors with 112/115 elements for land and 107/110 elements for water area⁵. The a priori values for the state vector are obtained from specific sources of model simulations. In order to estimate the altitude-dependent number density of CO₂ which is essential for calculating XCO₂, the radiative transfer equation must be converted. Theoretically, the least squares fitting method can be used for solving this problem by treating the radiative transfer as a fitting function and taking the elements in the state vector as unknown coefficients. In addition to the radiative transfer equation, the first derivatives of the intensities respecting any specific component of the state vector are required for performing the least squares fitting technique, i.e. the radiance Jacobians that can be generated by the forward model. In this algorithm, the problem is solved by an inverse method based on a Rogers (2000)-type of optimal estimation approach (Bösch *et al.*,2006, Connor *et al.*,2008). This inversion uses the Jacobians to estimate the state changes needed to minimize the differences between the observed and simulated spectra (GES DISC, 2013). Since XCO₂ is not one of the elements in the state vector, it is determined by the algorithm once the ‘state’ yielding the best match with the observed spectrum is found associated with errors in XCO₂ from various sources (such as vertical smoothing) and the XCO₂ column averaging kernel. There are 5 assumptions for the forward model: the measured radiances have been radiometrically calibrated; the thermal emission from the atmosphere is negligible compared to reflected sunlight, which is true for the O₂ A-band and CO₂ weak band and is reasonable for the CO₂ strong band; soundings that contain optically deep clouds or aerosols can be eliminated; inelastic scattering processes (e.g. Raman) are negligible at the wavelengths of interest to OCO-2; and the effects of airglow and absorption by the Chappuis bands of ozone in the O₂ A-band are also ignored (Crisp *et al.*,2010).

Based on several improvements on early versions of retrieval algorithm, the B2.9 version was applied on GOSAT L1B data and produced higher-level products for distribution. As the L1B data distributed by JAXA were updated to version v150151 which fixed the glint flag anomaly, the ACOS team decided to use B2.9 to reprocess the L1B data to replace the products originally

⁵ The 8 factors are aerosols (80 elements, i.e. 4×20 levels), temperature (one element), water vapor (one element), surface pressure (one element), albedo-land (6 elements, 2×3 bands), Cox-Munk (one element), CO₂ (20 levels/elements) and spectral dispersion with ‘shift’ and/or ‘stretch’ (3 and/or 3 elements).

generated from L1B v130130 which introduced large biases in L2 products. Compare to ground-based TCCON observations, the mean global bias in B2.9 retrievals was estimated to be 0.13ppm with a standard deviation of 1.97ppm (Osterman *et al.*,2011). Major revisions and improvements in B2.9 compared to the previous version include:

*Significantly affecting the retrieval results: ‘retrieved a constant zero-level offset correction in the A-band to reduce the signal level dependent bias in the O₂ A-band that is caused by the Band-1 analog signal nonlinearity. Many systematic biases were eliminated’; ‘rescaled O₂ A-band cross sections with a constant factor of 1.025 to reduce the 10hPa surface pressure bias’; ‘added ILS⁶ interpolation: this change increased the retrieved XCO₂ estimates by 1.5ppm, bringing them closer to TCCON estimates, and reducing the scatter in the retrievals’; ‘glint noise treatment: the empirical noise has been applied to both the ocean and land scenes’; ‘cloud screening applied to glint and land data in preprocessing’. Within the code: ‘static input data moved to a single HDF file’; ‘upgraded LIDORT⁷ version to 3.5T’; ‘reworked Jacobian calculations to use automatic derivatives’. Instrument capability: ‘added support for FTS Instrument in up-looking mode’; ‘added support for OCO-2 instrument mode’. Speed improvement: ‘use only two streams in the Low Streams Interpolator (LSI) part of the radiative transfer code when a low number of streams is required (was 4 previously)’. Spectroscopy: ‘Version 3.3 ABSCO⁸ tables were used’(Osterman *et al.*,2011).*

The B2.9 algorithm was further updated into B3.3 which provided more complete information about the state vector especially the vertical profiles of the atmospheric parameters. Figure 2.4 shows the data processing scheme of ACOS B3.3. The L1B data (raw spectra) are distributed and produced by JAXA based on L1A data (raw interferometric files). L1B data are then calibrated and processed by the ACOS team into ACOS L1B (calibrated radiance spectra). The L2 data (raw XCO₂) are generated based on ACOS L1B and B3.3 algorithm. Proper post-filtering and bias correction are carried out in order to provide scientifically usable XCO₂ data. Validated against TCCON observations, an increase in mean biases and a reduction in scatter were observed compared to B2.9 (Wunch *et al.*,2011b). The technical revisions and improvements of B3.3 algorithm compared to previous versions are as follows:

⁶ ILS: Instrument Line Shape.

⁷ LIDORT: Linearized Discrete Ordinate Radiative Transfer.

⁸ ABSCO: Absorption Coefficient.

Significantly affecting the retrieval results: ‘updated spectroscopy-ABSCO Coefficients V4.1.1’; ‘residual Fitting of first EOF (per band) replaces empirical noise’; ‘reduced aerosol optical depth a priori value to 0.05’; ‘significantly tightened surface pressure constraints, ± 1 hPa (roughly equal weight between data & prior)’; ‘fit explicitly for fluorescence over land from O₂ A-band’; ‘utilize a consistent L1B data version (v150151)’; ‘updated radiometric calibration & degradation’. Within the code: ‘updates to radiative transfer scheme (dedicated 2-stream solver)’; ‘updated solar model’. Spectroscopy: ‘version 4.1.1 ABSCO tables used in retrieval software’.

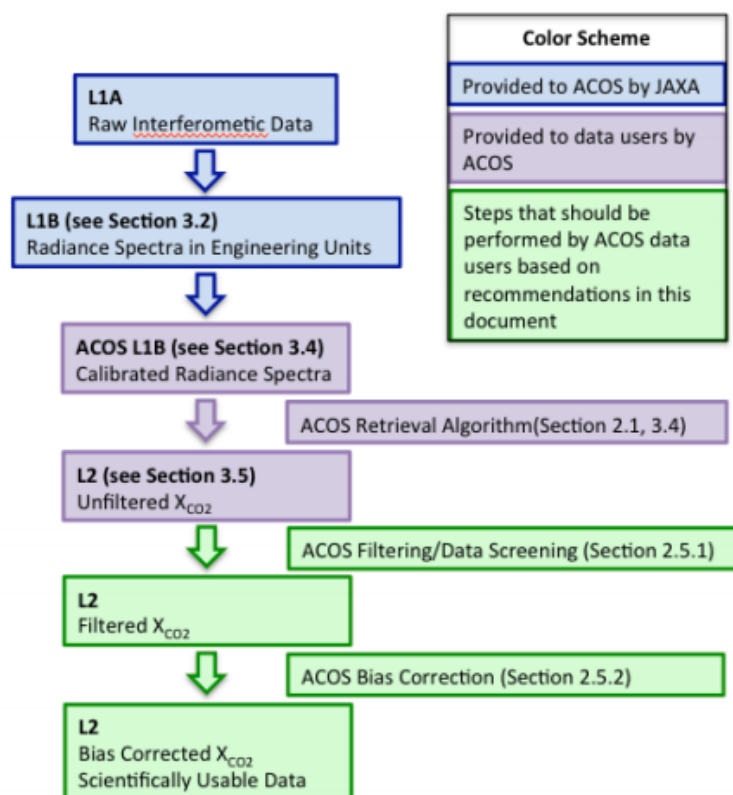


Figure 2.4 ACOS B3.3 Data Processing Flow

Source: ‘ACOS Level 2 Standard Product Data User’s Guide, v3.3’, Goddard Earth Science Data Information and Services Center (GES DISC), NASA, 2013.

The latest algorithm version (currently the 7th version of OCO-2 retrieval algorithm) is the B3.4 that was presented in AGU (American Geophysical Union) Fall Meeting 2013. There are a number of minor but important changes over previous versions in ILS model in SWIR band 1, spectroscopy, fitting of spectral residuals technique and explicit fitting for the Band 1 chlorophyll fluorescence signal over land (O’Dell *et al.*, 2013). There are no detailed characterizations of the

errors and biases in B3.4 products published to date. The latest version of ACOS L2/L2B products are B3.3 that are available at the ACOS-GES DISC website⁹.

2.3.3.2 Others

The NIES algorithm consists of three main steps: cloud-detection methods are used to select cloud-free observations; column abundances are retrieved by optimal estimation; the quality of retrievals are examined by excluding low-quality and/or aerosol-contaminated measurements (Yoshida *et al.*,2011). By using this algorithm it was found that the random errors in the retrieval mostly came from instrumental noise and the interference from auxiliary parameters (e.g. temperature, water vapor, pressure) is very small (Yoshida *et al.*,2011). However, large negative biases and standard deviations (-8.85ppm and 4.75ppm) were discovered when compared to ground-based TCCON measurements (Yoshida *et al.*,2012). A revision of the original algorithm was development taking into account the error characteristics such as solar irradiance database and handling of aerosol scattering (Yoshida *et al.*,2013). The results were greatly improved regarding the biases and standard deviations (-1.48ppm and 2.09ppm) compared to ground-based observations. Furthermore, the number of post-screened measurements was increased especially at mid-high latitudes in the NH.

The OCO algorithm estimates the column XCO₂ that best fits the measured spectrum. It uses a maximum a posteriori inverse method with weak a priori constraints and establishes a state vector that contains atmospheric, surface and instrumental properties (Connor *et al.*,2008). At low-mid latitudes, the errors for single soundings due to noise, geographical variability and spectroscopic parameters were estimated to be ~0.7-0.8ppm for ‘high-sun’ conditions and ~1.5-2.5ppm for ‘low-sun’ conditions (Connor *et al.*,2008). The findings on retrieval errors were further confirmed using an improved retrieval algorithm in a pre-launch study for the OCO-2 mission (Boesch *et al.*,2011). The improvement was achieved by employing a fast 2-orders-of-scattering (2OS) radiative transfer model instead of the linear scalar model. A linear scalar radiative transfer model fully linearizes the radiant (Spurr and Christi,2007) and is likely to lead to unacceptably large errors (Natraj *et al.*,2007). It was concluded that the accuracy of CO₂ retrievals was highly sensitive to a number of key parameters such as solar zenith angle, surface pressure, surface type and aerosol optical depth, e.g. a decreased sensitivity to near-surface CO₂ was captured over the

⁹ ACOS data access: ACOS-GES DISC website - <http://disc.sci.gsfc.nasa.gov/acdisc/data-holdings/acos-data-holdings>

area with large zenith angle, large aerosol optical depth and low surface albedo in the CO₂ and/or O₂ A-bands, which led to larger errors. The UoL-FP v3G algorithm was developed from the previous versions of OCO algorithm with a number of modifications and improvements with respect to the pressure levels, state vector, a priori information and spectroscopic parameter, etc. (Cogan *et al.*,2012). Based on the UoL-FP v3G algorithm and GOSAT L1B data, the average bias between XCO₂ retrievals and TCCON ground-based observations over 2 years were estimated to be -0.2ppm with a standard deviation of 2.26ppm and a correlation coefficient of 0.75.

Based on an optimal estimation model, the RemoTec algorithm seeks the best state vector by minimizing the least squares cost function. The algorithm for retrieving both CO₂ and CH₄ was discussed in detail (Butz *et al.*,2009, Butz *et al.*,2010, Butz *et al.*,2011). Comparing the first-year GOSAT retrievals over land with ground-based measurements from 6 TCCON sites on a station to station basis, the average bias was estimated as -0.05% with a standard deviation of 0.37%. The XCO₂ retrieved using the RemoTec algorithm was capable of reproducing general sources and sinks pattern such as seasonal cycle of CO₂ concentrations without any averaging (Butz *et al.*,2011).

Another retrieval algorithm developed by NIES is based on a PPDF (photon path length probability density function) radiative transfer model that accounts for the atmospheric light scattering caused by aerosol and cirrus cloud (Bril *et al.*,2007, Oshchepkov *et al.*,2008). The original PPDF retrieval method was comprised of three components: cloud parameters estimation using O₂ A-band at 0.76μm and H₂O-saturated band at 2.0μm; correction of the target CO₂ weak band at 1.58μm by utilizing the cloud parameters and estimated surface albedo; and CO₂ amount retrieval at the 1.58μm band based on a maximum a posteriori inversion method (Oshchepkov *et al.*,2008). This strategy is similar to the improved algorithm for SCIAMACHY observations that was introduced in 2.3.2.5 (Reuter *et al.*,2010) while the latter used O₂ A-band only to account for the effects of aerosol and cirrus cloud. This PPDF-based was capable of providing acceptably accurate CO₂ retrievals under meteorological conditions with thin cirrus cloud. The efficiency of aerosol and thin cirrus cloud correction was also demonstrated by comparing with other algorithms that neglect light scattering effects and associated change of photon path length. This method was further improved and tested by synthetic photon trajectories (Oshchepkov *et al.*,2009). With the improvements, the PPDF-based method was capable of not only rapid CO₂ retrievals in terms of radiative transfer spectral calculation over a wide spectral range but also accounting for the a priori knowledge of atmospheric optical characteristics. A validation study on the PPDF-based algorithm used the method to examine and reveal the light scattering effects

due to aerosol and thin cirrus cloud under different atmospheric and surface conditions (Oshchepkov *et al.*,2012). Optical path lengthening was found over most TCCON stations in the NH especially from June to September while optical path shortening was found for glint observations in tropical regions which were in line with the seasonal trends of aerosol optical depth derived from 3D aerosol transport model (Yumimoto and Takemura,2013). Despite that the CO₂ retrieval algorithms are being continuously updated and improved, the reliability of remote sensing CO₂ data remains a primary concern for practical use.

2.3.4 Reliability in Practice-GOSAT

Our ability to forecast and mitigate the warming of climate caused by CO₂ is critically dependent on understanding where, when and how CO₂ is interacting with the land and atmosphere (Frankenberg *et al.*,2011). However, a bias of a few tenths of 1ppm in CO₂ concentration can seriously hamper the accuracy of results for CO₂ sources and sinks. Therefore, from the perspective of CO₂ data users in carbon cycle and climate change studies, stringent requirements on the accuracy of the CO₂ data are necessary for making reliable conclusions and predictions.

Remote sensing CO₂ observations are expected to be capable of conquering the limitations of *in situ* measurements and ground-based FTS observations. However, further efforts are still needed to improve the accuracy of space-based CO₂ observations in terms of calibration, retrieval algorithm and bias correction, etc.

The TANSO-FTS L1B radiance spectra are distributed by JAXA in the form of engineering units (volts). JAXA also provides a series of calibration tables for converting these values to various units that are necessary for a specific retrieval algorithm. For example, GOSAT L1B spectra are converted from volts to photons/m²/sr/cm⁻¹ which is used by ACOS level-2 algorithms. The calibration information is derived from prelaunch calibration tests and on-orbit observations of internal light sources, deep space, the sun, the moon, and observations of calibration targets on the Earth's surface. These tabulated results are assumed to be accurate and constant for further data processing, or used to establish trends for time-dependent corrections. It was confirmed that the GOSAT and OCO instrument were calibrated to within their uncertainty requirements (Sakuma *et al.*,2010).

It is also important to pay attention to the geolocation errors. As reported in the ACOS B3.3 retrievals, the geolocation values are typically in error by 1 to 6km. These errors have negligible

impacts on airmass errors over flat surface however are highly likely to introduce airmass biases in regional with large topographic variability (ACOS- GES DISC, 2013).

The retrieved CO₂ values vary with algorithm. Though most retrieval algorithms follow a similar strategy for estimating the state vector and XCO₂ (i.e. optimal estimation or maximum a posteriori method), key physical processes are treated differentially in the forward model (e.g. modification of optical path by different types of aerosols) which could lead to biases in the retrieved CO₂ among different algorithms. Taking into account ACOS B2.9, NIES02.xx, NIESPPDF-D, RemoTec1.0 and UoL-FP:3G, Table 2.7 gives a summary of the specifications of different retrieval algorithms.

Table 2.7 Basic Specifications of Different Algorithms.

	ACOS B2.9	NIES02.xx	NIESPPDF-D	RemoTec1.0	UoL-FP:3G
AOD	<0.15	<0.1		<0.25	<0.5
SNR		<70	>75	>50	>50
ΔP [hPa]	<10	<20			<20
DFS	>1.15	>1	>1	>1	
ΔXCO ₂ [ppm]	<1.3				<1.6
Number of Gas Layers	20	15	22	12	20
Number of Aerosol and Cloud Layers	20	6	2-3	36 Gaussian Shaped	20
AC	4	2		1	3
Solar Irradiance Spectrum	G.C.Toon Model	G.C.Toon Model	G.C.Toon Model	G.C.Toon Model	G.C.Toon Model
Noise Treatment	Empirical	Empirical	True	True	True

Source: (Oshchepkov et al.,2013)

AOD: the total aerosol and cloud optical depth; SNR: signal-to-noise ratio; ΔP: the absolute difference between retrieved and prior surface pressure; DFS: degree of freedom for signal; ΔXCO₂: the a posteriori error of XCO₂; AC: the number of aerosol and cloud components.

Remote sensing validation is indispensable for ensuring that the geophysical parameters obtained from in-orbit radiometric measurements meet the requirement for scientific and pragmatic applications (Lambert *et al.*,2011). Furthermore, data validation needs to be carried out regularly throughout the in-orbit phase rather than in a ‘once a mission lifetime’ manner. Precise measurements from ground, aircrafts, ship and balloons are qualified for validating the remote sensing data. TCCON is the most commonly used source of reference measurements for the

validation of GOSAT observations as well as other space-based observations such as AIRS and SCIAMACHY (Toon *et al.*,2009, Butz *et al.*,2011, Heymann *et al.*,2012a, Schneising *et al.*,2012a, Schneising *et al.*,2012b, Uchino *et al.*,2012). TCCON is a ground-based network of FTSs that precisely measure the column amount of various trace gases, e.g. CO₂, CO, CH₄, N₂O and H₂O. In contrast to space-based observations, the ground-based FTS measures the absorption of direct sunlight. The similarity is that it uses NIR spectral region as some space instruments. In addition, the external information about the atmosphere (e.g. temperature and pressure) and NIR spectroscopy are needed for deriving the total column information. As great efforts have been made on minimizing the errors in the external information, the total columns are precise, e.g. <0.25% in CO₂ column (Wunch *et al.*,2011a). However, the absolute accuracy of the total columns is ~1% due to systematic biases in the spectroscopy. The errors can be compromised by calibrating the TCCON observations to the World Meteorological Organization (WMO) *in situ* trace gas measurement scales taking advantage of aircraft instrumentations (Wunch *et al.*,2010). It was discovered that ‘a single, global calibration factor for each gas accurately captures the TCCON total column data within error’.

The validity of different retrieval algorithms against TCCON was examined and the comparison was conducted among 6 retrieval algorithms including the 5 algorithms in Table 2.7 (Oshchepkov *et al.*,2013). It was found that NIES02.xx and RemoTec had best agreements with TCCON measurements. Validations of each algorithm against TCCON measurements at different time scales are shown in Table 2.8.

The effect of light scattering in each algorithm varies. After a cloud pre-filtering test, a PPDF method was applied on each algorithm and it was found that approximately 25% of GOSAT soundings processed by NIES 02.xx, ACOS B2.9, and UoL-FP: 3G and 35% processed by RemoTeC were contaminated by atmospheric light scattering. The aerosol amounts over bright surfaces tended to be overestimated by NIES 02.xx and ACOS B2.9 which led to underestimated XCO₂ (Oshchepkov *et al.*,2013).

Table 2.8 GOSAT CO₂ Retrieval Algorithm Validation against TCCON

	ACOS B2.9	NIES02.xx	NIESPPDF-D	RemoTec1.0	UoL-FP:3G
Single GOSAT and TCCON Scans					
N _c	3274 (1469)	3039 (1316)	1231	2237 (799)	3339 (1434)
a	0.90 (0.92)	1.09 (1.09)	1.13	1.23 (1.19)	0.96 (0.99)
Bias [ppm]	-0.25 (-0.76)	-1.13 (-1.41)	0.07	-0.21 (0.03)	0.12 (-0.42)
Σ [ppm]	2.06 (1.62)	2.17 (1.76)	2.48	2.66 (2.29)	2.45 (1.94)
R ²	0.79 (0.87)	0.83 (0.89)	0.79	0.83 (0.86)	0.72 (0.84)
r	0.78 (0.85)	0.81 (0.85)	0.73	0.73 (0.73)	0.70 (0.80)
i-Bias [ppm]	0.65 (0.40)	0.63 (0.40)	0.61	0.52 (0.55)	0.39 (0.33)
Observation Fraction [%]	0.65 (0.40)	57.8 (25.0)	23.4	42.5 (15.2)	63.5 (27.3)
Daily Mean GOSAT and TCCON Data					
N _a (days)	672 (356)	631 (327)	347	525 (232)	672 (395)
a	0.83 (0.88)	1.03 (1.03)	1.06	1.03 (1.02)	0.88 (0.99)
Bias [ppm]	-0.02 (1.74)	-1.15 (-1.39)	0.10	0.20 (0.00)	0.10 (-0.25)
σ [ppm]	2.11 (1.74)	1.85 (1.67)	2.23	2.15 (2.06)	2.34 (1.92)
R ²	0.74 (0.83)	0.86 (0.89)	0.81	0.83 (0.84)	0.72 (0.84)
r	0.78 (0.85)	0.86 (0.88)	0.78	0.81 (0.79)	0.74 (0.81)
i-Bias [ppm]	0.94 (0.53)	0.83 (0.53)	0.71	0.65 (0.52)	0.57 (0.39)

Source: (Oshchepkov et al.,2013)

GOSAT soundings were collected over land within a 5 radius circle over 11 TCCON sites. The TCCON XCO₂ data were mean values measured within ±1h of the GOSAT overpass. The statistical characteristics are: the number of GOSAT individual scans coincident with TCCON soundings (N_c), number of average points (N_a) meeting the coincidence criteria, the regression slope (a), bias (Bias), standard deviation (σ), determination coefficient (R²), Pearson's correlation coefficient (r), and interstation bias (i-Bias) between GOSAT and TCCON XCO₂. Values in parentheses are derived after additional scan selection by spectral variability in albedo).

In summary, remote sensing has been demonstrated as a promising tool for providing accurate observations of atmospheric CO₂ columns and concentrations at various spatiotemporal scales. It is capable of enhancing our understanding of the dynamics of carbon cycle by revealing valuable information that can hardly be discovered by existing *in situ* CO₂ measurements network. The

remote sensing observations are not perfectly accurate for being used independently or in combination with *in situ* measurements for carbon cycle science. However, progresses can be seen in recent studies with respect to improving the retrieval algorithms, identifying and quantifying the causes for error, and error correction for distributed end products, etc. As the retrieval methods and data processing techniques are improved, it is expected that the accuracy and quality of space-based CO₂ observations will be more adequate for independent or combined analyses.

2.4 Influential Factors

Although CO₂ amount and concentration are currently measured to reasonably high accuracy, cautions are needed for using these data acquired from either ground or space-based instruments. The CO₂ concentrations near the surface are significantly influenced by transport within the PBL and between the PBL and the troposphere. These atmospheric CO₂ transport processes are not simulated very accurately (Toon *et al.*,2009). Therefore, it is highly likely that the observed CO₂ concentration does not reflect the real distribution of sources and sinks.

Furthermore, as for estimating the CO₂ abundance/concentration through remote sensed spectra, a series of external factors (atmospheric and surface) influence the retrieval process. Such factors are mostly incorporated in the state vector that is estimated simultaneously with the XCO₂, e.g. temperature, surface pressure, water vapor, aerosols and land albedo. The influence of these factors on XCO₂, and the interaction among themselves are complicated. Biases in the state vector estimation could result in large errors in the XCO₂ retrievals. In this regard fundamental knowledge of how these factors influence atmospheric CO₂ concentrations and the retrieved values, (it) is necessary for the interpretation and explanation of the research results in Chapter 4.

2.4.1 CO₂ Atmospheric Transport

Exploring where and when the uptake of atmospheric CO₂ is a high research priority for understanding the carbon cycle and for designing verification systems to monitor the effectiveness of emission controls or emission reduction policies (Ciais *et al.*,2011). The transport of CO₂ in the atmosphere determines the concentration with a given distribution of sources and sinks (Rayner *et al.*,1999). Information about CO₂ sources and sinks can be derived from

variations in observed CO₂ concentrations via inverse modelling with atmospheric tracer transport models (Gurney *et al.*,2002).

As is similar to remote sensing CO₂ retrieval, a forward transport model describes the dynamic evolution of the system, i.e. the spatial distribution of CO₂ concentration at different spatiotemporal scales depending on the model resolution. The transport model is driven by external factors such as meteorological fields. An initial state of the target variable (CO₂ flux) and associated errors are a component of the inverse problem and are required to match the spatial and temporal resolution of the atmospheric transport model. At last, an inverse method is applied to estimate the 'real' CO₂ flux by minimizing the difference between the observed CO₂ concentrations and the simulations. The inversion of CO₂ flux usually adopts a statistical method based on the Bayes theorem in order to seek for the optimum of a set of parameters that minimizes the cost function based on the numerical transport model (Tarantola,2005). The geostatistical approach was introduced to this field (Michalak *et al.*,2005) and was further advanced (Gourdji *et al.*,2008) to formulate the inversion problem differently.

The transport of CO₂ in the atmosphere shows large variations at different spatiotemporal scales, e.g. spatial scales of local plume spread, regional mesoscale transport and global scale, and temporal scales of hourly, diurnal, synoptic, seasonal and interannual cycles (Maksyutov *et al.*,2008). The flux-resolving ability of the inverse model relies significantly on the design of the atmospheric transport model. Transport models are expected to account for the physical and dynamical state of the atmosphere over a long period of time to relate fluxes and concentrations since CO₂ is a long-lived species (Bruhwiler *et al.*,2005). Large-scale transport processes such as convection and horizontal diffusion are explicitly solved in those models. Sub-grid physical processes are usually parameterized for moist convection, penetrative mass flux, vertical diffusion, and boundary layer mixing by turbulence (Patra *et al.*,2003).

A challenge for simulating atmospheric CO₂ transport is how to model these transport processes accurately. Lagrangian and Eulerian models are used as advection schemes. Particularly, the application of Lagrangian modelling has experienced rapid growth over the past few years because it is a close simulation of the natural air flows (Lin *et al.*,2011). In contrast to Eulerian models in which the fixed grid cells are used, Lagrangian models track the movement of the air parcels along their moving trajectory with advantages on constraining numerical diffusion and adopting bigger model time steps. By using the polar coordinate system, Lagrangian models are

also able to avoid the problem associated with the regular-grid schemes used by Eulerian flux form, i.e. singularity near the poles as meridians converge and grid size becomes smaller.

Another important feature of transport models is the PBL/ABL that determines the mixing rate of CO₂. PBL is the lowest layer of the atmosphere and is directly related to the Earth's surface. In contrary to the free troposphere where no turbulence or only intermittent turbulence takes place, PBL is the layer where turbulences take place with a much higher intensity, e.g. rapid fluctuations of wind velocity, temperature and humidity¹⁰. The estimation or observation of the depth of PBL is crucial to simulation of CO₂ atmospheric transport since the turbulence dissipates with increased height from the surface layer through the PBL core to the PBL top or the entrainment layer¹¹. Four main external factors determine the depth and vertical structure of PBL: the free atmosphere wind speed, the surface heat (more exactly buoyancy) balance, the free atmosphere density stratification, the free atmosphere vertical wind shear or baroclinicity.

The spatiotemporal variability of PBL has been explored by a series of studies (Deardorff,1972, Moeng,1984, Moeng and Sullivan,1994, Noh *et al.*,2003, Zilitinkevich *et al.*,2007, Hu *et al.*,2010, Flaounas *et al.*,2011, Seidel *et al.*,2012, Leventidou *et al.*,2013). In theory, the PBL is thicker at lower-pressure zones, such as tropics, which leads to stronger vertical diffusion and hence lower diurnal variability measured by peak-to-peak amplitude. However, by comparing 25 TransCom (Transport Comparison Project) forward atmospheric transport models, the simulated PBL by some models was found thinner at tropics than at higher latitudes especially at nighttime (Law *et al.*,2008). In addition, the strength of vertical mixing does not necessarily increase with the PBL depth when a thick surface layer dominates the PBL. Furthermore, the daytime PBL can be simulated with less uncertainty while a huge uncertainty (up to a few hundred percent) can be encountered by nighttime PBL modelling. Evidences showed that models tend to underestimate nighttime concentrations (Geels *et al.*,2007), which means the PBL depth during nighttime is not resolved sufficiently, and the ability of transport models to resolve the PBL varies. This can lead to wide ranges in simulated diurnal variations and is thus a major source of uncertainty in transport models.

¹⁰ http://en.wikipedia.org/wiki/Planetary_boundary_layer

¹¹ The PBL core is between 0.1 and 0.7 of the PBL depth. The entrainment layer, also known as capping inversion layer, is between 0.7 and 1.0 of the PBL depth.

2.4.1.1 Seasonal/Interannual CO₂ Cycles

The large-temporal-scale variability of atmospheric CO₂ concentration concerning emissions from fossil fuel combustion and exchange with the terrestrial biosphere can be modelled reasonably well using a variety of atmospheric transport models. Global transport models are applied to investigate the movement of long-lived trace gases in the atmosphere such as CO₂. By validating with other trace gases of well-known patterns and model-to-model and model-to-observation comparison, a wide range of global transport models have been proved adequate especially at lower-mid northern hemisphere where reference observations are sufficient. Global transport models are also capable of explaining the contribution of land biosphere and the ocean to the state of atmospheric CO₂ concentrations (Tans *et al.*,1990, Fan *et al.*,1998, Kaminski *et al.*,1999, Baker *et al.*,2006a, Ciais *et al.*,2011, Feng *et al.*,2011, Schuh *et al.*,2013).

The models use both online and offline methods, various sub-grid parameterization and advection schemes, different model resolutions and sources of meteorological data. In order to quantitatively understand the importance of atmospheric transport models, several initial studies were conducted (Keeling *et al.*,1989, Taylor,1989, Tans *et al.*,1990, Enting *et al.*,1995). However, there were considerable variations among such studies regarding the global CO₂ budgets. The CO₂ Transport Comparison Project was initiated in 1993. Under this project, 12 transport models were compared to examine the spatiotemporal structure of flux and concentrations, and to further explore the influences of fossil fuel burning and biospheric exchange (Law *et al.*,1996). The ability of the 12 models to resolve fossil fuel emissions varied slightly with model resolution, e.g. high-resolution models tend to introduce higher source strength. It was found that coarse-resolution models were unable to resolve different emission sources in the same grid cell since sampling grid does not separate them accurately (Maksyutov *et al.*,2008). Exchange with terrestrial biosphere is a major cause of seasonal CO₂ cycle especially in the northern extra-tropics. This biospheric flux was obtained by combining local measurements of respiration and net primary productivity (NPP) with satellite measurements, validated by comparing the observed seasonality and GISS model (Fung *et al.*,1987). Due to a large latitudinal discrepancy of vegetation source and observed seasonality at mid-high latitudes in the NH, the analysis of fossil fuel combustion and biosphere was conducted for at least three years in order to illuminate the influence of initial condition.

In the comparison study by Law *et al.* (1996), minor differences of overall interhemispheric transport were found among the 12 models based on zonal annual mean surface concentrations,

with maximum concentrations around 50 N and small gradients in southern hemisphere. The concentration amplitudes derived by different models presented a large variability probably due to different vertical mixing strength modelling and disturbance of CO₂ sources to the models. The experiment of biosphere was conducted by examining the amplitude of seasonal cycle and the surface annual mean response. High horizontal resolution facilitates capturing the large seasonality observed from the biosphere experiment while vertical model resolution and corresponding sub-grid process tend to contribute more to the large seasonality with respect to fossil fuel burning. The discrepancy of the 12 models in vertical transport was clearly observed in winter.

Uncertainties on atmospheric transport modelling arise from erroneous spatiotemporal sampling, numerical truncation, biased initial input, wind fields and model formulation (Stohl,1998). A recent study examined the importance of transport model uncertainties for CO₂ flux estimation using remote sensing measurements (Houweling *et al.*,2010). It was found that even though the simulated CO₂ concentrations using different models agreed on average at the sub-ppm level, even modest differences can lead to significant discrepancies in inverted CO₂ fluxes. CO₂ flux estimation using remote sensing measurements not only requires high accuracy of the measurements, but also puts stringent requirements on the performance of atmospheric transport models.

2.4.1.2 Diurnal and Synoptic CO₂ Variability

Inversions can recover CO₂ fluxes at sub-regional scales with a relatively high density of CO₂ observations and adequate information on atmospheric transport in the region (Schuh *et al.*,2013). While a transport model serves well at large scales, it does not mean the model is necessarily qualified for shorter-timescale simulations. The ability to reliably estimate CO₂ fluxes from *in situ* and space-based CO₂ measurements is dependent on transport model performance at synoptic and shorter timescales (Patra *et al.*,2008). For daily to weekly timescales, the transport of CO₂ can result in a ‘contaminated’ area over 10,000 km² to one million km² (Gloor *et al.*,2001, Karstens *et al.*,2006). In this regard, whether the estimation is a reliable and accurate representation of surface flux relies to a great extent on the performance of transport models at synoptic and shorter timescales (e.g. diurnal) (Law et al. 2006, Patra et al. 2008).

A model intercomparison experiment was conducted by the TransCom group for exploring synoptic and diurnal variations of atmospheric CO₂ by comparing model simulations at various

sites. Nine trace gases were included in the experiment with different requirements on resolution varying from 'constant' to monthly timescale. All the models are required to be driven by analysed meteorological data over the period of 2000-2003 (Law *et al.*,2006). Under the framework of TransCom intercomparison experiment, the simulation results based on 25 transport models were analysed for diurnal variations and compared with CO₂ observations (Law *et al.*,2008). Four out of 25 are regional transport models including CHIMERE (Schmidt *et al.*,2001), COMET (Vermeulen *et al.*,2006), DEHM (Geels *et al.*,2002), and REMO (Langmann,2000)¹². Most models tended to overestimate low-amplitude locations and underestimate high-amplitude locations as a result of biased vertical mixing and incorrectly resolved surface flux. It was not consistent across the models with respect to the diurnal amplitude in summer when intense photosynthesis was presented. By ruling out the impacts of vertical resolution, the simulation of surface transport was expected to have played a significant role in the discrepancies. Large summer diurnal cycles that were seen in the observations can be modelled accurately in high latitudes in contrast to tropics where observation sites are sparse. Different diurnal CO₂ cycles across the models can be partly accounted for by the differences in sampling location and input data. CO₂ diurnal variations result from a balance between photosynthesis and soil respiration (Pérez *et al.*,2012). However, daily CO₂ amplitude also strongly depends on the seasonal vegetation activity (Haszpra *et al.*,2008).

The synoptic scale has a horizontal length scale of the order of 1000km and can be defined as 1-10 day CO₂ variation (American Meteorological Society, 2007). A simple approach for analyzing synoptic CO₂ variation is to examine the simulation-observation correlation which is more effective than model-model correlation. This is because synoptic CO₂ variation is mostly transport dominated and different models tend to simulate synoptic weather pattern in a similar manner (Patra *et al.*,2008). In addition, it is important to investigate the amplitude of variation based on daily average CO₂ concentrations, as well as to calculate model mean by averaging the retrieved time series for enhancing the SNR (Williams *et al.*,2013).

The 25 TransCom models (Law *et al.*,2008) were examined to investigate synoptic CO₂ variations based on simulated hourly atmospheric CO₂ concentrations and diurnally varying land fluxes (Patra *et al.*,2008). This study emphasized the importance of correctly simulating synoptic

¹² CHIMERE is an Eulerian mesoscale model with a resolution of 50km and boundary condition derived from LMDZ. COMET is a Lagrangian model with two simulating levels (the PBL and free atmosphere). DEHM has the resolution of 150 km with 50km nested region and the initial input is provided by TM3_vfg. REMO is driven by forecasted meteorology and continuous tracer transport.

weather pattern with forward transport models for surface flux inversion especially at regional scale. Flux representation and model horizontal resolution had a sizable impact on the quality of modelled synoptic CO₂ variations. The flux components had different influences on between-model discrepancy at different time of the year. The amplitude and correlation of model-data variability was strongly model and season dependent. Moreover, the importance of enhancing the resolution of biosphere flux was highlighted. The terrestrial biosphere component contributed most to synoptic CO₂ variation, followed by fossil fuel burning, with minor contribution by ocean exchange. The biosphere led to strong diurnal variability in summer hence a disagreement among models with respect to synoptic variation. In winter, when photosynthetic activities shift from the highest to flat, fossil fuel combustion becomes dominant in conjunction with biosphere respiration. Considering the difficulty of simulating synoptic variation due to intense biosphere photosynthesis, the simplicity in winter facilitates CO₂ transport simulation at a synoptic timescale. In addition, the model-data correlation increases with the distinguishability among different types of flux. By examining the growth rate of model-data correlation between when observations lagged the model and when observations led, the shape of CO₂ concentration peaks was identified, i.e. CO₂ concentrations tended to rise rapidly and dropped off slowly on most occasions.

2.4.1.3 Regional Scale

Regional scale where the global and the local scales meet and interact is a big challenge for quantifying the carbon balance in both a political context and a scientific domain (Dolman *et al.*,2006). The resolution of global models is too coarse to resolve the physical processes of CO₂ at finer scales, which hinders our understanding of the regional CO₂ cycles. In addition, some large-scale features are neglected by some models such as the concentration distribution over the south-western Europe (Geels *et al.*,2007).

It is difficult to simulate CO₂ transport at regional scale since local meteorology (e.g. the dominating synoptic weather system) and surface conditions (e.g. the heterogeneous surface land cover which is more discernible at finer scales) have a great impact on the atmospheric dynamic (Sarrat *et al.*,2007, Wang *et al.*,2007). In this regard, enhancing our understanding of the regional atmospheric transport system became a high research priority (Scott Denning *et al.*,2003, Chan *et al.*,2004, Geels *et al.*,2004, Nicholls *et al.*,2004, Lu *et al.*,2005, Pérez-Landa *et al.*,2007). These studies demonstrated the capacity of meso-scale models to correctly simulate surface flux,

atmospheric CO₂ concentrations and the gradient and variability. Meso-scale modelling usually focuses on an area of 300km by 300km (Sarrat *et al.*,2007), taking advantage of high spatial resolution (e.g. 2km), better PBL and surface energy parameterizations, and more detailed local wind circulations. Favorable modelling results also depend on various atmospheric and surface factors, e.g. high insolation without clouds, high temperatures and light winds, accurate understanding of the boundary layer supported by sufficient measurements (radio-sounding, aircraft and surface measurements) (Sato *et al.*,2011).

In general, meso-scale models were able to accurately simulate the surface flux, especially over certain land cover types such as crop sites (Corbin *et al.*,2010). Model-data comparisons showed a general agreement of simulations with the observations (Lac *et al.*,2013). By validating against aircraft measurements, the simulated interaction of CO₂ spatial distribution and temporal evolution with complex surface fluxes was regarded highly realistic (Imasu *et al.*,2010). With higher vertical resolutions than global transport models, meso-scale models were more capable of resolving CO₂ dispersion within the PBL (Geels *et al.*,2007). The CO₂ concentrations increase with height in summer and decrease in winter due to the seasonality of vertical mixing mechanism and the PBL height. The uptake of CO₂ and the PBL height in summer are approximately the annual maximum. The between-model and model-observation agreements are better in winter than in summer. The summer variability tends to be underestimated and the standard deviation of time series on an hourly or daily basis increases with model resolution. In addition, the variability of CO₂ concentration at low-altitude sites can be well captured but the amplitude tends to be underestimated. In contrast, at high-altitude stations, between-model and model-data differences are less notable, but the diurnal cycle is likely to be too complicated to be well captured.

Uncertainties on simulation at regional scales could arise from the errors in representation of a single location to specific grid cells or large regions (Dolman *et al.*,2006), the aggregation errors caused by the resolved fluxes that do not influence the overall concentration distribution (Kaminski *et al.*,2001), the rectification errors due to poor capacity for assessing the fluctuations in the height of the boundary layer (Denning *et al.*,1996), etc. Furthermore, the meteorological data are treated as prescribed input instead of a free variable (Wang *et al.*,2007). This degrades the sensitivity of models to the high-frequency disturbances and fluctuations of regional weather systems since regional models are intended to observe the fastest interaction involving both the surface and the atmosphere. A popular research topic is to examine the vertical mixing rate of CO₂ within the PBL and its contribution to atmospheric transport simulation uncertainty.

Conventional diagnostics for the examination are compared to analyze vertical mixing rates, data assimilation system and atmospheric analyses. However, diagnostics based on boundary layer depth and vertical concentration gradients do not always indicate the vertical mixing strength. Vertical mixing rates are anti-correlated with boundary layer depth at some sites, diminishing in summer when the boundary layer is deepest. In this regard, the concept of boundary layer equilibrium was introduced to predict an inverse proportionality between CO₂ vertical gradients and vertical mixing strength. It was found that frequently cited model-data discrepancies did not necessarily indicate systematic errors in atmospheric transport models (Williams *et al.*,2011).

As is similar to larger-scale modelling, the boundary layer plays a crucial role in spatiotemporal variations in CO₂ concentration. The lateral and upper boundary conditions vary with model. The variability of CO₂ concentration increases more rapidly than global transport models when approaching the surface due to not only increased horizontal resolution but also better resolved mixing processes within PBL and higher vertical resolution (Geels *et al.*,2007). The discrepancy can be reduced to a large degree by constraining sampling time to the afternoon and sampling a couple of hundred meters above the surface where the signal of heterogeneous flux is diluted. The errors in mixing height can contribute to a large part of model-data mismatch. An optimization of the mixing height is capable of reducing the bias in CO₂ transport to a large degree, e.g. 5-45% (day) and 60-90% (night) (Kretschmer *et al.*,2014).

In general, CO₂ concentration variability varies with spatial and temporal scales due to different physical processes that dominate the atmospheric transport of CO₂. The transport of CO₂ is more complex and difficult to simulate at regional scales since the heterogeneity of surface flux needs to be precisely captured and resolved by transport models with high spatial resolutions. The PBL (height/depth) is a dominant factor that influences the dispersion of CO₂ within. The PBL depth could change dramatically between daytime and nighttime. Therefore, short-timescale modelling (e.g. synoptic to daily) is more challenging compared to large scales since the day-night discrepancy in PBL depth could lead to large biases in simulated CO₂ transport.

2.4.2 State Vector

The state vector incorporates a series of surface and atmospheric parameters, as well as instrumental parameters and others in some cases. These parameters are crucial to remote sensing CO₂ retrieval as they determine atmospheric CO₂ concentrations and how CO₂ concentrations can be accurately measured by the instruments and retrieval algorithms. The parameters of priori

interest in both remote sensing CO₂ retrieval and atmospheric CO₂ cycles are temperature, pressure, water vapor and aerosol.

2.4.2.1 Temperature and Pressure

The vertical structure of the atmosphere is characterized by the vertical profiles of temperature and pressure. The pressure is a cause of the weight of air within a column above the surface. The pressure is height dependent and can be expressed as a function of surface pressure and

temperature according to the barometric law: $P(z) = P(z_0) \cdot e^{-\frac{Mgz}{RT_m}}$, where P is the pressure, z is the height, M is the molar mass of air (29g/mol), g is the gravitational acceleration (9.81m/g²), R is the universal gas constant (8.31 J/mol K), T_m is the geometric mean temperature (Stubbe,1972). A consequence of the height dependence of pressure is that the air amount is divided in half every 5.5 km since the number of air molecules is directly proportional to pressure. This means that half of the air is in the lowest 5.5km and the rest spreads above to the top of atmosphere. The height dependences of pressure and temperature are show in Figure 2.5.

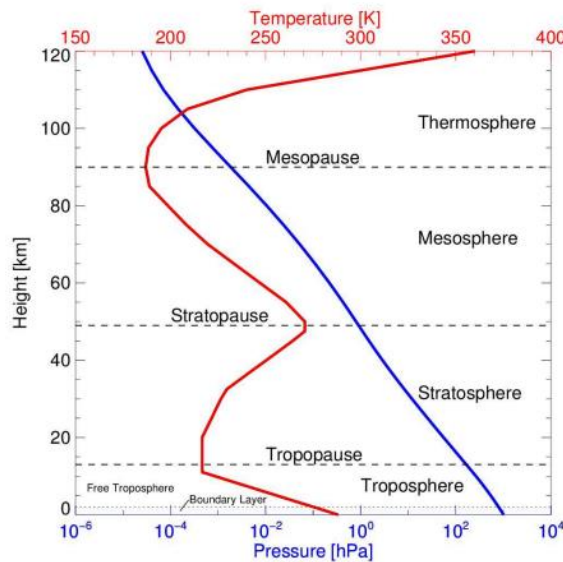


Figure 2.5 Height Dependences of Pressure (Blue) and Temperature (Red)

Source: US Standard Atmosphere (NOAA and Force,1976)

Temperature and pressure determine the density of CO₂ which can be converted to volume mixing ratio. At standard temperature and pressure, the density of CO₂ is around 1.98 kg/m³. Major change in temperature and pressure can also shift the state of CO₂, e.g. at one atmosphere

(near mean sea level pressure), CO₂ deposits directly to a solid at temperatures below -78.5 °C. Though the state shifting of CO₂ rarely occurs in the atmosphere, temperature and pressure influence the dispersion rate of CO₂ in addition to CO₂ density. By exploring the relationship between temperature, pressure and volume, the early gas laws were developed more than three centuries ago and have been advanced over time.

Boyle's law: For a given mass of ideal gas¹³ at constant temperature, the product of pressure and volume stays constant (Bonnor,1956). Boyle's Law is expressed as a mathematical equation of $P_1V_1 = P_2V_2$ or $V = k / P$, where P is pressure, V is volume and k is the constant.

Charles's law (the law of volume): For an ideal gas at constant pressure, the volume is directly proportional to temperature (Nurrenbern and Pickering,1987). $\frac{V_1}{T_1} = \frac{V_2}{T_2}$, where T is temperature (K).

Gay-Lussac's law (the pressure law): It states that the pressure exerted on the sides of a container by an ideal gas of fixed volume is proportional to its temperature (Crosland,1961). $\frac{P_1}{T_1} = \frac{P_2}{T_2}$.

Avogadro's law: The volume of an ideal gas is proportional to the number of moles present in the container (Dubowski and Essary,1996). $\frac{V_1}{n_1} = \frac{V_2}{n_2}$, where n is the number of moles.

Graham's law: The gas diffusion rate is inversely proportional to the square root of density or the root of molecular weight (Friedman,1974).

Combined and ideal gas law: The combined gas law or general gas equation that describes the relationships between temperature, pressure and volume can be expressed as $PV = k_sT$ or $\frac{PV_1}{T_1} = \frac{PV_2}{T_2}$, and can be developed into the ideal gas law $PV = nRT$ (or equivalent to $PV = kNT$) by incorporating the Avogadro's law, where R is the universal gas constant, P is the absolute pressure, N is the number of molecules and k is the Boltzmann constant (Burdick *et al.*,2006). The ideal gas law is a good approximation for most gases under moderate temperature and pressure. When considering only temperature, pressure, volume and the number of molecules,

¹³ An ideal gas is a theoretical gas composed of a set of randomly moving, non-interacting point particles.

this law implies that one of them is either directly or inversely proportional to another when the other two are kept constant. In addition, when temperature changes for a given number of gas molecules, either pressure or volume (or both) will change in direct proportion to temperature.

Although the gas laws provide implications for the relationships between temperature, pressure, volume and others, the impacts of temperature and pressure on CO₂ in the atmosphere are more complex. The dispersion of CO₂ depends on turbulence and is conditioned by thermal stratification of the atmosphere (Elansky *et al.*,2007) especially in undisturbed synoptic conditions (Pernigotti *et al.*,2007). Daily evolution of temperature profiles corresponds to the evolution of the thermal stratification of the atmosphere (Pérez *et al.*,2012). Pressure gradients (that cause wind) and surface geographical characteristics contribute to the turbulence. All these factors together comprise the stability of the atmosphere especially the lower PBL. The more stable the surface layer is, the more frequently high CO₂ concentrations tend to be observed (Pérez *et al.*,2009a).

Atmospheric stability can be described by the Monin-Obukhov length which mathematically involves absolute temperature, potential temperature and pressure, etc. (Monin and Obukhov,1954). The structure of the atmospheric layer can be investigated by Brunt–Väisälä frequency (or buoyance frequency) (Durran and Klemp,1982). Based on the formula of these atmospheric indicators, wind speed and temperature profiles in the lower atmosphere were incorporated into these two indicators and were analyzed together with CO₂ concentrations (Pérez *et al.*,2009a). Four classes of stability of the atmospheric layer were established: drainage, extremely stable, stable and unstable. A stratified structure was discovered for the PBL especially in spring and summer. The atmospheric stability and structure was differentiated between nighttime and daytime. A highly stable layer was observed near the ground during the night. The buoyance frequency increased with height during the day indicating a more stable atmospheric thermodynamic circumstance with lower temperature and pressure. During the night time, drainage was associated with very high frequencies at 40m and very low frequency from 100m, the lowest wind speed at 40m which decreased with height, the highest temperatures below 100m and very high CO₂ concentrations mainly in spring. The high CO₂ concentrations were associated with the very low dilution within a thin layer near the surface. Extremely stable situations were linked to moderate temperatures and the second highest CO₂ concentrations in spring. The dilution layer was thicker than that associated with drainage. Stable situations were characterized by the lowest temperatures and the second lowest CO₂ concentrations in summer. Unstable

situations were associated with the highest wind speed, superadiabatic temperature profiles below 100m and the lowest CO₂ concentrations.

A close relationship between CO₂ concentrations meteorological variables was proposed to establish atmospheric conditions linked to high CO₂ values (Pérez *et al.*,2009b). Six variables were considered: wind speed, wind direction and temperature at one level and differences between them at two levels. The selection of study area ensured horizontal homogeneity where non-irrigated crops and grass made up the surrounding vegetation. In this study, CO₂ concentration showed a significant decrease of 25ppm in spring and 16ppm in summer when wind speed increased greatly during the night. The decreases of CO₂ concentrations in autumn and winter were lower considering the same wind speed interval. A wind speed below 4ms⁻¹ was linked to high CO₂ concentrations. CO₂ concentrations were sensitive to temperature in spring and summer during the night and in autumn and winter during the day. Higher CO₂ concentrations were associated with higher temperature in spring and summer, as well as lower wind speed and no prevailing direction, etc. High CO₂ values during the night were observed when temperatures were higher than 10 °C in spring and 20 °C in summer. A clear inverse relationship between CO₂ concentrations and temperatures were obtained during the day in autumn and winter. This is attributed to low soil-and-plant-induced convection development due to low temperatures. In addition, difference between temperatures at 100m and 40m was used to indicate the strength of vertical exchange, i.e. a positive difference corresponded to inversion which was associated with higher CO₂ concentrations during the night.

In terms of remote sensing CO₂ retrieval, temperature and pressure cannot be ignored since the absorption of radiation at a given wavelength by a CO₂ molecule is temperature and pressure dependent. The absorption by CO₂ molecules generates absorption lines within the spectra of outgoing radiation from the Earth due to energy transition in CO₂ molecules. The energy transition is described by the wavelength and takes the forms of rotations, vibrations and electronic transitions¹⁴. The depth of lines is described by CO₂ concentration and the cross section. The pressure and temperature dependent cross section quantifies the efficiency of absorption at a given wavelength and characterizes the radiative transfer through the atmosphere.

¹⁴ These three types of transitions give rise to absorption of electromagnetic radiation. A CO₂ molecule gains a quantum of rotational energy in rotational transitions and a quantum of vibrational energy in vibrational transitions, and is promoted to an excited electronic state in electronic transitions.

Errors in CO₂ concentration retrieved using remote sensing observations is generally a combination of instrument noise, smoothing error, interference errors with non-CO₂ state vector elements, and forward model errors (O'Dell *et al.*,2012). The ACOS B2.9 algorithm was tested in terms of its capability of correcting imperfect non-CO₂ state vector elements such as temperature and water vapor. It was found that imperfect meteorology input did not cause additional bias to retrieved surface pressure and XCO₂. Surface pressure was taken as an evaluation indicator as it is the baseline for characterizing the vertical structure of the atmosphere and a positive bias in surface pressure could result in negative bias in XCO₂ (Oshchepkov *et al.*,2013). The RMS difference between the retrieved surface pressure and the imperfect a priori surface pressure was 1.7hPa. The mean XCO₂ difference was generally zero and the RMS difference was 0.38ppm, about 5% of the XCO₂ random error. 70% of the variance of XCO₂ was caused by the differences in the retrieved surface pressure. This test demonstrated the insensitivity of ACOS algorithm to biased input meteorology. However, errors are common in the retrieved state vector and are responsible for XCO₂ retrieval errors for the ACOS algorithms and others.

2.4.2.2 Water Vapor

Water vapor is a primary non-anthropogenic GHG that accounts for the largest percentage of direct greenhouse effect, e.g. 36% to 66% in clear sky and 66% to 85% with clouds (Maurellis and Tennyson,2003). CO₂ is able to cause warming and double the effect by water vapor which causes a ‘positive feedback’ and amplified the original warming. Human activities do not significantly affect atmospheric water vapor especially at local scales and the lifetime of water vapor is much shorter than other GHGs (typically 9 days in comparison with years). This is the major reason CO₂ is taken as the foremost GHG. The atmospheric concentration of water vapor is largely dependent on temperature, e.g. from <0.01% by mass in extremely cold regions up to 3% in saturated air at about 32 °C (Evans,2005).

The strength of absorption by different states of H₂O varies. Water vapor has the lowest attenuation coefficient¹⁵ compared to liquid water and ice for most of the spectral range from 0-100µm. All the three forms of transition give rise to the absorption of electromagnetic radiation by water vapor. Rotational transition causes absorption in the FIR spectrum from 50µm towards the microwave region; vibrational transition results in absorption in the MID region; and the

¹⁵ Attenuation coefficient is a quantity that describes how easily a material or a medium can be penetrated by light, sound, particles, energy or other matters.

lowest electronic energy transition is in the vacuum ultraviolet region. In reality, the energy transition is more complicated and so is the absorption spectrum, e.g. vibrations are accompanied by rotational transitions resulting in a vibration-rotation spectrum and vibrational overtones and combination bands occur in the near-infrared region (Rothman *et al.*,1987, Gordon *et al.*,2007).

Water vapor has stronger absorbing capacity and wider absorption band than other GHGs. The absorption by water vapor covers the visible region and the majority of the NIR region in 7 major bands as shown in Table 2.9.

Table 2.9 Major Water Vapor and CO₂ Absorption Bands in NIR

Gas	Center λ (μm)($\text{v}(\text{cm}^{-1})$)	Band Interval (cm^{-1})
Water Vapor	2.7 (3703)	2500-4500
	1.87 (5348)	4800-6200
	1.38 (7246)	6400-7600
	1.1 (9090)	8200-9400
	0.94 (10638)	10100-11300
	0.82 (12195)	11700-12700
	0.72 (13888)	13400-14600
CO ₂	4.3 (2526)	2000-2400
	2.7 (3703)	3400-3850
	2.0 (5000)	4700-5200
	1.6 (6250)	6100-6450
	1.4 (7143)	6850-7000

Source: http://irina.eas.gatech.edu/EAS8803_Fall2009/Lec6.pdf

The water vapor absorption spectrum covers most CO₂ absorption bands in NIR except the 1.6 μm which is the CO₂ weak band. Therefore, as for CO₂ retrieval using IR spectra (water vapor also absorbs MIR and FIR radiance as stated before) the interference of water vapor absorption needs to be considered for band selection. For instance, Saitoh *et al.* (2009) examined the impact of uncertainties in the estimates of surface temperature, surface emissivity, temperature profile and amounts of water vapor and ozone in the atmosphere on CO₂ retrieval from the 15 μm . The findings showed that the magnitudes of bias and random errors in retrieved CO₂ concentrations are proportional to those of bias and random errors in the model parameters, e.g. +1 K temperature bias produced up to 17% positive bias in retrieved CO₂ concentrations at around 200 hPa and 10% water vapor bias produced up to 4% positive bias at around 800 hPa; ± 1 K random errors in temperature profile led to $\pm 4\%$ random errors in retrieved CO₂ concentrations at around

800 hPa and $\pm 10\%$ random errors in water vapor profile produced $\pm 1.5\%$ random errors at around 800 hPa (Saitoh *et al.*,2009).

The CO₂ retrieval errors due to water vapor absorption can be constrained by analyzing the NIR spectra for estimating CO₂ concentrations near the surface. Most water vapor exists in the PBL (typically less than 2km depending on the geolocation). In this regard, the 14 μm water vapor absorption band can be used for obtaining CO₂ information at altitudes above 2km as the GOSAT instrument (TANSO-FTS) was designed. The 1.6 μm weak band and 2.0 μm strong band are used for CO₂ concentration estimation near the surface. The 1.6 μm band rules out the interference by the water vapor and most other GHGs. The 1.4 μm saturated water vapor absorption band can also be used for detecting high thin cirrus cloud (Heymann *et al.*,2012a, Heymann *et al.*,2012c). In clear sky, most radiation at this wavelength is absorbed by water vapor in the lower atmosphere and few signals can reach the space-based sensors; however in the presence of cirrus clouds above the water vapor, a significant amount of radiation is backscattered to space and received by the sensors.

2.4.2.3 Aerosols and Clouds

Aerosols are solid particles or liquid droplets suspended in the atmosphere. Typical aerosols are haze, dust, water droplets, soot and fumes in car exhaust, particulate air pollutants and smoke. The particle size is a key property to characterizing aerosols. The diameters of aerosols are mostly smaller than 1 μm and larger particles range from 1 μm to 15 μm . Aerosol size distribution is used for characterizing the size of a mixture of aerosols in the atmosphere which categorizes aerosols as different classes according to predefined size intervals (Tegen and Lacis,1996). Furthermore, the size of aerosols depends on relative humidity since aerosol particles grow when absorbing water vapor.

The interaction between electromagnetic radiation and spherical aerosol particles ($2\pi r^2 \geq \lambda$) is described by the Mie theory (Steinke and Shepherd,1988). These spheres are characterized by a real part and an imaginary part that describes the strength of radiation absorption and scattering. The wavelength dependence of aerosol extinction coefficient is less precipitous than Rayleigh scattering and is typically proportional to λ^{-a} , where a is the Angstrom exponent which is

typically 0-1.5. For strong absorbing aerosols the single scattering albedo¹⁶ is low while for non-absorbing aerosols the single scattering albedo is 1.

A high environmental priority is monitoring the concentrations of aerosols especially in urban areas (Retalis *et al.*,2010). Major *in situ* techniques for measuring aerosols include Aerosol Mass Spectrometer (AMS), Differential Mobility Analyzer (DMA), Aerodynamic Particle Sizer (APS), Wide Range Particle Spectrometer (WPS), Micro-Orifice Uniform Deposit Impactor(MOUDI), Condensation Particle Counter (CPC), Epiphaniometer and Electrical Low Pressure Impactor (ELPI). Remote sensing approaches for aerosol measurement typically use sun photometer and LIDAR.

Considering various aerosol sizes and properties, radiation with a wide range of wavelength can be absorbed and scattered by different types of aerosols. A close relationship between aerosols and visibility has been identified in extensive studies (Dzubay *et al.*,1982, Appel *et al.*,1985, Tsai and Cheng,1999, Eidels-Dubovoi,2002, Hand *et al.*,2002, B äumer *et al.*,2008, Retalis *et al.*,2010). By computing the dry light scattering coefficient, it was suggested that the sulfate aerosols were the dominant contributor to the degradation of visibility in the Big Bend National Park U.S. in 1999 (Hand *et al.*,2002). *In situ* measurements of the visibility, aerosol size distributions, aerosol scattering coefficients and meteorological variables such as relative humidity were obtained over Southwest Germany obtained during 5 consecutive days. A distinct decrease in visibility was detected linked to a significant increase of PM10 and aerosol optical thickness (B äumer *et al.*,2008).

In addition to scattering effect in the visible spectra, aerosol was also found capable of causing scattering in the IR spectra. This could compromise the accuracy of remote sensing inversions that use IR radiance such as CO₂ retrievals (Fraser and Kaufman,1985, Kaufman,1989, Ackerman,1997, Kaufman *et al.*,1997). The aerosol effect on remote sensing is expressed as a function of aerosol optical thickness (Fraser *et al.*,1977, Gordon *et al.*,1983) and the absorption is another important parameter it has been observed to vary several fold (Waggoner *et al.*,1981). As stated in previous sections, biased estimation of aerosol optical thickness or depth could result in significant errors in XCO₂ retrieval as the optical path length becomes inaccurate, e.g. overestimated AOD causes negative bias in XCO₂. The instrumentations and retrieval algorithms

¹⁶ The single scattering albedo is the ratio of scattering coefficient to extinction coefficient.

have been advanced in terms of accurately accounting for the scattering effects of aerosols as well as thin cirrus cloud.

In meteorology, a cloud is a visible mass of liquid droplets or frozen crystals made of water or various chemicals suspended in the atmosphere above the surface of a planetary body (Roosevelt,2008). Cloud is a major factor that affects the climate. It reflects the solar energy back to space which results in surface cooling while it also prevents the thermal emissions from escaping the earth which results in warming.

The impact of clouds on remote sensing XCO₂ retrieval is complex. It depends on the macro and micro-physical properties of the clouds. Incident solar radiance is partially reflected by the clouds and the strength of reflectance depends on the albedo and altitude of the clouds. The rest travels through the clouds as being scattered along the path. The reflectance and transmittance also rely on the composition of the clouds. For instance, on the one hand, when the clouds are contaminated by aerosols such as soot over urban areas, the reflectance gets weaker; on the other hand, growing liquid droplets and smaller particles due to the contamination enhances the reflectance. Therefore, a cloud screening procedure is undertaken for most space-based observations prior to distribution. Further filtering strategies are applied by different research groups and institutions based on the characteristics of the retrieval algorithms.

2.5 Summary

This chapter introduced the background of this research, familiarized the readers with the space-based instruments and algorithms for estimating CO₂ in the atmosphere and summarized the key factors that influence atmospheric CO₂ concentrations and CO₂ retrievals. Firstly, Section 2.2 discussed climate change and its effects on the environment. A close relationship between global warming and anthropogenic GHG emissions was presented. Mitigations against climate change in the energy sector were called for with concerted efforts at various levels. Ontario's electricity system was introduced in terms of its development, changes in the fuel mix over time, GHG emissions reduction and effective clean energy policies. The phasing-out of coal-fired power generation across the province raised research opportunity to monitor the change in CO₂ emissions and their effects on atmospheric CO₂ concentrations from space.

Secondly, Section 2.3 provided an overview of spectral absorption by CO₂ which is the fundamental physical basis for remote sensing atmospheric CO₂ observations. Then various CO₂-

relevant space-based instruments were introduced with respect to their spatiotemporal and spectral specifications, spectra usage and applications in practice. As the data source that supports this research, GOSAT (TANSO-FTS) CO₂ data and associated algorithms were discussed in detail. There is no firm conclusion on which algorithm performs best since they have different technical focuses and practical concerns and they have been validated and advanced continuously. Considering the data access and the completeness of CO₂ profiles and relevant parameters, the ACOS B3.3 dataset was selected as the data source for this research.

Lastly, Section 2.4 summarized several key meteorological parameters that one should take into account for interpreting and analyzing the measured or retrieved CO₂ concentrations. These parameters or derivatives (temperature, pressure, water vapor and aerosols) are incorporated in the state vector of most retrieval algorithms. The CO₂ retrieval errors are inevitable due to random errors in these parameters. The impact of temperature and pressure rests on changing the strength of absorption (absorption cross section) of radiation at a given wavelength by CO₂. Water vapor interferes in the estimation of CO₂ absorption at specific wavelengths. The influence of aerosols and cloud is that they can change the optical path length by reflecting and/or scattering radiations and consequently the CO₂ concentration estimations would be biased. The following Methods chapter describes the approach design for obtaining column and partial column CO₂ information and the strategy used for data analysis.

Chapter 3: Methods

3.1 Introduction

This study is to estimate the capability of remote sensing CO₂ data (CO₂ concentrations and CO₂ abundances) to reflect surface CO₂ emissions from Nanticoke coal-fired generating station. Column and partial column CO₂ information are generated and used based on the CO₂ full physics dataset. Monthly/seasonal variation in regional atmospheric CO₂ in Hamilton is explored. Another focus of this study is to examine the impacts of external factors (surface and atmospheric parameters) on the use of CO₂ data to estimate CO₂ enhancement by fossil fuel combustion.

The objective of this chapter is to (1) describe the overall research planning including proposed approaches, assumptions and reliability issues, (2) introduce the collection of the data, (3) examine the importance and limitations of the approaches, and (4) explain the approaches for data analysis on CO₂ enhancement estimation and external influence evaluation.

3.2 Research Planning

It is widely accepted that the lower part of atmosphere is mostly related to CO₂ emissions from the surface. As reviewed in Chapter 2, in CO₂ sources and sinks studies, space-based and ground-based CO₂ information for the full atmospheric column are used independently and the *in situ* CO₂ measurements on specific vertical levels are embedded in a CO₂ sources and sinks inversion model. However, CO₂ information about the lower part of atmosphere is rarely used independently for certain technical reasons, e.g. CO₂ vertical profiles are not available or there are concerns about the accuracy of the CO₂ data of lower atmosphere.

This research examines the partial-column CO₂ concentrations and CO₂ abundances, then conducts a comparison with column CO₂ information respecting their relationship with Nanticoke GS output, as well as their representations to the seasonal variations of CO₂ in Hamilton. The retrieval of partial-column CO₂ involves 6 procedures as shown in Figure 3.1: (1) extraction of target observations from ACOS Build3.3 dataset, (2) identification of background areas, (3) filtering of background observations, (4) extraction of relevant CO₂ information and useful

parameters, (5) calculation of partial-column CO₂ information based on the relevant parameters, and (6) calculation of CO₂ enhancement based on target and background observations. The selection of the ACOS CO₂ dataset among different data sources (Table 2.7 and Table 2.8) considers the data accessibility and the number of observations over the target and background areas.

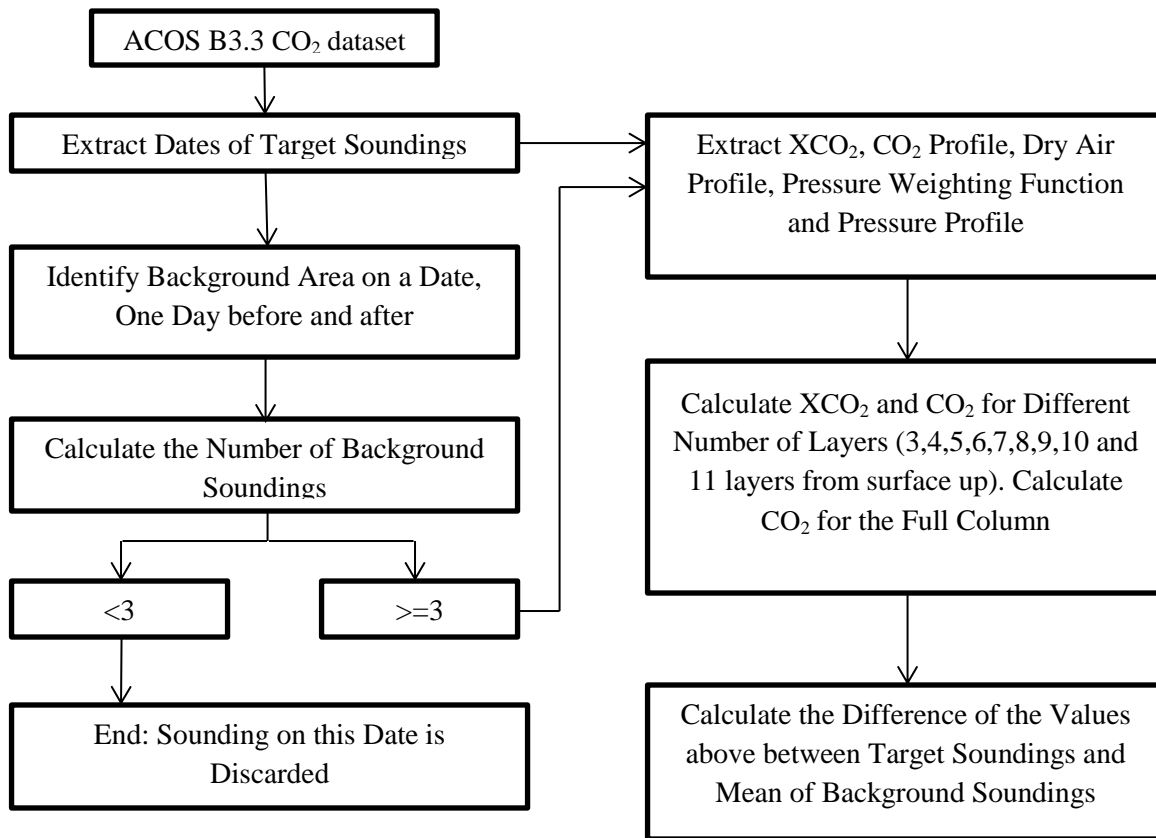


Figure 3.1 The Workflow for Partial-Column CO₂ and XCO₂ Retrieval

The calculated CO₂ enhancements are fitted with generating outputs that represent instant or early emission signals using different regression models (linear and non-linear). The observation-model differences are then related to the surface and atmospheric parameters. The uncertainty on surface CO₂ information is also taken into account. The influences of the external factors are explored by examining the pattern of association between the model residuals and one specific influential factor. In addition, a multivariate analysis is carried out to investigate the external influence, which assumes that the relationship between model residuals and influential factors can be linear, pure quadratic, interactions or full-quadratic.

Figure 3.2 shows the location of the observations (in Nanticoke and Hamilton) and the potential background area (the green shaded area).

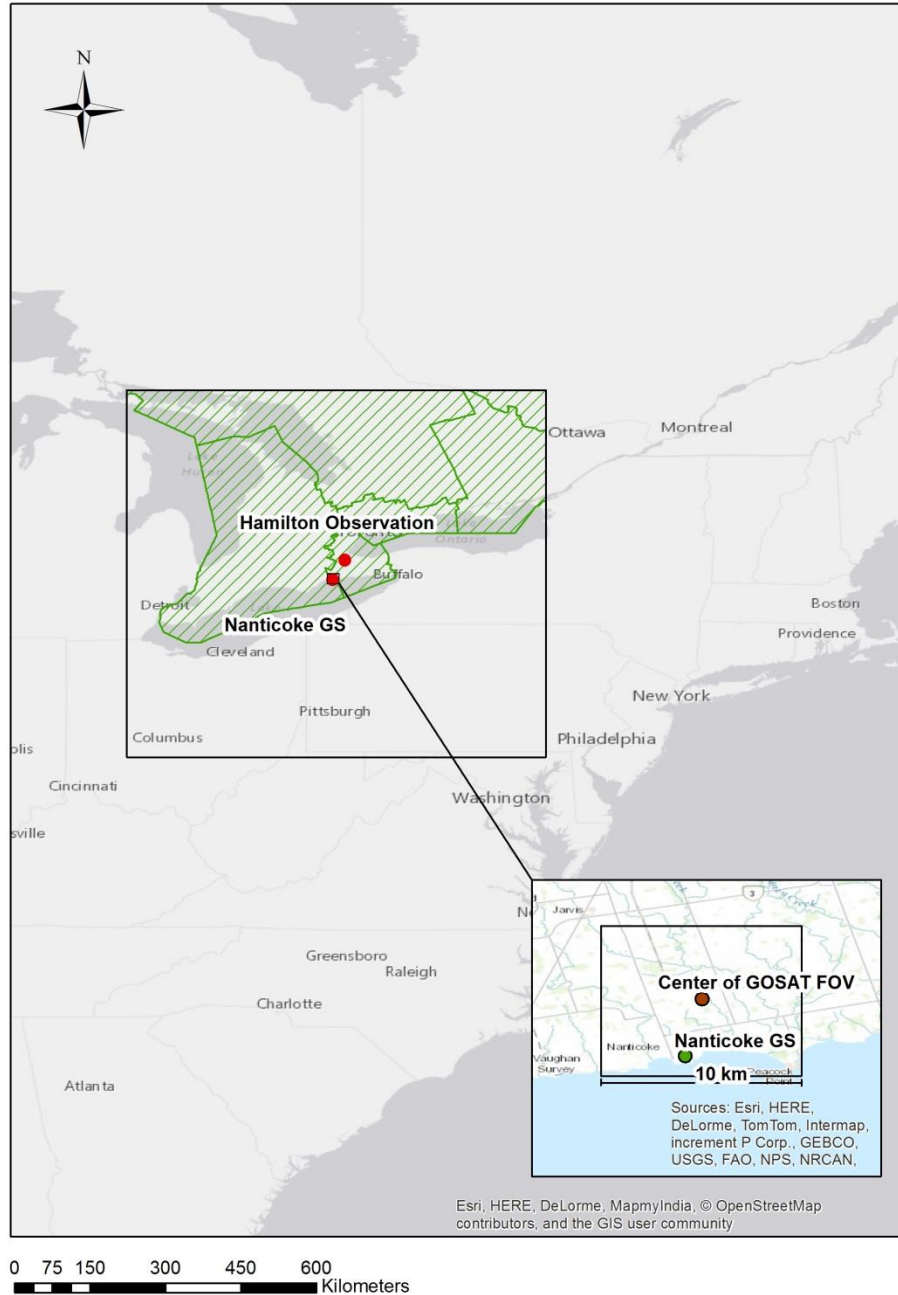


Figure 3.2 Location of Target and Background Areas

3.2.1 Method

3.2.1.1 Extraction of Target Soundings

A target sounding is one whose FOV (10km by 10km) covers Nanticoke GS. Minor difference in sounding geolocation is permitted due to errors in raw data calibration.

The ACOS data are in HDF5 format and basic data reading examples are given at the ACOS website. The dates with target soundings available are then captured and recorded.

3.2.1.2 Identification of Background Area

Combustion of fossil fuel is regarded as a major contributor to the increasing atmospheric CO₂ concentration; whereas the influence of biosphere cannot be ignored (ocean-atmosphere exchange is not considered in this study).

In order to reduce, if not to completely eliminate, the biosphere influence, the ‘background area’ is introduced and defined as an area (within a certain distance from the target area) where the fossil fuel flux is zero (or approximately zero) and the biosphere flux equals (or approximately equals) to that of the target area. It is necessary to note that in reality an ideal background area (with zero fossil fuel flux and identical biosphere flux) are likely unavailable under certain circumstances, e.g. a region with a complicated distribution of land use types and fossil fuel sources that cannot be resolved by the flux data used.

In this regard, criteria are indispensable to the identification of background area with approximately zero fossil fuel flux and approximately equal biosphere flux to that of target area:

$$F_{\text{background}} \leq F_{\text{target}}/100; \text{ and}$$

$$|B_{\text{target}} - B_{\text{background}}| \leq |B_{\text{target}}|/100.$$

where $F_{\text{background}}$ and F_{target} are fossil fuel fluxes for the background area and the target area; B_{target} and $B_{\text{background}}$ are biosphere fluxes for the target area and the background area. Since biosphere flux could be either positive or negative, an absolute calculation is conducted for biosphere flux criterion.

The area where the identification of a background area is implemented is a grid (11 degree by 11 degree) centered to the cell where Nanticoke GS is located. The temporal range is from one day before to one day after a target date since all potential background soundings within 11 degree span of longitude may not be made in a single day. Minor changes in location and shape of the background areas are accepted since the extraction of fossil fuel flux and biosphere flux are associated with the time of soundings and it is most likely that the fluxes vary with time. In order to determine the minimum number of observations to qualify a potential background area, two grids (3 degree by 3 degree) are compared and analyzed as introduced in Section 4.3.

3.2.1.3 Filtering of Background Soundings

On one hand, a low number of soundings are likely to misrepresent the CO₂ information in the background area since the regional CO₂ sources and sinks could be highly complex; on the other hand, the number of satellite scans is likely insufficient at high latitudes. In this respect, an appropriate threshold on the number of background soundings is essential to ensure both reliable data preparation for subsequent calculations and the number of observations to process.

The threshold is determined by comparing two areas at mid latitudes in North America. These two areas are selected based on two principles: (1) the sums of fossil fuel flux and biosphere flux for each cell are well distributed in each area and (2) the overall sums of fossil fuel flux and biosphere flux are comparable between the two areas.

Furthermore, the differences of CO₂ mixing ratios and/or CO₂ abundances on 111 days are calculated. Basic statistical analysis on the relationship between the differences and the numbers of soundings is carried out to assist in determining the threshold on the number of background soundings. The results of area comparison are described in the next chapter.

3.2.1.4 Extraction of Relevant Information

Upon the capture of target sounding and the selection of background soundings, a number of items are retrieved from each HDF5 file to calculate partial-column CO₂ information and proceed with data analysis. These items include:

- Column XCO₂ and uncertainties;
- CO₂ profiles (XCO₂ on each level) and uncertainties;

- Pressure profiles (pressure on each level);
- Dry air profiles (Dry air thickness for each layer); and
- Pressure weighting function

3.2.1.5 Partial-Column CO₂ Information Retrieval

It is critical to determine the height of the boundary of a partial column that is most capable of capturing signals from surface CO₂ emissions. Additionally, the variance in local physical and meteorological conditions among the target sounding and background soundings should be watched closely, specifically the difference in surface altitudes and discrepancy in surface pressures and vertical pressure intervals; thus an identical environment respecting particular factors needs to be ensured for comparing the target and backgrounds. Moreover, XCO₂ is the dry air mole fraction of CO₂ in the atmosphere; however, it is the CO₂ abundance that directly relates to the surface CO₂ emissions. Taking this into consideration, a comparison between XCO₂ and CO₂ needs to be done.

The ACOS B3.3 algorithm partitions the atmosphere into 19 layers (20 levels) from the surface to near the top of atmosphere (TOA). The pressure intervals between every two adjacent levels are approximately equal. According to Standard Atmosphere of International Civil Aviation Organization (ICAO) 1964 for the altitudes to 32km, the relationship of pressure and temperature with altitude is described in Table 3.1.

Table 3.1 Change of Pressure and Temperature with Altitude (ICAO, 1964)

Altitude (gpm)	Temperature (°C)	Pressure (mb)	Altitude (gpm)	Temperature (°C)	Pressure (mb)
-400	17.6	1062.2	7400	-33.1	388.0
-200	16.3	1037.5	7600	-34.4	377.1
0	15.0	1013.3	7800	-35.7	366.4
200	13.7	989.5	8000	-37.0	356.0
400	12.4	966.1	8200	-38.3	345.8
600	11.1	943.2	8400	-39.6	335.9
800	9.8	920.8	8600	-40.9	326.2
1000	8.5	898.7	8800	-42.2	316.7
1200	7.2	877.2	9000	-43.5	307.4
1400	5.9	856.0	9200	-44.8	298.4
1600	4.6	835.2	9400	-46.1	289.6
1800	3.3	814.9	9600	-47.4	281.0
2000	2.0	795.0	9800	-48.7	272.6
2200	0.7	775.4	10000	-50.0	264.4
2400	-0.6	756.3	10200	-51.3	256.4
2600	-1.9	737.5	10400	-52.6	248.6
2800	-3.2	719.1	10600	-53.9	241.0
3000	-4.5	701.1	10800	-55.2	233.6
3200	-5.8	683.4	11000	-56.5	226.3
3400	-7.1	666.2	11500	-56.5	209.2
3600	-8.4	649.2	12000	-56.5	193.3
3800	-9.7	632.6	12500	-56.5	178.7
4000	-11.0	616.4	13000	-56.5	165.1
4200	-12.3	600.5	13500	-56.5	152.6
4400	-13.6	584.9	14000	-56.5	141.0
4600	-14.9	569.7	14500	-56.5	130.3
4800	-16.2	554.8	15000	-56.5	120.5
5000	-17.5	540.2	15500	-56.5	111.3
5200	-18.8	525.9	16000	-56.5	102.9
5400	-20.1	511.9	17000	-56.5	87.9
5600	-21.4	498.3	18000	-56.5	75.0
5800	-22.7	484.9	19000	-56.5	64.1
6000	-24.0	471.8	20000	-56.5	54.7
6200	-25.3	459.0	22000	-54.5	40.0
6400	-26.6	446.5	24000	-52.5	29.3
6600	-27.9	434.3	26000	-50.5	21.5
6800	-29.2	422.3	28000	-48.5	15.9
7000	-30.5	410.6	30000	-46.5	11.7
7200	-31.8	399.2	32000	-44.5	8.7

Generally, the pressure intervals for target and background soundings range from 4500pa (45mb) to 5000pa (50mb). As shown in Table 3.1, the average ratio of altitude change to pressure change under 5km altitude is 10.57 m/mb (absolute value), which means the average thickness of layer under 5km is approximately 500m. And one should note that the thickness of layer increases with height.

In terms of using remote sensing CO₂ data to monitor or estimate surface CO₂ emissions, there is not a solid conclusion on how many layers a partial column of atmosphere should take the form of; in another word, how high the boundary of the partial atmosphere is. Therefore, in this study, partial columns with different numbers of layers are calculated simultaneously and analyzed. The number of layers ranges from 3 to 11, corresponding to the height of column from 1200m to 5500m approximately.

In order to retrieve CO₂ information for a partial column with a given number of layers, one should be acquainted with the ACOS B3.3 retrieval algorithm that was discussed in the previous chapter. Figure 3.3 shows the pressure system defined by ACOS B2.9 algorithm, in which the entire column of atmosphere is partitioned into 20 layers from 1050hpa to 0hPa.

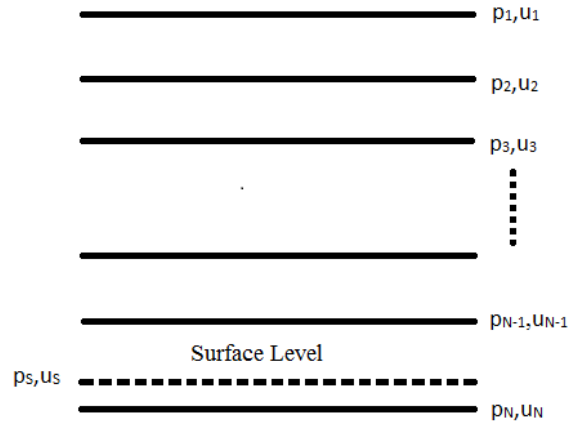


Figure 3.3 ACOS B2.9 Pressure System

Source: C. W. O'Dell et. al.: ACOS CO₂ retrieval algorithm

Here p_i and u_i denote the pre-defined pressure and CO₂ volume mixing ratio at level i, i=1,2...N.

The calculation of column XCO₂ is given by equation Eq. 3.1 (O'Dell *et al.*,2012):

$$XCO_2 = \frac{\sum_{i=1}^{N-1} (cu)_i \Delta p_i}{\sum_{i=1}^{N-1} c_i \Delta p_i} \quad (\text{Eq. 3.1})$$

where u is the dry air mole fraction of CO₂, and the subscript i indicate layer bounded by pressure level p_i and p_{i+1}, and the last layer is bounded by level p_{N-1} and surface level p_s. Δp_i is the

pressure difference of two adjacent levels, c is the density of dry air per unit pressure given by equation Eq. 3.2 (O'Dell *et al.*,2012):

$$c = \frac{1 - q}{gM_{dry}} \quad (\text{Eq. 3.2})$$

where q is humidity, g is gravity acceleration and M_{dry} is molar mass of dry air. It is assumed that c varies slightly and linearly within a layer, thus XCO_2 is reformed as:

$$XCO_2 = \sum_{i=1}^{N-1} h'_i \bar{u}_i \quad (\text{Eq. 3.3})$$

where $h'_i = \frac{\bar{c}_i \Delta p_i}{\sum_{i=1}^{N-1} \bar{c}_i \Delta p_i}$ (Eq. 3.4)

and denotes the pressure weight of dry air for layer i . The pressure weighting function on each level is then given as a function of h' :

$$h_i = \begin{cases} (1 - f_1)h'_1 & i = 1 \\ f_{i-1}h'_{i-1} + (1 - f_i)h'_i & i = 2 \dots N-2 \\ f_{N-2}h'_{N-2} + (1 - f_N)f_{N-1}h'_{N-1} & i = N-1 \\ f_N f_{N-1} h'_{N-1} & i = N \end{cases} \quad (\text{Eq. 3.5})$$

where f_i relates the XCO_2 at the center of a layer to that of two bounding levels, by which the XCO_2 of a layer is described as:

$$\bar{u}_i = (1 - f_i)u_i + f_i u_{i+1} \quad (\text{Eq. 3.6})$$

As for the surface layer, the XCO_2 is in the form of:

$$u_S = (1 - f_S)u_{N-1} + f_S u_N \quad (\text{Eq. 3.7})$$

It is critical to note that the ACOS CO_2 retrieval algorithm assumes that CO_2 concentration varies linearly with pressure, such that $f_i = \frac{1}{2}$ and

$$f_S = \frac{p_S - p_{N-1}}{p_N - p_{N-1}} \quad (\text{Eq. 3.8})$$

Note: The 8 equations above are cited from (O'Dell *et al.*,2012) corresponding to A1 to A8 respectively.

The ACOS B3.3 algorithm has been modified from B2.9 regarding the pressure levels, i.e. the atmospheric column starts from near-zero hpa instead of TOA; the surface level overlaps with level N which means the column ends with the surface level; and the column is always parted in 19 layers bounded by 20 levels with constant pressure interval through the whole atmospheric column. Therefore, Eq. 3.5 is simplified as:

$$h_i = \begin{cases} h'_i/2 & i=1 \\ h'_{i-1}/2 + h'_i/2 & i=2\dots N-1 \\ h'_{i-1}/2 & i=N \end{cases} \quad (\text{Eq. 3.9})$$

Considering the pressure weighting function \bar{h} has been extracted from the HDF5 files, the pressure weights for each layer can be calculated by inversing Eq. 3.9:

$$h'_i = \begin{cases} 2h_i & i=1 \\ 2h_i - h'_{i-1} & i=2\dots N-2 \\ 2h_{i+1} & i=N-1 \end{cases} \quad (\text{Eq. 3.10})$$

As stated, the B3.3 algorithm assumes that the CO₂ concentration varies linearly with pressure and c in Eq.3.2 varies slowly and linearly with pressure within a layer. Taking this into account, the XCO₂ in Eq.3.3 thus can be expressed as a function of pressure weighting function and dry air mole fraction of CO₂ on levels:

$$XCO_2 = \sum_{i=1}^N h_i u_i \quad (\text{Eq. 3.11})$$

So far, we are able to calculate partial-column CO₂ dry air mole fraction with any given number of layers; however, before doing so one must recalculate h_i for the partial column and the new pressure weighting function $\overline{h_{new}}$ should be normalized prior to use. In addition, CO₂ abundances are also available by multiplying the partial column XCO₂ and dry air abundances.

Importantly, attentions are needed for the physical and meteorological difference between the target site and background areas. It is highly likely that the pressure spans and dry air abundances etc. are different for partial columns with the same number of layers among different soundings.

In addition to calculating the partial column CO₂ information with a given number of layers, the background partial columns are adjusted to the target column in two possible ways as shown in Figure 3.4.

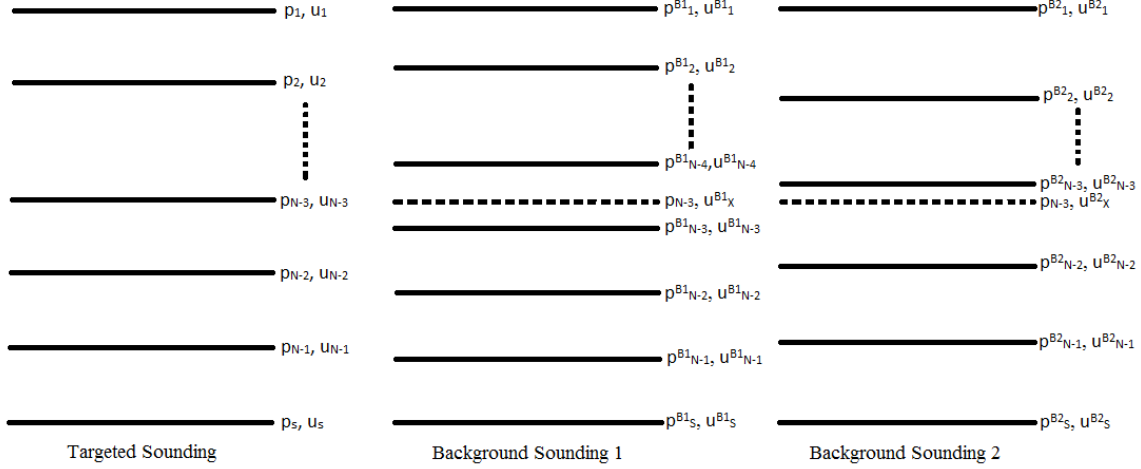


Figure 3.4 Different Pressure Systems of Target Sounding and Two Background Soundings

Assuming that p_i , p^{B1}_i and p^{B2}_i are different which normally is true, the objective is to compare target and background soundings in the same pressure span where the pressure span of the target sounding is taken as the standard. Here we take partial columns with 3 layers for example to illustrate how background soundings are adjusted to the target sounding.

Assuming that the pressure weighting function for the whole column has been converted to pressure weights of each layer $\overline{h'_{B1}}$ and $\overline{h'_{B2}}$ for background sounding 1 and 2 respectively, the adjustment is implemented differentially in two situations: (1) $p^{B1}_{N-3} < p_{N-3}$ for background sounding 1, and (2) $p^{B2}_{N-3} > p_{N-3}$ for background sounding 2.

As for background sounding 1, the pressure weights on the five levels ($\overline{h^{B1}}$) and XCO₂ on level p_{N-3} (u^{B1}_X) need recalculating. The pressure weights for the four low layers are taken from $\overline{h'_{B1}}$ to generate $\overline{h''_{B1}}$.

Formulated by Eq. 3.5, $\overline{h^{B1}}$ is expressed as Eq. 3.12.

According to Eq. 3.6 and Eq. 3.7, the XCO₂ on a pressure level can be acquired from the pressures and XCO₂ on two bounding levels by means of linear interpolation, thus u^{B1}_X can be calculated by Eq.3.13.

The partial column XCO₂ for background sounding 1 (from p_{N-3} to p^{B1}_S) is now available using Eq.3.11.

As for the calculation of partial column CO₂ abundances, the density of dry air per unit varies slowly and linearly over any given layer. However, the gradient is not provided in the HDF5 files. In order to obtain the dry air abundances from p_{N-3} to p^{B1}_S , in this study we assume that the gradient is close to 0 so that the dry air abundances for a part of layer is calculable by linear interpolation.

$$\overline{h^{B1}_i} = \begin{cases} \frac{h^{B1i} \cdot dofp}{2dp} & i=1 \\ \frac{h^{B1i} + h^{B1i-1} \cdot (1-dofp)}{2} & i=2 \\ \frac{h^{B1i} + h^{B1i-1}}{2} & i=3,4 \\ \frac{h^{B1i-1}}{2} & i=5 \end{cases} \quad (\text{Eq. 3.12})$$

where dp denotes the pressure interval of background sounding 1 and $dofp$ equals to absolute difference between p_{N-3} and p^{B1}_{N-3} .

$$u^{B1}_X = \frac{dofp}{dp} u^{B1}_{N-4} + \frac{dp-dofp}{dp} u^{B1}_{N-3} \quad (\text{Eq. 3.13})$$

The calculation of partial column CO₂ information for background sounding 2 is conducted in a similar manner. The pressure weights for the three low layers are taken from $\overline{h^{B2}_i}$ to generate $\overline{h^{B2}_i}$. Thus $\overline{h^{B2}_i}$ and u^{B2}_X are expressed as:

$$\overline{h}^{B^2}_i = \begin{cases} \frac{h^{B^2}_{B2i} \cdot (dp - dofp)}{2dp} & i=1 \\ \frac{h^{B^2}_{B2i}}{2} + \frac{h^{B^2}_{B2i-1} \cdot (1 - (dp - dofp))}{2dp} & i=2 \\ \frac{h^{B^2}_{B2i} + h^{B^2}_{B2i-1}}{2} & i=3 \\ \frac{h^{B^2}_{B2i-1}}{2} & i=4 \end{cases} \quad (\text{Eq. 3.14})$$

$$\text{and } u^{B^2}_X = \frac{dofp}{dp} u^{B^2}_{N-2} + \frac{dp - dofp}{dp} u^{B^2}_{N-3} \quad (\text{Eq. 3.15})$$

where dofp denotes the absolute difference between p_{N-3} and $p^{B^2}_{N-3}$.

The strategy for retrieving CO₂ information of a partial column with a higher number of layers (N>3) is the same. See Eq. 3.16 and Eq. 3.17. One should note that all recalculated pressure weighting functions for partial columns should be normalized before used for calculating partial column CO₂ dry air mole fraction.

$$\overline{h}^B_i = \begin{cases} \frac{h^{B^2}_{Bi} \cdot dofp}{2dp} & i=1 \\ \frac{h^{B^2}_{Bi}}{2} + \frac{h^{B^2}_{Bi-1} \cdot (1 - dofp)}{2dp} & i=2 \\ \frac{h^{B^2}_{Bi} + h^{B^2}_{Bi-1}}{2} & i=3 \dots N+1 \\ \frac{h^{B^2}_{Bi-1}}{2} & i=N+2 \end{cases} \quad (\text{Eq. 3.16})$$

For a background sounding whose partial column pressure span with N layers is lower than that of the target sounding, where dofp is the absolute pressure difference between target and background soundings, \overline{h}^B consists of the last N+1 elements of the recalculated pressure weights for layers.

$$\overline{h^B}_i = \begin{cases} \frac{h''_{Bi} \cdot (dp - dof p)}{2dp} & i=1 \\ \frac{h''_{Bi}}{2} + \frac{h''_{Bi-1} \cdot (1 - (dp - dof p))}{2dp} & i=2 \\ \frac{h''_{Bi} + h''_{Bi-1}}{2} & i=3 \dots N \\ \frac{h''_{Bi-1}}{2} & i=N+1 \end{cases} \quad (\text{Eq. 3.17})$$

For a background sounding whose partial column pressure span with N layers is higher than that of the target sounding and $\overline{h''_B}$ consists of the last N elements of the recalculated pressure weights for layers.

It is critical to mention that the absolute pressure difference between the target and background soundings is examined prior to calculation. Eq. 3.16 and Eq. 3.17 are formulated for the situations when the absolute pressure difference is smaller than the pressure interval of background soundings. For the cases when the absolute pressure difference is higher than one pressure interval, $N=N+1$ when background pressure span is lower than that of the target sounding and $N=N-1$ when background pressure span is higher. $N=N+2$ or $N=N-2$ when the absolute pressure difference is higher than twice the pressure interval of background soundings and so forth. Considering that the maximum number of layers for a partial column is 11 in this study, the absolute pressure difference does not exceed twice the pressure interval of background soundings. Furthermore, the calculation of dry air quantity and CO₂ abundances changes correspondingly.

3.2.2 Assumptions and Reliability Issues

This approach described in 3.2.1 follows and extends the assumptions from the ACOS B3.3 algorithm. In terms of retrieving pressure weighting function and calculating partial column CO₂ information, two assumptions are adopted by B3.3 algorithm: (1) CO₂ concentration varies linearly with pressure; and (2) the density of dry air per unit pressure varies slowly and linearly over any given layer.

Assumption (1) is transformed from the assumption in another retrieval algorithm for the OCO mission (Connor et al. 2008), i.e. the CO₂ concentration varies linearly in log pressure. According to Chris O'Neil who is the key developer of ACOS B3.3 algorithm, different interpolation

schemes were performed as a validation test, and the simple linear interpolation always performed plenty well for the ACOS research purposes. The differences with other interpolations are as tiny as 0.01 ppm to their collection.

Considering that the dry air quantity for a portion of a layer is indispensable to the calculation of partial column CO₂ information with a standardized pressure span and that the gradient and initial state of the density of dry air per unit pressure are not available from the retrieved results, the proposed approach in this study further assumes that the density of dry air per unit pressure stays constant over any given layer. This assumption based on assumption (2) is taken as appropriate and approved by the ACOS team.

The reliability of this approach is considered on four aspects. The first is the accuracy of the ACOS CO₂ data. As we know, the lower atmosphere is where the transportation of CO₂ occurs most intensively such as dispersion and convection and it is less ‘transparent’ than upper atmosphere due to clouds and aerosols etc. With this respect, the accuracy of CO₂ information for the lower layers or levels is questionable to some extent and needs examination when being used.

The second regards the designed strategy for selecting background soundings. By designing a ‘background area’ scenario, the objective is to ‘extract’ the CO₂ enhancement caused by fossil fuel combustion and to rule out the CO₂ either increased or decreased by the biosphere. However in practice, errors are very much likely to exist on the fossil fuel and biosphere fluxes between an ideal background area and a real one. It is expected that the impact of these errors are ignorable compared to CO₂ enhancement (concentration and/or abundance).

Even though fossil fuel combustion and biosphere-atmosphere exchange along with air-ocean transport are playing the most significant role in determining the CO₂ concentrations at various scales, there are a number of other factors that should be taken into account when one studies the local CO₂ concentration especially that near the surface. Therefore, the last reliability issue is about the influence of weather or meteorological factors such as wind speed, temperature, pressure, visibility, humidity and synoptic events.

The last is about the magnitude of biosphere flux and surface CO₂ emissions and the scale for analysis. The biosphere flux values (obtained from CarbonTracker 1 °flux data) range from -6.4e-05 to 6.8e-05 mol/m² s for the area (35 °N to 50 °N, -90 °W to -70 °W) in 2010, corresponding to -2.30e07 to 2.45e07 mol/(100km²) h. As for the CO₂ emissions from the power plant, the typical range of emission rate for pulverized coal power plant without CO₂ capture is 722 to 941 kg

CO₂/MWh (Rubin *et al.*,2004). The generating output on the dates of study from Nanticoke GS is 0-3600MW. Taking 795kg CO₂/MWh (the representative value defined in Rubin *et al.* 2004) as the emission rate for Nanticoke GS, the generating output can be transformed to a flux value of 0-6.5e07 mol/(100km²) h, assuming the size of CO₂ source equals to the size of GOSAT FOV (100km²). The biosphere flux and the power plant CO₂ emissions have the same order of magnitude, which also indicates that the scale of GOSAT FOV is proper for the comparison between biosphere and fossil fuel fluxes.

3.3 Data Collection

This study uses five types of data including power generating output, fossil fuel and biosphere fluxes, meteorology information and CO₂ retrievals. See Table 3.2 for data sources and descriptions.

Table 3.2 Data Sources and Data Description

Data Type	Data Access	Data Description
Power Generating Output	IESO	IESO archives the hourly outputs and capacities of its associated power plants. Historical data are available upon request.
Fossil Fuel and Biosphere Fluxes	CarbonTracker, NOAA	CarbonTracker provides fossil fuel, biosphere, wildfire and ocean fluxes and estimates CO ₂ mole fractions owing to each these fluxes. The spatial resolution is 1 degree on a global scale. Three-hourly and monthly fluxes are both distributed. In particular for fossil fuel flux, 4 inversions using the "Miller" emissions, and 4 using the ODIAC emissions are performed separately and the fluxes CarbonTracker distributes are the mean of these two emissions products. The fluxes open to the public are updated to the end of 2010. Additional data are available through communication.
Meteorology	Environment Canada	Information about temperature, humidity, wind speed, wind direction, visibility, pressure and general weather description observed from weather stations on an hourly basis are available from Environment Canada
Meteorology-PBL Depth	NARR, ESRL	The PBL depth data are retrieval from NCEP North American Regional Reanalysis, Earth System Research Laboratory.
CO ₂ Retrievals	ACOS Task, NASA	ACOS CO ₂ dataset starts with Build 2.10 and is up to Build 3.4 presently. ACOS L2S products for B2.9 and B3.3 that contain full physical retrievals are publicly available through the ACOS website. Files are in the format of HDF5. Applicable data processing tools include IDL, Python and MATLAB. The ACOS Task involves a number of institutions: JPL NASA, California Institute of Technology, and Colorado State University. The ACOS Task is terminated in September 2012 for resetting the OCO-2 Team and preparing for the OCO-2 mission. The B3.3 data package was released in June 2013 by the OCO-2 Team.

It is worth mentioning that three-hourly flux data are used in this study. The time of spacecraft's overpass is approximately 18:30 EST. Considering that the local CO₂ concentration at a specific point in time is most likely to be related to the fluxes for a period of time backwards, the sixth three-hour fluxes are used instead of the seventh.

3.4 Importance and Limitations

This study carries out partial column CO₂ retrievals and compares them with column CO₂ information with respect to the relationship with surface point emissions. In the meanwhile, the ability of remote sensing CO₂ information of reflecting monthly or seasonal variations of regional CO₂ is investigated. As a case study of Nanticoke GS and Hamilton, findings are expected to provide useful information about the usage of partial column CO₂ data at a point or regional scale, and provide insight for future studies on CO₂ sources and sinks using remote sensing CO₂ data.

However, one should be aware of the limitations of this study and that further efforts for improvement are needed. The coverage of spacecraft scans at high latitudes is not as sufficient as at low latitudes and the target observation mode is not applied for the study area. Consequently, in this study we use one single sounding to represent a point CO₂ emitter on the ground. More importantly, the point CO₂ source represented by one sounding is compared with a background area represented by a number of soundings. Therefore, the confidence in some of the outcomes and corresponding conclusions is highly likely to rely on the quality of the target sounding.

As for the concept of partial column in this study, it refers to a number of consecutive layers starting from the surface. However, a partial column with a few layers starting from any given pressure level is not considered. Future studies are encouraged to evaluate the performance of partial column CO₂ information in a more comprehensive manner.

Another limitation lies in the identification of background area and the flux data used for the identification. The spatial resolution of the flux data used in this study is 1 degree by 1 degree which is not qualified for resolving the background area on a smaller scale. However, an ideal background area or the background soundings are expected to be selected on a comparable scale with the target soundings. With a coarse flux resolution, there is a possibility that potential background soundings are ignored due to unmatched fossil fuel and biosphere fluxes of cells that they are located within. It is also possible that some selected soundings are not adequate since they may be vulnerable to surrounding CO₂ sources or sinks while the cell fluxes fulfill the identification criteria. High resolution fossil fuel flux data (1km) are available but not applied in this study due to limited access and computation concerns. A question one may ask is what the appropriate resolution is. There is no clear answer to this since it is very difficult to determine the characteristic scale on which the surface sources and sinks with different sizes and capacities are influencing the atmospheric CO₂ concentration of the column or partial column. Moreover, the

high-resolution flux data are also likely to ‘over resolve’ the target and background areas; therefore a selected background sounding may not be qualified as a representation of background CO₂ concentrations.

3.5 Hypotheses and Proposed Analysis

In this research, 4 main hypotheses are put forward and this section introduces a series of subsequent investigations that verify the hypotheses:

1. Overall, the CO₂ concentration and/or CO₂ abundance of the target sounding are higher than the average values of background soundings;
2. The difference of CO₂ concentration and/or CO₂ abundance between target and background soundings has an observable relation with the power plant generating output either linearly or nonlinearly.
3. Partial column XCO₂/CO₂ performs better than column XCO₂/CO₂ in resolving CO₂ emissions from a strong localized point source. One may be interested in seeking out the number of layers a partial column should adopt.
4. A monthly or seasonal variation of XCO₂/CO₂ for Hamilton urban area is observable using the ACOS CO₂ data. As a validation of the background area identification strategy, using the difference of XCO₂/CO₂ can generate desirable outcomes that are comparable to using target soundings alone.

In order to test these hypotheses, a data analysis framework is established that involves both quantitative and qualitative methods in the following steps:

1. Calculate the correlation of the column XCO₂ and CO₂ abundances of target soundings with the generating output during the study period, by year and by season.
2. Identify the minimum number of background soundings required to certify the selection of background area.
3. Visualize the shape of CO₂ profile for target soundings and identify the first inflection point manually which is expect to indicate the optimal number of layers that a partial column should take.

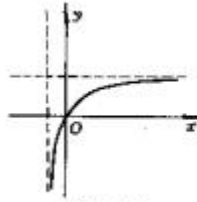
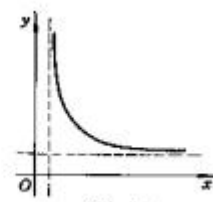
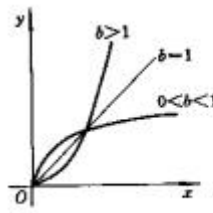
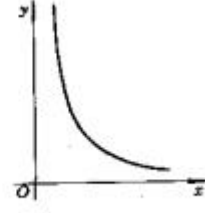
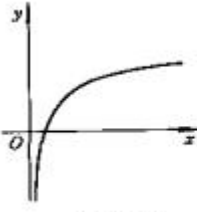
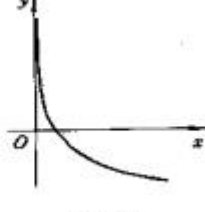
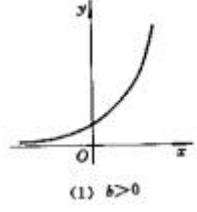
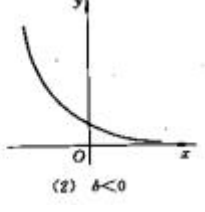
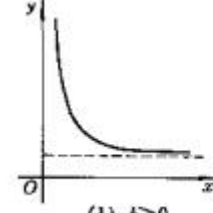
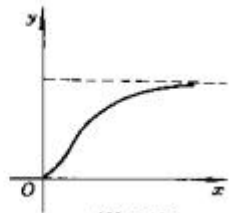
4. Determine the possible forms of regression through scatter plot of the difference of XCO_2 and CO_2 against generating output.
5. Perform linear and nonlinear regressions between the difference of XCO_2 and CO_2 and generating output. Partial columns with different numbers of layers and average outputs for the past two hours and three hours are all examined.
6. Calculate statistical indicators such as mean, maximum, minimum and standard deviation of CO_2 dry air mole fraction of each level for all selected target soundings.
7. Examine the uncertainty on retrieved CO_2 dry air mole fraction of each layer for all selected target soundings to explore possible reasons for discrepancy in the performance of partial columns with different numbers of layers.
8. Compare the weather factors gained from Hamilton Station and London Station and evaluate the reliability of using them to indicate the weather conditions at the target site.
9. Classify the target soundings by regression residual. Grade each meteorological parameter and explore possible clustering patterns that the accuracy of calculation may be partially dependent on one or more parameters.
10. Plot column XCO_2/CO_2 and partial column XCO_2/CO_2 with the ‘optimal’ number of layers in time series for the target sounding in Hamilton urban area. Compare them based on the goodness of fit to the Fourier curve that is expected to be representative of CO_2 natural seasonality.

3.5.1 Nonlinear Regression

In addition to linear correlation between the difference of XCO_2/CO_2 and generating output, nonlinear functions are also examined. The form of nonlinear functions that should be taken in this study is determined by interpreting the scatter plot of XCO_2/CO_2 difference against generating output.

Typical forms of nonlinear regression are summarized in Table 3.3. The transformations from nonlinear equations to linear equations are also described in Table 3.3.

Table 3.3 Forms of Nonlinear Regression

Curvilinear Equations	Transformation	Transformed Equations	Curvilinear Figures	
$\frac{1}{y} = a + \frac{b}{x}$	$X = \frac{1}{x}$ $Y = \frac{1}{y}$	$Y = a + bX$		
$y = ax^b$	$X = \ln x$ $Y = \ln y$	$Y = \ln a + bX$		
$y = a + b \ln x$	$X = \ln x$ $Y = y$	$Y = a + bX$		
$y = ae^{bx}$	$X = x$ $Y = \ln y$	$Y = \ln a + bX$		
$y = ae^{\frac{b}{x}}$	$X = \frac{1}{x}$ $Y = \ln y$	$Y = \ln a + bX$		

3.5.2 Meteorological Condition

For the purpose of estimating the influence of meteorological system on local CO₂ concentration thus the target-background difference, possible influential meteorological parameters are examined in association with the surface XCO₂ uncertainty and the regression residual. The involved meteorological parameters include wind speed, wind direction deviation, temperature, pressure, humidity, and weather event/description.

In order to better explore the potential influence, for the meteorological parameters that are expressed quantitatively, the magnitude of each parameter for all target dates is partitioned into 10 scales so that the meteorological parameters can be rated on a scale from 1 to 10 in ascending order of factor values. As for the weather event/description, it is scaled from 1 to 6 corresponding to ‘clear’, ‘mainly clear’, ‘mostly cloudy’, ‘cloudy’, ‘fog’/‘haze’, and ‘rain shower’/‘thunderstorm’/‘snow shower’ etc.

A linear or nonlinear function is then taken as a reference and the residuals of dXCO₂ or dCO₂ are calculated. The influence of one specific meteorological parameter is estimated based on the residuals and factor scales on all target days. The target soundings are also grouped as strong fit and weak fit. The meteorological parameters are examined within each group.

Considering the temporal pattern of GOSAT sounding, e.g. winter observations may be insufficient, most meteorological parameters can be not normally distributed; for particular parameters, the distribution of original data can be very non-uniform such as temperature. In order to examine the significance of any conclusion to be drawn on the impacts of external factors, the influential parameters are modified by excluding extraordinary values to obtain a more uniform distribution. This is achieved using a resampling approach: the original data are sorted in ascending order; a certain proportion (7% to 20%) of data are removed on the one or both ends and the ratio between the low end and the high end is randomly determined, i.e. the ‘proportion’ starts with 7% and the percentage of data to remove can be 0% on the low-value end and 7% on the high-value end, and so forth; a linear hypothesis test¹⁷ is then carried out on the remaining (adjusted) data and the ‘proportion’ will increase if the adjusted data cannot pass the test; the goodness of fit of all possible sets of adjusted data to a straight line is also calculated and used for

¹⁷ Matlab & Simulink – MathWorks: <http://www.mathworks.com/help/stats/linhypstest.html>

determining the proper adjusted data set if the linear test is not passed despite 20% of original data being removed.

The influence of meteorological parameters on model performance is also examined using multivariate analysis that involves all the relevant parameters. The multivariate analysis is conducted with different assumptions on the relationship of the meteorological parameters with the model residuals: linear, pure quadratic, interactions and full quadratic.

3.6 Summary

This chapter proposes a system approach to evaluate the capability of remote sensing CO₂ data to estimate surface CO₂ emissions at point and regional scales. In this chapter, the research planning, data collection, the importance and limitation of proposed approaches, and the hypotheses and data analysis are described.

In particular, one is able to replicate the retrieval outcomes by using the method in 3.2.1. Partial column CO₂ information with different numbers of layers is retrievable as well as that for a given pressure span. The methods are based on two assumptions from the original ACOS B3.3 retrieval algorithm and one assumption extended from them. These assumptions are analyzed and verified by mathematical means by the previous ACOS Team. The method is applicable to soundings by ACOS B3.3 algorithm or similar which retrieves and provides information about CO₂ profiles, dry air profiles, pressure weighting function and so forth. However, due to possibly inaccurate raw CO₂ retrieval data, one should note that the uncertainty on the CO₂ information for specific layers may need examinations and the reliability needs evaluation prior to use.

A key procedure in the proposed approach is the identification of background area. Two thresholds are determined to constrain the fossil fuel and biosphere fluxes for background soundings, though theoretically a background area is defined as one with zero fossil fuel flux and identical biosphere flux to that of the target site. One could also use other methods for identifying potential background area with necessary data available such as high resolution flux data, nightlight image or population map that indicates the intensity of human residency/activities and thus CO₂ emissions.

To validate the hypotheses, quantitative and qualitative data analysis methods are adopted. The results are presented in Chapter 4.

Chapter 4: Results

4.1 Introduction

This chapter presents the results and findings using the methods introduced in Chapter 3. Built on the procedures of the data analysis strategy, the results and findings are organized in nine sections: (1) a description of target soundings, and corresponding column XCO₂ and CO₂ abundance statistics, (2) a pre-analysis of background area, (3) a prediction of best number of layers for partial column CO₂ retrieval, (4) possible forms of regression between difference of XCO₂ / CO₂ and generating output, (5) results of regression, (6) partial column XCO₂ and CO₂ statistics, (7) a comparison of meteorological parameters obtained from Hamilton Station and London Station, (8) evaluation on the influence of meteorological parameters, and (9) monthly and seasonal XCO₂ variation of Hamilton urban area.

By presenting and analyzing the results quantitatively and qualitatively, the research hypotheses (see Section 3.5) are tested and the research questions can be answered. This chapter is limited to the results of data processing and basic explanations. Interpretations and evaluations on these results and findings will be discussed in detail in the next chapter.

4.2 Target Column XCO₂ and CO₂ Abundance

This section introduces the results of basic statistics on column XCO₂ and CO₂ information for target soundings.

A target sounding is defined as one whose FOV Nanticoke Generating Station locates within or is very close to. Throughout September 2009 to May 2013, 71 target soundings are captured. The number of soundings that met all selection criteria is presented by year in Table 4.1.

The generating outputs of Nanticoke Station are retrieved for corresponding dates. Generally, the time of sounding is very close to 18:30 EST and the outputs from the station in the current and previous hours are retrieved. Considering that the CO₂ emissions from the power plant are very likely to have a delayed effect on the local CO₂ concentration, especially for upper atmosphere,

the average output for two hours backwards and three hours backwards are calculated as well. The XCO₂ and uncertainty, CO₂ abundance and output on target dates are shown in Table A.1.

Table 4.1 Number of Soundings by Year

	2009	2010	2011	2012	2013	Total
Number of Soundings	3	24	20	21	3	71

The dual y-axes plot for XCO₂ (target and background) and generating output (one-hour output for example) is shown in Figure 4.1. The natural CO₂ seasonality¹⁸ can be observed from this graph which is an approximation of the Fourier function. The CO₂ seasonality before 2012 is associated with strong fluctuations while it is smoother with a shallower cycle over the 2012-2013 period.

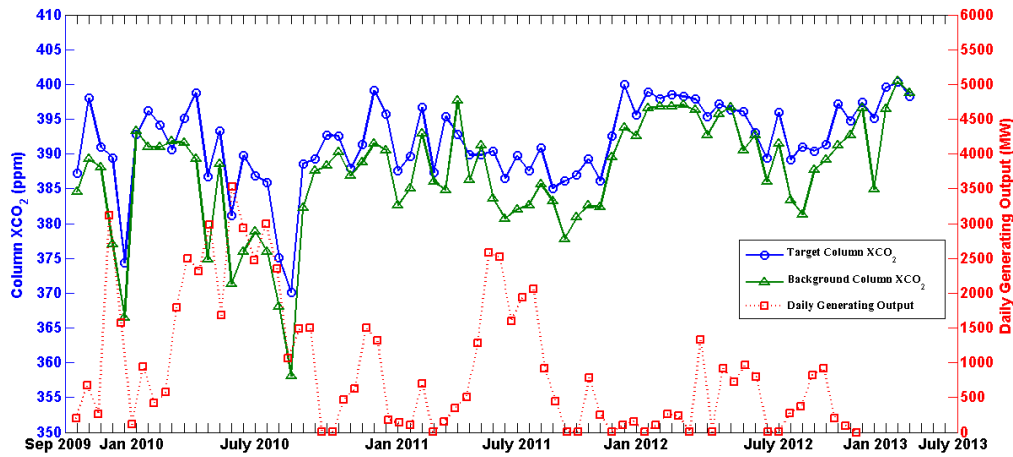


Figure 4.1 Target and Background Column XCO₂ and One-Hour Output

The daily variations of generating outputs (the daily output is represented by hourly averaged value) over the whole period (from the first sounding date to the last) are shown in Figure 4.2 along with the smoothing spline of CO₂ observations. The graph shows that the generating outputs before 2012 are higher and more variable than during the later 2012-13 period. High power generation occurred mainly during 2009-2010 winter, 2010 summer and 2011 summer.

¹⁸ The natural CO₂ seasonality refers to the monthly CO₂ cycle that is obtained from the Keeling Curve. The Keeling Curve is a graph which plots the ongoing change in concentration of CO₂ in Earth's atmosphere since 1958 in Mauna Loa.

The policy decision to reduce coal consumption and close the coal-fired generators clearly affected electricity output from the Nanticoke station. In addition, the atmospheric CO₂ concentrations do not necessarily follow the trend of generating outputs.

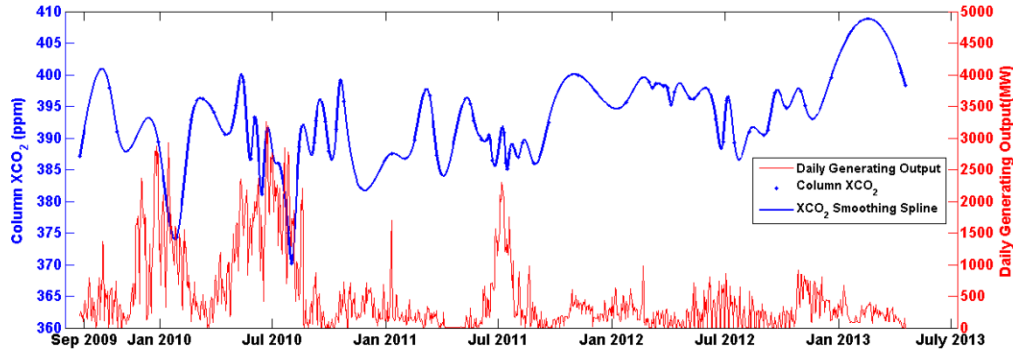


Figure 4.2 Smoothing Spline of XCO₂ and Daily Generating Outputs

The scatter plot of XCO₂ against output (one-hour) is shown in Figure 4.3. High generating outputs are expected to yield high atmospheric CO₂ concentrations. However, as shown in the graph, CO₂ concentrations vary by 15-20ppm whether coal-fired electricity output is less than 500 MW or around 2500-3000 MW.

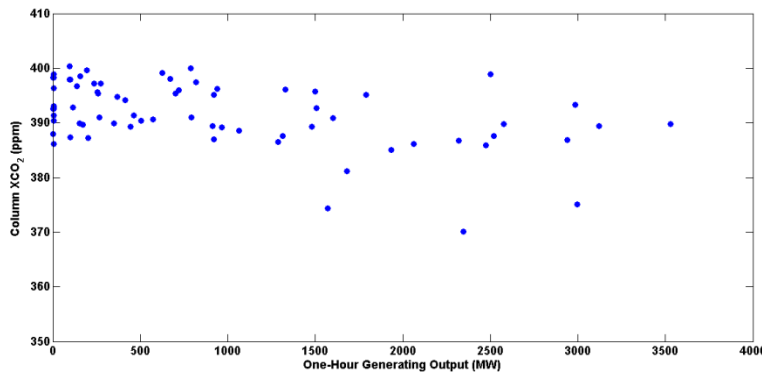


Figure 4.3 Target XCO₂ against One-Hour Output

Prior to calculating the correlation between XCO₂ and output, the type of correlation needs to be determined and the data normality tested. Figure 4.4 is the histogram of XCO₂ that indicates the data normality.

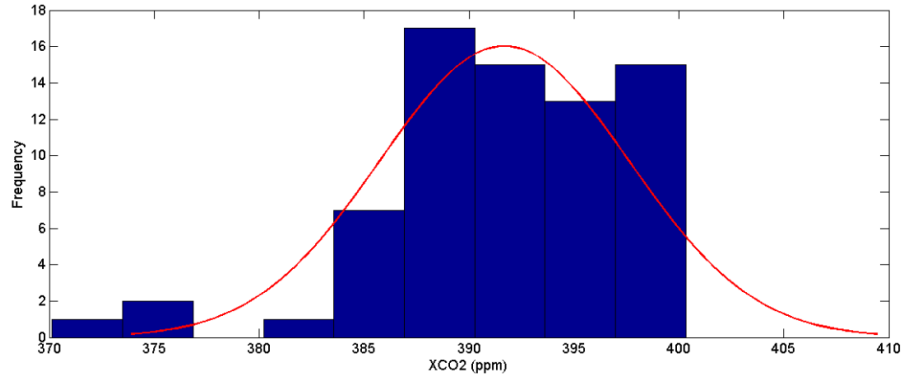


Figure 4.4 Histogram of XCO₂ Data

The Lilliefors test¹⁹ shows that the hypothesis ‘the data are normally distributed’ cannot be rejected at the 0.05 (and 0.001) level. Therefore, a Pearson’s correlation is carried out on XCO₂ and output. The correlation results are summarized in Table 4.2. Similarly, the correlation results for CO₂ abundance (indicated as CO₂) and generating output are also calculated and presented in Table 4.2

Table 4.2 Pearson’s Correlation between XCO₂ and Output

		One-Hour Output	Two-Hour Average Output	Three-Hour Average Output
XCO ₂	RHO	-0.4617	-0.4549	-0.4603
	PVAL	5.0715e-05	6.7460e-05	5.3612e-05
CO ₂	RHO	-0.4420	-0.4465	-0.4530
	PVAL	1.1398e-04	9.4913e-05	7.2889e-05

¹⁹ Lilliefors goodness-of-fit test of composite normality examines whether the data come from an unspecified normal distribution. ‘Lilliefors test is suitable for situations where a fully-specified null distribution is not known, and its parameters must be estimated’. [H,P,KSTAT,CRITVAL] = lillietest(X, ALPHA) is the MATLAB syntax for performing Lilliefors test. H=0 indicates that the null hypothesis ‘the data are normally distributed’ cannot be rejected at the significance level of ALPHA. H=1 indicates that the null hypothesis can be rejected at the significance level of ALPHA. Small values of P imply that the validity of the null hypothesis can be doubted. When the test statistic KSTAT is higher than the critical value CRITVAL, the null hypothesis can be rejected at a significance level of ALPHA. (MATLAB MathWorks 2012)

where RHO denotes the correlation coefficient and PVAL²⁰ is the result of significance test. Hereafter, for better understanding and comparison, RHO rounds off to 4 decimal places.

As Table 4.2 shows, the column XCO₂ and the CO₂ are negatively correlated to output. The PVALs indicate that the correlations are significant. The relationship between CO₂ concentrations and generating outputs (one hour) is also examined by year: the correlation coefficient is -0.3136 for 2010, -0.3404 for 2011 and -0.3073 for 2012.

The CO₂ natural seasonality and CO₂ emission seasonality are analyzed to seek out possible reasons for the negative correlation between CO₂ concentrations and generating outputs. The CO₂ seasonality is represented by the CO₂ measurements acquired from the Chibougamau Station, Ontario (49.68 N, 74.34 W, 393m) on a monthly basis for 2010 (the hourly measurements are integrated), as shown in Figure 4.5.

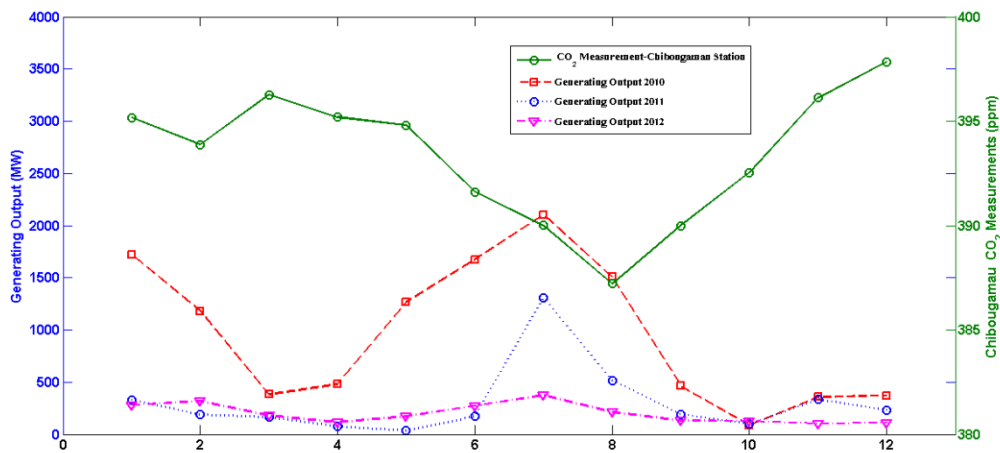


Figure 4.5 CO₂ Concentration Seasonality and CO₂ Emission Seasonality

As per Ontario's policy decision to reduce electricity generation from coal-fired stations, Nanticoke GS became a marginal plant that was only used when the system faced peak demand (Figure 4.5). Output exceeded 1000 MW only periodically: winter (Jan., Feb.) 2010, summer 2010 and summer 2011. The 2010 output curve is the inverse of the natural CO₂ concentration curve as output decreased while CO₂ concentration increased from January to March, then output rose while CO₂ concentration decreased from April to July. In all three years, output was low

²⁰ PVAL is the outcome from a significance test for testing the hypothesis of no correlation against the alternative of non-zero correlation. A small PVAL (usually less than 0.05) indicates that the correlation is significantly different from 0.

from September to December. The ‘2010 pattern’ was less pronounced in 2011 as large outputs were restricted to July and August. The operational decisions at Nanticoke GS result in output levels that explain at least part of the negative correlation measured between output and CO₂ concentrations (Table 4.2).

The detectability of ground emission signal from the observed concentration is further examined by analyzing an individual month (July) and an individual season (July-September) over 2010 to 2012. By doing so, the influence of the natural seasonality of CO₂ concentration is expected to be constrained. The results are shown in Figure 4.6a (July) and 4.6b (July, August and September).

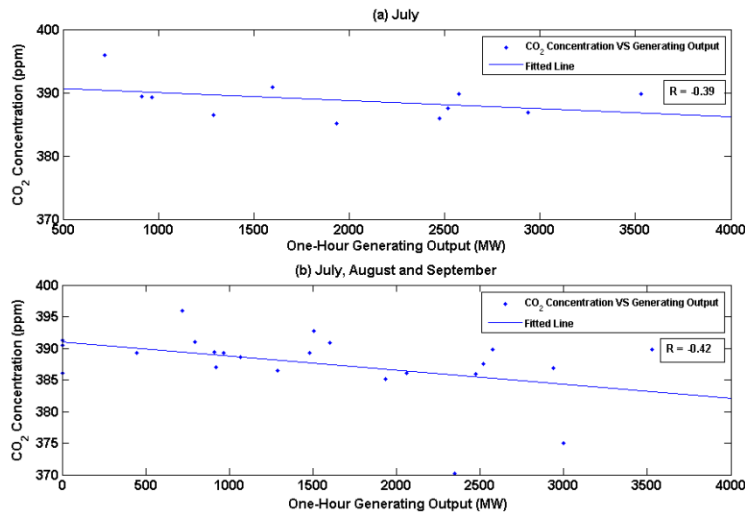


Figure 4.6 Generating Output and CO₂ Concentrations of Individual Month and Individual Season

Negative correlations are obtained for July and the ‘summer-fall’ season. Associated with previous findings in this section, it implies that the ability of absolute CO₂ concentrations to reflect ground emissions is poor due to the dominant CO₂ natural seasonality despite strong CO₂ emissions in July and the ‘season’. Therefore, the proposed method (in Chapter 3) is carried out and the results are presented in the following sections.

4.3 Background Area Pre-analysis

This section presents the results of determining the minimum number of soundings for certifying a background area. Two areas at mid latitudes in North America are compared, i.e. two grids of 3 degree by 3 degree centered to A (44.5 °N, 79.5 °W) and B (40.5 °N, 83.5 °W) respectively. Basic statistics regarding these two areas are as follows: the distribution of cellular flux (the sum

of fossil fuel flux and biosphere flux) of each area, comparison of the sum of cellular flux between two areas, and the difference of column and partial column XCO₂ between two areas.

4.3.1. Flux Heterogeneity

The flux heterogeneity refers to the characteristics of inner distribution of flux within each area. A low heterogeneity is expected to imply comparable soundings respecting XCO₂ within each area without considering the influence of external factors. In other words, the deviation of XCO₂ of each area is expected to be small.

In total, 111 days are captured throughout the year 2010, 2011 and 2012 when soundings are available in both areas. The mean and standard deviation of cellular fluxes are calculated for each area on each day. The standard deviation is taken as the indicator for flux heterogeneity.

The average mean and average standard deviation are 3.23e-06 mol/m² s and 1.13e-06 mol/m² s respectively for area A, 3.56e-06 mol/m² s and 9.25 e-07 mol/m² s respectively for area B.

As for the difference of gross regional fluxes, the average is -2.96e-06 mol/m² s and the standard deviation is 1.50e-05 mol/m² s.

4.3.2 Column and Partial Column XCO₂

For the 111 days, the difference of column and partial column XCO₂ (with a given number of layers) is calculated. In the meantime, the mean, maximum, minimum, amplitude and standard deviation of XCO₂ difference are shown in Table 4.3. The partial column XCO₂ within a given pressure span is not considered here.

Table 4.3 Statistics of XCO₂ Difference between Two Areas

	Mean (ppm)	Max (ppm)	Min (ppm)	Amplitude (ppm)	STD (ppm)
Column	-1.13	12.74	-13.26	26.00	4.08
3-Layer Partial Column	1.16	47.60	-42.03	89.63	15.99
4-Layer Partial Column	0.48	42.92	-38.68	81.60	14.13
5-Layer Partial Column	-0.11	38.46	-35.51	73.98	12.47
6-Layer Partial Column	-0.60	34.44	-32.61	67.05	11.06
7-Layer Partial Column	-0.97	30.92	-29.95	60.86	9.86
8-Layer Partial Column	-1.22	27.90	-27.53	55.43	8.87
9-Layer Partial Column	-1.39	25.33	-25.38	50.71	8.04
10-Layer Partial Column	-1.49	23.15	-23.49	46.64	7.35
11-Layer Partial Column	-1.55	21.30	-21.83	43.13	6.78

Then three is set as the minimum number of soundings for identifying a background area. 13 days are eliminated from the 111 days because the number of soundings in either of the two areas is less than three. The recalculated statistics are shown in Table 4.4.

Table 4.4 Statistics of XCO₂ Difference with Number of Soundings Larger than Three

	Mean (ppm)	Max (ppm)	Min (ppm)	Amplitude (ppm)	STD (ppm)
Column	-0.74	12.74	-9.49	22.23	3.44
3-Layer Partial Column	3.37	47.60	-35.29	82.89	13.01
4-Layer Partial Column	2.40	42.92	-30.08	73.01	11.47
5-Layer Partial Column	1.55	38.46	-25.50	63.96	10.12
6-Layer Partial Column	0.84	34.44	-21.62	56.05	8.98
7-Layer Partial Column	0.29	30.92	-18.37	49.28	8.02
8-Layer Partial Column	-0.12	27.90	-16.84	44.74	7.24
9-Layer Partial Column	-0.42	25.33	-15.88	41.21	6.59
10-Layer Partial Column	-0.63	23.15	-14.95	38.10	6.05
11-Layer Partial Column	-0.79	21.30	-14.10	35.39	5.60

By setting three as the minimum number of soundings, significant ‘outliers’ in terms of CO₂ concentration are removed. The mean of XCO₂ difference for both column and partial columns become closer to zero and the standard deviations get smaller.

Consequently, five days are removed from the target soundings since the numbers of background soundings are not sufficient on these days.

4.4 Estimate of Number of Layers

Before proceeding with the calculation of target and background soundings, the number of layers for a partial column in terms of best correlation with output is predicted by analysing the shape of CO₂ profiles of target soundings, as shown in Figure 4.7.

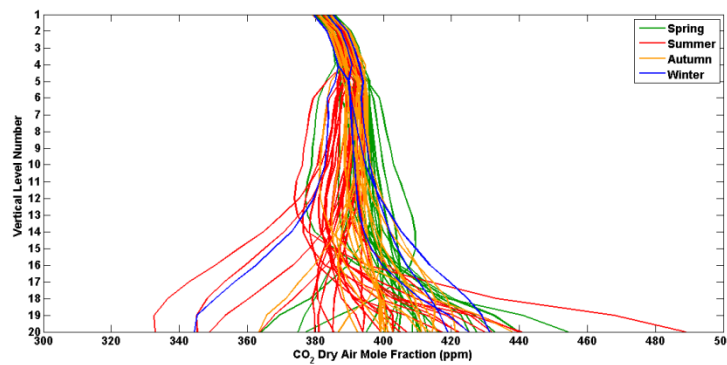


Figure 4.7 Shape of Target CO₂ Profiles

The shape of CO₂ profiles of background soundings (150 samples randomly selected) is drawn in Figure 4.8.

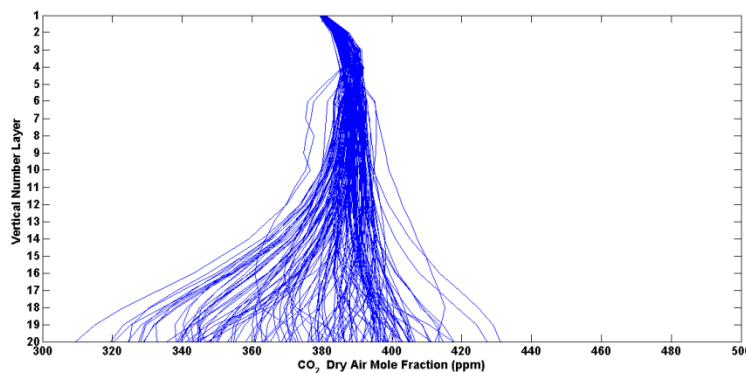


Figure 4.8 Shape of Background CO₂ Profiles-150 Samples Randomly Selected

As for target observations, a few lowest CO₂ concentrations and the highest concentration occur in summer. The variations of CO₂ concentrations on different days and among different vertical levels in summer are very large. The concentrations are generally lower than spring and autumn. Spring and autumn account for high and moderate CO₂ concentrations with relatively small vertical variations. CO₂ concentrations in winter are among the highest with the smallest vertical variations despite limited number of observations. Compared to the background lines, the target lines are more located and stretching to the right which indicates higher CO₂ concentrations overall. In addition, both the target and background lines tend to converge and turn at 11 on the y-axis (the first inflection point²¹) which is the edging level of the 9th and 10th layer from surface up. The implication is a partial column with 9 or 10 layers is likely to be the optimal for reflecting the surface flux.

4.5 Data Fitting

In addition to linear correlation, non-linear curve fitting is also examined between the difference of XCO₂ / CO₂ and generating output. Typical forms of non-linear function have been introduced in 3.5.1. Potential non-linear functions for the data are determined by interpreting the scatter plot of XCO₂ / CO₂ difference against generating output.

The differences of column and partial column XCO₂ between target and background soundings are summarized in Table A.2. The scatter plots of column dXCO₂ and 10-layer partial column dXCO₂ against one-hour generating output are drawn in Figure 4.9 and Figure 4.10.

²¹ For differential calculus, an inflection point for a curve is a point where the curvature changes from positive to negative, or vice versa. The identified inflection point for the target soundings is expected to recognize the under-performance of higher layers in reflecting ground CO₂ emissions.

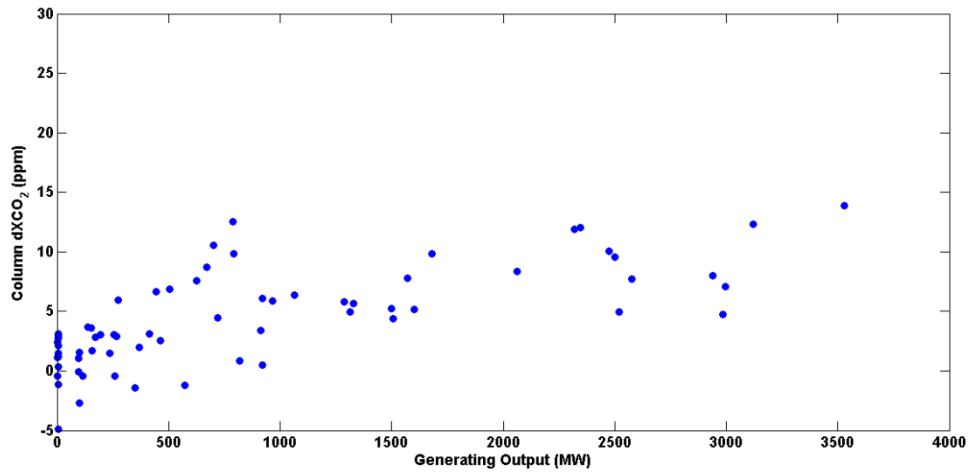


Figure 4.9 Column dXCO₂ against Generating Output

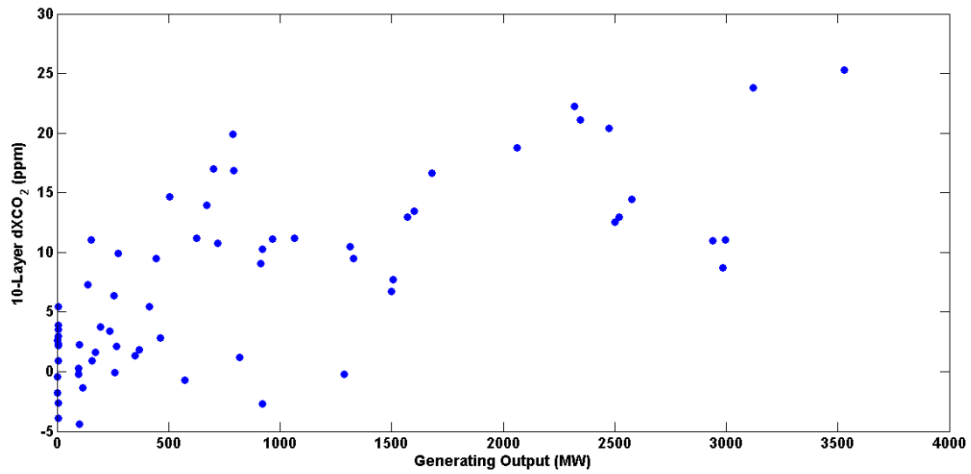


Figure 4.10 10-Layer Partial Column dXCO₂ against Generating Output

Figure 4.11 shows the smoothing spline of column dXCO₂ against one-hour generating output.

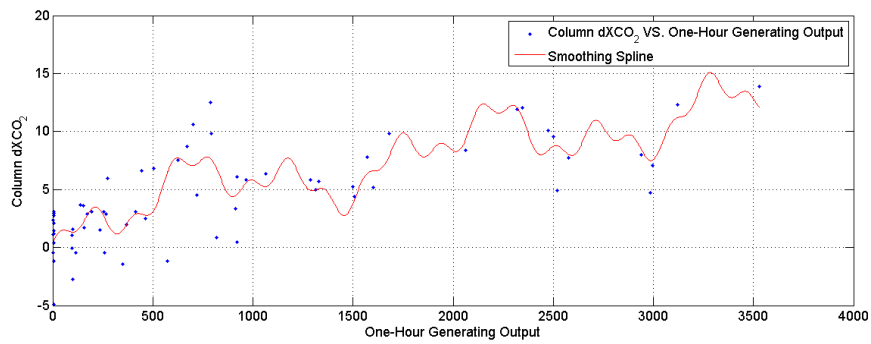


Figure 4.11 Column dXCO₂ Smoothing Spline

A number of nonlinear functions for regression are pre-tested before the results are presented, including exponential, logarithmic, Fourier, Gaussian, polynomial, power, rational, and sum of sine. These functions are capable of generating monotonic curves that are expected to express the relationship between generating output and CO₂ enhancement. Importantly, any regression with a complicated curve shape is not considered even though the goodness of fit may be relatively high, e.g. more than 1 wave peaks/troughs. Besides, a regression with identical or too similar result with another is not considered for result presentation either, e.g. Fourier and 2-degree polynomial regressions generate the same key regression statistics. The functions that are determined to present in the next section are summarized in Table 4.5.

Table 4.5 Potential Functions for Linear and Nonlinear Regression

Forms	Equations
Linear	$y = ax + b$
Nonlinear	Power Function $y = ax^b + c$
	Polynomial Function $y = ax^2 + bx + c$
	Rational Function $y = (ax + b) / (x + c)$
	Sum of Sine $y = a \sin(bx + c)$

Particularly, 2-degree polynomial function, 3-degree polynomial function, 1-degree rational function and 2-degree rational function are all options for nonlinear function selection. Based on the criteria for presenting nonlinear regression results, 2-degree polynomial and 1-degree (1 numerator degree and 1 denominator degree) rational functions are analyzed.

4.6 Regression Results

This section presents the results of linear and nonlinear correlations. One-hour output, two-hour average generating output and three-hour average generating output are considered for the correlations.

For linear correlations, the correlation coefficients and significance levels are calculated for column dXCO₂ and dCO₂ and partial column dXCO₂ and dCO₂. Different numbers of layers (from 3 to 11) are taken for a partial column. And the partial column dXCO₂ and dCO₂ are calculated for a given number of layers and a standardized pressure span.

For estimating the goodness of fit of nonlinear regression, the R-square²² statistic (R^2) and RMSE²³ are calculated for each nonlinear regression. For linear regression, only R^2 is calculated. For better comparison between regressions, the R^2 rounds off to 4 decimal places. The $dXCO_2$ and dCO_2 are measured in ppm and mole/layer respectively.

All regression functions are expressed using original coefficients instead of those after normalized by the mean and standard deviation.

Since the generating output on May 02, 2013 is 0 and this is contradictory to the definition domain for performing some nonlinear regressions, a positive bias of 0.0001MW is added which is consistent to the precision of R^2 .

4.6.1 Linear Correlation

Linear correlation is carried out for column and each partial column (Pearson's correlation is carried out for normally distributed data and Spearman correlation for non-normally distributed data). The correlation coefficients, the regressed slope and intercept round off to 4 decimal places. In Table 4.6, the best correlations for column data and partial column data with different numbers of layers are selected and summarized in descending order of correlations coefficient.

²² R-squared (R^2) is a statistical measure of how close the data are to the fitted regression line. Normally, R^2 is between 0 and 1. 0 indicates that the model explains none of the variability of the response data around its mean. 1 indicates that the model explains all the variability of the response data around its mean. A negative R^2 is possible if the model does not contain a constant term and the fit is poor (worse than just fitting the mean)

²³ The root mean squared error. A value closer to 0 indicates a better fit.

Table 4.6 Summary of Linear Correlation

	Correlation Coefficient	R ²	Intercept on Y-Axis	N-Layer / N-Pressure	dXCO ₂ / dCO ₂	Generating Output Averaging	Regression
11-Layer	0.7108	0.5107	2.6340	N-Layer	dXCO ₂	One Hour	$y = 0.0049x + 2.6340$ (Eq. 4.1)
9-Layer	0.7066	0.5065	2.8223	N-Layer	dXCO ₂	One Hour	$y = 0.0059x + 2.8223$ (Eq. 4.2)
Column	0.7062	0.4988	1.7890	N-Layer	dXCO ₂	One Hour	$y = 0.0029x + 1.7890$ (Eq. 4.3)
10-Layer	0.7039	0.5110	2.7289	N-Layer	dXCO ₂	One Hour	$y = 0.0054x + 2.7289$ (Eq. 4.4)
8-Layer	0.6919	0.4767	3.0870	N-Layer	dXCO ₂	One Hour	$y = 0.0066x + 3.0870$ (Eq. 4.5)
7-Layer	0.6877	0.4627	2.9947	N-Layer	dXCO ₂	Two Hour	$y = 0.0073x + 2.9947$ (Eq. 4.6)
6-Layer	0.6735	0.4548	2.7780	N-Layer	dXCO ₂	Two Hour	$y = 0.0080x + 2.7780$ (Eq. 4.7)
5-Layer	0.6585	0.4337	2.2590	N-Layer	dXCO ₂	Three Hour	$y = 0.0090x + 2.5290$ (Eq. 4.8)
4-Layer	0.6263	0.3922	2.4400	N-Layer	dXCO ₂	Three Hour	$y = 0.0100x + 2.4400$ (Eq. 4.9)
3-Layer	0.5957	0.3549	2.0980	N-Layer	dXCO ₂	Three Hour	$y = 0.0112x + 2.0980$ (Eq. 4.10)

4.6.2 Power Regression

Power regression is carried out for full column and each partial column. The R² is used for evaluating the goodness of fit. The best power regressions in terms of the R² statistic for column dXCO₂ and dCO₂ and partial column dXCO₂ and dCO₂ are summarized in Table 4.7, in descending order of R².

Table 4.7 Summary of Power Regression

	R ²	RMSE	Intercept on Y- Axis	N-Layer / N- Pressure	dXCO ₂ / dCO ₂	Generating Output Averaging	Regression
10-Layer	0.5446	5.07	0.3148	N-Layer	dXCO ₂	One Hour	$y = 0.1915x^{0.5614} + 0.3148$ (Eq. 4.11)
11-Layer	0.5428	4.67	0.4739	N-Layer	dXCO ₂	One Hour	$y = 0.1664x^{0.5681} + 0.4739$ (Eq. 4.12)
9-Layer	0.5408	5.59	0.1308	N-Layer	dXCO ₂	One Hour	$y = 0.2180x^{0.5565} + 0.1308$ (Eq. 4.13)
Column	0.5402	2.80	0.2985	N-Layer	dXCO ₂	One Hour	$y = 0.1349x^{0.5306} + 0.2985$ (Eq. 4.14)
8-Layer	0.5151	6.62	-0.1111	N-Layer	dXCO ₂	One Hour	$y = 0.2723x^{0.5437} - 0.1111$ (Eq. 4.15)
7-Layer	0.4967	7.58	-0.3632	N-Layer	dXCO ₂	One Hour	$y = 0.2996x^{0.5440} - 0.3632$ (Eq. 4.16)
6-Layer	0.4806	8.49	-0.0201	N-Layer	dXCO ₂	Three Hour	$y = 0.1621x^{0.6298} - 0.0201$ (Eq. 4.17)
5-Layer	0.4555	10.05	-0.6912	N-Layer	dXCO ₂	Three Hour	$y = 0.1932x^{0.6228} - 0.6912$ (Eq. 4.18)
4-Layer	0.4104	12.21	-0.8772	N-Layer	dXCO ₂	Three Hour	$y = 0.1840x^{0.6414} - 0.8702$ (Eq. 4.19)
3-Layer	0.3707	14.79	-1.4600	N-Layer	dXCO ₂	Three Hour	$y = 0.1907x^{0.6505} - 1.4600$ (Eq. 4.20)

4.6.3 Polynomial Regression

2-degree polynomial regression is carried out for column dXCO₂ and dCO₂ and partial column dXCO₂ and dCO₂ with different numbers of layers. The best polynomial regressions in terms of the R² for column dXCO₂ and dCO₂ and partial column dXCO₂ and dCO₂ are summarized in Table 4.8, in descending order of R².

Table 4.8 Summary of Polynomial Regression

	R ²	RMSE	Intercept on Y- Axis	N-Layer / N- Pressure	dXCO ₂ / dCO ₂	Generating Output Averaging	Regression
10-Layer	0.5354	5.12	1.5330	N-Layer	dXCO ₂	Two Hour	$y = -(1.28e-6)x^2 + 0.0091x + 1.5330$ (Eq. 4.21)
9-Layer	0.5354	5.63	1.4470	N-Layer	dXCO ₂	One Hour	$y = -(1.47e-6)x^2 + 0.0101x + 1.4470$ (Eq. 4.22)
11-Layer	0.5336	4.72	1.6650	N-Layer	dXCO ₂	One Hour	$y = -(1.19e-6)x^2 + 0.0083x + 1.6650$ (Eq. 4.23)
Column	0.5301	2.83	1.1120	N-Layer	dXCO ₂	One Hour	$y = -(8.29e-7)x^2 + 0.0053x + 1.112$ (Eq. 4.24)
8-Layer	0.5139	6.63	1.3870	N-Layer	dXCO ₂	One Hour	$y = -(2.08e-6)x^2 + 0.0125x + 1.3870$ (Eq. 4.25)
7-Layer	0.5013	7.54	1.0620	N-Layer	dXCO ₂	Three Hour	$y = -(2.34e-6)x^2 + 0.0140x + 1.0620$ (Eq. 4.26)
6-Layer	0.4837	8.46	0.9957	N-Layer	dXCO ₂	Three Hour	$y = -(2.14e-6)x^2 + 0.0141x + 0.9957$ (Eq. 4.27)
5-Layer	0.4600	10.01	0.4369	N-Layer	dXCO ₂	Three Hour	$y = -(2.54e-6)x^2 + 0.0162x + 0.4369$ (Eq. 4.28)
4-Layer	0.4168	12.14	0.0824	N-Layer	dXCO ₂	Three Hour	$y = -(2.86e-6)x^2 + 0.0182x + 0.0824$ (Eq. 4.29)
3-Layer	0.3782	14.71	-0.6011	N-Layer	dXCO ₂	Three Hour	$y = -(3.28e-6)x^2 + 0.0205x - 0.6011$ (Eq. 4.30)

4.6.4 Rational Regression

This subsection presents the results of rational regression (one numerator degree and one denominator degree) for column dXCO₂ and dCO₂ and partial column dXCO₂ and dCO₂ with different numbers of layers. For rational regression, the unit of dCO₂ have been changed from mole/FOV to 10⁸mole/FOV. The best regressions for column dXCO₂ / dCO₂ and partial column dXCO₂ / dCO₂ are summarized in Table 4.9, in descending order of R².

Table 4.9 Summary of Rational Regression

	R ²	RMSE	Intercept on Y-Axis	N-Layer / N- Pressure	dXCO ₂ / dCO ₂	Generating Output Averaging	Regression
10-Layer	0.5447	5.07	0.9403	N-Layer	dXCO ₂	One Hour	$y = \frac{26.02x + 1637}{x + 1741}$ (Eq. 4.31)
11-Layer	0.5429	4.67	1.0230	N-Layer	dXCO ₂	One Hour	$y = \frac{24.28x + 1827}{x + 1786}$ (Eq. 4.32)
9-Layer	0.5421	5.58	0.5966	N-Layer	dXCO ₂	Two Hour	$y = \frac{30.03x + 902.6}{x + 1513}$ (Eq. 4.33)
Column	0.5400	2.81	0.6296	N-Layer	dXCO ₂	One Hour	$y = \frac{13.29x + 871.4}{x + 1384}$ (Eq. 4.34)
8-Layer	0.5217	6.57	0.5966	N-Layer	dXCO ₂	One Hour	$y = \frac{30.03x + 902.6}{x + 1513}$ (Eq. 4.35)
7-Layer	0.5038	7.53	0.4953	N-Layer	dXCO ₂	Three Hour	$y = \frac{35.17x + 883.7}{x + 1784}$ (Eq. 4.36)
6-Layer	0.4858	8.45	0.4908	N-Layer	dXCO ₂	Three Hour	$y = \frac{41.83x + 1098}{x + 2237}$ (Eq. 4.37)
5-Layer	0.4613	9.99	-0.1070	N-Layer	dXCO ₂	Three Hour	$y = \frac{45.66x - 230.3}{x + 2152}$ (Eq. 4.38)
4-Layer	0.4168	12.14	-0.3858	N-Layer	dXCO ₂	Three Hour	$y = \frac{51.60x - 873.9}{x + 2265}$ (Eq. 4.39)
3-Layer	0.3773	14.72	-1.0138	N-Layer	dXCO ₂	Three Hour	$y = \frac{57.62x - 2349}{x + 2317}$ (Eq. 4.40)

4.6.5 Sum of Sine

This subsection presents the results of sum of sine regression for column $dXCO_2$ and dCO_2 and partial column $dXCO_2$ and dCO_2 with different numbers of layers. The best regressions for column $dXCO_2 / dCO_2$ and partial column $dXCO_2 / dCO_2$ are summarized in Table 4.10, in descending order of R^2 .

Table 4.10 Summary of Sum of Sine Regression

	R^2	RMSE	Intercept on Y- Axis	N-Layer / N- Pressure	$dXCO_2$ / dCO_2	Generating Output Averaging	Regression
10- Layer	0.5309	5.15	1.7865	N-Layer	$dXCO_2$	Two Hour	$y = 17.46 \sin((0.4477e-3)x + 0.1025)$ (Eq. 4.41)
9-Layer	0.5309	5.65	1.7300	N-Layer	$dXCO_2$	Two Hour	$y = 18.80 \sin((0.4613e-3)x + 0.0922)$ (Eq. 4.42)
11- Layer	0.5284	4.75	1.9114	N-Layer	$dXCO_2$	One Hour	$y = 16.25 \sin((0.4396e-3)x + 0.1179)$ (Eq. 4.43)
Column	0.5234	2.85	1.2773	N-Layer	$dXCO_2$	One Hour	$y = 9.5820 \sin((0.4695e-3)x + 0.1337)$ (Eq. 4.44)
8-Layer	0.5087	6.56	1.7439	N-Layer	$dXCO_2$	One Hour	$y = 20.30 \sin((0.5196e-3)x + 0.0860)$ (Eq. 4.45)
7-Layer	0.4984	7.57	1.3963	N-Layer	$dXCO_2$	Three Hour	$y = 21.98 \sin((0.5390e-3)x + 0.0636)$ (Eq. 4.46)
6-Layer	0.4815	8.48	1.3219	N-Layer	$dXCO_2$	Three Hour	$y = 24.02 \sin((0.5024e-3)x + 0.0551)$ (Eq. 4.47)
5-Layer	0.4580	10.02	0.8145	N-Layer	$dXCO_2$	Three Hour	$y = 26.23 \sin((0.5255e-3)x + 0.0311)$ (Eq. 4.48)
4-Layer	0.4156	12.15	0.4769	N-Layer	$dXCO_2$	Three Hour	$y = 28.68 \sin((0.5374e-3)x + 0.0166)$ (Eq. 4.49)
3-Layer	0.3777	14.71	-0.1750	N-Layer	$dXCO_2$	Three Hour	$y = 31.27 \sin((0.5544e-3)x - 0.0056)$ (Eq. 4.50)

4.6.6 Summary

Table 4.11 summarizes the R^2 of the best fittings for each type of regression.

Table 4.11 Summary of R^2 for Linear and Nonlinear Regressions

	Linear	Power	Polynomial	Rational	Sum of Sine
Column	0.4988	0.5402	0.5301	0.5400	0.5234
11-Layer Partial Column	0.5107	0.5428	0.5336	0.5429	0.5284
10-Layer Partial Column	0.5110	0.5446	0.5354	0.5447	0.5309
9-Layer Partial Column	0.5065	0.5408	0.5354	0.5421	0.5309
8-Layer Partial Column	0.4767	0.5151	0.5139	0.5217	0.5087
7-Layer Partial Column	0.4627	0.4967	0.5013	0.5038	0.4984
6-Layer Partial Column	0.4548	0.4806	0.4837	0.4858	0.4815
5-Layer Partial Column	0.4337	0.4555	0.4600	0.4613	0.4580
4-Layer Partial Column	0.3922	0.4104	0.4168	0.4168	0.4156
3-Layer Partial Column	0.3549	0.3707	0.3782	0.3773	0.3777

All four types of nonlinear regressions yield better fitting results than linear correlation based on R^2 . For all types of regression, partial columns with 9, 10 and 11 layers are able to better fit the data than full columns. The goodness of fit increases with the number of layers that comprise a partial column; however, minor decreases are observed for 11-layer partial columns compared to 10-layer partial columns for all regressions.

Table 4.12 summarizes the intercept on Y-axis of the best fittings for each type of regression. The intercept is an indicator of systematic difference of XCO_2 between the target and background soundings when the GS is not generating power. The values are expected to be positive since the selection of background areas is based on fossil fuel flux which involves emissions from transportation and it is expected that transportation in the background areas is less than Nanticoke area. The 'positive intercept' is based on the assumption that the influence of biosphere is

negligible compared to fossil fuel flux. This is highly likely true considering the time of satellite overpass.

Table 4.12 Summary of Intercept on Y-Axis for Linear and Nonlinear Regressions

	Linear	Power	Polynomial	Rational	Sum of Sine
Column	1.7890	0.2985	1.1120	0.6296	1.2773
11-Layer Partial Column	2.6340	0.4739	1.6650	1.0230	1.9114
10-Layer Partial Column	2.7289	0.3148	1.5330	0.9403	1.7865
9-Layer Partial Column	2.8223	0.1308	1.4470	0.5966	1.7300
8-Layer Partial Column	3.0870	-0.1111	1.3870	0.5966	1.7439
7-Layer Partial Column	2.9947	-0.3632	1.0620	0.4953	1.3963
6-Layer Partial Column	2.7780	-0.0201	0.9957	0.4908	1.3219
5-Layer Partial Column	2.2590	-0.6912	0.4369	-0.1070	0.8145
4-Layer Partial Column	2.4400	-0.8772	0.0824	-0.3858	0.4769
3-Layer Partial Column	2.0980	-1.4600	-0.6011	-1.0138	-0.1750

Table 4.13 summarizes output averaging information of the best fittings for each type of regression. The ‘output averaging’ indicator reveals the weakening rate of surface emission signals with increasing altitude. The differences among 1-hour, 2-hour and 3-hour generating outputs are insignificant as can be seen from Table A.1. However, partial columns with different thicknesses are able to differentiate the strengths of surface emission signals over time. As shown in the table below, thinner partial columns tend to be more sensitive to surface emissions over a period, i.e. over the past 2 or 3 hours; whereas thicker partial columns are more sensitive to instant surface emissions, i.e. the 1-hour output.

Table 4.13 Summary of Output Averaging for Linear and Nonlinear Regressions

	Linear	Power	Polynomial	Rational	Sum of Sine
Column	One	One	One	One	One
11-Layer Partial Column	One	One	One	One	One
10-Layer Partial Column	One	One	One	One	One
9-Layer Partial Column	One	One	One	One	One
8-Layer Partial Column	One	One	One	One	One
7-Layer Partial Column	Two	One	Three	Three	Three
6-Layer Partial Column	Two	Three	Three	Three	Three
5-Layer Partial Column	Three	Three	Three	Three	Three
4-Layer Partial Column	Three	Three	Three	Three	Three
3-Layer Partial Column	Three	Three	Three	Three	Three

4.7 Partial Column XCO₂ Statistics

In order to better understand the discrepancy among a full column and partial columns in relating with generating outputs, this section presents some fundamental statistics on XCO₂ on each level.

The XCO₂ on the first 10 levels for target soundings is shown in Table A.53. Table 4.14 presents the mean, maximum, minimum and standard deviation of XCO₂ on each level for all target soundings. The statistics of background soundings are on a comparable and similar level but not presented. The 20th level corresponds to the surface level.

Table 4.14 Statistics of XCO₂ on Each Level of Target Soundings

	Mean (ppm)	Max (ppm)	Min (ppm)	Amplitude (ppm)	STD (ppm)
Column	391.77	400.33	370.15	30.18	6.02
1	382.17	385.62	378.94	6.68	1.79
2	386.75	390.63	383.41	7.22	1.80
3	388.68	392.73	385.20	7.54	1.90
4	390.18	394.68	386.36	8.32	2.05
5	390.79	395.99	383.22	12.78	2.95
6	390.96	398.79	379.27	19.52	3.79
7	390.96	399.88	378.11	21.78	4.05
8	390.93	400.83	377.49	23.34	4.30
9	390.85	401.99	376.54	25.45	4.69
10	390.75	402.96	376.16	26.80	5.09
11	390.56	404.99	374.37	30.62	5.93
12	390.45	406.56	373.73	32.83	6.69
13	390.55	408.38	370.08	38.30	7.67
14	390.8	409.34	364.69	44.65	8.64
15	391.67	409.51	357.46	52.04	9.98
16	392.97	413.66	350.51	63.15	11.74
17	395.37	419.42	342.80	76.62	14.45
18	397.88	433.46	336.50	96.96	17.67
19	402.01	467.71	332.44	135.26	22.84
20	404.55	488.85	332.83	156.02	26.30

The XCO₂ uncertainties on the first 10 levels for all target soundings are presented in Table A.54. The statistics of XCO₂ uncertainties on all levels are shown in Table 4.15. The 10th level corresponds to the surface level.

Table 4.15 Statistics of XCO₂ Uncertainty on Each Level of Target Soundings

	Mean (ppm)	Max (ppm)	Min (ppm)	Amplitude (ppm)	STD (ppm)
Column	1.0693	3.0036	0.4634	2.5402	0.5408
1	1.4374	1.4374	1.4372	0.0002	0
2	2.5114	2.5147	2.5039	0.0108	0.0021
3	3.2206	3.2331	3.1999	0.0332	0.0069
4	3.9479	3.9816	3.8923	0.0893	0.0182
5	4.5219	5.4032	4.1964	1.2068	0.2187
6	3.2849	6.1203	2.3687	3.7517	0.6412
7	3.5338	6.8829	2.4884	4.3945	0.7374
8	3.7649	7.5515	2.6515	4.9000	0.8034
9	4.0302	8.4172	2.8063	5.6110	0.9006
10	4.2990	9.1974	3.0404	6.1570	0.9631
11	4.8980	11.0888	3.4761	7.6127	1.1505
12	5.4286	12.8173	3.9628	8.8545	1.2921
13	6.0640	15.4326	4.6575	10.7751	1.4954
14	6.5136	17.8536	5.2770	12.5766	1.6884
15	7.3169	21.3761	6.4175	14.9586	1.9652
16	7.8909	24.7128	7.1528	17.5600	2.3094
17	9.6835	29.2442	8.6590	20.5852	2.7070
18	11.8179	33.6705	9.8057	23.8648	3.1846
19	16.9900	39.1763	12.7572	26.4191	3.8253
20	25.4657	44.7533	20.8217	23.9316	3.7154

As seen from the two tables above, the CO₂ variations in the lower atmosphere are much more significant than in upper atmosphere. Over the study period, the amplitude in XCO₂ is 156.02 ppm for the surface layer (referring to the 20th layer) and the uncertainty on XCO₂ of this layer can reach as high as approximately 45ppm. The stability of XCO₂ increases and the XCO₂ uncertainty decreases with altitude.

4.8 Weather Indicators and Station Comparison

This section enumerates a number of weather indicators at Hamilton station and London station on Target dates and examines the consistency between two weather stations. The weather indicators includes: wind speed and direction, temperature, pressure, visibility, humidity and local synoptic events.

4.8.1 Wind Speed and Direction

The wind speed and direction information obtained from two weather stations is shown in Table A.55. Note that wind direction is analyzed though the sounding geo-location is very close to Nanticoke GS (3 - 4 km approximately since sounding geo-location varies with time slightly) and the FOV covers the point source. It is still possible that a deviated wind direction from the direction between the source and the center of FOV may result in a biased observation of CO₂ concentration in correlation with the coal-fired power plant. The wind direction is retrieved in the unit of 10s deg. The direction from the source to the center of FOV is approximately 190 ° (19 10sdeg). The difference in source-to-center direction due to sounding geo-location variation is negligible. The influence of wind direction deviation (the absolute difference between wind direction and source-to-center direction) on model residual will be analyzed.

The linear correlation coefficient in one-hour wind speed between two stations is 0.6460 and is 0.7853 for three-hour wind speed. The statistics on the difference of wind speed are shown in Table 4.16.

Table 4.16 Statistics on Wind Speed Difference

	Mean (km/h)	Max (km/h)	Min (km/h)	Amplitude (km/h)	STD (km/h)
One-Hour Difference	0.60	11	-18	29	5.20
Three-Hour Difference	1.30	11.67	-10.33	22	4.31

Two weather stations are reasonably consistent with each other in wind speed based on ‘Mean’ and ‘STD’. Large maximum and minimum differences and amplitude imply significant discrepancies on a few particular days. Overall, the wind at the Hamilton airport is stronger than that at the London airport, probably due to its closer proximity to Lake Ontario (approximately 15km) versus the distance from London to Lake Erie (approximately 40 km).

4.8.2 Temperature

Similarly, temperature information obtained from both weather stations is shown in Table A.56. The linear correlation coefficient in one-hour temperature between two stations is 0.9827 and is 0.9876 for three-hour temperature. The statistics on the difference of temperature are shown in Table 4.17.

Table 4.17 Statistics on Temperature Difference

	Mean (°C)	Max (°C)	Min (°C)	Amplitude (°C)	STD (°C)
One-Hour Difference	-0.68	4.60	-6.30	10.9	1.96
Three-Hour Difference	-0.46	2.97	-5.17	8.14	1.66

No significant difference in temperature is observed between two stations. The temperature in Hamilton area is lower than that in London area.

4.8.3 Humidity

The linear correlation coefficient in one-hour humidity between two stations is 0.7635 and is 0.8155 for three-hour humidity. The statistics on the difference of humidity are shown in Table 4.18.

Table 4.18 Statistics on Humidity Difference

	Mean (%)	Max (%)	Min (%)	Amplitude (%)	STD (%)
One-Hour Difference	1.29	22.00	-34.00	56.00	10.33
Three-Hour Difference	1.83	21.67	-20.00	41.67	8.71

The relative humidity can differ between the two areas. Generally Hamilton is slightly moister than London. Large discrepancies in humidity are detected on specific days. This is also probably due to the difference in the proximity of the weather stations to the lakes. Given that Nanticoke is located on the shore of Lake Erie, the humidity obtained from Hamilton Station is expected to be more representative of Nanticoke values.

4.8.4 Pressure

The linear correlation in one-hour pressure between two stations is 0.9826 and is 0.9786 for three-hour pressure. The statistics on the difference of pressure measurements are shown in Table 4.19.

Table 4.19 Statistics on Pressure Difference

	Mean (kPa)	Max (kPa)	Min (kPa)	Amplitude (kPa)	STD (kPa)
One-Hour Difference	0.46	1.11	0.26	0.85	0.11
Three-Hour Difference	0.46	1.25	0.24	1.01	0.12

The surface pressure of Hamilton is higher than that of London. Based on the small standard deviation of measured pressure difference, the measured surface pressures from the two weather stations are expected to be highly representative of the pressure information of the target area.

4.8.5 Weather Description

The hourly weather descriptions for Hamilton station and London station are presented in Table A.59. Main terms for describing the weather are clear, mainly clear, mostly cloudy and cloudy. Others include snow, fog, haze and thunderstorm, etc. but the occurrence is much less frequent than the four main weather terms.

In addition, there is little variability in visibility. The observed maximum visibility for both stations is 24.1 km. However, for a certain period before the archive was updated the observed maximum visibility is 10km. The hourly visibility is hardly biased from the maximum value unless under special weather conditions such as fog, snow, thunderstorm etc.

4.9 Influence of Weather Conditions

This section presents the results of scaling of the weather factors: wind speed and direction, temperature, pressure, humidity and weather event/description by using the method in 3.5.2.

In order to estimate the influence of these factors on $dXCO_2$ or dCO_2 , the 10-layer rational regression is taken as an example to illustrate how the meteorological parameters are possibly related to the XCO_2 uncertainty and regression residuals.

4.9.1 Meteorological Parameters Scaling

As described in the Methods Chapter, the fitting residuals, all meteorological parameters (wind speed, wind direction deviation, temperature, humidity, surface pressure and weather description/event) and XCO₂ uncertainty are scaled from 1 to 10 (except for weather description, i.e. 1 to 6) based on different criteria. See Table A.60 to A.64 for the scales of the meteorological parameters (Hamilton one-hour data). The histograms are presented as follows. Only relative humidity data are normally distributed. By scaling the meteorological parameters, the impacts of systematic errors on influence evaluation due to using approximated meteorological parameters (since no information is available for Nanticoke area) can be constrained.

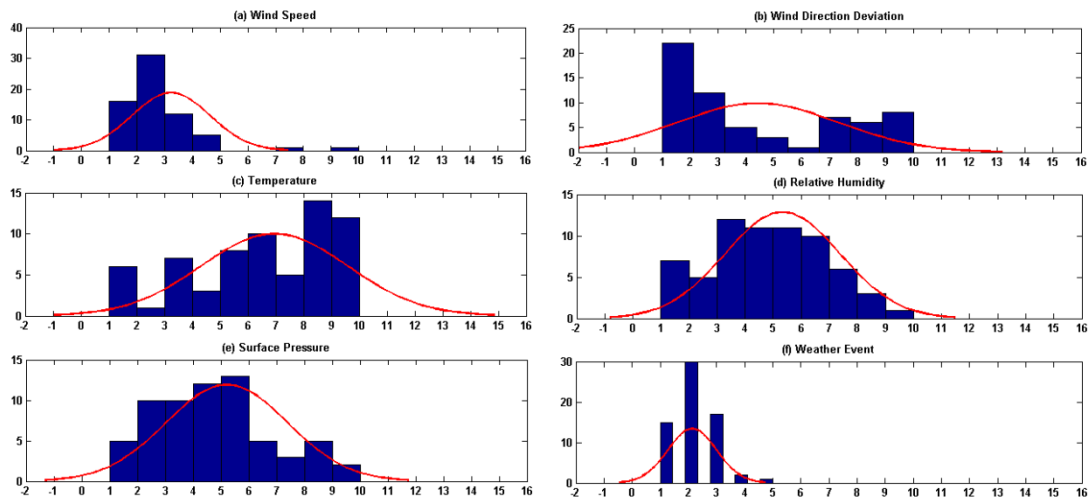


Figure 4.12 Histograms of Wind Speed (a), Wind Direction Deviation (b), Temperature (c), Humidity (d), Pressure (e) and Weather Event (f)

4.9.2 Influence Evaluation: 10-Layer Partial Column

The 10-layer rational function $y = \frac{26.02x + 1637}{x + 1741}$ is taken as the reference function for calculating residuals of dXCO₂. The residual plot is shown in Figure 4.13. The absolute values of residuals in dXCO₂ are normally distributed as shown in Figure 4.14 and are scaled from 1 to 10 as shown in Table A.65. The absolute residuals and the scales are non-normally distributed.

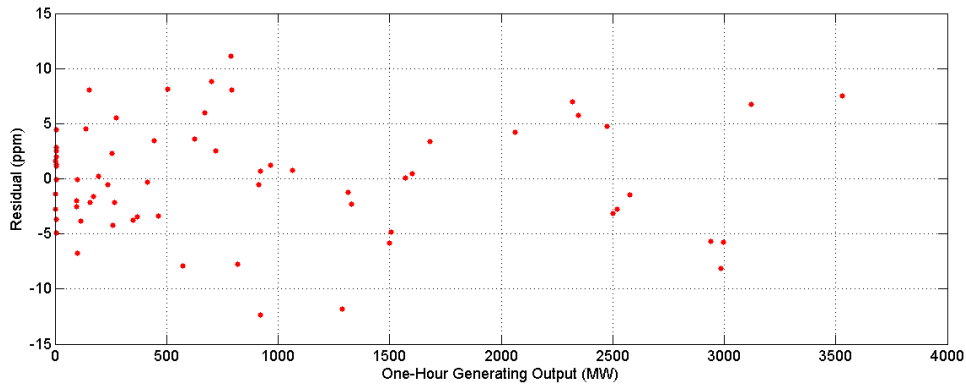


Figure 4.13 Residual Plot of 10-Layer Rational Regression

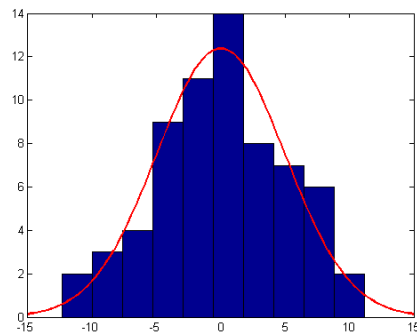


Figure 4.14 Histogram of Original Residuals

The Spearman correlation is carried out on the scale of absolute residual and the scale of meteorological parameters. The coefficients are shown in Table 4.20.

Table 4.20 Correlations between Regression Residual Scale and Meteorological Parameter Scale

Weather Factors	Hamilton		London	
	One-Hour	Three-Hour	One-Hour	Three-Hour
Wind Speed	-0.0647	-0.1103	0.0186	-0.0869
Wind Direction Deviation	0.1571			
Temperature	0.0631	0.0484	0.0649	0.0600
Humidity	0.3518	0.3495	0.1529	0.1618
Pressure	-0.0144	-0.0183	-0.0010	-0.0348
Weather Event/Description	0.0326	NA	-0.0797	NA

No single parameter is strictly correlated with the regression residual. In order to explore more on the relationship between residual and meteorology, it is necessary to categorize each variable and examine the clustering pattern if there is any. The residuals are divided into two groups: strong fit (scale \leq 5) and weak fit (scale \geq 6). The two groups and relevant scaling information are summarized in Table A.66. The percentages of high-scale influential factors in target groups are calculated to evaluate the strength of influence as shown in Table 4.21.

Table 4.21 The Statistics of Potential Influential Factors on Residuals

	Residual	Output	Surface XCO ₂ Uncertainty	Wind Speed	Wind Direction Deviation	Temperature	Humidity	Pressure	Weather Event
Percentage of High Scale (%)	21.21	18.18	22.73	28.79	34.38	74.24	46.97	43.08	30.77
Percentage of High in Strong (%)		15.38	23.08	30.77	34.00	76.92	42.31	40.38	30.77
Percentage of High in Weak (%)		28.57	21.43	21.43	35.71	62.29	64.29	53.85	30.77
Percentage of High in Positive/Negative (%)		18.75/ 17.65	21.88/ 23.52	25.00/ 32.35	34.38/ 34.38	75.00/ 73.53	59.38/ 35.29	51.61/ 35.29	32.26/ 29.41
Percentage of High in Positive/Negative Strong (%)		12.50/ 17.86	20.83/ 25.00	25.00/ 35.71	37.50/ 30.77	75.00/ 78.57	54.17/ 32.14	54.17/ 28.57	33.33/ 28.57
Percentage of High in Positive/Negative Weak (%)		37.50/ 16.67	25.00/ 16.67	25.00/ 16.67	25.00/ 50.00	75.00/ 50.00	75.00/ 50.00	42.85/ 66.67	28.57/ 33.33
Average Scale in Strong		2.88	2.62	3.33	4.34	6.94	5.12	5.12	2.12
Average Scale in Weak		4.21	1.79	2.85	4.71	7.00	6.14	5.62	2.23

Considering the statistical distribution of each item above, the high scale denotes scale 6 to 10 for residual, output, wind direction deviation, temperature, humidity and pressure, 4 to 10 for XCO₂ uncertainty and wind speed, 3 to 6 for weather event. The ‘Strong’ and ‘Weak’ refer to strong fit and weak fit groups respectively. The table above facilitates examining the impacts of each parameter on the target variable (regression residual). For instance, the percentage of ‘high output’ in strong class is 15.38% while is 28.57% in the weak class, which indicates that higher outputs are likely to cause larger residuals. Another significant influential factor is humidity.

The results with alternative definition of high scale are shown in Table 4.22, i.e. the high scale denotes scale 3 to 10 for output and XCO₂ uncertainty, 4 to 10 for wind speed, 8 to 10 for temperature, 6 to 10 for wind direction deviation, humidity and pressure, and 3 to 6 for weather event. By modifying the criteria, it is guaranteed that the strong fit or weak fit and high scale or low scale take a share of total that is closest to 50%. The three modified items are output, surface XCO₂ uncertainty and temperature.

Table 4.22 The Statistics of Potential Influential Factors on Residuals: Alternative Criteria

	Output	Surface XCO ₂ Uncertainty	Temperature
Percentage of High Scale (%)	43.94	34.85	46.97
Percentage High in Strong (%)	38.46	38.46	44.23
Percentage High in Weak (%)	64.29	21.43	57.14
Percentage of High in Positive/ Negative (%)	46.88/41.18	37.50/32.35	50.00/44.12
Percentage of High in Positive/Negative Strong (%)	41.67/35.71	41.67/35.71	41.67/46.43
Percentage of High in Positive/Negative Weak (%)	62.50/66.67	25.00/16.67	75.00/33.33

It is noteworthy that the impact of surface XCO₂ uncertainty on the absolute values of residual is not significant as seen in both tables above. However, large surface XCO₂ uncertainties tend to overestimated rather than underestimate the residuals especially for the weak residual class.

Likewise, the influence of meteorological parameters on the surface-level XCO₂ uncertainty can also be explored. Table 4.23 shows the statistics of these influential factors on XCO₂ uncertainty. The definition of high scale is the same with that used for Table 4.21.

Table 4.23 The Statistics of Potential Influential Factors on Surface XCO₂ Uncertainty

	Surface XCO ₂ Uncertainty	Output	Wind	Temperature	Humidity	Pressure	Weather Event
Percentage of High Scale (%)	22.73	18.18	28.79	74.24	46.97	43.08	30.77
Percentage of High in Low (%)		21.57	27.45	88.24	39.22	40.00	28.00
Percentage of High in High (%)		6.67	33.33	26.67	73.33	53.33	40.00
Average Scale in Low		3.26	3.18	7.80	4.94	5.00	2.10
Average Scale in High		3.00	3.40	4.07	6.67	5.93	2.27

Table 4.23 shows that low temperature, high humidity and high surface pressure are the major causes of large surface XCO₂ uncertainties since they are more dominant in the high surface uncertainty class.

The influences of various factors on regression residuals and surface layer XCO₂ uncertainties can be examined using this method. However, these variables especially the meteorological parameters are expected to have an interactive and conjunct impact on the regression residuals and XCO₂ uncertainties. The following tables show the frequency of association between every two variables with high and low scales.

Table 4.24 Frequency of Association between High/High Scale Variables (%)

	High Wind Speed	High Temperature	High Humidity	High Pressure	High Weather
High Wind Speed		24.24	12.12	9.09	6.06
High Temperature	24.24		30.30	22.73	21.21
High Humidity	12.12	30.30		19.70	19.70
High Pressure	9.09	22.73	19.70		10.61
High Weather	6.06	21.21	19.70	10.61	

Table 4.25 Frequency of Association between High/Low Scale Variables (%)

	Low Wind Speed	Low Temperature	Low Humidity	Low Pressure	Low Weather
High Wind Speed		4.55	16.67	19.70	22.73
High Temperature	50.00		43.94	51.52	53.03
High Humidity	34.85	16.67		27.27	27.27
High Pressure	34.85	21.21	24.24		33.33
High Weather	24.24	9.09	10.61	19.70	

Table 4.26 Frequency of Association between Low/Low Scale Variables (%)

	Low Wind Speed	Low Temperature	Low Humidity	Low Pressure	Low Weather
Low Wind Speed		21.21	36.36	36.36	46.97
Low Temperature	21.21		9.09	4.55	16.67
Low Humidity	36.36	9.09		28.79	42.42
Low Pressure	36.36	4.55	28.79		36.36
Low Weather	46.97	16.67	42.42	36.36	

Table 4.27 A Summary of Frequency of Association between Variables (%)

	High and High	High to High	High to Low	Low to High	Low to Low
Wind to Temperature	28.79/74.24	24.24	4.55	50.00	21.21
Wind to Humidity	28.79/46.97	12.12	16.67	34.85	36.36
Wind to Pressure	28.79/43.08	9.09	19.70	34.85	36.36
Wind to Weather	28.79/30.77	6.06	22.73	24.24	46.97
Temperature to Humidity	74.24/46.97	30.30	43.94	16.67	9.09
Temperature to Pressure	74.24/43.08	22.73	51.52	21.21	4.55
Temperature to Weather	74.24/30.77	21.21	53.03	9.09	16.67
Humidity to Pressure	46.97/43.08	19.70	27.27	24.24	28.79
Humidity to Weather	46.97/30.77	19.70	27.27	10.61	42.42
Pressure to Weather	43.08/30.77	10.61	33.33	19.70	36.36

Note: The sum of each row may be not perfectly 100% due to rounding. The column 'high and high' denotes the overall percentage of each parameter.

Based on Table 4.27, the relationship between every two meteorological parameters can be explored. For instance, as for wind and temperature, weak wind and high temperature are most frequently observed over the study period. The pairing between high temperature and calm weather (as opposed to extreme weather events) dominates the relationship between the two variables. Not a dominant relationship can be observed for every two particular variables, e.g. the relationship between humidity and pressure is fairly uniformly distributed among high-high, high-low, low-high and low-low. The pairing between wind speed and wind direction deviation is analyzed separately. The combination of low-scale wind speed and low-scale wind direction deviation takes a share of 46.88% of total, low-scale wind speed and high-scale wind direction deviation 18.75%, high-scale wind speed and low-scale wind direction deviation 23.43%, high-scale wind speed and high-scale wind direction deviation 10.94%. Strong winds are more likely to be associated with small wind direction deviations and large wind direction deviations tend to be associated with weak winds.

However, the pattern of variable association is expected to vary with season. In this regard, summer is analyzed individually and the result is shown in Table 4.28, similar to Table 4.27.

Table 4.28 A Summary of Frequency of Association between Variables in Summer (%)

	High and High	High to High	High to Low	Low to High	Low to Low
Wind to Temperature	24/100	24	0	76	0
Wind to Humidity	24/40	8	16	32	44
Wind to Pressure	24/28	8	16	20	56
Wind to Weather	24/0	0	24	0	76
Temperature to Humidity	100/40	40	60	0	0
Temperature to Pressure	100/28	28	72	0	0
Temperature to Weather	100/0	0	100	0	0
Humidity to Pressure	40/28	24	68	4	4
Humidity to Weather	40/0	0	40	0	60
Pressure to Weather	28/0	0	28	0	72

Summer is characterized by low wind speed, high temperature, medium humidity, low pressure and good weather condition. Prominent pairing patterns are observed: ‘low to high’ for wind and temperature, ‘low to low’ for wind and pressure, ‘low to low’ for wind and weather, ‘high to low’ for temperature and humidity, ‘high to low’ for temperature and pressure, ‘high to low’ for temperature and weather, ‘high to low’ for humidity and pressure, ‘low to low’ for humidity and weather, ‘low to low’ for pressure and weather.

4.9.3 Influence Evaluation: 3-Layer Partial Column

It is expected that the meteorological parameters have a more apparent effect on the lower atmosphere. Therefore, an evaluation on the influence of weather on 3-layer partial column is also carried out.

The 3-layer polynomial function $y = -(3.28e-6)x^2 + 0.0205x - 0.6011$ is taken for calculating regression residuals (3-layer dXCO₂ and three-hour average generating output). The residual plot is shown in Figure 4.15.

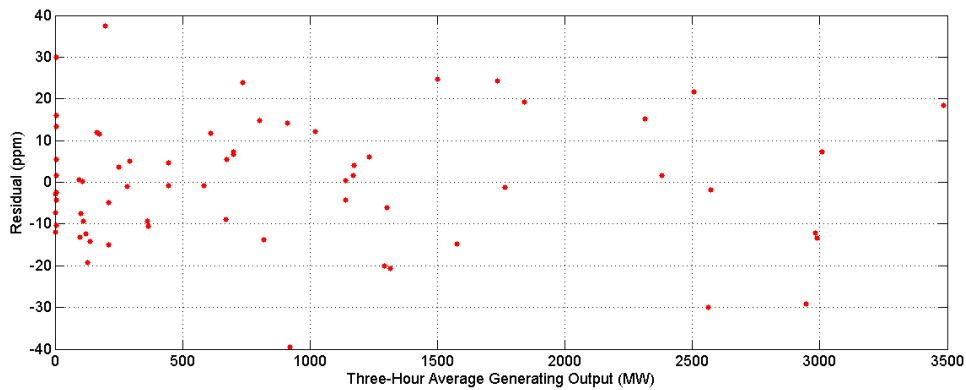


Figure 4.15 Residual Plot of 3_Layer Polynomial Regression

According to the distribution of 3-layer regression residuals, the high scale is composed of scale 5 to 10. The definition of high scale for other factors is consistent with that used for Table 4.21.

Table 4.29 Statistics of Potential Influential Factors on Residuals

	Residual	Output	Surface XCO ₂ Uncertainty	Wind Speed	Wind Direction Deviation	Temperature	Humidity	Pressure	Weather Event
Percentage of High Scale (%)	22.73	18.18	22.73	28.79	34.38	74.24	46.97	43.08	30.77
Percentage of High in Strong (%)		11.76	27.45	33.33	33.96	70.59	47.06	52.00	32.00
Percentage of High in Weak (%)		40.00	6.67	13.33	36.36	86.67	46.67	13.33	26.67
Percentage of High in Positive/Negative (%)		21.21/ 15.15	18.18/ 27.27	27.27/ 30.30	27.27 / 41.93	75.76/ 72.73	45.45/ 48.48	43.75/ 42.42	28.13/ 33.33
Percentage of High in Positive/Negative Strong (%)		12.50/ 11.11	25.00/ 29.63	37.50/ 29.63	25.93/ 42.31	66.67/ 74.07	50.00/ 44.44	56.52/ 48.15	26.09/ 37.04
Percentage of High in Positive/Negative Weak (%)		44.44/ 33.33	0.00/ 16.67	0.00/ 33.33	33.33/ 40.00	100.00/ 66.67	33.33/ 66.67	11.11/ 16.67	33.33/ 16.67
Average Scale in Strong		2.69	2.61	3.33	4.40	6.55	5.29	5.48	2.18
Average Scale in Weak		4.8	1.87	2.87	4.55	8.33	5.47	4.33	2.00

Similarly, compared to Table 4.21, higher outputs tend to cause large residuals. Large residuals are more frequently associated with high temperature and low surface pressure. However, the large surface XCO₂ uncertainty does not fully contribute to the large model residuals, which may imply a larger contribution from background observations. In addition, high wind speeds do not necessarily cause large model residuals. Wind direction deviation tends to cause negative

observation-model biases, but the influence of wind direction deviation on the model goodness of fit (percentage of high in strong VS percentage of high in weak) is not prominent.

4.9.4 Simplified Regression and Modified Parameter Scaling

As seen from Figure 4.12, only relative humidity is normally distributed and none of the meteorological parameters are uniformly distributed. In this respect, it is likely that the results in Table 4.21 and 4.23 are at least partially dependent on the scaling of relevant parameters. This section presents the results (as Table 4.21 and 4.23) with alternatively scaled parameters by resampling for each parameter (as described in Section 3.5.2) and simplifying the regression model (using both thick partial column and thin partial column). The meteorological parameters are then adjusted and the regression model is reconstructed for each parameter as well (taking rational regression for 10-layer model and polynomial regression for 3-layer model, which is in agreement with previous sections). The re-analyzed parameters include: wind speed, wind direction deviation, temperature, humidity and surface pressure.

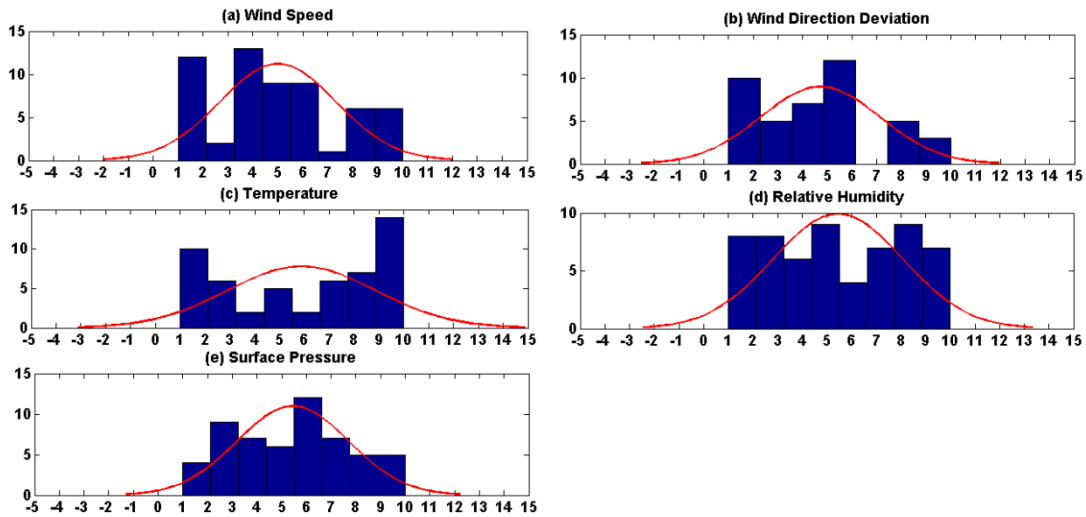


Figure 4.16 Histograms of Scaled Meteorological Parameters (Adjusted)

The revised scales of meteorological parameters have more uniformly distributed counts than those in Figure 4.12. The regression models are re-evaluated for each parameter using different sets of generating output and $dXCO_2$ (the removed observations vary among parameters) and the model residuals are re-calculated. Table 4.30 shows the results for influence of each parameter on 10-layer model residual.

Table 4.30 Influence of Adjusted Meteorological Parameters on 10-Layer Model Residuals

	Wind Speed	Wind Direction Deviation	Temperature	Humidity	Pressure
Percentage of Weak Fit Residual: 6-10 (%)	20.70	19.05	17.31	25.86	25.45
Percentage of High Scale Parameter: 6-10 (%)	37.93	35.71	55.77	46.55	52.73
Percentage of High in Strong (%)	41.30	38.24	48.84	39.53	51.22
Percentage of High in Weak (%)	25.00	25.00	88.89	66.67	57.14
Percentage of High in Positive/ Negative (%)	44.44/ 32.26	33.33/ 38.10	64.00/ 48.15	60.71/ 33.33	64.29/ 40.74
Percentage of High in Positive/Negative Strong (%)	47.62/ 36.00	35.29/ 41.18	52.63/ 45.83	55.00/ 26.09	65.00/ 38.10
Percentage of High in Positive/Negative Weak (%)	33.33/ 16.67	25.00/ 25.00	100.00/ 66.67	75.00/ 57.14	62.50/ 50.00
Average Scale in Strong	5.28	4.76	5.44	5.05	5.39
Average Scale in Weak	3.91	4.50	8	6.6	5.64

Compared to Table 4.21, no significant changes are observed except the influence of temperature. In Table 4.21, high temperatures are shown as slightly contributing to strong fit; however, in

Table 4.30 it is observed that high temperatures are highly associated with large observation-model biases. This is because winter observations are mostly removed and the temperature data are more uniformly distributed. Under this context, high temperatures (mostly in summer) are contributing to complex dispersion of CO₂ in the atmosphere hence to the large observation-model difference.

The regression equations and associated goodness of fit are shown in Table 4.31, along with the goodness of fit using 2-hour and 3-hour averaged output. These results are consistent with the results reported in previous sections: CO₂ concentrations in a thicker partial column have a higher correlation with 1-hour output.

Table 4.31 Regression Equations and Goodness of Fit: 10-Layer dXCO₂, Adjusted Meteorology

	Wind Speed	Wind Dir. Dev.	Temperature	Humidity	Pressure
Regression Equation	$y = \frac{26.64x+1890}{x+1627}$ 1-hour output	$y = \frac{34.88x+4327}{x+3003}$ 1-hour output	$y = \frac{22.37x+1224}{x+1216}$ 1-hour output	$y = \frac{26.55x+1477}{x+1679}$ 1-hour output	$y = \frac{30x+2996}{x+2417}$ 2-hour output
Goodness of Fit (1-h output)	0.5728	0.6098	0.5860	0.5696	0.5885
Goodness of Fit (2-h output)	0.5670	0.5919	0.5765	0.5649	0.5898
Goodness of Fit (3-h output)	0.5514	0.5873	0.5666	0.5508	0.5847

The results for influence analysis using 3-layer partial column is shown in Table 4.32 and the associated regression models and goodness of fit are shown in Table 4.33.

Table 4.32 Influence of Adjusted Meteorological Parameters on 3-Layer Model Residuals

	Wind Speed	Wind Direction Deviation	Temperature	Humidity	Pressure
Percentage of Weak Fit Residual: 6-10 (%)	13.79	16.67	19.23	15.51	18.18
Percentage of High Scale Parameter: 6-10 (%)	37.93	35.71	55.77	46.55	52.73
Percentage of High in Strong (%)	42.00	40.00	47.62	48.98	57.78
Percentage of High in Weak (%)	12.5	14.29	90.00	33.33	30.00
Percentage of High in Positive/ Negative (%)	35.71/ 40.00	35.00/ 36.36	75.00/ 39.29	46.15/ 46.88	48.15/ 57.14
Percentage of High in Positive/Negative Strong (%)	40.00/ 44.00	37.50/ 42.11	66.67/ 33.33	52.38/ 46.43	50.00/ 65.22
Percentage of High in Positive/Negative Weak (%)	0.00/ 20.00	25.00/ 0	100.00/ 75.00	20.00/ 50.00	40.00/ 20.00
Average Scale in Strong	5.18	4.94	5.31	5.59	5.67
Average Scale in Weak	3.88	3.57	8.3	4.67	4.5

Overall, the results are very similar with those reported in Table 4.29. The influence of wind direction deviation is weakened (average scale in strong is larger than that in weak) since observations with large direction deviations are removed and the remaining direction data have

negligible impacts on the estimation of local CO₂ concentration. In addition, the influence of high temperature on 3-layer CO₂ estimation becomes more obvious than in Table 4.29 and 4.30.

Table 4.33 Regression Equations and Goodness of Fit: 3-Layer dXCO₂, Adjusted Meteorology

	Wind Speed	Wind Dir. Dev.	Temperature	Humidity	Pressure
Regression Equation	$y = -3.2e-255x^2 + 0.02029x + 1.255$	$y = -1.964e-04x^2 + 0.01576x + 2.704$	$y = -4.595e-42x^2 + 0.02341x + 0.7042$	$y = -3.271e-x - 0.3753$	$y = -3.417e-34x^2 + 0.02063x + 0.3134$
Goodness of Fit (1-h output)	0.3491	0.3175	0.3713	0.4151	0.3478
Goodness of Fit (2-h output)	0.3634	0.3246	0.3824	0.4323	0.3639
Goodness of Fit (3-h output)	0.3746	0.3298	0.3938	0.4463	0.3773

It is shown that 3-layer partial columns are more correlated with 3-h output, which is in agreement with the early findings (Table 4.13). The influence of these meteorological parameters on the surface XCO₂ uncertainty is further examined and the results are shown in Table 4.34.

Table 4.34 The Influence of Adjusted Meteorology on Surface XCO₂ Uncertainty

	Wind Speed	Wind Dir Dev	Temperature	Humidity	Pressure
Percentage of High Scale XCO ₂ Uncertainty: 4-10 (%)	43.13	19.05	9.62	24.13	41.82
Percentage of High Scale Meteorology (%)	37.93	35.71	55.77	46.55	52.73
Percentage of High in Low (%)	42.42	29.41	59.57	38.64	46.88
Percentage of High in High (%)	32.00	62.5	20.00	71.43	60.87
Average Scale in Low	5.27	4.47	6.12	4.86	5.31
Average Scale in High	4.64	5.75	3.6	7.29	5.65

The conclusions on the impacts of relevant parameters on surface XCO₂ uncertainty remain the same with the adjusted meteorology: low temperature and high humidity tend to contribute more to high XCO₂ uncertainty than other parameters.

4.9.5 Influence of Categorical Meteorological Parameters

This section examines the impacts of original categorical meteorological data on model residuals through multivariate regression analysis. By doing so, it is expected that the impacts of meteorological parameters can be evaluated in a more quantitative way. However, due to limited information about the identical quantitative relationship between model residuals and meteorological parameters, it is assumed that the influence of each independent variable on the dependent variable is linear, interaction or quadratic (pure quadratic and full quadratic).

The parameters considered include model residual, generating output, wind speed, wind direction deviation, temperature, relative humidity and surface pressure.

Firstly, the quantitative relationship takes the linear form and assumes that there is no interaction between independent variables:

$$y = \beta_0 + \beta_o x_o + \beta_{ws} x_{ws} + \beta_{wdd} x_{wdd} + \beta_t x_t + \beta_h x_h + \beta_p x_p \quad \text{Eq. 4.1}$$

where y is the dependent variable model residual or surface XCO₂ uncertainty, x_o and β_o denote the values of output and the coefficient for output, x_{ws} and β_{ws} denote the values of wind speed and coefficient for wind speed, x_{wdd} and β_{wdd} denote the values of wind direction deviation and coefficient for wind direction deviation, x_t and β_t denote the values of temperature and coefficient for temperature, x_h and β_h denote the values of humidity and coefficient for humidity, x_p and β_p denote the values of pressure and coefficient for pressure.

The regressed linear function of output and meteorology on 10-layer model residuals is:

$$y = -229.89 + 0.0002x_o + 0.0212x_{ws} - 0.0426x_{wdd} + 0.0707x_t + 0.0177x_h + 2.3010x_p \quad \text{Eq. 4.2}$$

As indicated by Eq. 4.2, the 10-layer model residuals increase with all the influential factors except wind direction deviation, which can agree with the findings in previous sections. However, Eq. 4.2 is not significant at the 0.05 level and the R² (~0.05) is too low to conclude a linear relationship between 10-layer model residuals and surface and meteorological parameters with confidence. The linear regression for 3-layer model residuals is more significant and has better goodness of fit, which implies that the meteorology may have stronger impacts on the thinner partial columns than on the thicker partial columns. But it is still rejected at the 0.05 level. In contrast, the linear regression for the surface XCO₂ uncertainty is more significant and accepted at the 0.05 level. The R² is 0.3682 and the linear function is expressed in Eq. 4.3.

$$y = 43.10 + 0.0003x_o + 0.1785x_{ws} + 0.0528x_{wdd} - 0.1688x_t + 0.0513x_h + 0.1255x_p \quad \text{Eq. 4.3}$$

Eq. 4.3 is in high agreement with the findings from Table 4.23, i.e. the surface XCO₂ uncertainty decreases with temperature but increases with humidity and surface pressure. Theoretically, the generating output and wind do not affect the uncertainty of CO₂ retrieval.

It is highly likely that the influence of meteorology on the model residual is non-linear. In this regard, interaction and quadratic regressions are carried out on each independent parameter and

the partial correlations are examined. Three forms of regressions are analyzed: pure quadratic, interactions and full quadratic. Taking the 10-layer model results for example, the RMSE is 4.8359 for pure quadratic, 4.4464 for interactions and 4.3109 for full quadratic. Figure 4.17 and 4.18 show the results for interactions and full quadratic regressions respectively.

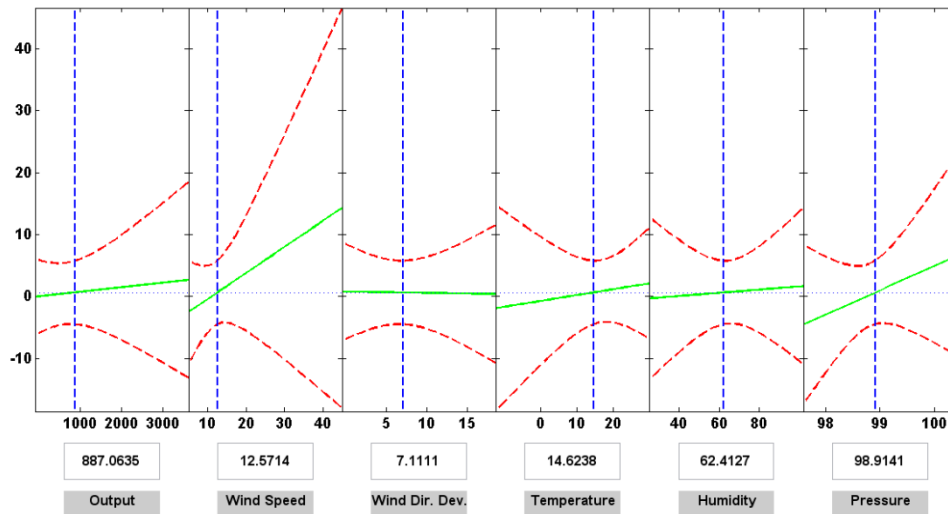


Figure 4.17 Interactions Regression for 10-Layer Model Residuals

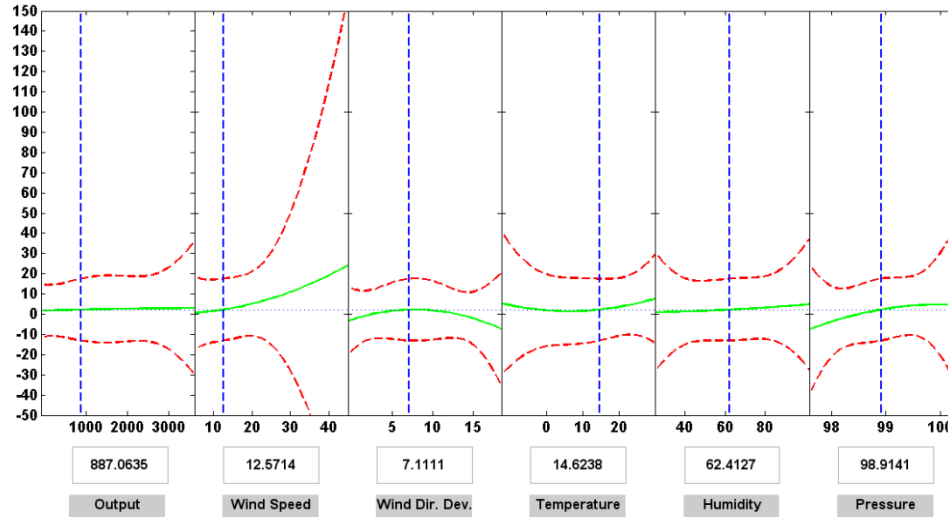


Figure 4.18 Full Quadratic Regression for 10-Layer Model Residuals

These two graphs above show the partial correlation for each independent parameter. The impact of output on 10-layer model residual is negligible in ‘full quadratic’ while in ‘interactions’ high outputs (typically larger than 890MW as indicated) tend to lead to large model residuals with overestimated observation-model differences. Strong winds (speed > 12.6km/h) can cause large

model residuals with overestimated observation-model differences in the weak fit, which agrees with the findings in previous sections. High wind direction deviation ($>70^\circ$) can lead to underestimated observation-model differences, which is in agreement with the previous sections and physical knowledge. High temperatures ($>14.6^\circ$) can cause overestimation of observation-model differences while low temperatures are more associated with an underestimation. The conclusions on the impacts of humidity and pressure are also very similar to what has been observed from Table 4.21 and 4.30.

As a further step, the impacts of meteorological parameters on 3-layer model residuals are also examined. The RMSE is 14.2265 for pure quadratic, 13.2434 for interactions and 13.1107 for full quadratic. Figure 4.19 and 4.20 show the results of interactions and full quadratic regressions respectively.

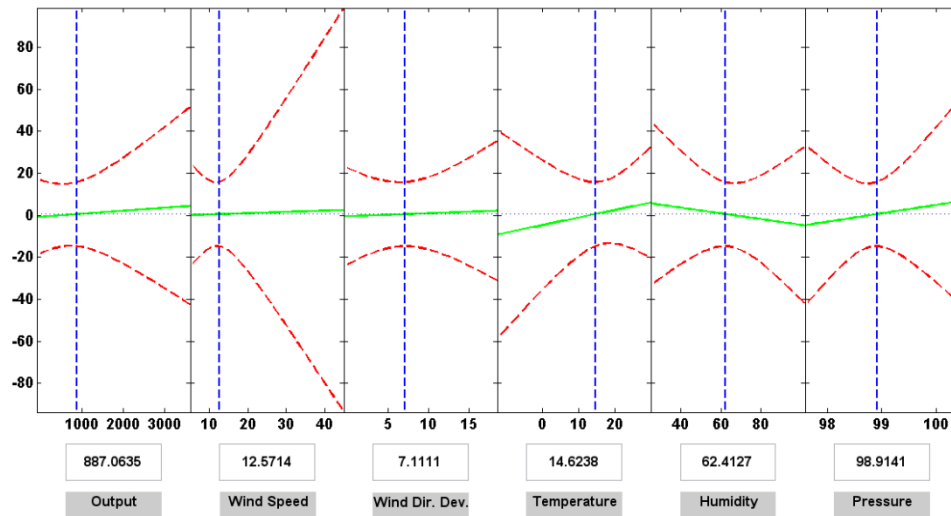


Figure 4.19 Interactions Regression for 3-Layer Model Residuals

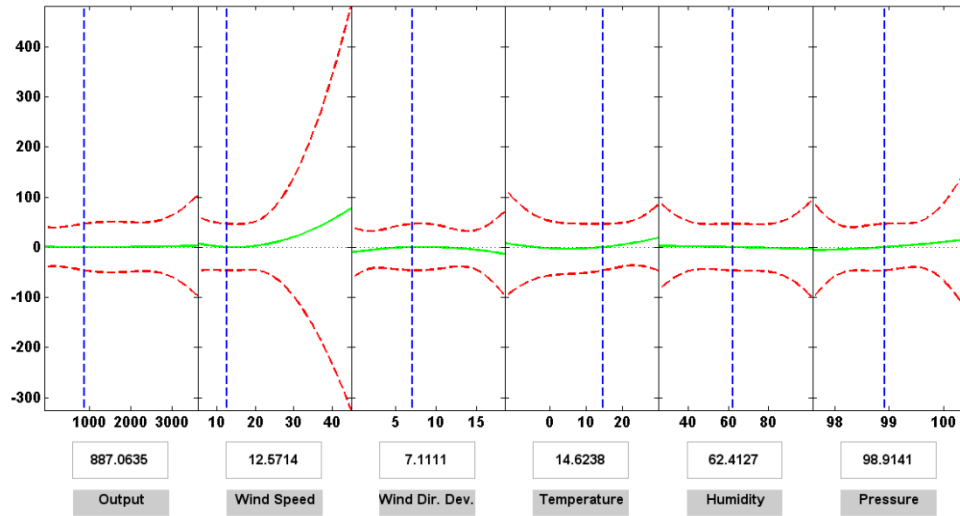


Figure 4.20 Full Quadratic Regression for 3-Layer Model Residuals

Though the 3-layer model residuals are not very well fitted by the ‘interactions’ or the ‘full quadratic’ that take into account six influential parameters, we can still gain some information about the impacts of these parameters and their similarity to the findings in previous sections. For example, similar to Table 4.29 and 4.32, high temperatures tend to overestimate the 3-layer observation-model differences; high humidity is more likely to cause underestimation of the observation-model differences; and high pressures are more associated with overestimation of the differences.

In terms of the contradictory results about the impact of temperature, a further analysis is carried out to verify that the impact of temperature is mainly related to the depth of PBL, i.e. generally high temperatures are connected to deep PBL; however, the relationship between these two variables is not strictly proportional or monotonically increasing. In this regard, PBL depth data are retrieved from NARR ESRL (NCEP North American Regional Reanalysis). All the observations are divided as shallow group (PBL depth $\leq 1000\text{m}$) and deep group (PBL depth $> 1000\text{m}$). These two groups are fitted with 2-degree power generation separately and compared to each other based on R^2 and RMSE. 10-layer and 3-layer partial column, 1-hour output and 3-h output are analyzed. Table 4.35 shows the result.

Table 4.35 Power Regression Results for Shallow and Deep Groups

		Shallow	Deep
10-layer	1-hour output		
	R ²	0.583	0.5458
	RMSE	4.937	5.161
	3-hour output		
	R ²	0.583	0.5221
	RMSE	5.064	5.16
3-layer	1-hour output		
	R ²	0.4356	0.351
	RMSE	14.63	15.06
	3-hour output		
	R ²	0.4882	0.3512
	RMSE	13.9	15.05

The R² and RMSE of the shallow group are better than the deep group. When the PBL is shallow, there is no much difference between 1-hour and 3-hour using 10-layer dXCO₂; when the PBL gets deeper, it is easier for the early emission to get out of the FOV and 10-layer partial column is able to observe this difference, therefore 1-hour R² is somewhat higher than 3-hour R².

As for the 3-layer dXCO₂, when the PBL is shallow, a thin partial column is able to capture the emission signal but not qualified for accounting for the effect of natural CO₂ cycle and the XCO₂ uncertainty of the surface layer is larger than a thick layer; therefore, the R² is worse than 10-layer and there is a gap between 1-hour and 3-hour R². When the PBL is deep (e.g. deeper than the 3-layer partial column), early emissions escape faster and the partial column misses a certain part of the instant emissions as well, so the R² is quite similar between 1-h and 3-h. (Generally, 1-hour output and 3-hour output have a <1% difference).

Additionally, when the shallow and deep group are redefined as PBL depth ≤ 900m and PBL depth ≥ 1300m, the difference of R² between shallow and deep groups gets larger. In order to assess the statistical significance, a resampling test (permutation with 1000 samplings) is carried out and the difference of R² is taken as the test statistic. It is found that PBL depth has a sizable impact on model residuals. The influence on 10-layer model residuals is less significant than that on 3-layer model residuals, which means the thicker partial column CO₂ data are less vulnerable to external factors. It is also noteworthy that the influence of PBL depth on model residuals is not prominently significant. This is similar to the case of other meteorological parameters, indicating that no single external factors are dominantly influencing the model performance. In contrast to temperature, the change of distribution of PBL depth data enhances the conclusion on PBL's

depth rather than cause a conflict. This is because the depth of PBL is determined by a gradient of temperature with height. It is relevant to, but not determined by the surface temperatures. However, high temperatures facilitate accurate CO₂ retrieval with low uncertainty. The complicated role of temperature in CO₂ retrieval and CO₂ atmospheric dispersion is the main reason for the difference of temperature's impact on model residuals as observed in Table 4.21 and Table 4.29/4.30/4.32.

In summary, Section 4.9 examines the influence of surface and atmospheric parameters on model residuals and XCO₂ uncertainty. This is achieved in three ways. Firstly, all the influential parameters are scaled into 1 to 10 (1 to 6 for weather description). The influence of parameters is explored by examining the pattern of association between one of the independent variables (surface or atmospheric parameters) and the dependent variable (model residual or XCO₂ uncertainty). Secondly, considering that any conclusion may partially depend on the distribution of the parameters involved, the influential parameters are adjusted and re-examined. A discrepancy is observed in terms of the conclusion on the impact of 'high temperature' since the number of winter observations during the study period is very limited while they have a great impact on the distribution of temperature data overall. Finally, a multivariate analysis is carried out on the categorical meteorological parameters and the partial correlation is investigated on each parameter. By doing so, we are able to examine the numeric relationship between a meteorological parameter and the model residual. The results are highly consistent with those achieved by scaling modified parameters. However, the multivariate analysis is based on and limited to the assumption that the relationship between the dependent and independent variables are linear, interactions or quadratic (pure quadratic or full quadratic).

4.10 Monthly and Seasonal Variations in CO₂ in Hamilton

This section presents the results for visualizing and analyzing the monthly/seasonal variations in CO₂ concentrations in Hamilton area. One sounding is available in Hamilton urban area and 55 observations are captured for 2010, 2011 and 2012. 2009 and 2013 are not considered due to incomplete temporal coverage.

The trend of column and partial column CO₂ concentrations are drawn to examine their capability of reflecting monthly/seasonal CO₂ variations.

4.10.1 Target Soundings in Hamilton

Satellite observations over the target site in Hamilton on 55 days are retrieved from ACOS B3.3 dataset associated with the XCO₂ uncertainty of the column and the first 10 levels from surface up. The column and partial column XCO₂ are calculated.

Column XCO₂ on target days is shown in Figure 4.21. The XCO₂ is averaged in monthly bins for each year. As can be seen, the CO₂ seasonality is not highly observable put into the same scale of XCO₂ as partial columns. The variations over specific periods can be insignificant, e.g. Mar 2011 to Oct 2011 and Feb 2012 to Jun 2012.

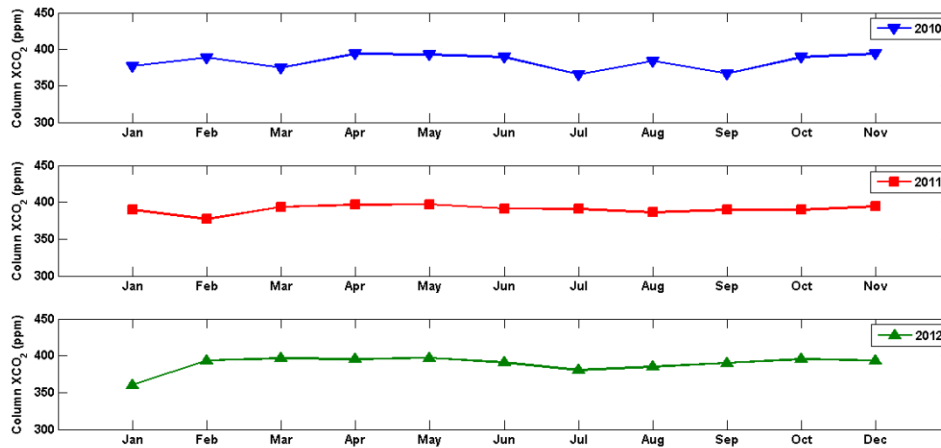


Figure 4.21 Monthly Average Column XCO₂ for Year 2010, 2011 and 2012

4.10.2 Partial Column XCO₂

In order to examine the performance of partial columns on presenting the seasonal variations of CO₂ concentration, the partial column XCO₂ with 4, 6, 8 and 10 layers are drawn in Figure 4.22 to 4.25.

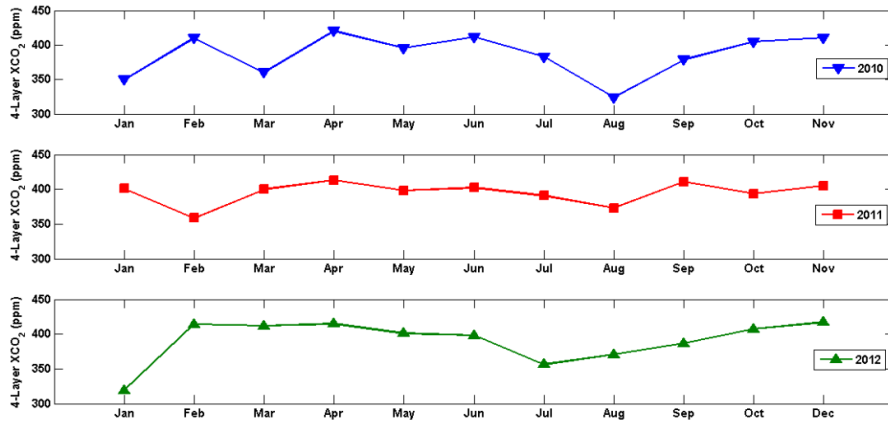


Figure 4.22 Monthly Average 4-Layer Partial Column XCO₂ for Year 2010, 2011 and 2012

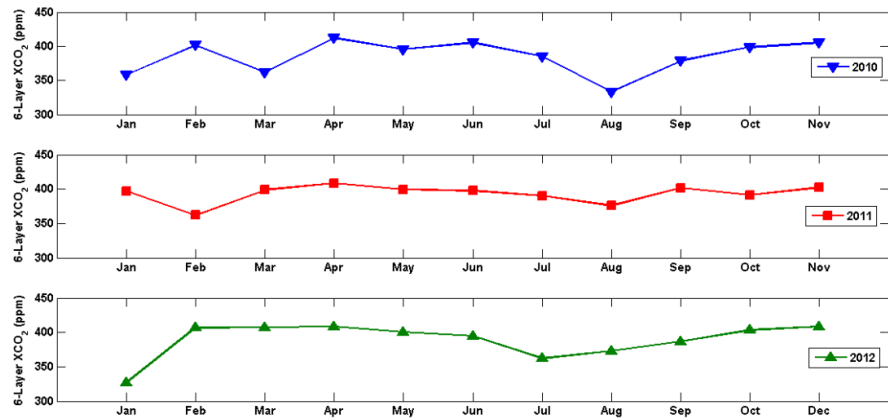


Figure 4.23 Monthly Average 6-Layer Partial Column XCO₂ for Year 2010, 2011 and 2012

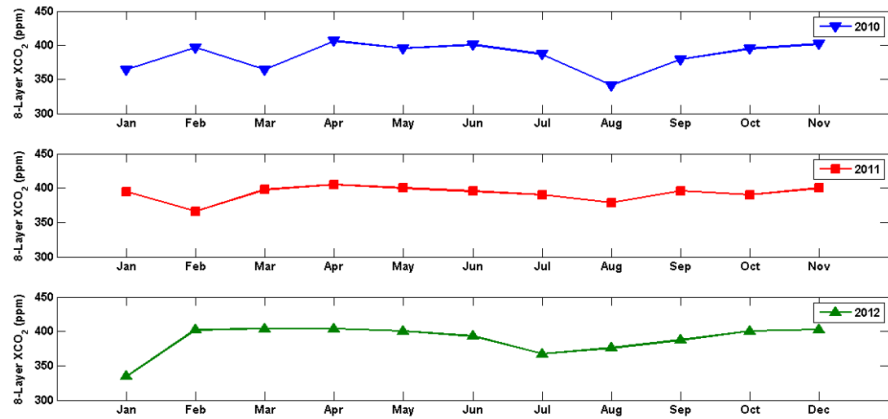


Figure 4.24 Monthly Average 8-Layer Partial Column XCO₂ for Year 2010, 2011 and 2012

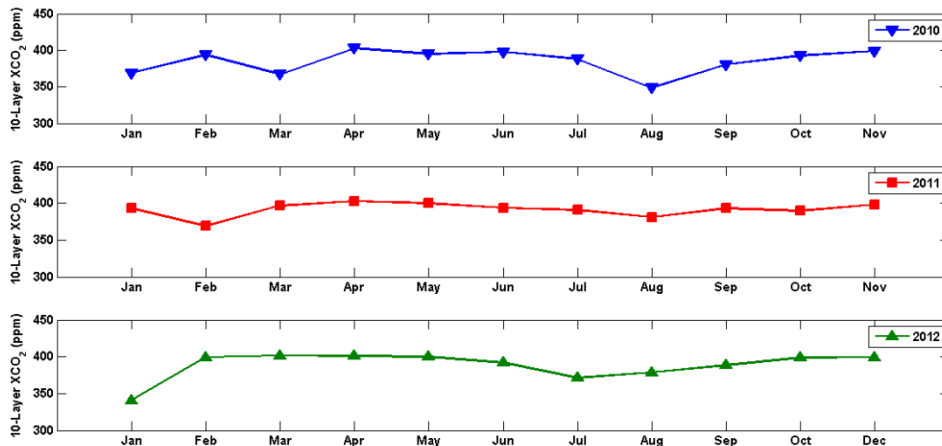


Figure 4.25 Monthly Average 10-Layer Partial Column XCO₂ for Year 2010, 2011 and 2012

Column and partial column XCO₂ for the year 2010, 2011 and 2012 are shown in Figure 4.26, Figure 4.27 and Figure 4.28.

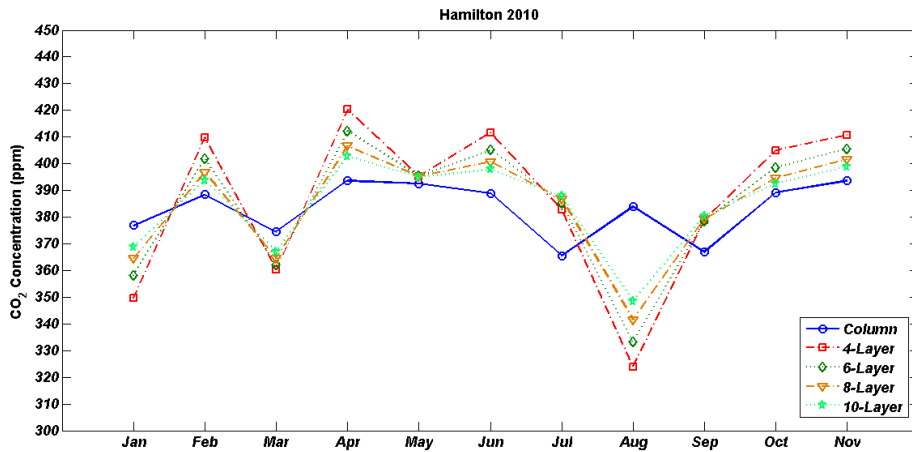


Figure 4.26 Column and Partial Column XCO₂ for 2010

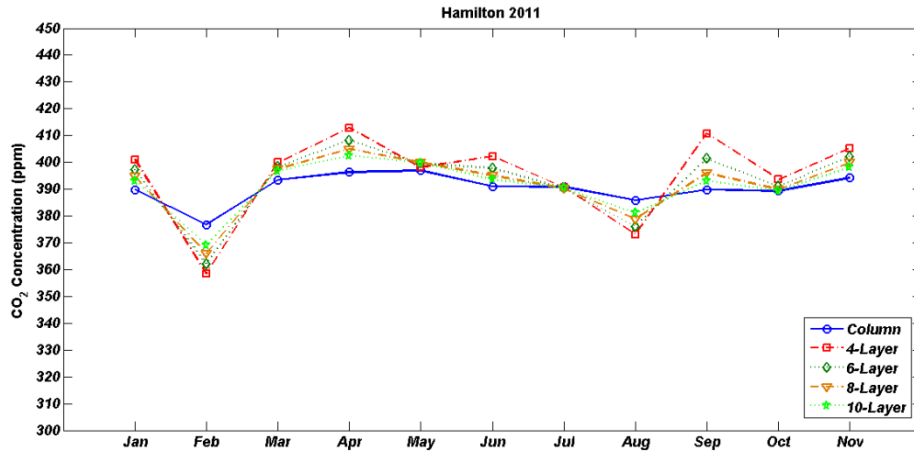


Figure 4.27 Column and Partial Column XCO₂ for 2011

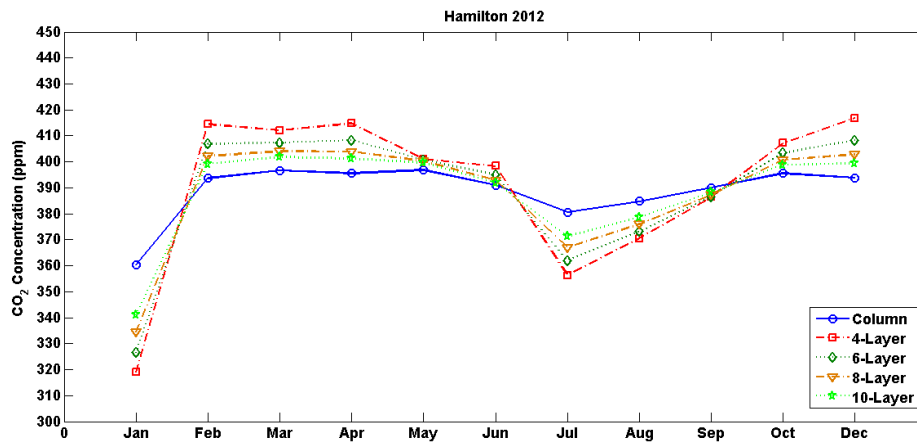


Figure 4.28 Column and Partial Column XCO₂ for 2012

Table 4.36 Goodness of Fit: CO₂ Seasonality by Full Column and Partial Columns

	2010	2011	2012
Column	0.5743	0.8366	0.6947
3-Layer	0.5829	0.5429	0.7122
4-Layer	0.5917	0.6133	0.7303
5-Layer	0.5978	0.6762	0.7447
6-Layer	0.6018	0.7286	0.7550
7-Layer	0.6041	0.7704	0.7614
8-Layer	0.6053	0.8016	0.7640
9-Layer	0.6057	0.8236	0.7634
10-Layer	0.6054	0.8378	0.7600
11-Layer	0.6043	0.8464	0.7542

The column and partial column XCO_2 for the three years are fitted to a Fourier curve that is expected to be able to present CO_2 natural seasonality. The goodness of fit is shown in Table 4.36. the 9-layer partial column yields the best goodness of fit for 2010 and all partial columns perform better than the full column; 11-layer partial column yield the best goodness of fit for 2011 and the performance of full column stand in the midst of 9-layer and 10-layer partial columns; 8-layer partial column yields the best goodness of fit for 2012 and all partial columns perform better than the full column.

4.11 Summary

In this chapter, the results that are obtained by applying the methods in Chapter 3 are presented in 9 sections.

Section 4.2 introduced the basic statistics on column XCO_2 and CO_2 and their correlation with generating output.

Section 4.3 examined the inner heterogeneity of two comparable ‘background area’ and identified 3 as the number of background soundings for approving a background area, which means a target day with <3 background soundings would not be processed.

In Section 4.4, the optimal number of layers for a partial column was predicted based on the shape of CO_2 vertical profiles.

Section 4.5 explored possible function forms of column/partial column $dXCO_2/dCO_2$ dependent on generating output according to the scatter plot. In addition to linear correlation, power function, 2-degree polynomial function, 2-degree power function, 1-degree rational function and 1-term sum of sine were decided to be analyzed for nonlinear correlation.

Section 4.6 showed the correlation results with each correlation form presented in a separate sub-section. At the end of each sub-section, results from column and partial column with a given number of layers were compared with respect to R^2 , RMSE (coefficient for linear correlation), intercept on y-axis, generating output averaging, N-layer or N-pressure, $dXCO_2$ or dCO_2 . At last, 5 correlation forms were compared in the ‘*Summary*’.

In order to prepare for analyzing the results in Section 4.6, Section 4.7 introduced basic statistics on the XCO_2 and associated uncertainties on the first levels from surface up.

In Section 4.8, a number of meteorological parameters that are likely to influence the regression results (in terms of observation-model bias) were investigated for all target days. The weather information was obtained from Hamilton Station and London Station. These two stations are located approximately 40km to the northeast and 100km to the west of Nanticoke Generating Station respectively. The weather factors involved temperature, station pressure, relative humidity, wind speed and direction, and weather event/description. Each factor was scaled from 1 to 10 indicating low to high values except that the weather event/description was scaled from 1 to 6. In the end of this section, the weather factors' scales were compared between two weather stations.

Section 4.9 examined the influence of the abovementioned parameters on the regression residuals. The residuals were scaled from 1 to 10 as well and grouped as 'strong fit' and 'weak fit', 'positive' and 'negative'. The scales of meteorological parameters were divided as 'low' and 'high'. Subsequently, the percentages of low and high weather scales in corresponding residual groups are calculated. In the meanwhile, the uncertainty on the surface-level XCO_2 was taken as an example to explore how weather factors could possibly affect XCO_2 uncertainty especially in lower atmosphere. The meteorological parameters are then resampled based on the uniformity of data distribution and the influential parameters are examined using the same approach. The categorical meteorological data are also used for a multivariate analysis to numerically explore the impacts of these parameters on the model performance.

Section 4.10 is mainly about comparing the capabilities of column XCO_2 and partial column XCO_2 of reflecting CO_2 monthly or seasonal variation in Hamilton area. 55 soundings were captured across the year of 2010, 2011 and 2012. The trend of XCO_2 is visualized for each year.

Explanations and discussions on these results are in the next chapter.

Chapter 5: Discussion

The column CO₂ concentrations were not capable of presenting a clear quantitative relationship with the generating outputs. In order to estimate the enhancement of CO₂ concentration due to surface emissions, the concept of ‘background’ was introduced as reference. This was demonstrated as an effective measure for constraining the influence of another significant surface flux (biosphere). A clear quantitative relationship between Nanticoke generating outputs and CO₂ enhancements (abundances and concentrations) was observed. In addition, CO₂ concentrations and partial columns performed better in reflecting surface emissions than CO₂ abundances and full column respectively. The linear/nonlinear regressions showed that reduced CO₂ emissions from the strong localized source led to decreased enhancement of local CO₂ concentrations. Furthermore, a number of factors especially the meteorological parameters were investigated and demonstrated as influential on the model residuals. Finally, partial column XCO₂ was found more capable of presenting natural CO₂ seasonality than column XCO₂.

5.1 CO₂ Concentrations and Surface Emissions

The seasonal CO₂ variations can be observed from the column XCO₂ sequences in Figure 4.1. However, the surface emissions from Nanticoke GS cause very strong fluctuations to CO₂ concentrations especially before 2012 when the generating outputs are high. The disturbance becomes weaker in 2012 which leads to smaller CO₂ variations while a clearer seasonal trend is observed.

Despite the apparent disturbance of surface emissions on local CO₂ concentrations, the absolute concentrations are not strictly determined by the strength of emissions. This is further confirmed by Figure 4.2 that takes into account the daily generating outputs over the study period and the smoothing spline of column XCO₂. The power generation increases significantly in 2010 summer and 2011 summer. However, the concentrations drop in these two periods. This is because the local concentrations are not merely determined by surface emissions (fossil fuel flux) but also the biosphere flux and other factors (such as atmospheric transport). As the power generation falls in 2012, the biosphere flux becomes dominant in Nanticoke area. Therefore the ‘natural CO₂

seasonality' becomes clearer which is expected to be an approximation of Fourier curve (Jones,2013, Newman *et al.*,2013).

The scatter plot and correlation result show that the column XCO₂ and generating outputs are negatively correlated, which means that statistically the CO₂ concentration tends to fall as the generating outputs increases. The negative correlation coefficient is mainly caused by the adverse trends of ground CO₂ emissions (coal-fired electricity generation) and CO₂ natural seasonality. Therefore, it is impractical to estimate the strength of surface emissions with absolute XCO₂ or to quantify the local XCO₂ based on one single type of flux (fossil fuel flux in this study). In this regard, the concept of background area (Kort *et al.*,2012) is introduced to eliminate or significantly reduce the influence of biosphere flux (CO₂ natural seasonality) among others.

5.2 Background Selection and CO₂ Profiles

The purpose of introducing the background area can be achieved since the selection of background must fulfill the requirement of 'identical or similar biosphere flux' that is described in the Methods chapter. In addition, setting 3 as the threshold for number of background observations better serves the purpose. Comparing Table 4.3 and Table 4.4, it is apparent that the quality of background is improved by eliminating the unqualified background with 1 or 2 observations.

The selection of background area for the target observations is reasonably good. Based on Figure 4.7 and Figure 4.8, the overall CO₂ concentrations in background areas are lower than those retrieved from the target observations. The power generation at the target site mostly accounts for this bias. The difference between target and background soundings is characterized by the vertical variations below level 11 which is the edging level for the 9th and 10th layer from surface up. Below level 11, the target vertical CO₂ profiles (concentrations on each pressure level) tend to increase as approaching to the surface except for a few observations mainly in summer; whereas a proportion of background profiles decrease towards the surface and the rest increase insignificantly whose concentrations are still lower than the target observations with similar vertical shapes. As for the atmosphere above level 11, both target and background CO₂ profiles stay relatively stable from level 11 upwards until level 5 and then drop sharply towards the top of atmosphere. This implies: (1) the lower atmosphere below level 11 (lower troposphere) is most sensitive to surface fluxes, which is in agreement with global CO₂ modelling studies (Scott Denning *et al.*,2003, Belikov *et al.*,2011, Lac *et al.*,2013); (2) level 5 is very likely to be the top

of troposphere and the vertical variations of CO₂ in this part of atmosphere is very small hence this part of atmosphere (upper troposphere) is insensitive to surface fluxes, which is in line with the current knowledge in the vertical distribution of air in the atmosphere (Iraci *et al.*,2013) as well as the modelling studies; and (3) the abundance of CO₂ decreases greatly from level 5 (highly likely the lower edge of stratosphere) towards the top of atmosphere since the air mass in the stratosphere is very low and the CO₂ concentrations decrease with height above level 5 as shown in the graph. Moreover, the quality of background areas fulfills the purpose of this study since the influence of fossil fuel flux is negligibly small as shown in Figure 4.8 (according to the background selection criteria the background fossil fuel flux is mostly not perfectly zero). Very few background observations present significant increased surface CO₂ concentrations due to surface emissions. Therefore, the CO₂ variations in the lower troposphere are largely due to biosphere flux.

The lower graph in Figure 4.7 shows that the target observations in different seasons which are differentiated by color. Largest variations of CO₂ as well as vertical variations are observed in summer. This is because the role land biosphere plays in determining local CO₂ concentration greatly grows in this season and the interaction between biosphere flux and fossil fuel flux becomes intense. The fossil fuel flux plays as a significant disturbance to local CO₂ instead of the dominant determinant as it is in other seasons. The conclusion agrees with seasonal CO₂ flux studies (Jarvis *et al.*,1997, Takahashi *et al.*,2002, Euskirchen *et al.*,2012, Basu *et al.*,2014b). In addition, compared to other seasons the PBL is thicker in summer which means the dispersion is relatively faster and more complicated. This further contributes to the observed large CO₂ variations in summer. Moderate horizontal CO₂ variations and smallest vertical variations are observed in autumn as the sun goes south which leads to weakened influence of biosphere flux and the power generation falls in the meanwhile (see Figure 4.1 and Figure 4.2). This implies no dominance between the two fluxes in autumn. The horizontal CO₂ variations and vertical variations in spring stand in the midst of summer and autumn. Observations in winter do not present large variations, but the CO₂ concentrations are overall higher than spring and autumn though the number of winter observations is limited. This is attributable to thinner PBL (thinner PBL tends to lead to slow dispersion hence high concentrations near the surface), moderate power generation (very high in 2009-2010 winter) and constrained biosphere flux.

5.3 Data Fitting

By differencing the target and background observations (XCO_2 and CO_2), a ‘pattern’ is presented in the scatter plot against generating outputs as shown in Figure 4.9, 4.10 and 4.11. The column $dXCO_2$ and 10-layer partial column $dXCO_2$ increase with generating output.

Linear correlation and 4 forms of nonlinear regressions are carried out on column and partial column dCO_2 and $dXCO_2$. Indicated by R^2 (Table 4.11), linear regression yields the worst goodness of fit which implied that the linear function is the most untenable description of the relationship between the CO_2 enhancement and generating output. The best curve fitting is achieved by rational function. The performances of the other nonlinear functions vary with the thickness of partial columns. For instance, polynomial function performs best among the three for thinner partial columns while power function beats the other two for thicker partial columns. The goodness of fit increases with the thickness of partial column and reach the climax at 10 layers for all 5 types of regressions. Then R^2 begins to decrease at 11 layers and is expected to continue to decrease towards the full column. This verifies the hypothesis mentioned in 5.2 that a partial column with 9 or 10 layers is most sensitive to the surface emissions (or more specifically, the CO_2 enhancement by surface emissions). The advantages of 9-layer, 10-layer and 11-layer partial columns over the full column are not prominently significant since the horizontal CO_2 variations and vertical variations are small and predictable above level 11 as discussed for Figure 4.7 and Figure 4.8. The full column yields better R^2 than thin partial columns with number of layer from 3 to 8. This is because the dispersion of CO_2 in the PBL dominates the lower troposphere in the distribution of CO_2 and the surface emission signal is strongly disturbed. A consequence of this is that the 3-layer $dXCO_2$ does not satisfactorily fit to a curve.

The intercept on y-axis denotes the $dXCO_2$ when the generating output is zero. It is calculated as an indicator of the systematic difference in CO_2 concentration between target and background areas taking into account biosphere flux and transportations since the selection of background area is based on the biosphere and fossil fuel fluxes. In addition to fossil fuel combustion for power generation, the fossil fuel flux also involves transportation. It is difficult to quantify the systematic difference since the local CO_2 concentrations are determined by various factors other than surface fluxes, e.g. the meteorology. However, it is assumed that the theoretical value of the intercept is positive as the transportation is expected to be denser in Nanticoke than in the background area (mostly 2 or 3 cells to the north). The influence of biosphere is expected to be

negligibly small considering the proximity of biosphere flux between target and background areas and the time of satellite overpass i.e. both around 6:30pm. For the nonlinear regressions as shown in Table 4.12, thinner partial columns tend to yield negative intercept especially for power and polynomial functions. This is because the lower atmosphere is too unstable to reflect surface flux, which can also be concluded from Table 4.15. The average XCO₂ uncertainty of the surface level (the 20th level) is about 25 ppm and the maximum is as high as about 45 ppm. The column XCO₂ uncertainty is very small compared to individual levels since the column XCO₂ is achieved by averaging the XCO₂ on different levels using pressure weights.

The sensitivity of full column and partial columns to surface emissions can be characterized by the generating output averaging as described in Table 4.13. Thicker partial columns tend to be more sensitive to instant surface emissions and thus the best regression is achieved by using 1-hour output. Thinner partial columns are more capable of capturing the emissions over a certain period, i.e. 2 or 3 hours in this study. These phenomena can be explained by the structure of the atmosphere and the balance between PBL dispersion and horizontal transport. The PBL is dominated by strong vertical mixing especially in the daytime. The CO₂ molecules that can spread out of the PBL into the upper troposphere (in the same atmospheric column) are very few since vertical mixing is weaker outside the PBL than within and horizontal transport plays more significant roles in distributing CO₂. Consequently, the upper part of a thicker partial column is very insensitive to the early emission signals due to dilution by strong horizontal transport, but it is sensitive to the instant emissions that quickly disperse into the upper partial column; hence the thicker partial column becomes dominated by instant signals, i.e. the 1-hour output. In contrast, the early emission signals can be captured by thinner partial columns to some extent since the emissions can persist in the source area despite the existence of winds under certain circumstances (Chow *et al.*,2009) and the width of FOV (10km) is almost twice the height of the thickest partial columns we have studied. CO₂ emissions in the past 2 or 3 hours are still contributing to the local CO₂ concentrations near the surface. In addition, the 3-hour averaged signal is ~1% stronger than the 1-hour signal (the 3rd-hour signal backward is ~1.5% stronger than the instant signal), which means it is likely for the thinner partial column to capture the early signals. Therefore, the best regressions for thinner partial column are achieved by using 3-hour generating output.

It is also noteworthy that all types of regressions demonstrate the advantage of N-layer and dXCO₂ over N-pressure and dCO₂ respectively because all the best regressions (columns and partial columns) are achieved by N-layer and dXCO₂. N-layer denotes a background partial

column with the same number of layers as the target sounding while N-pressure stipulates that the background and target soundings are compared within identical pressure spans taking the target as reference (see Chapter Methods). This implies that ‘the same proportion of the atmospheric column’ is a better criterion than ‘the same or similar air mass’ under which the target and background observations should be compared. A possible reason for this is the difference in the vertical structure of the atmosphere in the target and background areas. The dispersion and transport of CO₂ are more dependent on the atmospheric vertical structure than on vertical pressure levels. In addition, by means of calculating the difference of CO₂ concentrations, the surface emissions can be better captured than by calculating the difference of absolute CO₂ abundances. This implies that even though the number of CO₂ molecules is in theory most related to the surface emissions, the nature of the space or the ‘medium’ where CO₂ is emitted to must be considered.

5.4 Surface and Atmospheric Parameters

The influences of generating output, surface XCO₂ uncertainty and meteorological parameters on the model residuals (observation-model biases) are analyzed separately. In order to explore the causes of large residuals, Table 4.21 and Table 4.23 should be analyzed jointly since these parameters are oriented to the target site while the model residuals also involve background soundings.

High outputs tend to be associated with large model residuals since a larger proportion of high outputs are linked to the ‘weak class’ of residual than to the ‘strong class’ and are more likely to underestimate the model values in the ‘weak class’. The large observation-model biases on high-output days are mostly attributed to the background observations since high outputs are very unlikely to be linked to large surface XCO₂ uncertainty (Table 4.23). This is because most extremely high outputs are observed in summer time (and winter 2009-2010) when the biosphere flux in the background areas is expected to be strong during the daytime. Therefore, the early biosphere signal can still be captured by the satellite observation which consequently leads to low local CO₂ concentrations near the surface. This is also why the ‘percentage of high in positive weak’ is higher than the ‘percentage of high in negative weak’ in Table 4.21.

The influence of wind speed on the observation-model biases and the association with surface XCO₂ uncertainties are not as prominent as the output. Very few days with strong wind are observed during the study period. High-scale wind speeds are more likely to be associated with

high surface XCO₂ uncertainties. As a result, the surface emission signals are diluted in the satellite observations and more likely to lead to negative observations-model biases. However, this influence is not significant (Table 4.21). This is because it is more likely that high-scale wind speeds are associated with low-scale wind direction deviations and high-scale wind direction deviations are associated with low-scale wind speeds. Moreover, the sounding FOV covers the strong localized source, which means the surface emissions can be well captured despite strong winds or large wind direction deviation. In addition, the electricity generating activities during the observation hours on all target days are continuous which implies unremitting surface signals. In this respect, the influence of wind on detecting surface emissions can be constrained.

High temperatures make a major share (74.2%, against 25.8% of low temperatures) during the study period and contribute to low XCO₂ uncertainties (Table 4.23). On cold days, XCO₂ uncertainties become large, i.e. in Table 4.23 the percentage of low-scale temperature is 25.8% overall while is 73.3% (100% minus 26.7%) in the high uncertainty class. This can lead to observation-model biases as a result. Temperature has a moderate impact on the observation-model biases as observed from Table 4.21, i.e. low temperatures tend to lead to large model residuals to some extent. However, this conclusion reverses when the meteorological data are modified by removing the extraordinary values (mostly winter and early spring measurements and observations on extreme warm days). This is because of the complicated role of temperature in the CO₂ retrieval accuracy and CO₂ dispersion in the atmosphere (dispersion rate and the depth of mixing layer). By means of multivariate analysis, it is confirmed that high temperatures are more likely to cause large observation-model differences.

The significant impacts of relative humidity on model residuals and surface XCO₂ uncertainties can be observed clearly from Table 4.21 and Table 4.23 respectively. High humidity leads to large surface XCO₂ uncertainties. The percentage of high humidity is 47.0% overall while it increases to 73.3% in the class of high surface XCO₂ uncertainties which is a deviation of around 26%; similarly, the percentage of high humidity in the weak class of model residuals is as high as 62.3% (~15% deviation) which means large observation-model biases are largely due to target observations on wet days. However, the influence of high humidity is insignificant on observation-model biases using thin partial column since the percentage of high-scale humidity in the strong fit is very similar to that in the weak fit. It is also noteworthy that high humidity tends to overestimate the dXCO₂ in both strong class and weak class of model residuals, which is largely attributed to the overestimated target XCO₂. A possible reason for the overestimation is the underestimated water vapor. Another possible reason is the connection between high volume

of water vapor and aerosols/clouds. The connection between these parameters is beyond the scope of this research but it could be simply inferred from Table 4.27. The occurrence of high-scale humidity and high-scale weather on the same day (~20%, theoretical maximum is 30.8%) is relatively frequent considering the overall percentages of these two parameters (47.0% and 30.8% respectively). If aerosols and thin cirrus clouds present in the FOV and are not precisely accounted for by the retrieval algorithms, the optical path length can be shortened leading to positive bias in XCO₂.

Accurate estimation of the surface pressure is crucial to CO₂ retrievals. A biased surface pressure can lead to inaccurate estimated XCO₂. It is obvious that large model residuals and surface XCO₂ uncertainties are associated with high surface pressure. As for the model residuals, high pressure is more likely to cause overestimation of XCO₂ which probably implies that the optical path length is underestimated for target observations on high-pressure days. However, the observation-model biases tend to be negative in the weak class of residual. This is mainly due to biased background observations since the deviation of the percentage of high-scale pressure in weak class is ~24% from the overall high-pressure percentage and this number is more than twice the influence of high pressure on the surface XCO₂ uncertainty (a deviation of ~10% from the percentage of high pressure in high-scale uncertainty from the overall percentage).

Meteorological conditions can have a moderate impact on the surface XCO₂ uncertainty. But the influence on the observation-model bias is not significant since most observations are made under clear-sky conditions. Extreme weathers are rarely observed over the study period. The high-scale weathers are mostly accounted for by ‘mostly cloud’ which can be quantified by the retrieval algorithm within reasonable accuracy.

These analyses estimate the influence of individual factors on the XCO₂ uncertainties and model residuals. In addition, high surface XCO₂ uncertainty does not necessarily lead to large model residuals (Table 4.21). By comparing the ‘deviations’ of high humidity based on Table 4.21 and Table 4.23, the model residual is not completely due to the surface XCO₂ uncertainty; for other factors such as low temperature, the surface XCO₂ uncertainty does not fully contribute to the model residual. The ‘deviations’ are very close to each other for surface pressure which means the model residuals due to surface pressure are highly due to inaccurate target observations. With respect to a specific parameter, a larger deviation in model residuals than in the XCO₂ uncertainty may imply major contribution by biased background observations though the background soundings are averaged with a specific threshold of sounding number. A systematic reason for the

observed biased ‘deviations’ is the different data distributions of XCO₂ uncertainty and model residual hence the scaling criteria are different. Other possible reasons include, but are not limited to that XCO₂ uncertainty is different from retrieval error and that no single factor could fully account for the XCO₂ uncertainty and model residual.

Based on Table 4.27, exploring the pairing between different factors can provide a better understanding of their influence. The evaluation on the frequency of one specific type of combination (e.g. high-to-high) needs to consider the overall percentages of high scale factors that are involved. For example, the overall high-scale percentage of wind speed is 28.8% and is 74.2% for high-scale temperature. Therefore, the theoretical maximum frequency (in %) of high-to-high is the lower one of 28.8% and 74.2%. In this regard, the most frequent combinations of wind speed and temperature are high-to-high and low-to-high. Similarly, the most frequent combinations between temperature and surface pressure are high-to-low and low-to-high, which is in line with current physical knowledge.

5.5 Seasonal CO₂ Variation in Hamilton

The ability of remote sensing CO₂ observations to reflect seasonal variations is examined in Section 4.10. An investigation into the difference between a full column and partial columns is carried out. The location of GOSAT observation is within Hamilton urban area where no strong point CO₂ sources are observed and the biosphere flux is expected to be relatively uniformly distributed.

Both the full column and partial columns can well present the natural CO₂ seasonality. However, the seasonal variations are larger by using partial columns and decrease with the thickness of the partial columns, which implies that a partial column is more sensitive to surface fluxes than a full column. The original observations without averaging (two outliers are removed) are fitted to the Fourier curve individually for 2010, 2011 and 2012. The findings are similar to those in the early part of this study that examines the difference between column CO₂ information and partial column CO₂ information in estimating the surface emissions (fossil fuel flux alone). The similarity is that partial columns generally have stronger capability of reflecting surface fluxes than full column and a partial column with a particular thickness yields the best goodness of fit. There are a number of differences. For 2010, all partial columns perform better than the full column and the ‘optimal’ number of layers is nine. For 2011, the performance of partial columns increases with the thickness till 11-layer and it is not examined when the R² would stop rising.

The R^2 of full column stands in the midst of 9-layer and 10-layer partial columns. For 2012, the R^2 increases with thickness and starts to decline from 8-layer; all partial columns generate better fittings than the full column. The difference across these 3 years can be partially explained by the CO_2 variations and data representation. For instance, on the one hand, the variations in 2011 are much smaller than the other two years so the full column and thick partial columns yield comparable results; on the other hand, the misrepresentation of the monthly average CO_2 concentration in particular months (e.g. January and February) by thin partial columns leads to large observation-model differences since the surface layer does not well represent the surface fluxes in these months. This is also why the thick partial columns perform better than thin partial column in estimating CO_2 enhancement by fossil fuel combustion even though some thin partial columns are able to capture the CO_2 emissions in the mixing layer.

5.6 Comparisons with Other Studies

The main body of this research is the application of GOSAT CO_2 data in LPS study. It is important to place and understand the results of this research in the context of other contributions to the field of study. This section focuses on the comparisons with other studies.

Despite a wide range of work having contributed to better understanding the sources and sinks of CO_2 and CO_2 distribution in the atmosphere, there are limited recent studies on LPS using remotely sensed CO_2 data independently that this research can be directly compared to. However, there are some particular aspects this research and other studies have in common.

The concept of ‘background area’ or ‘control zone’ was introduced in an early study of isotope ^{14}C in terrestrial environment (Isogai *et al.*,2002), though to some extent it differs from the ‘background’ that was used in LPS studies afterwards. The background referred to an area that is supposedly not influenced by gaseous discharges (NI, typically upwind of source and/or 5km from it) while the influenced area is regarded as in the main wind direction and within a few kilometers from the source (IZ) (Roussel-Debet *et al.*,2006). Based on these criteria, Roussel-Debet *et al.* took approximately 230 samples and analysed the ^{14}C content in the areas surrounding 15 nuclear power plants in French over the period between 1994 and 2003. The samples were from plant species (lettuces, vegetables, grass, etc.), dairy products, meats and other products (honey, grape juice, etc.). Though the atmospheric CO_2 concentration was not directly investigated, the ^{14}C content in terrestrial environment was analyzed to indicate the gaseous discharges from nuclear power plants and its relationship with CO_2 emissions from fossil fuel

combustion. In their study, a small but significant difference between IZ and NI was identified and the decline of ^{14}C estimated on the basis of specific activity measured in samples were consistent with the a global reduction in ^{14}C in correlation with the increase in atmospheric CO_2 (Roussel-Debet *et al.*,2006).

Satellite observation is an indispensable integral part of an observation system designed to monitor megacity CO_2 , associated with surface and airborne measurements (Duren and Miller,2012). The ‘background’ (background CO_2 concentrations) has been used for the estimation of megacity CO_2 using GOSAT observations of XCO_2 . Kort *et al.* conducted such a study over Los Angeles and Mumbai. By differencing observations over the megacity with those in nearby background, robust and statistically significant XCO_2 enhancements of 3.2 ± 1.5 ppm for Los Angeles and 2.4 ± 1.2 ppm for Mumbai were identified. These enhancements can be exploited to track anthropogenic emission trends over time. Moreover, XCO_2 changes were estimated as small as 0.7 ppm in Los Angeles, corresponding to a 22% change in emissions at the 95% confidence level (Kort *et al.*,2012). The identification of background area differs from our research. Nightlight images were used to indicate the intensity of human activity and hence CO_2 emissions. ‘Basin’ (source area) and ‘desert’ (background area) were determined and the CO_2 concentration enhancements were calculated. We applied a different strategy for background identification because of the different characteristics of the CO_2 source and different research emphases (i.e., point VS area, estimation of CO_2 enhancement by coal-fired power generation VS the footprint of CO_2 emissions from the urban area). Another big difference is that in the study by Kort *et al.*, target mode is applied for the overpass of Los Angeles and Mumbai, which facilitates continuous (not spatially adjacent) observations over the basin and desert areas. In this regard, the desert is likely to be contaminated by the basin, which possibly leads to underestimated CO_2 enhancements. In contrast, the target area and background area in our research can be regarded as ‘isolated’ since the background area is identified based on fossil fuel and biosphere fluxes. Consequently, CO_2 enhancements of over 10ppm can be observed on particular days when the power generation at Nanticoke GS is intensive. This is partially due to the different CO_2 source strengths as well. In addition, the study by Kort *et al.* is based on CO_2 column concentrations, the vertical distribution of CO_2 emitted from the urban area to the atmosphere was not considered.

Similarly, Schneising *et al.* used SCIAMACHY CO_2 data (column XCO_2) to estimate the CO_2 enhancement in three metropolitan regions for the period from 2003 to 2009 (Schneising *et al.*,2013). The background areas were selected on the same latitude as the source areas to eliminate the solar zenith angle dependencies which can be a potential source of error. The

selection of background area was based on the map of annual mean CO₂ concentrations made with SCIAMACHY observations and the areas with lower concentrations were defined as background. The discrepancy in local CO₂ seasonality (mainly due to biosphere flux) was not considered, which may cause biased enhancement estimation. Despite the different strategy from our research and other studies for selecting the background and estimating the enhancement, significant CO₂ enhancements for several anthropogenic source regions were still detected. While exactly identical patterns of retrieved XCO₂ and anthropogenic emissions cannot be expected due to CO₂ transport and dispersion, the study demonstrated the detectability of anthropogenic CO₂ emissions and that other satellite missions with high spatial resolution and wide swath imaging capacity would facilitate constraining anthropogenic emissions down to point-source scale (Schneising *et al.*,2013).

In this research, GOSAT data (from ACOS dataset) are used to estimate the CO₂ enhancements caused by a strong localized point source and the vertical structure of the CO₂ retrievals are investigated. A desirable next step is to examine the use of space-based observations for CO₂ emission detection and quantification. This requires high spatial resolution and continuous observations (spatially adjacent) for mapping the source area. However, this cannot be fully achieved by GOSAT or OCO-2 data since a large part of surface and atmosphere information may be missed between samples and the generation of gridded map by averaging the observations would lead to a coarse resolution. In 2010, the satellite mission Carbon Monitoring Satellite (CarbonSat) was proposed and selected by European Space Agency (ESA) to be one of two candidate missions for the 8th Earth Explorer (EE-8, to be launched in 2019) opportunity mission in order to continue the satellite CO₂ and CH₄ global series after SCIAMACHY, GOSAT and OCO-2. CarbonSat is designed to additionally monitor anthropogenic point source emissions explicitly by making use of high spatial resolution (goal: 2×2 km² in raster form) and good spatial coverage (goal: 500 km swath width). CarbonSat is being optimized and studies are ongoing to quantify the observation precision and accuracy under all possible measurement conditions. A CarbonSat verification study by Bovensmann *et al.* (2010) used coal-fired power plant as an example and discussed the potential of CarbonSat data as an independent verification of reported anthropogenic CO₂ emissions. The study found that the errors for the retrieved CO₂ emissions are linearly dependent on wind speed and neglecting enhanced aerosols can lead to retrieval errors in the range of 0.2–2.5MtCO₂/yr (Bovensmann *et al.*,2010). A further study that focused on error estimation identified a systematic error of less than ~4.9% and a random error of less than ~6.7% for 50% of all the large power plants in the US (≥5Mt CO₂/yr). The systematic error was less than

~12.4% and the random error was less than ~13% for 90% of all the power plants. In addition, using 5 satellites as a constellation can improve the random errors by approximately a factor of two but did not result in large reduction of systematic errors. The satellite configuration that achieved daily coverage was recommended (Velazco *et al.*,2011). These two pre-launch studies emphasize the importance of LPS study (strong localized fossil fuel power plants) while the difference from our research is that the prospective data products (CarbonSat) will provide spatially continuous measurements of CO₂ concentrations and facilitates the estimation of annual CO₂ emissions for the purpose of verifying annually reported emissions.

5.7 Summary

This chapter discusses the results as described in the last chapter on five main aspects, including: (1) the relationship between column CO₂ and surface emissions, (2) the characteristics of the background observations, (3) the regression results generated by using partial column dXCO₂ and dCO₂, (4) a number of influential factors (meteorology and surface emission strength) on the observation-model bias and surface XCO₂ uncertainty, and (5) the difference between partial column and column XCO₂ in presenting CO₂ seasonality. A series of key findings are explained associated with their implications and causations.

The natural seasonality of local CO₂ concentration in Nanticoke and surface emission strength (represented by power generating output) interfere with each other. While an approximated Fourier curve can be observed over the study period, the curve smoothness is undermined by surface emissions. In addition, the absolute CO₂ concentration does not necessarily increase with surface emissions since biosphere flux is also a major determinant which can vary significantly over time.

In this regard, the concept of ‘background’ is introduced to reduce the influence of biosphere flux so that the impact of fossil fuel flux can be investigated. The effectiveness of background selection criteria is verified and the selected background observations are reasonably satisfactory. The overall background CO₂ concentrations are lower than the target area. Additionally, the vertical CO₂ profiles especially near the surface imply no strong interference of surface emissions in the selected areas.

The comparison between partial column and column dXCO₂/CO₂ is carried out and the results match with the expectations. By quantitatively relating them with the generating outputs, the

superiority of partial column is demonstrated. Partial columns with particular thickness (i.e. 9, 10 and 11 layers) yield better goodness of fit for all 5 types of regressions. The thinner partial columns do not better serve the purpose of estimating surface emissions. This agrees with the current knowledge of the vertical structure of the atmosphere. The primary causal factor is the PBL dispersion which can overweigh the wind (horizontal transport near surface) especially considering the occurrence of strong wind is very few on the target days. The balance between PBL dispersion and horizontal transport is also revealed to some degree by examining the 'generating output averaging'. The thinner partial columns appear more sensitive to early emission signals indicating relatively strong vertical dispersion within the PBL while thicker partial columns are dominated by the current emission signals indicating relatively strong horizontal transport above the PBL hence the upper part of the partial column could not capture the early emission signals. Compared with thin partial columns and the full column, a thick partial column (9 or 10 layers) is capable of not only accounting for the strong signal from the surface but also mostly ruling out the influence of the free atmosphere CO₂ which can be from other regions.

A number of key influential factors on CO₂ retrievals and the observation-model biases are discussed. The scaling approach aims to form 'high scale' and 'low scale' that are closest to each other regarding the percentage of total. The influence of these factors are estimated quantitatively by calculating the percentage of high/low scale in a target group which can be 'higher model residuals', 'positive/negative residuals' and 'high surface XCO₂ uncertainty', etc. A bias in the strength of influence of a specific factor on XCO₂ uncertainties and model residuals implies the contribution of background observations to the observation-model biases. This bias can also be accounted for by the variations and distributions of the two parameters that are compared.

At last, the seasonal variations of CO₂ in Hamilton are studied by comparing absolute CO₂ concentrations in a full column and partial columns. The superiority of partial columns over full column in representing the surface fluxes (not limited to fossil flux) is demonstrated by fitting CO₂ concentrations to a Fourier curve. In particular years (2010 and 2012) all partial columns with different thicknesses yield better results than the full column; for others (2011), there is a boundary for the partial column thickness that leads to higher capability than the full column to reflect regional CO₂ seasonality.

Chapter 6: Conclusion

6.1 Introduction

This study set out to explore the capability of remote sensing CO₂ observations to estimate surface fluxes in two study areas independent of *in situ* measurements. In particular, this study has sought to investigate innovative ways to use remote sensing data to estimate the surface fossil fuel flux in Nanticoke area. Moreover, as a pilot study this study aims to demonstrate the usefulness of remote sensing technique for evaluating the performance of energy/climate change policies (e.g. Ontario's coal phase-out) and stimulating further actions. The general empirical and theoretical literature on these subjects is inconclusive but it provides useful information for this study to answer the following research questions:

1. How is the performance of remote sensing CO₂ observations on estimating surface fluxes?
2. How can remote sensing CO₂ observations be used innovatively?
3. How can partial column CO₂ information be retrieved from existing observation datasets?
4. What is the relationship of full/partial column CO₂ information with the surface emissions by Nanticoke GS?
5. How is Ontario's 'phasing out coal for power generation' influencing the local CO₂ concentration in Nanticoke area?

6.2 Research design

In order to answer these questions, a systematic approach is developed in terms of technical methods and statistical analysis:

1. All the target soundings are retrieved from the ACOS B3.3 dataset over the late 2009 to early 2013 period. The ground location of these observations is within 5km of the Nanticoke GS which is half the size of GOSAT TANSO-FTS FOV. The power plant generating output information is obtained from IESO. The output data on the target hour(s) of the target days are prepared. The absolute values of column CO₂ concentrations are then compared with the generating outputs to examine their relationship.

2. The background soundings are also retrieved on the target dates. The background area is characterized by negligible fossil fuel flux and similar biosphere flux with the target area. By deducting the background CO₂ concentrations and abundances from the target observations, the influence of biosphere flux is expected to be significantly reduced if not completely eliminated.
3. The CO₂ concentrations and abundances of partial columns with different thicknesses (represented by the number of layers) are calculated based on the vertical profiles of CO₂ concentration and pressure weighting function, etc. These data are then fitted with generating outputs over different lengths of time counting backwards from the satellite overpass hour (i.e. the 19th hour of the day). The fitting function takes both linear and nonlinear forms.
4. The influence of a number of factors on the surface XCO₂ uncertainty and the observation-model differences is examined quantitatively. All these parameters are scaled linearly and divided into two classes-‘high scale’ and ‘low scales’. The influence of a specific factor on a target parameter (surface XCO₂ uncertainty or observation-model differences) is evaluated by calculating and comparing the difference in the percentage of a particular class of influential factor in a particular class of target parameter.
5. The Hamilton urban area is also studied for comparing column and partial column CO₂ information with respect to their capabilities of presenting CO₂ seasonal variations over the period of 2010-2013. The evaluation on CO₂ variations is based on monthly averaged CO₂ concentrations. The original data without averaging are fitted on real time scale to a Fourier curve which is taken as an approximation of the ‘natural CO₂ seasonality’. The goodness of fit R² is adopted as the single indicator for estimating the performance of column and partial column CO₂ data.

6.3 Key Findings

Based on the proposed approach, a series of findings are obtained:

1. The absolute column CO₂ concentrations could not clearly differentiate the surface emissions (fossil fuel flux) from the surface fluxes indicating the necessity of introducing background observations and calculating CO₂ enhancement.

2. Based on qualitative interpretation, the selection of background observation is reasonable satisfactory since the overall concentration is lower than the target area and vertical CO₂ profiles near the surface indicate no strong surface emissions.
3. The enhancement of CO₂ concentration due to coal-fired power generation at Nanticoke GS increases with the strength of surface emissions monotonically overall and the modelled trend is more nonlinear than linear. However, the growth rate (curve slope) decreases gradually as the generating outputs increase.
4. Partial column CO₂ information with specific numbers of layers (9, 10 and 11) yields better goodness of fit than the full column for all types of fitting functions. The sensitivity to recent surface emissions (2-3 hours) and current emissions (1 hour) varies with the partial column of different thicknesses.
5. The influential factors are investigated individually. These factors can lead to surface XCO₂ uncertainty and observation-model bias to various degrees. They can be associated with either a positive or negative observation-model bias.
6. The CO₂ seasonality in Hamilton is better measured by partial column CO₂ concentrations compared to column CO₂ concentrations. This ‘better fit’ is regardless of the partial column thickness in 2010 and 2012 while in 2011 only the partial columns with selected thicknesses yield better goodness of fit to the Fourier curve.

6.4 Contributions and Implications

These findings answer the research questions with associated theoretical, technical and policy implications. Despite this study being conducted in specific areas in Ontario, the implications obtained from this research agree with the current knowledge in associated research fields and put forward a few significant thoughts and conclusions that can be used for reference in other studies and practices.

The major contributions of this research to the current state of knowledge are:

1. Local scale CO₂ measurement technique: although CO₂ transport and sources and sinks estimation at large scales, e.g. regional scales, are a high research priority, the study of local CO₂ can also reveal important information about the surface emissions and CO₂ dynamics as

the measurement techniques are being advanced. In this research, the remote sensing CO₂ observation technique (by acquiring the snapshot of CO₂ vertical profiles within a specific area, i.e. 3-D CO₂ information) showed its potential in this domain. A strong localized CO₂ source (Nanticoke GS) is quantitatively estimated by using the remote sensing CO₂ data as the size of FOV is compatible with the dominant scale at which the CO₂ transport and dispersion occurs.

2. Innovations in CO₂ enhancement measurement: CO₂ enhancements are calculated to account for the contribution of one single type of land flux (fossil fuel flux) to the atmospheric CO₂ concentration. While the identification of background/reference area can be achieved in various ways, the method in this research is designed in a more quantitative manner by taking advantage of the fossil fuel flux and biosphere flux data. The results testify the hypothesis that a quantitative relationship between the CO₂ enhancements and generating outputs can be observed.
3. Tailored remote sensing data product: in this research, partial column CO₂ information is generated based on the full physics provided by the ACOS dataset and compared with full column CO₂ information. The comparison result is consistent with the hypothesis, which demonstrates the superiority of partial column CO₂ information in particular circumstances, e.g. to estimate the strength of fossil fuel flux and account for the influence of biosphere at the same time.

It is a complicated task to use remote sensing XCO₂ alone to detect surface fluxes since the surface fluxes can be very complex and have independent influences on the local CO₂ concentrations. The characteristics of the lower atmosphere especially the PBL and the upper atmosphere are distinctly differentiated from each other and the air movements are dominated by different physical processes. However, the potential of remote sensing CO₂ data can be underestimated if a study is restricted to the conventional ways of using remote sensing data. An innovative approach can fulfill various special research purposes depending on the data structure and data accessibility, e.g. some CO₂ retrieval algorithms do not provide CO₂ profiles though the profiles are essential to retrieving the final product of column XCO₂.

As noted in extensive literature, the surface atmosphere is perceived as the part of atmosphere that is most sensitive to surface emissions. This statement makes sense from a holistic perspective since the surface layer is closest to the surface CO₂ sources and sinks and it is mostly where the dispersion and transport of CO₂ occurs. However, the accuracy of this statement is highly scale-

dependent and the practical technical limitations must be considered when drawing any conclusions on this subject. In the Hamilton CO₂ seasonality case, thin partial columns lead to better goodness of fit to the ‘Natural CO₂ seasonality’ than full columns because no strong CO₂ sources and sinks (especially the former) are likely to exist and the surface fluxes can be taken as uniformly distributed overall. Therefore, it can be inferred that the surface layer CO₂ concentrations obtained from satellite observations well represent the actual surface fluxes. In contrast, in the Nanticoke case study, the target is a strong localized point source which is interacting with the biosphere flux within a region. Moreover, the target site is not located right in the centre of the satellite instrument FOV while the instrument measures the CO₂ concentration within the whole FOV for the whole column. In other words, a misrepresentation of the target point source or a biased sampling by the satellite is likely to happen. As a consequence, along with other reasons mentioned before, not all partial columns can better represent the strength of surface emissions than the full column.

One particular energy program in Ontario with extended theoretical underpinnings and regular interim evaluations is the Ontario’s Long-Term Energy Plan. The ‘coal phase-out’ that is highly emphasized in this plan is the single largest climate change initiative in North America. The absolute CO₂ emissions by coal-fired power generation can thus be significantly reduced. As mentioned before, present studies on climate change modelling claim that the atmospheric global CO₂ concentration would not decrease immediately after all anthropogenic CO₂ emissions stop. However, on the local scale, this study demonstrates the effectiveness of aggressive energy/CO₂ policy since the enhancement of local CO₂ concentrations due to coal combustion is reduced by constraining power generation at Nanticoke GS. More active climate change and energy policies and effective measures are highly encouraged at different scales even though the contribution of shutting down one fossil fuel power plant to global or regional CO₂ concentrations can be difficult to quantify.

6.5 Limitations and Future Research

This study provides an exploratory and evaluative perspective on the application of remote sensing CO₂ data, and is conducted in the context of Ontario’ energy plan that aims to phase out coal for power generation. As a direct consequence of the proposed methods, this study encounters a number of limitations, which need to be considered:

1. As Nanticoke GS is a site of particular research interest and due to lack of reference CO₂ data, it is difficult to validate the CO₂ retrievals.
2. Due to limited access to other types of data for identifying background areas, validations on the identified background areas are not carried out. Therefore, the quality of the background selection is evaluated based on fundamental statistics in the ‘pre-analysis’ and figures that show CO₂ profile shapes.
3. The influence of reduced CO₂ emissions on local (point) atmospheric CO₂ concentrations is evaluated, but the impacts on regional CO₂ concentrations are not quantified.
4. The meteorological information obtained from Hamilton weather station is used as an approximation of the meteorology of the target area considering the data accessibility. The discrepancy is not evaluated.

Despite the limitations, the proposed approaches and results in this research provide insights into great potential of using remote sensing CO₂ data in innovative ways. The column CO₂ data by space-based and ground-based instruments and surface sampling CO₂ data are the primary data source for CO₂ flux and CO₂ cycle studies. In this study, a derived type of data (i.e. partial column CO₂ data) is demonstrated as more capable of representing surface flux(es) than column CO₂ information.

This research serves as a pilot study and more examinations on the performance of partial column CO₂ are encouraged in other regions where reference *in situ* observations are available. It is expected that this ‘new’ type of data can be widely used in future studies on identifying surface CO₂ fluxes. In this regard, it is expected the mainstream retrieval algorithms can provide more detailed data that can be used for different purposes innovatively.

In order to promote the role of remote sensing in policy evaluation and policy making and to generate achievable policy strategies and development targets with regards to climate change mitigation, environmental management and protection, etc., there is a need for more case studies at the local level to allow further assessment of local dimensions of this subject. LPS is of high concern for CO₂ monitoring and management; therefore, on this subject remote sensing will be an effective tool for providing continuous, real-time and accurate information about the state of LPSs.

Moreover, it is of high interest to examine the influence of a particular energy or climate change policy on the regional CO₂ concentrations and at larger scales by incorporating more space-based observations. The CO₂ monitoring spacecraft such as OCO-2 and CarbonSat can be a promising asset to current data sources. The larger number of observations than GOSAT and high accuracy should be effective to fill the gaps in current data sources. As new instruments are to serve in orbit and more advanced algorithms are developed, it is encouraging to see the potential of remote sensing technology to be exploited for CO₂ studies from both scientific and policy evaluation perspectives.

Appendix A: Tables

Table A.1 CO₂ Dry Air Mole Fractions and Nanticoke Generating Outputs

XCO ₂ (ppm)	Uncertainty (ppm)	CO ₂ Abundance (10 ¹⁰ mol/FOV)	One-Hour Output (MW)	Two-Hour Average Output (MW)	Three-Hour Average Output (MW)
387.18	1.19	1.33	203	242	307.00
397.98	0.57	1.40	670	676.5	672.67
391.03	1.66	1.36	267	234	210.67
389.40	1.74	1.37	3120	3084.5	3007.67
374.31	3.00	1.30	1569	1217.5	1140.67
392.82	2.04	1.38	114	113.5	111.67
396.17	0.73	1.38	938	889	823.67
394.10	0.90	1.40	415	396.5	444.00
390.63	0.71	1.35	574	618.5	670.00
395.15	0.83	1.41	1789	1836.5	1959.00
398.83	0.46	1.38	2502	2534	2562.67
386.74	0.54	1.35	2319	2323	2314.00
393.31	0.64	1.37	2984	2983.5	2981.67
381.12	0.72	1.33	1679	1723.5	1764.33
389.82	0.68	1.36	3528	3518.5	3484.67
386.81	0.95	1.34	2938	2937.5	2944.67
385.94	0.90	1.34	2474	2483	2505.67
375.06	0.75	1.31	2998	2994.5	2987.33
370.15	0.78	1.29	2347	2378	2380.67
388.58	0.86	1.36	1066	1133.5	1168.33
389.24	0.86	1.36	1482	1391	1350.00
392.69	1.23	1.36	1506	1571	1575.00
392.60	1.24	1.38	2	2	2.00
387.93	1.44	1.35	2	2	2.00
391.38	1.62	1.36	463	437.5	362.67
399.09	2.08	1.42	625	624.5	583.33
395.78	1.90	1.38	1499	1415.5	1290.33
387.59	0.94	1.33	1314	1345	1232.67
389.70	1.97	1.38	173	143.5	138.67
396.68	1.60	1.39	137	174.5	173.67
387.32	0.86	1.36	102	101	102.33
395.42	0.65	1.38	701	667	698.67
392.79	0.54	1.37	4	4	4.00
389.86	0.64	1.36	152	181	197.67
389.86	0.78	1.36	350	499	698.67
390.42	0.64	1.36	503	653.5	736.33
386.51	0.69	1.34	1287	1306.5	1313.33
389.77	0.66	1.35	2576	2574	2572.67
390.86	0.82	1.34	1600	1701.5	1839.33
386.10	0.80	1.32	2061	2049.5	2039.33
385.09	0.83	1.35	1934	1953	1962.33
387.58	0.90	1.37	2518	2530	2546.00

386.98	0.88	1.35	919	1079	1140.00
389.24	1.03	1.36	445	444.5	443.67
386.08	0.96	1.35	5	65	126.67
392.52	1.34	1.38	5	5	5.00
399.95	1.87	1.41	789	731	611.67
395.65	0.97	1.37	254	716	250.67
398.89	1.06	1.40	5	5	5.00
397.92	0.95	1.40	98	98	97.67
398.55	0.95	1.41	156	129.5	120.00
398.26	0.75	1.40	6	6	6.00
397.88	0.76	1.40	102	104.5	106.33
395.31	0.88	1.38	259	250.5	282.00
397.24	0.77	1.38	237	277	293.67
396.31	0.84	1.39	4	4	4.00
396.15	0.73	1.38	1330	1280	1302.00
393.05	0.73	1.36	5	5	5.00
389.38	0.59	1.36	912	911.5	911.67
395.99	0.93	1.33	720	849	1020.00
389.21	0.68	1.36	966	1126	1173.33
391.03	0.81	1.37	792	801	803.33
390.42	0.95	1.37	4	4	4.00
391.32	1.19	1.36	4	4	4.00
397.20	1.16	1.39	275	191.5	162.33
394.70	1.67	1.38	369	366.5	366.33
397.38	2.04	1.41	820	820	820.00
395.14	0.83	1.39	920	920	920.00
399.57	2.93	1.4	195	200.5	209.67
400.33	0.71	1.42	96	95.5	95.67
398.32	0.71	1.41	0	0	0

The unit of CO₂ abundance is converted from molecule quantity per square meter (as in original file) to mole per FOV for the whole column.

Table A.2 Difference of Column and Partial Column XCO₂ and CO₂

Column dXCO ₂ (ppm)	10-Layer dXCO ₂ (ppm)	10-Pressure dXCO ₂ (ppm)	Generating Output (MW)
8.74	13.93	14.72	670
2.92	2.12	3.15	267
12.33	23.83	23.86	3120
7.82	12.93	12.11	1569
-0.46	-1.34	-0.75	114
3.11	5.43	5.55	415
-1.19	-0.74	-0.19	574
4.97	10.50	10.18	1314
9.56	12.57	13.00	2502
11.91	22.23	20.46	2319
4.73	8.68	8.64	2984
9.84	16.62	14.34	1679
13.88	25.28	23.56	3528
7.99	11.00	10.11	2938
10.06	20.39	19.34	2474
7.05	11.05	8.58	2998
12.04	21.09	21.03	2347
6.34	11.20	10.79	1066
4.38	7.71	7.67	1506
2.38	2.59	3.07	2
1.11	-0.43	0.25	2
2.52	2.80	3.32	463
7.56	11.20	12.06	625
5.22	6.72	7.63	1499
2.86	1.59	1.19	173
3.70	7.30	7.88	137
-2.72	-4.40	-4.73	102
10.58	16.98	16.39	701
-4.90	-2.65	-2.65	4
3.59	11.03	10.59	152
-1.43	1.36	1.28	350
6.84	14.67	14.73	503
5.83	-0.20	-0.75	1287
7.73	14.46	14.24	2576
5.16	13.44	13.30	1600
8.38	18.79	17.70	2061
4.94	12.98	12.42	2518

6.10	10.30	9.25	919
6.63	9.49	8.70	445
-1.14	-3.89	-4.24	5
2.94	2.98	3.33	5
12.52	19.9	19.68	789
3.06	6.40	6.42	254
3.08	2.18	2.98	5
1.06	-0.22	0.61	98
1.72	0.89	1.52	156
1.20	2.33	3.18	6
1.57	2.26	3.29	102
-0.44	-0.06	0.00	259
1.51	3.39	4.26	237
1.46	3.87	3.85	4
5.69	9.48	8.97	1330
0.37	0.94	0.84	5
3.37	9.04	8.27	912
4.49	10.79	10.71	720
5.86	11.10	10.18	966
9.81	16.87	15.59	792
2.74	3.52	4.59	4
2.11	5.43	5.43	4
5.97	9.89	9.83	275
1.95	1.87	2.28	369
0.85	1.19	1.98	820
0.48	-2.71	-1.68	920
3.06	3.73	3.83	195
-0.08	0.27	1.14	96
-0.44	-1.80	-0.98	0

XCO₂ difference for the whole column and the partial column with 10 layers are taken as examples. Note that dXCO₂ indicates the difference of CO₂ dry air mole fraction, and 10-pressure dXCO₂ denotes the difference of partial column XCO₂ with a given pressure span (taking the 10-layer pressure span of a targeted sounding as the standard).

Table A.3 Linear Correlation for Column dXCO₂ and dCO₂

	One-Hour Output	Two-Hour Average Output	Three-Hour Average Output
Column dXCO ₂ RHO	0.7062	0.6998	0.6897
Column dXCO ₂ PVAL	3.49e-11	6.24e-11	1.50e-10
Column dXCO ₂ R ²	0.4988	0.4897	0.4758
Column dCO ₂ RHO	0.2069	0.1969	0.1952
Column dCO ₂ PVAL	0.1000	0.1100	0.1161
Column dCO ₂ R ²	0.0428	0.0388	0.0381

Table A.4 Linear Correlation for 3-Layer Partial Column dXCO₂ and dCO₂

	One-Hour Output	Two-Hour Average Output	Three-Hour Average Output
3-Layer dXCO ₂ RHO	0.5765	0.5876	0.5957
3-Layer dXCO ₂ PVAL	2.04e-07	1.07e-07	6.59e-08
3-Layer dXCO ₂ R ²	0.3323	0.3453	0.3549
3-Layer dCO ₂ RHO	0.4995	0.5100	0.5221
3-Layer dCO ₂ PVAL	9.79e-06	6.10e-06	3.46e-06
3-Layer dCO ₂ R ²	0.2495	0.2601	0.2726
3-Pressure dXCO ₂ RHO	0.5604	0.5720	0.5800
3-Pressure dXCO ₂ PVAL	4.95e-07	2.62e-07	1.66e-07
3-Pressure dXCO ₂ R ²	0.3141	0.3272	0.3364
3-Pressure dCO ₂ RHO	0.5467	0.5589	0.5665
3-Pressure dCO ₂ PVAL	1.02e-06	5.37e-07	3.57e-07
3-Pressure dCO ₂ R ²	0.2989	0.3124	0.3209

Table A.5 Linear Correlation for 4-Layer Partial Column dXCO₂ and dCO₂

	One-Hour Output	Two-Hour Average Output	Three-Hour Average Output
4-Layer dXCO ₂ RHO	0.6099	0.6197	0.6263
4-Layer dXCO ₂ PVAL	2.72e-08	1.44e-08	9.31e-09
4-Layer dXCO ₂ R ²	0.3720	0.3840	0.3922
4-Layer dCO ₂ RHO	0.5194	0.5281	0.5395
4-Layer dCO ₂ PVAL	3.93e-06	2.59e-06	1.48e-06
4-Layer dCO ₂ R ²	0.2698	0.2789	0.2910
4-Pressure dXCO ₂ RHO	0.5905	0.6007	0.6070
4-Pressure dXCO ₂ PVAL	9.03e-08	4.86e-08	3.29e-08
4-Pressure dXCO ₂ R ²	0.3486	0.3608	0.3684
4-Pressure dCO ₂ RHO	0.5763	0.5872	0.5931
4-Pressure dCO ₂ PVAL	2.06e-07	1.09e-07	7.71e-08
4-Pressure dCO ₂ R ²	0.3518	0.3448	0.3518

Table A.6 Linear Correlation for 5-Layer Partial Column dXCO₂ and dCO₂

	One-Hour Output	Two-Hour Average Output	Three-Hour Average Output
5-Layer dXCO ₂ RHO	0.6456	0.6538	0.6585
5-Layer dXCO ₂ PVAL	2.42e-09	1.33e-09	9.29e-10
5-Layer dXCO ₂ R ²	0.4168	0.4274	0.4337
5-Layer dCO ₂ RHO	0.5473	0.5536	0.5630
5-Layer dCO ₂ PVAL	9.92e-07	7.14e-07	4.32e-07
5-Layer dCO ₂ R ²	0.2995	0.3065	0.3169
5-Pressure dXCO ₂ RHO	0.6253	0.6339	0.6382
5-Pressure dXCO ₂ PVAL	9.92e-09	5.54e-09	4.11e-09
5-Pressure dXCO ₂ R ²	0.3911	0.4018	0.4072
5-Pressure dCO ₂ RHO	0.6129	0.6222	0.6261
5-Pressure dCO ₂ PVAL	2.25e-08	1.23e-08	9.46e-09
5-Pressure dCO ₂ R ²	0.3756	0.3871	0.3920

Table A.7 Linear Correlation for 6-Layer Partial Column dXCO₂ and dCO₂

	One-Hour Output	Two-Hour Average Output	Three-Hour Average Output
6-Layer dXCO ₂ RHO	0.6706	0.6735	0.6700
6-Layer dXCO ₂ PVAL	3.64e-10	2.90e-10	3.80e-10
6-Layer dXCO ₂ R ²	0.4463	0.4548	0.4588
6-Layer dCO ₂ RHO	0.5381	0.5421	0.5512
6-Layer dCO ₂ PVAL	1.58e-06	1.30e-06	8.10e-07
6-Layer dCO ₂ R ²	0.2895	0.2938	0.3038
6-Pressure dXCO ₂ RHO	0.6571	0.6585	0.6557
6-Pressure dXCO ₂ PVAL	1.03e-09	9.33e-10	1.15e-09
6-Pressure dXCO ₂ R ²	0.4182	0.4265	0.4294
6-Pressure dCO ₂ RHO	0.6354	0.6426	0.6445
6-Pressure dCO ₂ PVAL	4.99e-09	3.00e-09	2.61e-09
6-Pressure dCO ₂ R ²	0.4037	0.4129	0.4154

Table A.8 Linear Correlation for 7-Layer Partial Column dXCO₂ and dCO₂

	One-Hour Output	Two-Hour Average Output	Three-Hour Average Output
7-Layer dXCO ₂ RHO	0.6875	0.6877	0.6842
7-Layer dXCO ₂ PVAL	9.11e-11	8.91e-11	1.20e-10
7-Layer dXCO ₂ R ²	0.4596	0.4627	0.4651 0.2841
7-Layer dCO ₂ RHO	0.5263	0.5245	0.5330
7-Layer dCO ₂ PVAL	2.84e-06	3.08e-06	2.04e-06
7-Layer dCO ₂ R ²	0.2769	0.2751	0.2841
7-Pressure dXCO ₂ RHO	0.6598	0.6621	0.6629
7-Pressure dXCO ₂ PVAL	8.42e-10	7.05e-10	6.65e-10
7-Pressure dXCO ₂ R ²	0.4354	0.4384	0.4394
7-Pressure dCO ₂ RHO	0.6535	0.6565	0.6570
7-Pressure dCO ₂ PVAL	1.35e-09	1.08e-09	1.04e-09
7-Pressure dCO ₂ R ²	0.4271	0.4310	0.4316

Table A.9 Linear Correlation for 8-Layer Partial Column dXCO₂ and dCO₂

	One-Hour Output	Two-Hour Average Output	Three-Hour Average Output
8-Layer dXCO ₂ RHO	0.6919	0.6917	0.6862
8-Layer dXCO ₂ PVAL	6.26e-11	6.34e-11	1.03e-10
8-Layer dXCO ₂ R ²	0.4767	0.4773	0.4773
8-Layer dCO ₂ RHO	0.5074	0.5031	0.5104
8-Layer dCO ₂ PVAL	6.87e-06	8.36e-06	6.00e-06
8-Layer dCO ₂ R ²	0.2574	0.2531	0.2605
8-Pressure dXCO ₂ RHO	0.6855	0.6837	0.6778
8-Pressure dXCO ₂ PVAL	1.08e-10	1.25e-10	2.04e-10
8-Pressure dXCO ₂ R ²	0.4523	0.4527	0.4512
8-Pressure dCO ₂ RHO	0.6844	0.6831	0.6763
8-Pressure dCO ₂ PVAL	1.18e-10	1.31e-10	2.31e-10
8-Pressure dCO ₂ R ²	0.4469	0.4480	0.4460

Table A.10 Linear Correlation for 9-Layer Partial Column dXCO₂ and dCO₂

	One-Hour Output	Two-Hour Average Output	Three-Hour Average Output
9-Layer dXCO ₂ RHO	0.7066	0.7066	0.6957
9-Layer dXCO ₂ PVAL	1.68e-11	1.70e-11	4.50e-11
9-Layer dXCO ₂ R ²	0.5065	0.5106	0.5043
9-Layer dCO ₂ RHO	0.4944	0.4941	0.4955
9-Layer dCO ₂ PVAL	1.22e-05	1.24e-05	1.17e-05
9-Layer dCO ₂ R ²	0.2445	0.2441	0.2455
9-Pressure dXCO ₂ RHO	0.6878	0.6858	0.6731
9-Pressure dXCO ₂ PVAL	8.89e-11	1.05e-10	2.98e-10
9-Pressure dXCO ₂ R ²	0.4778	0.4811	0.4735
9-Pressure dCO ₂ RHO	0.6869	0.6859	0.6733
9-Pressure dCO ₂ PVAL	9.58e-11	1.04e-10	2.92e-10
9-Pressure dCO ₂ R ²	0.4722	0.4751	0.4679

Table A.11 Linear Correlation for 10-Layer Partial Column dXCO₂ and dCO₂

	One-Hour Output	Two-Hour Average Output	Three-Hour Average Output
10-Layer dXCO ₂ RHO	0.7039	0.7005	0.6877
10-Layer dXCO ₂ PVAL	2.16e-11	2.92e-11	8.91e-11
10-Layer dXCO ₂ R ²	0.5110	0.5125	0.5047
10-Layer dCO ₂ RHO	0.4620	0.4596	0.4605
10-Layer dCO ₂ PVAL	4.71e-05	5.17e-05	5.00e-05
10-Layer dCO ₂ R ²	0.2135	0.2113	0.2120
10-Pressure dXCO ₂ RHO	0.6898	0.6865	0.6730
10-Pressure dXCO ₂ PVAL	7.47e-11	9.89e-11	3.01e-10
10-Pressure dXCO ₂ R ²	0.4833	0.4840	0.4750
10-Pressure dCO ₂ RHO	0.6904	0.6877	0.6729
10-Pressure dCO ₂ PVAL	7.09e-11	8.96e-11	3.02e-10
10-Pressure dCO ₂ R ²	0.4806	0.4808	0.4720

Table A.12 Linear Correlation for 11-Layer Partial Column dXCO₂ and dCO₂

	One-Hour Output	Two-Hour Average Output	Three-Hour Average Output
11-Layer dXCO ₂ RHO	0.7108	0.7063	0.6913
11-Layer dXCO ₂ PVAL	1.15e-11	1.74e-11	6.60e-11
11-Layer dXCO ₂ R ²	0.5107	0.5098	0.5009
11-Layer dCO ₂ RHO	0.4273	0.4233	0.4237
11-Layer dCO ₂ PVAL	0.0002	0.0002	0.0002
11-Layer dCO ₂ R ²	0.1826	0.1791	0.1795
11-Pressure dXCO ₂ RHO	0.6773	0.6764	0.6686
11-Pressure dXCO ₂ PVAL	2.13e-10	2.29e-10	4.26e-10
11-Pressure dXCO ₂ R ²	0.4587	0.4575	0.4471
11-Pressure dCO ₂ RHO	0.6774	0.6761	0.6684
11-Pressure dCO ₂ PVAL	2.11e-10	2.35e-10	4.34e-10
11-Pressure dCO ₂ R ²	0.4588	0.4571	0.4467

Table A.13 Power Regression R² Statistics for Column dXCO₂ and dCO₂

	One-Hour Output	Two-Hour Average Output	Three-Hour Average Output
Column dXCO ₂ R ²	0.5402	0.5226	0.5047
Column dXCO ₂ RMSE	2.80	2.85	2.91
Column dCO ₂ R ²	0.0631	0.0552	0.0549
Column dCO ₂ RMSE	1.93e8	1.94e8	1.94e8

Table A.14 Power Regression R² Statistics for 3-Layer Partial Column dXCO₂ and dCO₂

	One-Hour Output	Two-Hour Average Output	Three-Hour Average Output
3-Layer dXCO ₂ R ²	0.3504	0.3617	0.3707
3-Layer dXCO ₂ RMSE	15.03	14.90	14.79
3-Layer dCO ₂ R ²	0.2710	0.2782	0.2905
3-Layer dCO ₂ RMSE	7.96e7	7.92e7	7.85e7
3-Pressure dXCO ₂ R ²	0.3326	0.3439	0.3523
3-Pressure dXCO ₂ RMSE	14.49	14.37	14.28
3-Pressure dCO ₂ R ²	0.3182	0.3300	0.3374
3-Pressure dCO ₂ RMSE	7.96e7	7.89e7	7.85e7

Table A.15 Power Regression R² Statistics for 4-Layer Partial Column dXCO₂ and dCO₂

	One-Hour Output	Two-Hour Average Output	Three-Hour Average Output
4-Layer dXCO ₂ R ²	0.3934	0.4031	0.4103
4-Layer dXCO ₂ RMSE	12.38	12.28	12.21
4-Layer dCO ₂ R ²	0.2951	0.2998	0.3115
4-Layer dCO ₂ RMSE	8.85e7	8.82e7	8.75e7
4-Pressure dXCO ₂ R ²	0.3708	0.3803	0.3867
4-Pressure dXCO ₂ RMSE	11.86	11.77	11.71
4-Pressure dCO ₂ R ²	0.3551	0.3653	0.3707
4-Pressure dCO ₂ RMSE	8.70e7	8.63e7	8.59e7

Table A.16 Power Regression R² Statistics for 5-Layer Partial Column dXCO₂ and dCO₂

	One-Hour Output	Two-Hour Average Output	Three-Hour Average Output
5-Layer dXCO ₂ R ²	0.4434	0.4507	0.4555
5-Layer dXCO ₂ RMSE	10.16	10.09	10.05
5-Layer dCO ₂ R ²	0.3359	0.3361	0.3457
5-Layer dCO ₂ RMSE	9.28e7	9.27e7	9.21e7
5-Pressure dXCO ₂ R ²	0.4193	0.4262	0.4299
5-Pressure dXCO ₂ RMSE	9.72	9.66	9.63
5-Pressure dCO ₂ R ²	0.4051	0.4128	0.4155
5-Pressure dCO ₂ RMSE	8.90e7	8.84e7	8.82e7

Table A.17 Power Regression R² Statistics for 6-Layer Partial Column dXCO₂ and dCO₂

	One-Hour Output	Two-Hour Average Output	Three-Hour Average Output
6-Layer dXCO ₂ R ²	0.4736	0.4781	0.4806
6-Layer dXCO ₂ RMSE	8.55	8.51	8.49
6-Layer dCO ₂ R ²	0.3208	0.3184	0.3277
6-Layer dCO ₂ RMSE	9.74e7	9.76e7	9.69e7
6-Pressure dXCO ₂ R ²	0.4469	0.4507	0.4516
6-Pressure dXCO ₂ RMSE	8.17	8.15	8.14
6-Pressure dCO ₂ R ²	0.4338	0.4386	0.4386
6-Pressure dCO ₂ RMSE	8.97e7	8.93e7	8.93e7

Table A.18 Power Regression R² Statistics for 7-Layer Partial Column dXCO₂ and dCO₂

	One-Hour Output	Two-Hour Average Output	Three-Hour Average Output
7-Layer dXCO ₂ R ²	0.4967	0.4947	0.4950
7-Layer dXCO ₂ RMSE	7.58	7.59	7.59
7-Layer dCO ₂ R ²	0.3208	0.3108	0.319
7-Layer dCO ₂ RMSE	1.06e8	1.07e8	1.06e8
7-Pressure dXCO ₂ R ²	0.4741	0.4714	0.4699
7-Pressure dXCO ₂ RMSE	7.21	7.23	7.24
7-Pressure dCO ₂ R ²	0.4676	0.4657	0.4633
7-Pressure dCO ₂ RMSE	9.12e7	9.13e7	9.16e7

Table A.19 Power Regression R² Statistics for 8-Layer Partial Column dXCO₂ and dCO₂

	One-Hour Output	Two-Hour Average Output	Three-Hour Average Output
8-Layer dXCO ₂ R ²	0.5151	0.5100	0.5077
8-Layer dXCO ₂ RMSE	6.62	6.65	6.67
8-Layer dCO ₂ R ²	0.3007	0.2877	0.2944
8-Layer dCO ₂ RMSE	1.12e8	1.13e8	1.12e8
8-Pressure dXCO ₂ R ²	0.4926	0.4866	0.4823
8-Pressure dXCO ₂ RMSE	6.31	6.35	6.38
8-Pressure dCO ₂ R ²	0.4890	0.4837	0.4783
8-Pressure dCO ₂ RMSE	9.08e7	9.13e7	9.18e7

Table A.20 Power Regression R² Statistics for 9-Layer Partial Column dXCO₂ and dCO₂

	One-Hour Output	Two-Hour Average Output	Three-Hour Average Output
9-Layer dXCO ₂ R ²	0.5408	0.5396	0.5299
9-Layer dXCO ₂ RMSE	5.59	5.60	5.66
9-Layer dCO ₂ R ²	0.2893	0.2807	0.2800
9-Layer dCO ₂ RMSE	1.14e8	1.15e8	1.15e8
9-Pressure dXCO ₂ R ²	0.5132	0.5105	0.4991
9-Pressure dXCO ₂ RMSE	5.40	5.42	5.48
9-Pressure dCO ₂ R ²	0.5096	0.5062	0.4949
9-Pressure dCO ₂ RMSE	8.78e7	8.81e7	8.91e7

Table A.21 Power Regression R² Statistics for 10-Layer Partial Column dXCO₂ and dCO₂

	One-Hour Output	Two-Hour Average Output	Three-Hour Average Output
10-Layer dXCO ₂ R ²	0.5446	0.5404	0.5292
10-Layer dXCO ₂ RMSE	5.07	5.10	5.16
10-Layer dCO ₂ R ²	0.2561	0.2459	0.2449
10-Layer dCO ₂ RMSE	1.23e8	1.24e8	1.24e8
10-Pressure dXCO ₂ R ²	0.5173	0.5117	0.4991
10-Pressure dXCO ₂ RMSE	4.91	4.94	5.00
10-Pressure dCO ₂ R ²	0.5172	0.5108	0.4980
10-Pressure dCO ₂ RMSE	8.82e7	8.88e7	8.99e7

Table A.22 Power Regression R² Statistics for 11-Layer Partial Column dXCO₂ and dCO₂

	One-Hour Output	Two-Hour Average Output	Three-Hour Average Output
11-Layer dXCO ₂ R ²	0.5428	0.5360	0.5239
11-Layer dXCO ₂ RMSE	4.67	4.71	4.77
11-Layer dCO ₂ R ²	0.2221	0.2110	0.2101
11-Layer dCO ₂ RMSE	1.33e8	1.33e8	1.34e8
11-Pressure dXCO ₂ R ²	0.4882	0.4800	0.4661
11-Pressure dXCO ₂ RMSE	4.50	4.54	4.60
11-Pressure dCO ₂ R ²	0.4915	0.4823	0.4680
11-Pressure dCO ₂ RMSE	8.83e7	8.91e7	9.03e7

Table A.23 2-Degree Polynomial Regression R² Statistics for Column dXCO₂ and dCO₂

	One-Hour Output	Two-Hour Average Output	Three-Hour Average Output
Column dXCO ₂ R ²	0.5301	0.5152	0.4965
Column dXCO ₂ RMSE	2.83	2.88	2.93
Column dCO ₂ R ²	0.0440	0.0389	0.0383
Column dCO ₂ RMSE	1.95e8	1.96e8	1.96e8

Table A.24 2-Degree Polynomial Regression R² Statistics for 3-Layer Partial Column dXCO₂ and dCO₂

	One-Hour Output	Two-Hour Average Output	Three-Hour Average Output
3-Layer dXCO ₂ R ²	0.3506	0.3665	0.3782
3-Layer dXCO ₂ RMSE	15.03	14.84	14.71
3-Layer dCO ₂ R ²	0.2666	0.2786	0.2939
3-Layer dCO ₂ RMSE	7.98e7	7.92e7	7.83e7
3-Pressure dXCO ₂ R ²	0.3329	0.3491	0.3604
3-Pressure dXCO ₂ RMSE	14.49	14.31	14.19
3-Pressure dCO ₂ R ²	0.3188	0.3361	0.3463
3-Pressure dCO ₂ RMSE	7.96e7	7.89e7	7.80e7

Table A.25 2-Degree Polynomial Regression R² Statistics for 4-Layer Partial Column dXCO₂ and dCO₂

	One-Hour Output	Two-Hour Average Output	Three-Hour Average Output
4-Layer dXCO ₂ R ²	0.3925	0.4069	0.4168
4-Layer dXCO ₂ RMSE	12.39	12.24	12.14
4-Layer dCO ₂ R ²	0.2883	0.2979	0.3124
4-Layer dCO ₂ RMSE	8.89e7	8.83e7	8.74e7
4-Pressure dXCO ₂ R ²	0.3697	0.3844	0.3935
4-Pressure dXCO ₂ RMSE	11.88	11.74	11.65
4-Pressure dCO ₂ R ²	0.3545	0.3704	0.3785
4-Pressure dCO ₂ RMSE	8.70e7	8.59e7	8.54e7

Table A.26 2-Degree Polynomial Regression R² Statistics for 5-Layer Partial Column dXCO₂ and dCO₂

	One-Hour Output	Two-Hour Average Output	Three-Hour Average Output
5-Layer dXCO ₂ R ²	0.4404	0.4528	0.4600
5-Layer dXCO ₂ RMSE	10.18	10.07	10.01
5-Layer dCO ₂ R ²	0.3230	0.3289	0.3410
5-Layer dCO ₂ RMSE	9.36e7	9.32e7	9.24e7
5-Pressure dXCO ₂ R ²	0.4156	0.4282	0.4345
5-Pressure dXCO ₂ RMSE	9.75	9.64	9.59
5-Pressure dCO ₂ R ²	0.4020	0.4160	0.4212
5-Pressure dCO ₂ RMSE	8.92e7	8.81e7	8.77e7

Table A.27 2-Degree Polynomial Regression R² Statistics for 6-Layer Partial Column dXCO₂ and dCO₂

	One-Hour Output	Two-Hour Average Output	Three-Hour Average Output
6-Layer dXCO ₂ R ²	0.4701	0.4793	0.4837
6-Layer dXCO ₂ RMSE	8.57	8.50	8.46
6-Layer dCO ₂ R ²	0.3089	0.3111	0.3226
6-Layer dCO ₂ RMSE	9.82e7	9.81e7	9.73e7
6-Pressure dXCO ₂ R ²	0.4426	0.4518	0.4548
6-Pressure dXCO ₂ RMSE	8.21	8.14	8.12
6-Pressure dCO ₂ R ²	0.4303	0.4410	0.4430
6-Pressure dCO ₂ RMSE	8.99e7	8.91e7	8.89e7

Table A.28 2-Degree Polynomial Regression R² Statistics for 7-Layer Partial Column dXCO₂ and dCO₂

	One-Hour Output	Two-Hour Average Output	Three-Hour Average Output
7-Layer dXCO ₂ R ²	0.4967	0.4990	0.5013
7-Layer dXCO ₂ RMSE	7.58	7.56	7.54
7-Layer dCO ₂ R ²	0.3135	0.3064	0.3172
7-Layer dCO ₂ RMSE	1.06e8	1.07e8	1.06e8
7-Pressure dXCO ₂ R ²	0.4730	0.4753	0.4759
7-Pressure dXCO ₂ RMSE	7.22	7.20	7.20
7-Pressure dCO ₂ R ²	0.4675	0.4713	0.4707
7-Pressure dCO ₂ RMSE	9.12e7	9.09e7	9.09e7

Table A.29 2-Degree Polynomial Regression R² Statistics for 8-Layer Partial Column dXCO₂ and dCO₂

	One-Hour Output	Two-Hour Average Output	Three-Hour Average Output
8-Layer dXCO ₂ R ²	0.5139	0.5127	0.5120
8-Layer dXCO ₂ RMSE	6.63	6.64	6.64
8-Layer dCO ₂ R ²	0.2914	0.2805	0.2892
8-Layer dCO ₂ RMSE	1.13e8	1.13e8	1.13e8
8-Pressure dXCO ₂ R ²	0.4901	0.4886	0.4860
8-Pressure dXCO ₂ RMSE	6.33	6.34	6.35
8-Pressure dCO ₂ R ²	0.4874	0.4872	0.4831
8-Pressure dCO ₂ RMSE	9.10e7	9.10e7	9.14e7

Table A.30 2-Degree Polynomial Regression R² Statistics for 9-Layer Partial Column dXCO₂ and dCO₂

	One-Hour Output	Two-Hour Average Output	Three-Hour Average Output
9-Layer dXCO ₂ R ²	0.5318	0.5354	0.5264
9-Layer dXCO ₂ RMSE	5.65	5.63	5.68
9-Layer dCO ₂ R ²	0.2640	0.2602	0.2601
9-Layer dCO ₂ RMSE	1.16e8	1.16e8	1.16e8
9-Pressure dXCO ₂ R ²	0.5032	0.5058	0.4952
9-Pressure dXCO ₂ RMSE	5.46	5.44	5.50
9-Pressure dCO ₂ R ²	0.5001	0.5023	0.4917
9-Pressure dCO ₂ RMSE	8.86e7	8.84e7	8.93e7

Table A.31 2-Degree Polynomial Regression R² Statistics for 10-Layer Partial Column dXCO₂ and dCO₂

	One-Hour Output	Two-Hour Average Output	Three-Hour Average Output
10-Layer dXCO ₂ R ²	0.5353	0.5354	0.5248
10-Layer dXCO ₂ RMSE	5.12	5.12	5.18
10-Layer dCO ₂ R ²	0.2304	0.2243	0.2237
10-Layer dCO ₂ RMSE	1.25e8	1.25e8	1.26e8
10-Pressure dXCO ₂ R ²	0.5072	0.5063	0.4943
10-Pressure dXCO ₂ RMSE	4.96	4.97	5.03
10-Pressure dCO ₂ R ²	0.5072	0.5058	0.4936
10-Pressure dCO ₂ RMSE	8.91e7	8.92e7	9.03e7

Table A.32 2-Degree Polynomial Regression R² Statistics for 11-Layer Partial Column dXCO₂ and dCO₂

	One-Hour Output	Two-Hour Average Output	Three-Hour Average Output
11-Layer dXCO ₂ R ²	0.5336	0.5306	0.5189
11-Layer dXCO ₂ RMSE	4.72	4.74	4.79
11-Layer dCO ₂ R ²	0.1969	0.1893	0.1885
11-Layer dCO ₂ RMSE	1.35e8	1.35e8	1.35e8
11-Pressure dXCO ₂ R ²	0.4763	0.4729	0.4599
11-Pressure dXCO ₂ RMSE	4.55	4.57	4.62
11-Pressure dCO ₂ R ²	0.4791	0.4750	0.4616
11-Pressure dCO ₂ RMSE	8.94e7	8.97e7	9.09e7

Table A.33 1-Degree Rational R² Statistics for Column dXCO₂ and dCO₂

	One-Hour Output	Two-Hour Average Output	Three-Hour Average Output
Column dXCO ₂ R ²	0.5400	0.5247	0.5044
Column dXCO ₂ RMSE	2.81	2.87	2.93
Column dCO ₂ R ²	0.0746	0.0647	0.0648
Column dCO ₂ RMSE	1.93	1.94	1.94

Table A.34 1-Degree Rational R² Statistics for 3-Layer Partial Column dXCO₂ and dCO₂

	One-Hour Output	Two-Hour Average Output	Three-Hour Average Output
3-Layer dXCO ₂ R ²	0.3523	0.3670	0.3773
3-Layer dXCO ₂ RMSE	15.01	14.84	14.72
3-Layer dCO ₂ R ²	0.2737	0.3243	0.3400
3-Layer dCO ₂ RMSE	0.81	0.78	0.77
3-Pressure dXCO ₂ R ²	0.3349	0.3496	0.3594
3-Pressure dXCO ₂ RMSE	14.47	14.31	14.20
3-Pressure dCO ₂ R ²	0.3203	0.3361	0.3447
3-Pressure dCO ₂ RMSE	0.80	0.79	0.78

Table A.35 1-Degree Rational R² Statistics for 4-Layer Partial Column dXCO₂ and dCO₂

	One-Hour Output	Two-Hour Average Output	Three-Hour Average Output
4-Layer dXCO ₂ R ²	0.3954	0.4083	0.4168
4-Layer dXCO ₂ RMSE	12.36	12.23	12.14
4-Layer dCO ₂ R ²	0.2975	0.3045	0.3184
4-Layer dCO ₂ RMSE	0.88	0.88	0.87
4-Pressure dXCO ₂ R ²	0.3730	0.3860	0.3936
4-Pressure dXCO ₂ RMSE	11.84	11.72	11.65
4-Pressure dCO ₂ R ²	0.3573	0.3716	0.3780
4-Pressure dCO ₂ RMSE	0.87	0.86	0.85

Table A.36 1-Degree Rational R² Statistics for 5-Layer Partial Column dXCO₂ and dCO₂

	One-Hour Output	Two-Hour Average Output	Three-Hour Average Output
5-Layer dXCO ₂ R ²	0.4451	0.4555	0.4613
5-Layer dXCO ₂ RMSE	10.14	10.05	9.99
5-Layer dCO ₂ R ²	0.3386	0.3424	0.3530
5-Layer dCO ₂ RMSE	0.93	0.93	0.92
5-Pressure dXCO ₂ R ²	0.4211	0.4316	0.4362
5-Pressure dXCO ₂ RMSE	9.70	9.61	9.57
5-Pressure dCO ₂ R ²	0.4069	0.4188	0.4222
5-Pressure dCO ₂ RMSE	0.90	0.88	0.88

Table A.37 1-Degree Rational R² Statistics for 6-Layer Partial Column dXCO₂ and dCO₂

	One-Hour Output	Two-Hour Average Output	Three-Hour Average Output
6-Layer dXCO ₂ R ²	0.4754	0.4827	0.4858
6-Layer dXCO ₂ RMSE	8.53	8.47	8.45
6-Layer dCO ₂ R ²	0.3245	0.3249	0.3337
6-Layer dCO ₂ RMSE	0.97	0.98	0.96
6-Pressure dXCO ₂ R ²	0.4487	0.4557	0.4572
6-Pressure dXCO ₂ RMSE	8.16	8.11	8.10
6-Pressure dCO ₂ R ²	0.4357	0.4443	0.4447
6-Pressure dCO ₂ RMSE	0.90	0.89	0.89

Table A.38 1-Degree Rational R² Statistics for 7-Layer Partial Column dXCO₂ and dCO₂

	One-Hour Output	Two-Hour Average Output	Three-Hour Average Output
7-Layer dXCO ₂ R ²	0.5033	0.5033	0.5038
7-Layer dXCO ₂ RMSE	7.53	7.53	7.52
7-Layer dCO ₂ R ²	0.3329	0.3219	0.3322
7-Layer dCO ₂ RMSE	1.05	1.06	1.05
7-Pressure dXCO ₂ R ²	0.4806	0.4803	0.4789
7-Pressure dXCO ₂ RMSE	7.17	7.17	7.18
7-Pressure dCO ₂ R ²	0.4739	0.4753	0.4727
7-Pressure dCO ₂ RMSE	0.91	0.91	0.91

Table A.39 1-Degree Rational R² Statistics for 8-Layer Partial Column dXCO₂ and dCO₂

	One-Hour Output	Two-Hour Average Output	Three-Hour Average Output
8-Layer dXCO ₂ R ²	0.5217	0.5179	0.5156
8-Layer dXCO ₂ RMSE	6.57	6.60	6.62
8-Layer dCO ₂ R ²	0.3134	0.2983	0.3068
8-Layer dCO ₂ RMSE	1.11	1.13	1.11
8-Pressure dXCO ₂ R ²	0.4989	0.4947	0.4902
8-Pressure dXCO ₂ RMSE	6.27	6.30	6.33
8-Pressure dCO ₂ R ²	0.4952	0.4924	0.4865
8-Pressure dCO ₂ RMSE	0.91	0.91	0.91

Table A.40 1-Degree Rational R² Statistics for 9-Layer Partial Column dXCO₂ and dCO₂

	One-Hour Output	Two-Hour Average Output	Three-Hour Average Output
9-Layer dXCO ₂ R ²	0.5410	0.5421	0.5313
9-Layer dXCO ₂ RMSE	5.59	5.58	5.65
9-Layer dCO ₂ R ²	0.2960	0.2857	0.2601
9-Layer dCO ₂ RMSE	1.13	1.14	1.14
9-Pressure dXCO ₂ R ²	0.5132	0.5131	0.5005
9-Pressure dXCO ₂ RMSE	5.40	5.40	5.47
9-Pressure dCO ₂ R ²	0.5096	0.5093	0.4967
9-Pressure dCO ₂ RMSE	0.88	0.88	0.89

Table A.41 1-Degree Rational R² Statistics for 10-Layer Partial Column dXCO₂ and dCO₂

	One-Hour Output	Two-Hour Average Output	Three-Hour Average Output
10-Layer dXCO ₂ R ²	0.5447	0.5422	0.5299
10-Layer dXCO ₂ RMSE	5.07	5.09	5.15
10-Layer dCO ₂ R ²	0.2637	0.2509	0.2504
10-Layer dCO ₂ RMSE	1.22	1.23	1.23
10-Pressure dXCO ₂ R ²	0.5171	0.5134	0.4996
10-Pressure dXCO ₂ RMSE	4.91	4.93	5.00
10-Pressure dCO ₂ R ²	0.5205	0.5129	0.4988
10-Pressure dCO ₂ RMSE	0.89	0.89	0.90

Table A.42 1-Degree Rational R² Statistics for 11-Layer Partial Column dXCO₂ and dCO₂

	One-Hour Output	Two-Hour Average Output	Three-Hour Average Output
11-Layer dXCO ₂ R ²	0.5429	0.5372	0.5239
11-Layer dXCO ₂ RMSE	4.67	4.70	4.77
11-Layer dCO ₂ R ²	0.2304	0.2162	0.2158
11-Layer dCO ₂ RMSE	1.32	1.33	1.33
11-Pressure dXCO ₂ R ²	0.4866	0.4798	0.4649
11-Pressure dXCO ₂ RMSE	4.51	4.54	4.60
11-Pressure dCO ₂ R ²	0.4897	0.4824	0.4669
11-Pressure dCO ₂ RMSE	0.88	0.89	0.90

Table A.43 Sum of Sine R² Statistics for Column dXCO₂ and dCO₂

	One-Hour Output	Two-Hour Average Output	Three-Hour Average Output
Column dXCO ₂ R ²	0.5234	0.5099	0.4922
Column dXCO ₂ RMSE	2.85	2.89	2.94
Column dCO ₂ R ²	0.0434	0.0388	0.0381
Column dCO ₂ RMSE	1.95e8	1.96e8	1.96e8

Table A.44 Sum of Sine R² Statistics for 3-Layer Partial Column dXCO₂ and dCO₂

	One-Hour Output	Two-Hour Average Output	Three-Hour Average Output
3-Layer dXCO ₂ R ²	0.3487	0.3652	0.3777
3-Layer dXCO ₂ RMSE	15.05	14.86	14.71
3-Layer dCO ₂ R ²	0.2642	0.2766	0.2920
3-Layer dCO ₂ RMSE	0.80e8	0.79e8	0.78e8
3-Pressure dXCO ₂ R ²	0.3311	0.3478	0.3599
3-Pressure dXCO ₂ RMSE	14.51	14.33	14.19
3-Pressure dCO ₂ R ²	0.3170	0.3350	0.3461
3-Pressure dCO ₂ RMSE	0.80e8	0.79e8	0.78e8

Table A.45 Sum of Sine R² Statistics for 4-Layer Partial Column dXCO₂ and dCO₂

	One-Hour Output	Two-Hour Average Output	Three-Hour Average Output
4-Layer dXCO ₂ R ²	0.3899	0.4050	0.4156
4-Layer dXCO ₂ RMSE	12.42	12.26	12.15
4-Layer dCO ₂ R ²	0.2843	0.2953	0.303
4-Layer dCO ₂ RMSE	0.89e8	0.89e8	0.878e8
4-Pressure dXCO ₂ R ²	0.3672	0.3825	0.3925
4-Pressure dXCO ₂ RMSE	11.90	11.75	11.66
4-Pressure dCO ₂ R ²	0.3518	0.3686	0.3777
4-Pressure dCO ₂ RMSE	0.87e8	0.86e8	0.85e8

Table A.46 Sum of Sine R² Statistics for 5-Layer Partial Column dXCO₂ and dCO₂

	One-Hour Output	Two-Hour Average Output	Three-Hour Average Output
5-Layer dXCO ₂ R ²	0.4370	0.4500	0.4580
5-Layer dXCO ₂ RMSE	10.22	10.10	10.02
5-Layer dCO ₂ R ²	0.3187	0.3242	0.3373
5-Layer dCO ₂ RMSE	0.94e8	0.94e8	0.93e8
5-Pressure dXCO ₂ R ²	0.4122	0.4255	0.4326
5-Pressure dXCO ₂ RMSE	9.77	9.66	9.60
5-Pressure dCO ₂ R ²	0.4195	0.4133	0.4195
5-Pressure dCO ₂ RMSE	0.88e8	0.88e8	0.88e8

Table A.47 Sum of Sine R² Statistics for 6-Layer Partial Column dXCO₂ and dCO₂

	One-Hour Output	Two-Hour Average Output	Three-Hour Average Output
6-Layer dXCO ₂ R ²	0.4663	0.4762	0.4815
6-Layer dXCO ₂ RMSE	8.60	8.52	8.48
6-Layer dCO ₂ R ²	0.3051	0.3078	0.3191
6-Layer dCO ₂ RMSE	0.99e8	0.98e8	0.98e8
6-Pressure dXCO ₂ R ²	0.4389	0.4488	0.4526
6-Pressure dXCO ₂ RMSE	8.23	8.16	8.13
6-Pressure dCO ₂ R ²	0.4270	0.4379	0.4407
6-Pressure dCO ₂ RMSE	0.90e8	0.89e8	0.89e8

Table A.48 Sum of Sine R² Statistics for 7-Layer Partial Column dXCO₂ and dCO₂

	One-Hour Output	Two-Hour Average Output	Three-Hour Average Output
7-Layer dXCO ₂ R ²	0.4918	0.4950	0.4984
7-Layer dXCO ₂ RMSE	7.62	7.59	7.57
7-Layer dCO ₂ R ²	0.3081	0.3022	0.3128
7-Layer dCO ₂ RMSE	1.07e8	1.07e8	1.06e8
7-Pressure dXCO ₂ R ²	0.4683	0.4714	0.4731
7-Pressure dXCO ₂ RMSE	7.25	7.23	7.22
7-Pressure dCO ₂ R ²	0.4633	0.4678	0.4683
7-Pressure dCO ₂ RMSE	0.92e8	0.92e8	0.91e8

Table A.49 Sum of Sine R² Statistics for 8-Layer Partial Column dXCO₂ and dCO₂

	One-Hour Output	Two-Hour Average Output	Three-Hour Average Output
8-Layer dXCO ₂ R ²	0.5087	0.5084	0.5086
8-Layer dXCO ₂ RMSE	6.56	6.66	6.66
8-Layer dCO ₂ R ²	0.2845	0.2761	0.2835
8-Layer dCO ₂ RMSE	1.13e8	1.14e8	1.13e8
8-Pressure dXCO ₂ R ²	0.4850	0.4844	0.4828
8-Pressure dXCO ₂ RMSE	6.36	6.36	6.37
8-Pressure dCO ₂ R ²	0.4664	0.4832	0.4802
8-Pressure dCO ₂ RMSE	0.93e8	0.91e8	0.92e8

Table A.50 Sum of Sine R² Statistics for 9-Layer Partial Column dXCO₂ and dCO₂

	One-Hour Output	Two-Hour Average Output	Three-Hour Average Output
9-Layer dXCO ₂ R ²	0.5266	0.5309	0.5229
9-Layer dXCO ₂ RMSE	5.68	5.65	5.70
9-Layer dCO ₂ R ²	0.2595	0.2442	0.2504
9-Layer dCO ₂ RMSE	1.16e8	1.18e8	1.17e8
9-Pressure dXCO ₂ R ²	0.4982	0.5015	0.4920
9-Pressure dXCO ₂ RMSE	5.49	5.47	5.52
9-Pressure dCO ₂ R ²	0.4953	0.4971	0.4886
9-Pressure dCO ₂ RMSE	0.89e8	0.89e8	0.90e8

Table A.51 Sum of Sine R² Statistics for 10-Layer Partial Column dXCO₂ and dCO₂

	One-Hour Output	Two-Hour Average Output	Three-Hour Average Output
10-Layer dXCO ₂ R ²	0.5300	0.5309	0.5213
10-Layer dXCO ₂ RMSE	5.15	5.15	5.20
10-Layer dCO ₂ R ²	0.2258	0.2208	0.2203
10-Layer dCO ₂ RMSE	1.25e8	1.26e8	1.26e8
10-Pressure dXCO ₂ R ²	0.5023	0.5021	0.4911
10-Pressure dXCO ₂ RMSE	4.99	4.99	5.04
10-Pressure dCO ₂ R ²	0.5024	0.5001	0.4903
10-Pressure dCO ₂ RMSE	0.90e8	0.90e8	0.91e8

Table A.52 Sum of Sine R² Statistics for 11-Layer Partial Column dXCO₂ and dCO₂

	One-Hour Output	Two-Hour Average Output	Three-Hour Average Output
11-Layer dXCO ₂ R ²	0.5284	0.5263	0.5155
11-Layer dXCO ₂ RMSE	4.75	4.76	0.1857
11-Layer dCO ₂ R ²	0.1926	0.1864	0.2158
11-Layer dCO ₂ RMSE	1.35e8	1.36e8	1.36e8
11-Pressure dXCO ₂ R ²	0.4715	0.4690	0.4570
11-Pressure dXCO ₂ RMSE	4.57	4.58	4.64
11-Pressure dCO ₂ R ²	0.4740	0.4711	0.4553
11-Pressure dCO ₂ RMSE	0.90e8	0.90e8	0.91e8

Table A.53 XCO₂ on the 10 Levels of Targeted Soundings (ppm)

Level 1	Level 2	Level 3	Level 4	Level 5	Level 6	Level 7	Level 8	Level 9	Level 10
381.15	381.41	382.73	384.80	389.13	395.04	404.29	414.31	428.20	437.83
389.22	389.97	391.18	392.36	393.85	395.96	398.05	400.07	400.53	401.17
396.85	399.00	402.16	405.27	409.51	413.66	419.41	424.69	428.99	431.10
381.08	379.46	376.26	372.97	367.62	362.54	356.16	350.52	345.12	344.33
391.40	392.04	392.95	394.03	395.66	397.92	401.11	404.38	408.51	411.23
392.66	393.28	394.24	395.40	397.38	399.65	402.76	405.71	409.40	410.81
386.73	386.69	386.97	387.83	390.04	393.04	398.11	403.32	411.80	416.27
377.52	377.05	377.67	379.81	385.36	392.61	405.47	418.87	440.91	454.35
404.99	406.56	408.38	409.34	409.40	407.80	403.48	397.75	386.91	377.16
385.68	385.05	384.44	384.11	384.25	384.61	386.16	387.63	391.95	393.89
392.41	392.65	393.22	393.85	394.99	396.10	398.00	399.44	402.72	402.66
388.31	387.08	384.89	382.23	378.04	373.26	366.92	360.35	353.46	348.66
388.21	387.91	387.92	387.91	388.65	389.50	391.87	394.13	399.15	401.52
393.01	392.43	391.36	389.60	386.75	383.21	378.46	373.49	367.76	363.45
392.70	393.2	393.96	394.70	395.72	396.67	397.76	398.67	399.30	399.20
381.29	378.77	375.04	370.74	364.97	359.32	353.16	348.09	344.98	345.20
378.51	375.16	370.08	364.69	357.46	350.51	342.80	336.50	332.44	332.83
386.13	385.26	384.75	384.10	384.38	385.48	388.81	393.24	400.93	406.74
392.70	393.2	393.96	394.70	395.72	396.67	397.76	398.67	399.30	399.20
391.62	391.78	392.42	393.05	394.09	395.52	397.22	399.13	399.70	400.40
385.89	385.16	384.79	384.79	385.54	387.13	389.79	393.03	396.80	400.48
389.19	389.64	390.51	391.37	392.66	394.55	396.81	399.28	400.95	402.74
395.15	396.64	399.21	401.81	405.63	409.81	414.52	418.72	420.47	421.09
393.24	394.34	396.13	397.89	400.17	403.04	406.09	409.12	410.54	411.06
396.80	396.99	396.46	395.36	392.62	389.57	384.10	378.42	369.33	364.00
391.94	392.67	394.04	395.90	399.24	403.58	410.15	416.97	426.85	432.63
391.22	390.77	389.67	388.54	386.66	384.91	382.28	379.70	376.69	374.89
395.31	395.85	396.76	397.72	399.23	400.54	402.29	403.28	404.15	402.71
374.37	373.73	374.69	377.59	385.08	395.18	413.60	433.46	467.71	488.85
383.80	383.18	383.10	383.78	386.25	389.51	396.09	402.70	414.65	421.59
383.48	382.75	382.55	383.37	386.18	389.69	396.75	403.78	418.35	425.20
383.79	383.1	382.94	383.51	386.00	389.61	397.12	405.15	420.62	429.68
388.86	387.92	386.64	385.22	383.54	381.77	380.39	379.03	379.73	379.76
391.44	390.92	390.43	389.46	388.52	387.26	386.43	385.49	385.24	385.01
378.50	377.04	376.23	376.45	378.81	382.75	392.14	403.10	425.85	440.71
381.86	380.98	380.93	381.49	384.63	389.28	399.03	409.63	427.83	439.85
381.11	379.63	378.50	378.22	379.24	380.60	385.78	392.06	406.45	417.18

388.90	387.59	386.06	384.22	382.43	380.95	380.38	380.62	382.85	385.44
392.24	391.36	390.34	388.72	386.78	384.86	383.04	381.81	380.73	380.95
391.89	390.55	388.67	386.30	382.92	379.53	375.10	371.24	365.53	363.31
389.40	389.03	389.21	389.68	391.06	393.30	397.01	401.34	406.56	410.68
397.95	399.64	402.06	404.29	406.89	410.02	412.80	415.15	415.01	414.31
391.79	392.27	393.08	394.29	396.41	399.63	404.89	410.69	419.27	425.02
400.93	401.88	402.90	403.67	404.17	404.81	404.72	404.32	402.14	400.06
398.89	399.67	400.57	401.39	402.27	403.45	404.42	405.14	405.01	404.38
398.73	399.54	400.59	401.64	403.02	404.65	406.38	407.83	408.65	408.47
391.91	392.42	393.68	395.61	399.50	404.47	412.34	420.51	432.75	439.94
391.09	391.44	392.51	394.32	398.17	403.13	411.14	419.50	432.30	439.75
395.91	396.2	396.52	396.93	397.61	398.45	399.43	400.18	401.00	400.54
390.23	390.55	391.67	393.61	397.77	402.97	411.35	415.88	422.87	425.19
394.71	395.02	395.68	396.63	398.37	400.26	403.18	405.67	409.34	409.99
397.55	397.93	398.40	398.87	399.41	399.69	399.77	399.10	397.80	394.85
393.92	393.7	393.60	393.43	393.52	393.29	393.58	393.41	394.35	393.95
384.18	383.05	382.26	381.94	383.22	385.50	391.52	398.47	412.78	422.12
389.79	389.64	390.38	391.98	396.01	401.23	407.85	413.39	425.44	431.81
387.41	386.16	384.97	383.92	383.97	384.73	387.87	391.49	399.14	404.91
391.15	390.04	389.01	387.84	387.25	387.21	388.71	390.98	395.30	399.20
390.90	389.82	388.78	387.73	386.90	386.65	387.16	388.40	390.02	392.43
391.30	389.58	387.49	385.93	386.76	388.76	393.09	398.54	407.01	413.87
394.60	394.90	395.88	396.90	398.65	400.93	404.10	407.53	410.27	412.45
393.93	394.18	394.69	395.13	395.72	396.78	397.71	398.87	398.75	399.01
393.89	394.80	396.27	397.86	400.09	403.17	406.76	410.39	413.53	415.73
397.13	398.02	398.92	399.43	399.17	399.25	397.68	395.67	389.84	386.63
397.26	398.53	400.24	401.96	404.16	406.75	410.33	413.74	416.73	418.90
396.63	397.21	398.36	400.02	403.19	406.89	412.30	417.39	424.35	427.44
396.66	396.94	397.48	398.31	399.96	401.90	404.82	407.54	411.67	412.97

The order of level is consistent with the pressure partition method, i.e. the 10th level corresponds to the surface level.

Table A.54 XCO₂ Uncertainty of the 10 Levels of Targeted Soundings (ppm)

Level 1	Level 2	Level 3	Level 4	Level 5	Level 6	Level 7	Level 8	Level 9	Level 10
7.5085	8.3824	9.5066	10.3957	11.7432	13.0647	15.7831	19.1731	25.7894	33.8694
5.6531	6.1757	6.7029	6.9660	7.4270	7.7970	9.7588	12.5772	19.2336	28.1546
6.1277	6.6853	7.2360	7.4947	7.9110	8.2912	10.3774	13.5045	20.7459	29.8187
6.3532	6.9640	7.6138	7.9851	8.5723	9.1358	11.3293	14.4973	21.6319	30.5217
6.0697	6.6336	7.1992	7.4649	7.8538	8.1172	9.9296	12.7457	19.6086	28.6583
4.4591	4.9553	5.5624	6.0023	6.8107	7.3268	8.9173	10.6908	15.3090	23.7255
4.1171	4.6061	5.2358	5.7303	6.6507	7.2456	8.8119	10.3760	14.4788	22.7757
7.2736	8.0729	9.0495	9.7656	10.8352	11.8649	14.3151	17.5587	24.3008	32.6939
3.4761	3.9628	4.6575	5.2770	6.4175	7.1528	8.6590	9.8057	12.7572	20.8217
3.6525	4.1392	4.8177	5.4057	6.4919	7.1893	8.7202	9.9993	13.3391	21.4827
3.9347	4.4153	5.0491	5.5757	6.5671	7.2168	8.7589	10.1954	14.0225	22.2772
4.1223	4.6084	5.2344	5.7300	6.6584	7.2574	8.8378	10.4440	14.6381	22.9385
4.0202	4.5052	5.1412	5.6547	6.6102	7.2278	8.7922	10.2996	14.2421	22.5027
4.7120	5.2075	5.7838	6.1706	6.8826	7.3440	8.9926	10.9852	16.1057	24.6474
4.7885	5.2682	5.8048	6.1470	6.8245	7.3285	9.2138	11.5732	17.2720	25.8745
4.3867	4.8661	5.4490	5.8772	6.7020	7.2659	8.9780	10.8912	15.7023	24.1149
4.3884	4.8698	5.4569	5.8881	6.7151	7.2776	8.9817	10.8923	15.6975	24.1022
4.6209	5.1060	5.6725	6.0608	6.7958	7.2972	9.0114	11.0307	16.0791	24.5806
11.0888	12.8173	15.4326	17.8536	21.3761	24.7128	29.2442	33.6705	39.1763	44.7533
5.1706	5.6743	6.2159	6.5301	7.0992	7.4972	9.2834	11.6679	17.5222	26.2472
5.3658	5.8837	6.4320	6.7365	7.2663	7.6310	9.4118	11.8831	17.9668	26.7534
5.5762	6.0950	6.6244	6.8974	7.3799	7.7594	9.7047	12.4719	19.0289	27.9089
6.0509	6.6039	7.1518	7.4077	7.8152	8.1561	10.1599	13.1846	20.2885	29.3458
5.9513	6.4945	7.0312	7.2793	7.6761	7.9895	9.9367	12.8603	19.7849	28.8239
5.4600	5.9853	6.5499	6.8863	7.5179	8.0806	10.2134	13.0687	19.5511	28.2740
5.6184	6.1362	6.6582	6.9167	7.3752	7.7445	9.7346	12.6038	19.3663	28.3018
4.4871	4.9752	5.5647	5.9873	6.7841	7.3183	9.0022	10.9205	15.7640	24.1951
4.0089	4.4959	5.1347	5.6468	6.6011	7.2194	8.7932	10.3202	14.2990	22.5501
3.7283	4.2148	4.8840	5.4528	6.5097	7.1889	8.7280	10.0622	13.5516	21.7048
3.9967	4.4829	5.1234	5.6401	6.6029	7.2228	8.7911	10.3063	14.2744	22.5285
4.3648	4.8469	5.4370	5.8753	6.7031	7.2629	8.9188	10.7013	15.1935	23.5832
4.0260	4.5124	5.1484	5.6566	6.6075	7.2234	8.8002	10.3416	14.3695	22.6301
4.0260	4.5122	5.1494	5.6602	6.6171	7.2415	8.8366	10.3968	14.4439	22.6984
4.0527	4.5360	5.1637	5.6652	6.6095	7.2286	8.8216	10.3932	14.4816	22.7583
4.7371	5.2163	5.7571	6.1078	6.7961	7.2943	9.1259	11.3899	16.9575	25.5568
4.4948	4.9802	5.5621	5.9759	6.7585	7.2815	8.9640	10.8979	15.8109	24.2645
4.7253	5.2095	5.7628	6.1290	6.8300	7.3216	9.0945	11.2543	16.5505	25.0980

4.6533	5.1380	5.7007	6.0810	6.8077	7.3125	9.0681	11.1730	16.4000	24.9145
4.7831	5.2796	5.8508	6.2267	6.9205	7.3819	9.0797	11.1805	16.4988	25.0616
4.8877	5.3758	5.9181	6.2558	6.9004	7.3581	9.1679	11.4664	17.1026	25.7341
5.4078	5.9151	6.4370	6.7090	7.2021	7.5699	9.4707	12.1378	18.5465	27.4056
5.8697	6.4135	6.9604	7.2257	7.6481	7.9603	9.8359	12.6377	19.3632	28.3448
4.7353	5.2292	5.8004	6.1833	6.8882	7.3517	9.0085	10.9991	16.0741	24.6159
4.8706	5.3713	5.9407	6.3069	6.9719	7.4039	9.0734	11.1729	16.5168	25.1149
4.6027	5.0985	5.6888	6.1013	6.8585	7.3465	8.9670	10.8582	15.7383	24.2152
4.4510	4.9489	5.5616	6.0151	6.8364	7.3455	8.8782	10.5700	15.0617	23.4745
4.1857	4.6759	5.3017	5.7864	6.6853	7.2608	8.8286	10.4320	14.6212	22.9332
4.1554	4.6455	5.2750	5.7670	6.6771	7.2610	8.8187	10.3764	14.4645	22.7661
4.4098	4.9037	5.5119	5.9587	6.7839	7.3141	8.9073	10.6598	15.2393	23.6433
4.3063	4.7948	5.4039	5.8609	6.7120	7.2634	8.8670	10.5845	15.0240	23.3842
4.4708	4.9615	5.5559	5.9829	6.7798	7.3000	8.9383	10.7943	15.5690	24.0030
4.1184	4.6055	5.2337	5.7292	6.6558	7.2558	8.8376	10.4315	14.6078	22.9078
4.2558	4.7419	5.3527	5.8168	6.6872	7.2555	8.8743	10.5916	15.0294	23.3773
3.8257	4.3128	4.9720	5.5222	6.5454	7.2014	8.7455	10.1412	13.8079	21.9973
4.4978	4.9923	5.5920	6.0252	6.8223	7.3362	8.9362	10.7301	15.3597	23.7775
4.1307	4.6167	5.2405	5.7284	6.6414	7.2331	8.823	10.4387	14.6460	22.9474
4.4880	4.9752	5.5612	5.9789	6.7644	7.2850	8.9499	10.8536	15.7111	24.1573
4.7688	5.2558	5.8092	6.1719	6.8662	7.3530	9.1300	11.3173	16.7255	25.2902
5.2774	5.7774	6.2988	6.5810	7.0978	7.4685	9.3165	11.8647	18.0614	26.8722
5.0644	5.5670	6.1176	6.4491	7.0484	7.4482	9.1729	11.4414	17.1204	25.8056
5.7162	6.2404	6.7635	7.0151	7.4505	7.7998	9.7757	12.6552	19.4481	28.4139
5.8912	6.4372	6.9903	7.2677	7.7291	8.1173	10.1254	13.0600	19.9223	28.8779
4.2712	4.7564	5.3638	5.8315	6.7043	7.2778	8.8757	10.5389	14.7501	23.0352
6.4310	7.0365	7.6656	8.0062	8.5443	9.0739	11.3011	14.5711	21.9106	30.9093
4.0774	4.5667	5.2029	5.7089	6.6474	7.2462	8.8030	10.3411	14.3756	22.6496
4.0695	4.5596	5.1985	5.7061	6.6451	7.2459	8.8021	10.3255	14.3086	22.5730

Table A.55 Wind Speed and Direction (One-hour) at Hamilton Station and London Station

Hamilton Wind Speed (km/h) /Wind Direction (10s deg)		London Wind Speed (km/h)		Difference of Wind Speed (km/h)	
One-Hour	Three-Hour	One-Hour	Three-Hour	One-Hour	Three-Hour
17/4	21.67	17	14.33	0	7.33
22/23	24.67	11	13	11	11.67
11/26	11.67	11	9.67	0	2
17/26	18	17	17.67	0	0.33
13/24	19	7	11.67	6	7.33
7/10	8.67	6	7.33	1	1.33
13/24	20	24	30.33	-11	-10.33
7/22	14.33	15	21.67	-8	-7.33
15/20	18.33	17	17.67	-2	0.67
15/16	11.33	13	14.33	2	-3
7/19	6.33	4	4.67	3	1.67
19/28	21.67	13	15.33	6	6.33
11/21	16	13	16	-2	0
11/23	8.67	9	8	2	0.67
9/28	9.33	6	8.67	3	0.67
0/Na	6	6	11.33	-6	-5.33
15/22	19	9	14.33	6	4.67
11/22	14.33	7	12.33	4	2
33/24	34	26	30	7	4
6/6	6.33	7	7	-1	-0.67
20/32	24.67	13	19	7	5.67
44/21	43	35	41.67	9	1.33
9/7	9.67	4	3.33	5	6.33
6/2	4	9	6.67	-3	-2.67
13/30	21	7	13.33	6	7.67
7/32	10.33	11	13.67	-4	-3.33
11/4	12.33	13	9.67	-2	2.67
13/22	19	15	24.33	-2	-5.33
9/20	7.33	17	15.67	-8	-8.33
7/15	10.33	9	11.67	-2	-1.33
11/2	8	9	12	2	-4
11/31	13	7	9.67	4	3.33
22/32	17.33	19	17.67	3	-0.33
6/20	9.33	6	8.67	0	0.67
9/18	11	6	8.67	3	2.33
11/24	14.67	11	11.67	0	3
9/27	11	6	5.67	3	5.33

9/20	16	17	19	-8	-3
13/21	18.67	15	14.33	-2	4.33
6/4	10.67	11	10.33	-5	0.33
9/30	9	7	9.67	2	-0.67
15/4	15	9	7.67	6	7.33
10/34	12	11	11.67	-1	0.33
11/18	12.33	9	11.67	2	0.67
16/5	14.67	8	11.67	8	3
0/Na	23.33	18	20.67	-18	2.67
13/29	15.67	6	10.67	7	5
10/26	9.33	11	15	-1	-5.67
13/24	12	9	12.33	4	-0.33
17/20	20.33	12	16	5	4.33
12/18	15.67	12	13.67	0	2
14/33	22	18	18	-4	4
17/24	22.67	8	13	9	9.67
6/23	6.5	9	13	-3	-6.5
15/7	14	12	12	3	2
9/20	13.67	16	17.33	-7	-3.67
4/26	5.33	NA	NA	NA	NA
12/22	17.67	14	14.67	-2	3
8/26	14.67	11	11.67	-3	3
17/22	22	17	17.67	0	4.33
9/17	9.33	12	10	-3	-0.67
6/1	8.333333	8	6.33	-2	2
8/21	10	4	5.67	4	4.33
10/24	11.66667	9	10.33	1	1.33
10/18	15.66667	11	16.33	-1	-0.67
20/18	23	14	17.67	6	5.33

Table A.56 Temperature at Hamilton Station and London Station

Hamilton Temperature (°C)		London Temperature (°C)		Difference of Temperature (°C)	
One-Hour	Three-Hour	One-Hour	Three-Hour	One-Hour	Three-Hour
7.7	7.97	5.7	6.4	2	1.57
12.3	13.1	10.8	12.1	1.5	1
-8.2	-7.57	-5	-5.27	-3.2	-2.3
-6	-4.5	-5	-4.9	-1	0.4
2.9	4.23	2.5	4.23	0.4	0
8.7	10.93	11.7	12.73	-3	-1.8
16.2	21.87	22.5	24.07	-6.3	-2.2
13.4	14.5	14.6	15.87	-1.2	-1.37
25.5	26.67	24.8	26.17	0.7	0.5
20.8	21.7	22.1	22.87	-1.3	-1.17
21.6	22.43	23	23.2	-1.4	-0.77
15.9	16.6	17.4	17.87	-1.5	-1.27
28.8	30.4	30.9	31.83	-2.1	-1.43
22.9	22.63	20.3	20.7	2.6	1.93
24.7	26.07	25.2	25.73	-0.5	0.33
26.5	27.77	25.6	27.03	0.9	0.73
21.1	23.33	24.1	25.1	-3	-1.77
19.2	22.33	21	23.03	-1.8	-0.7
24.6	25.07	24.5	25.33	0.1	-0.27
8.9	11.33	14	16.37	-5.1	-5.03
10.3	11.47	10.1	11.33	0.2	0.13
15.9	16.37	15.5	16	0.4	0.37
1.3	2.37	1.5	3.4	-0.2	-1.03
4.6	6.33	5.6	7.67	-1	-1.33
-9	-7.97	-8.7	-7.97	-0.3	0
-4.6	-3.7	-5.4	-4.57	0.8	0.87
3.8	6.13	6.8	9.47	-3	-3.33
26.7	28.1	28.6	29.5	-1.9	-1.4
22.9	24.7	22.8	23.97	0.1	0.73
23.2	24.03	25.8	26.67	-2.6	-2.63
20.9	22.23	22	22.53	-1.1	-0.3
22.9	24.47	22.9	24.17	0	0.3
26	27.17	25.4	26.07	0.6	1.1
28.5	29.5	29.2	29.73	-0.7	-0.23
22.7	24.03	21.9	22.87	0.8	1.17
26.2	27.9	27.3	27.87	-1.1	0.03
22.3	23.23	26.2	27.07	-3.9	-3.83
22	24.07	23.1	23.9	-1.1	0.17

20.1	21.7	20.5	21.93	-0.4	-0.23
17.3	19.03	19.3	22.57	-2	-3.53
13.9	16.37	12.1	14.63	1.8	1.73
0.9	1.37	0.4	1.57	0.5	-0.2
-4.6	-1.07	-3.4	-2.5	-1.2	1.43
11.8	13.8	13	14.57	-1.2	-0.77
13.6	16.43	18.5	21.1	-4.9	-4.67
-0.7	1.2	0.1	1.77	-0.8	-0.57
11.8	13.73	10.2	12.37	1.6	1.37
11.9	13.83	10.1	12.1	1.8	1.73
17.5	18.87	12.9	15.9	4.6	2.97
9.2	10.53	10	10.9	-0.8	-0.37
23.5	25.7	24.4	25.87	-0.9	-0.17
25.8	27.53	24.8	26.5	1	1.03
26.8	28.9	28	29.37	-1.2	-0.47
28.9	29.3	27.2	28.7	1.7	0.6
25.6	26.27	25.6	27.37	0	-1.1
24.9	26.57	25.4	26.57	-0.5	0
24.7	27.03	22	24.63	2.7	2.4
16.4	19.03	18.3	20.23	-1.9	-1.2
11.6	12.53	11.1	11.97	0.5	0.57
16.5	18.13	17.5	19.13	-1	-1
13	13.77	13.3	14.47	-0.3	-0.7
1.5	2.07	2	2.93	-0.5	-0.87
4.5	5.97	3.7	5.83	0.8	0.13
-11.3	-9.7	-8.2	-8.77	-3.1	-0.93
8.6	9.6	7.9	9.37	0.7	0.23
14	16	18.6	21.17	-4.6	-5.17

Table A.57 Humidity at Hamilton Station and London Station

Hamilton Humidity (%)		London Humidity (%)		Difference of Humidity (%)	
One-Hour	Three-Hour	One-Hour	Three-Hour	One-Hour	Three-Hour
100	97.33	79	75.67	21	21.67
69	63.33	80	72.67	-11	-9.33
75	74.67	86	85	-11	-10.33
79	73	74	76.33	5	-3.33
62	54	67	60.33	-5	-6.33
48	41.33	41	32.33	7	9
59	51.67	48	45.33	11	6.33
70	61.33	68	61.33	2	0
46	43.67	43	47	3	-3.33
69	66	60	57.67	9	8.33
55	51.33	50	49.67	5	1.67
52	47.67	45	43.67	7	4
66	60.33	46	44.67	20	15.67
90	89	78	81	12	8
61	55	50	47	11	8
71	63.67	73	67	-2	-3.33
67	59.33	45	42	22	17.33
67	63.33	62	57	5	6.33
57	60.33	57	54.67	0	5.67
61	55.33	61	53	0	2.33
58	52.33	74	63	-16	-10.67
43	43.67	48	47.33	-5	-3.67
81	76.67	72	64	9	12.67
69	62.67	79	64.67	-10	-2
57	51.67	62	60.67	-5	-9
55	53.67	56	54.33	-1	-0.67
84	78.67	76	57	8	21.67
74	66	55	53.67	19	12.33
49	46.33	49	46	0	0.33
66	63	50	45.33	16	17.67
79	73.67	64	60.33	15	13.33
49	43	36	33.33	13	9.67
58	54.33	50	51.33	8	3
59	57.67	57	54.33	2	3.33
62	57.33	62	57.33	0	0
51	45	48	48	3	-3
42	43	66	63	-24	-20
67	57.67	65	61.33	2	-3.67

64	56.67	70	61.33	-6	-4.67
72	67.67	85	63.67	-13	4
72	62.33	75	65	-3	-2.67
83	80	73	69	10	11
75	69.67	69	64.67	6	5
41	36.67	46	40	-5	-3.33
87	77.33	73	63.33	14	14
38	33	47	40.67	-9	-7.67
27	23	35	29	-8	-6
40	36.67	46	41.33	-6	-4.67
59	52.67	93	71.67	-34	-19
51	45	41	39	10	6
36	33.33	30	28.67	6	4.67
54	53.67	48	44	6	9.67
54	47	47	42.67	7	4.33
40	35.5	47	41.33	-7	-5.83
53	51.67	60	56.33	-7	-4.67
51	48.33	54	51	-3	-2.67
51	42.33	61	50.33	-10	-8
74	65	66	57	8	8
64	57.67	68	63	-4	-5.33
72	68.67	70	62.67	2	6
74	73	79	74.33	-5	-1.33
78	74	81	71.67	-3	2.33
92	86.67	87	81.67	5	5
80	78.33	84	85.33	-4	-7
37	37	46	39.67	-9	-2.67
46	43	44	36.33	2	6.67

Table A.58 Pressure at Hamilton Station and London Station

Hamilton Pressure (kPa)		London Humidity (kPa)		Difference of Humidity (kPa)	
One-Hour	Three-Hour	One-Hour	Three-Hour	One-Hour	Three-Hour
99.09	99.15	97.98	97.9	1.11	1.25
98.37	98.27	97.93	97.83	0.44	0.44
99.58	99.55	99.18	99.15	0.4	0.4
98.35	98.29	98	97.97	0.35	0.33
98.88	98.86	98.46	98.46	0.42	0.4
100.15	100.12	99.6	99.62	0.55	0.51
97.79	97.78	97.21	97.24	0.58	0.54
98.72	98.73	98.17	98.19	0.55	0.54
98.46	98.47	98.04	98.05	0.42	0.42
99.03	99.03	98.52	98.52	0.51	0.51
99.06	99.05	98.6	98.61	0.46	0.44
99.03	99	98.62	98.61	0.41	0.39
98.75	98.72	98.28	98.26	0.47	0.46
98.14	98.16	97.75	97.74	0.39	0.43
99.04	99.04	98.63	98.67	0.41	0.37
98.52	98.53	98.16	98.17	0.36	0.36
98.55	98.52	98.11	98.09	0.44	0.43
99.31	99.31	98.85	98.86	0.46	0.45
97.79	97.78	97.48	97.42	0.31	0.36
99.02	99.02	98.5	98.47	0.52	0.55
98.44	98.35	98.18	98.1	0.26	0.25
97.66	97.62	97.14	97.11	0.52	0.51
99.99	99.98	99.45	99.48	0.54	0.5
98.79	98.74	98.3	98.27	0.49	0.47
100.35	100.25	99.88	99.81	0.47	0.44
99.14	99.14	98.73	98.74	0.41	0.41
99.24	99.2	98.72	98.7	0.52	0.5
98.94	98.98	98.5	98.51	0.44	0.47
98.66	98.67	98.21	98.19	0.45	0.48
98.36	98.37	97.88	97.89	0.48	0.48
98.44	98.46	97.88	97.91	0.56	0.54
98.81	98.79	98.44	98.44	0.37	0.35
98.41	98.39	98.08	98.05	0.33	0.34
98.34	98.37	97.93	97.95	0.41	0.42
98.74	98.74	98.26	98.27	0.48	0.47
98.87	98.85	98.51	98.48	0.36	0.36
98.53	98.51	98.25	98.26	0.28	0.24
98.89	98.91	98.41	98.43	0.48	0.47

98.6	98.63	98.09	98.12	0.51	0.51
98.88	98.85	98.41	98.36	0.47	0.5
99.36	99.33	99.01	98.99	0.35	0.34
99.84	99.84	99.34	99.31	0.5	0.53
99.74	99.69	99.29	99.26	0.45	0.44
99.11	99.11	98.58	98.59	0.53	0.53
99.4	99.37	98.88	98.84	0.52	0.53
99.83	99.77	99.43	99.39	0.4	0.38
99.2	99.23	98.86	98.9	0.34	0.33
99.31	99.33	98.85	98.89	0.46	0.44
98.54	98.5	98.08	98.08	0.46	0.43
98.23	98.2	97.69	97.71	0.54	0.49
99.19	99.19	98.75	98.76	0.44	0.44
98.72	98.65	98.37	98.29	0.35	0.36
98	97.94	97.6	97.53	0.4	0.41
99.14	99.13	98.71	98.69	0.43	0.44
98.58	98.55	98.1	98.06	0.48	0.49
98.66	98.67	98.2	98.21	0.46	0.45
NA	NA	98.71	98.71	NA	NA
98.88	98.86	98.44	98.42	0.44	0.43
98.38	98.28	98	97.93	0.38	0.35
98.92	98.91	98.47	98.46	0.45	0.45
98.96	98.98	98.42	98.46	0.54	0.52
99.87	99.86	99.39	99.38	0.48	0.48
99.42	99.4	98.94	98.92	0.48	0.47
99.26	99.24	98.77	98.75	0.49	0.49
100.08	100.1	99.56	99.59	0.52	0.51
99.61	99.65	99.01	99.05	0.6	0.6

Table A.59 Weather Event/Description at Hamilton Station and London Station

19 th Hour	Hamilton Weather		London Weather		
	18 th Hour	17 th Hour	19 th Hour	18 th Hour	17 th Hour
Fog	Fog	Mainly Clear	Mostly Cloudy	Mostly Cloudy	Mostly Cloudy
Clear	Clear	Clear	Clear	Clear	Clear
Mostly Cloudy	Mostly Cloudy	Mostly Cloudy	Cloudy	Cloudy	Snow Showers
Clear	Clear	Mainly Clear	Mostly Cloudy	Mostly Cloudy	Snow Showers
Mainly Clear	Mainly Clear	Clear	Clear	Mainly Clear	Mainly Clear
Cloudy	Mostly Cloudy	Mostly Cloudy	Cloudy	Cloudy	Cloudy
Mainly Clear	Mainly Clear	Mainly Clear	Mainly Clear	Mainly Clear	Mainly Clear
Mostly Cloudy	Mostly Cloudy	Mostly Cloudy	Mainly Clear	Mainly Clear	Mostly Cloudy
Clear	Clear	Mainly Clear	Clear	Clear	Mainly Clear
Mainly Clear	Mostly Cloudy	Mostly Cloudy	Mainly Clear	Mostly Cloudy	Mostly Cloudy
Clear	Clear	Clear	Clear	Clear	Clear
Clear	Mainly Clear	Mainly Clear	Mainly Clear	Mainly Clear	Mainly Clear
Mainly Clear	Mainly Clear	Mainly Clear	Clear	Clear	Mainly Clear
Mostly Cloudy	Mostly Cloudy	Mostly Cloudy	Mainly Clear	Mostly Cloudy	Thunderstorms,Rain Showers
Clear	Mainly Clear	Mainly Clear	Mainly Clear	Mostly Cloudy	Mostly Cloudy
Mainly Clear	Mainly Clear	Mainly Clear	Mainly Clear	Mainly Clear	Mainly Clear
Mainly Clear	Mainly Clear	Mostly Cloudy	Mainly Clear	Mainly Clear	Mainly Clear
Mainly Clear	Mainly Clear	Clear	Mainly Clear	Clear	Mainly Clear
Mainly Clear	Mainly Clear	Mainly Clear	Mostly Cloudy	Mostly Cloudy	Mainly Clear
Clear	Clear	Clear	Clear	Mainly Clear	Clear

Mainly Clear	Mostly Cloudy	Mainly Clear	Mainly Clear	Mainly Clear	Mainly Clear
Mainly Clear	Mostly Cloudy	Mostly Cloudy	Clear	Mainly Clear	Mostly Cloudy
Mostly Cloudy	Mostly Cloudy	Mostly Cloudy	Clear	Clear	Mainly Clear
Clear	Clear	Clear	Clear	Clear	Mainly Clear
Clear	Mainly Clear	Mainly Clear	Mainly Clear	Mainly Clear	Mainly Clear
Mainly Clear	Mainly Clear	Mostly Cloudy	Clear	Clear	Mainly Clear
Mostly Cloudy	Mostly Cloudy	Mostly Cloudy	Cloudy	Mostly Cloudy	Mostly Cloudy
Mainly Clear	Mostly Cloudy	Mostly Cloudy	Mainly Clear	Mainly Clear	Mainly Clear
Mainly Clear	Mainly Clear	Mainly Clear	Clear	Mainly Clear	Mainly Clear
Mostly Cloudy	Mostly Cloudy	Mostly Cloudy	Mainly Clear	Mainly Clear	Mainly Clear
Mainly Clear	Mainly Clear	Mostly Cloudy	Mainly Clear	Mainly Clear	Mostly Cloudy
Mainly Clear	Mainly Clear	Mainly Clear	Clear	Mainly Clear	Mainly Clear
Mainly Clear	Mainly Clear	Mainly Clear	Mainly Clear	Mainly Clear	Mostly Cloudy
Mostly Cloudy	Mostly Cloudy	Mostly Cloudy	Mostly Cloudy	Mostly Cloudy	Mostly Cloudy
Mostly Cloudy	Mostly Cloudy	Mostly Cloudy	Cloudy	Cloudy	Cloudy
Clear	Mainly Clear	Mainly Clear	Clear	Clear	Clear
Mainly Clear	Mostly Cloudy	Mostly Cloudy	Mainly Clear	Mostly Cloudy	Mostly Cloudy
Mostly Cloudy	Mainly Clear	Mostly Cloudy	Mainly Clear	Rain Showers	Mostly Cloudy
Mostly Cloudy	Mostly Cloudy	Mostly Cloudy	Mostly Cloudy	Mostly Cloudy	Mostly Cloudy

Mainly Clear	Mainly Clear	Mainly Clear	Mainly Clear	Clear	Clear
Clear	Clear	Clear	Clear	Clear	Clear
Mainly Clear	Mostly Cloudy	Mostly Cloudy	Clear	Clear	Clear
Clear	NA	NA	Mainly Clear	Mainly Clear	Mostly Cloudy
Mainly Clear	NA	NA	Mainly Clear	Mainly Clear	Mainly Clear
Mainly Clear	NA	NA	Mainly Clear	NA	NA
Clear	NA	NA	Mainly Clear	NA	NA
Mainly Clear	NA	NA	Mainly Clear	NA	NA
Mainly Clear	NA	NA	Mostly Cloudy	NA	NA
Mostly Cloudy	NA	NA	Fog	Rain Showers	NA
Mostly Cloudy	NA	NA	Mostly Cloudy	NA	NA
Mainly Clear	NA	NA	Mainly Clear	NA	NA
Mainly Clear	NA	NA	Mainly Clear	NA	NA
Mainly Clear	NA	NA	Mostly Cloudy	NA	NA
Mainly Clear	NA		Mainly Clear	NA	
Mostly Cloudy	NA	NA	Mainly Clear	NA	NA
Mainly Clear	NA	NA	Mainly Clear	NA	NA
NA Mostly Cloudy	NA NA	NA NA	NA Mostly Cloudy	NA NA	NA NA
Mostly Cloudy	NA	NA	Mostly Cloudy	NA	NA

Clear	NA	NA	Clear	NA	NA
Cloudy	NA	NA	Cloudy	NA	NA
Mostly Cloudy	NA	NA	Mostly Cloudy	NA	NA
Mainly Clear	NA	NA	Haze	Haze	Haze
Clear	NA	NA	Snow Showers	Snow Showers	Snow Showers
Mainly Clear	NA	NA	Mainly Clear	NA	NA
Mostly Cloudy	NA	NA	Mainly Clear	NA	NA

Table A.60 Scale of Wind Speed and Wind Direction Deviation

One-Hour/Wind Direction Deviation	Scale Hamilton		Scale London	
	One-Hour	Three-Hour	One-Hour	Three-Hour
4/9	5	5	3	3
5/3	6	3	3	3
3/4	2	3	2	2
4/4	4	5	4	4
3/3	4	1	3	3
2/5	2	1	2	2
3/3	5	7	8	8
2/2	3	4	5	5
4/1	4	5	4	4
4/2	2	3	3	3
2/1	1	1	1	1
5/5	5	3	4	4
3/2	4	3	4	4
3/3	2	2	2	2
3/7	2	1	2	2
1/Na	1	1	3	3
4/2	4	2	3	3
3/2	3	1	3	3
8/3	8	8	7	7
2/8	1	1	1	1
5/8	6	3	5	5
10/2	10	10	10	10
3/7	2	1	1	1
2/10	1	2	1	1
3/7	5	1	3	3
2/8	2	3	3	3
3/9	3	3	2	2
3/2	4	4	6	6
3/1	1	5	4	4
2/3	2	2	3	3
3/10	2	2	3	3
3/7	3	1	2	2
5/8	4	5	4	4
2/7	2	1	2	2
3/1	2	1	2	2
3/3	3	3	3	3
3/5	2	1	1	1

3/1	4	5	5
3/2	4	4	3
2/9	2	3	2
3/7	2	1	2
4/9	3	2	2
3/9	3	3	3
3/3	3	2	3
4/8	3	2	3
1/Na	5	5	5
3/6	3	1	2
3/4	2	3	4
3/3	3	2	3
4/1	5	3	4
3/1	3	3	3
4/8	5	5	4
4/3	5	2	3
2/3	1	2	3
4/7	3	3	3
3/1	3	4	4
1/4	1	NA	NA
3/2	4	4	3
2/4	3	3	3
4/2	5	5	4
3/2	2	3	2
2/10	2	2	1
2/2	2	1	1
3/3	2	2	2
3/1	3	3	4
5/1	5	4	4

Table A.61 Scale of Temperature

Scale Hamilton		Scale London	
One-Hour	Three-Hour	One-Hour	Three-Hour
5	5	4	4
6	6	5	6
1	1	1	1
2	2	1	1
4	4	3	4
5	6	6	6
7	8	8	9
7	7	6	7
10	10	9	9
8	8	8	8
9	9	9	8
7	7	7	7
10	10	10	10
9	9	8	8
9	9	9	9
10	10	9	9
9	9	9	9
8	8	8	8
9	9	9	9
6	6	6	7
6	6	5	5
7	7	7	7
4	4	3	3
4	4	4	5
1	1	1	1
2	2	1	2
4	4	4	5
10	10	10	10
9	9	8	9
9	9	9	9
9	8	8	8
9	9	8	9
10	10	9	9
10	10	10	10
9	9	8	8
10	10	10	10
9	9	9	9
9	9	9	9

8	8	8	8
8	8	8	8
7	7	6	6
4	3	3	3
2	3	2	2
6	6	6	6
7	7	7	8
3	3	3	3
6	6	5	6
6	6	5	6
8	8	6	7
6	6	5	5
9	9	9	9
10	10	9	9
10	10	10	10
10	10	10	10
10	9	9	9
10	10	9	9
9	10	8	9
7	8	7	8
6	6	5	6
7	7	7	7
7	6	6	6
4	3	3	3
4	4	4	4
1	1	1	1
5	5	5	5
7	7	7	8

Table A.62 Scale of Humidity

Scale Hamilton		Scale London	
One-Hour	Three-Hour	One-Hour	Three-Hour
10	10	8	9
6	6	8	8
7	7	9	10
8	7	7	9
5	5	6	6
3	3	2	1
5	4	3	3
6	6	7	6
3	3	3	4
6	6	5	6
4	4	4	4
4	4	3	3
6	6	3	3
9	9	8	10
5	5	4	4
7	6	7	7
6	5	3	3
6	6	6	5
5	6	5	5
5	5	5	5
5	4	7	7
3	3	3	4
8	8	7	7
6	6	8	7
5	4	6	6
4	5	5	5
8	8	8	5
7	6	4	5
4	4	4	4
6	6	4	3
8	7	6	6
4	3	1	1
5	5	4	4
5	5	5	5
5	5	6	6
4	3	3	4
3	3	6	7
6	5	6	6

6	5	7	6
7	7	9	7
7	6	8	7
8	8	7	8
7	7	7	7
2	2	3	2
9	8	7	7
2	2	3	3
1	1	1	1
2	2	3	3
5	4	10	8
4	3	2	2
2	2	1	1
4	5	3	3
4	4	3	3
2	2	3	3
4	4	5	5
4	4	4	4
4	3	5	4
7	6	6	5
6	5	7	7
7	7	7	7
7	7	8	9
7	7	9	8
9	9	10	10
8	8	9	10
2	2	3	2
3	3	3	2

Table A.63 Scale of Surface Pressure

Scale Hamilton		Scale London	
One-Hour	Three-Hour	One-Hour	Three-Hour
6	6	4	3
3	3	3	3
8	8	8	8
3	3	4	4
5	5	5	5
10	10	9	10
1	1	1	1
4	5	4	4
3	4	4	4
6	6	6	6
6	6	6	6
6	6	6	6
5	5	5	5
2	3	3	3
6	6	6	6
4	4	4	4
4	4	4	4
7	7	7	7
1	1	2	2
6	6	5	6
3	3	4	4
1	1	1	1
9	9	9	9
5	5	5	5
10	10	10	10
6	6	6	7
6	7	6	6
5	6	5	6
4	4	4	4
3	3	3	3
3	4	3	3
5	5	5	5
3	3	4	4
3	3	3	4
5	5	5	5
5	5	6	6
4	4	5	5
5	5	5	5

4	4	4	4
5	5	5	5
7	7	7	7
9	9	9	9
8	8	8	8
6	6	6	6
7	7	7	7
9	9	9	9
6	7	7	7
7	7	7	7
4	4	4	4
3	3	3	3
6	6	6	7
4	4	5	5
2	2	2	2
6	6	6	6
4	4	4	4
4	4	4	5
NA	NA	6	6
5	5	5	5
3	3	4	4
5	5	5	5
5	6	5	5
9	9	9	9
7	7	7	7
6	7	6	7
9	10	9	10
8	8	7	8

Table A.64 Scale of Weather Event/Description

Scale Hamilton	Scale London
5	3
1	1
3	4
1	3
2	1
4	4
2	2
3	2
1	1
2	2
1	1
1	2
2	1
3	2
1	2
2	2
2	2
2	2
2	3
1	1
2	2
2	1
3	1
1	1
1	2
2	1
3	4
2	2
2	1
3	2
2	2
2	1
2	2
3	3
3	4
1	1
2	2
3	2

3	3
2	2
1	1
2	1
1	2
2	2
2	2
1	2
2	2
2	3
3	5
3	3
2	2
2	2
2	3
2	2
3	2
2	2
NA	NA
3	3
3	3
1	1
4	4
3	3
2	5
1	6
2	2
3	2

Table A.65 The Scale of 10-Layer Absolute Residuals in dXCO₂

dXCO ₂ Residual (ppm)	Scale of Absolute Residual	Scale of Output
6.02	5	2
-2.16	2	1
6.79	6	9
0.11	1	5
-3.83	4	1
-0.33	1	2
-7.90	7	2
-1.23	1	4
-3.16	3	8
6.97	6	7
-8.10	7	9
3.37	3	5
7.55	7	10
-5.69	5	9
4.73	4	8
-5.76	5	9
5.75	5	7
0.74	1	4
-4.87	4	5
1.62	2	1
-1.40	2	1
-3.40	3	2
3.64	3	2
-5.82	5	5
-1.62	2	1
4.53	4	1
-6.73	6	1
8.84	8	2
-3.65	3	1
8.07	7	1
-3.78	4	1
8.11	7	2
-11.80	10	4
-1.45	2	8
0.49	1	5
4.25	4	6
-2.79	3	8
0.70	1	3

3.44	3	2
-4.90	4	1
1.97	2	1
11.14	10	3
2.27	2	1
1.17	1	1
-2.50	2	1
-2.12	2	1
1.31	2	1
-0.07	1	1
-4.25	4	1
-0.56	1	1
2.87	3	1
-2.32	2	4
-0.07	1	1
-0.52	1	3
2.51	2	3
1.21	1	3
8.09	7	3
2.52	3	1
4.43	4	1
5.53	5	1
-3.46	3	2
-7.78	7	3
-12.32	10	3
0.26	1	1
-1.98	2	1
-2.75	3	1

Table A.66 Two Residual Groups and Relevant Statistics

	Residual Scale	Plus (1) / Minus (-1)	Output Scale	XCO ₂ Uncert. Scale	Wind Speed Scale	Wind Direction Deviation Scale	Temperature Scale	Humidity Scale	Pressure Scale	Weather Event Scale
	1	1	5	5	4	4	2	8	3	1
	1	1	1	5	3	5	1	8	6	1
	1	1	5	2	3	2	9	5	5	3
	1	1	3	2	3	2	9	6	5	3
	1	1	4	2	3	1	8	6	7	2
	1	1	1	2	3	1	6	2	6	2
	1	1	3	1	3	3	10	4	4	2
	1	-1	1	1	3	4	6	2	7	2
	1	-1	1	2	4	1	10	4	2	2
	1	-1	2	2	2	3	5	3	10	4
	1	-1	3	1	2	3	10	2	6	2
	1	-1	1	2	4	1	6	4	3	3
	1	-1	4	5	2	3	7	6	4	3
	2	1	1	1	3	3	6	1	6	2
	2	1	1	3	2	8	6	5	6	1
	2	1	1	3	3	8	7	7	7	1
	2	1	1	2	3	7	2	7	8	1
	2	1	3	2	4	7	10	4	4	3
	2	-1	1	3	5	7	6	5	3	2
	2	-1	8	1	2	9	10	5	3	3
	2	-1	1	4	3	8	1	5	10	1
	2	-1	1	1	3	0	5	2	9	2
	2	-1	1	2	1	6	3	2	9	1
	2	-1	1	4	5	8	6	6	3	1
	2	-1	4	1	4	7	10	4	4	2
	2	-1	1	2	4	1	7	9	7	2
	3	1	1	2	3	1	7	7	5	3
	3	1	1	2	3	5	9	2	6	2
	3	1	5	1	5	2	7	4	6	1
	3	1	2	2	3	7	8	6	4	3
	3	1	2	4	3	1	4	8	9	3
	3	-1	8	1	4	5	10	3	3	1
	3	-1	2	3	10	2	7	3	1	2
	3	-1	2	4	3	1	7	7	5	4
	3	-1	1	1	3	2	9	4	4	2
	3	-1	1	1	5	2	7	3	8	3
	3	-1	8	2	3	1	9	3	4	2
	4	1	6	2	3	3	10	4	5	1
	4	1	1	3	2	7	6	6	3	3
	4	1	1	4	2	3	2	4	6	2

Strong Fit

	4	1	8	3	3	8	9	5	6	1
	4	-1	1	2	3	10	9	8	3	2
	4	-1	1	4	3	3	4	5	5	2
	4	-1	1	2	3	9	8	5	4	3
	4	-1	5	10	8	3	9	5	1	2
	4	-1	1	3	2	4	8	7	5	2
	5	1	1	3	4	9	7	7	5	1
	5	1	7	2	4	3	9	6	4	2
	5	1	2	6	4	0	5	10	6	5
	5	-1	5	4	2	2	4	6	5	1
	5	-1	9	2	3	10	9	9	2	3
	5	-1	9	2	1	2	10	7	4	2
	6	1	9	4	3	4	1	7	8	3
	6	1	7	1	4	2	8	6	6	2
	6	-1	1	2	3	9	4	8	6	3
	7	1	10	1	3	3	10	6	5	2
	7	1	1	1	2	1	9	6	3	3
	7	1	3	2	1	2	9	4	NA	NA
	7	1	2	1	3	3	9	4	5	2
	7	-1	3	4	2	7	4	7	9	3
	7	-1	2	1	3	4	7	5	1	2
	7	-1	9	1	2	10	9	4	6	1
	8	1	2	1	3	2	10	7	5	2
	10	1	3	4	4	8	4	8	9	2
	10	-1	4	1	5	9	10	5	3	2
	10	-1	3	1	2	2	4	9	7	2

Weak Fit

Table A.67 Targeted Soundings in Hamilton

Column XCO ₂	3Layers	4Layers	5Layers	6Layers	7Layers	8Layers	9Layers	10Layers	11Layers
364.68	288.27	300.60	311.42	320.68	328.50	335.03	340.45	344.94	348.70
389.18	400.49	398.66	397.09	395.81	394.77	393.91	393.18	392.56	392.01
388.43	415.05	409.78	405.38	401.85	399.03	396.82	395.09	393.73	392.63
353.64	300.31	304.27	308.82	313.63	318.41	322.99	327.27	331.19	334.72
395.41	419.78	416.22	413.03	410.29	407.97	406.02	404.37	402.98	401.79
394.88	425.04	420.28	415.98	412.29	409.19	406.65	404.58	402.89	401.49
392.42	394.97	395.34	395.47	395.46	395.39	395.29	395.17	395.03	394.88
392.53	415.55	411.64	408.15	405.18	402.71	400.70	399.09	397.82	396.79
390.16	371.66	375.66	379.01	381.73	383.91	385.61	386.95	387.98	388.78
391.95	395.81	395.52	395.16	394.82	394.50	394.21	393.97	393.76	393.59
384.74	376.85	377.34	378.06	378.90	379.74	380.54	381.27	381.95	382.55
365.43	319.68	323.98	328.54	333.11	337.47	341.53	345.23	348.55	351.50
380.96	361.66	363.36	365.26	367.21	369.11	370.88	372.48	373.92	375.20
386.85	397.57	394.26	391.70	389.84	388.54	387.67	387.10	386.77	386.60
366.90	331.24	333.46	336.23	339.31	342.46	345.53	348.43	351.14	353.62
388.11	417.67	411.22	405.81	401.47	398.05	395.42	393.43	391.95	390.86
390.39	400.32	398.66	397.14	395.82	394.75	393.94	393.37	392.99	392.80
393.59	413.74	410.72	407.95	405.52	403.45	401.70	400.22	398.98	397.95
389.84	403.44	400.97	398.87	397.19	395.83	394.74	393.85	393.12	392.49
354.12	291.00	296.83	303.00	309.16	315.06	320.51	325.48	329.94	333.88
399.51	422.63	419.99	417.50	415.23	413.20	411.40	409.79	408.36	407.08
396.76	425.52	420.94	416.90	413.49	410.64	408.29	406.34	404.73	403.38
398.30	418.55	416.07	413.74	411.66	409.84	408.27	406.89	405.69	404.63
399.16	412.45	411.42	410.34	409.29	408.32	407.40	406.54	405.73	404.98
379.44	346.96	351.44	355.67	359.55	363.02	366.03	368.62	370.81	372.65
396.30	415.53	412.93	410.52	408.39	406.56	405.02	403.72	402.63	401.69
396.96	396.90	398.19	399.07	399.60	399.88	399.97	399.95	399.84	399.69
393.79	417.82	413.55	409.83	406.71	404.13	402.06	400.41	399.11	398.08
389.13	392.86	391.69	390.77	390.10	389.63	389.33	389.16	389.10	389.09
390.35	404.47	401.33	398.79	396.81	395.27	394.11	393.25	392.63	392.16
390.85	391.03	390.64	390.38	390.27	390.26	390.32	390.40	390.50	390.62
386.28	376.95	377.36	378.03	378.88	379.81	380.75	381.66	382.51	383.29
385.50	366.59	368.89	371.13	373.24	375.19	376.93	378.45	379.79	380.96
389.83	417.05	410.73	405.53	401.45	398.33	396.00	394.30	393.09	392.22
389.37	395.35	393.66	392.27	391.20	390.43	389.90	389.56	389.37	389.29
394.24	406.85	405.23	403.66	402.24	401.01	399.93	398.99	398.16	397.45
360.32	315.88	319.01	322.70	326.65	330.60	334.38	337.91	341.14	344.04

393.70	419.32	414.40	410.26	406.93	404.27	402.16	400.49	399.17	398.09
397.26	415.92	413.05	410.50	408.34	406.55	405.07	403.84	402.82	401.95
395.53	419.38	415.03	411.30	408.24	405.77	403.81	402.24	401.01	400.00
397.10	409.91	408.29	406.79	405.46	404.33	403.37	402.54	401.84	401.22
397.32	431.80	425.91	420.72	416.34	412.72	409.80	407.45	405.57	404.04
396.93	424.05	419.34	415.22	411.77	408.93	406.65	404.82	403.37	402.18
392.47	400.31	398.94	397.77	396.81	396.04	395.46	395.02	394.69	394.43
397.39	420.10	416.35	413.04	410.25	407.92	406.02	404.48	403.24	402.22
396.16	381.87	385.70	388.80	391.21	393.06	394.43	395.44	396.17	396.69
391.00	400.68	398.32	396.39	394.90	393.76	392.94	392.35	391.97	391.72
380.66	353.63	356.33	359.17	361.98	364.65	367.09	369.28	371.24	372.97
384.77	369.59	370.52	371.73	373.13	374.59	376.02	377.38	378.63	379.77
387.91	373.68	375.23	376.77	378.26	379.68	380.99	382.19	383.26	384.24
393.51	390.96	391.21	391.49	391.79	392.12	392.44	392.74	393.03	393.30
388.76	395.48	392.95	391.01	389.64	388.82	388.51	388.54	388.74	388.92
395.08	402.52	401.46	400.43	399.52	398.74	398.09	397.56	397.13	396.80
396.05	416.21	412.89	409.89	407.31	405.14	403.36	401.89	400.70	399.74
393.84	422.18	416.80	412.18	408.40	405.34	402.89	400.92	399.34	398.06

Table A.68 XCO₂ Uncertainty of the Column and 10 levels

Column	Lv1	Lv2	Lv3	Lv4	Lv5	Lv6	Lv7	Lv8	Lv9	Lv10
0.99	4.57	5.06	5.63	6.03	6.80	7.35	9.08	11.07	15.89	24.33
1.42	5.73	6.24	6.73	6.93	7.30	7.61	9.63	12.61	19.59	28.65
1.36	5.65	6.15	6.63	6.84	7.23	7.58	9.67	12.70	19.73	28.76
2.26	6.03	6.60	7.21	7.52	8.00	8.36	10.23	13.02	19.73	28.67
1.69	5.65	6.17	6.70	6.97	7.44	7.82	9.83	12.72	19.47	28.40
0.78	4.14	4.63	5.27	5.77	6.69	7.27	8.82	10.37	14.45	22.74
0.69	4.07	4.56	5.20	5.70	6.64	7.24	8.81	10.36	14.44	22.73
0.67	4.14	4.63	5.25	5.73	6.64	7.23	8.84	10.48	14.77	23.08
0.72	4.38	4.87	5.45	5.88	6.71	7.26	8.94	10.82	15.61	24.03
0.75	4.43	4.91	5.48	5.90	6.71	7.26	8.95	10.86	15.74	24.19
0.69	4.35	4.83	5.42	5.85	6.68	7.24	8.92	10.80	15.57	23.98
0.73	4.44	4.91	5.49	5.90	6.70	7.26	9.04	11.08	16.10	24.53
0.83	4.60	5.08	5.63	6.01	6.76	7.30	9.13	11.30	16.62	25.13
0.82	4.71	5.19	5.73	6.09	6.78	7.29	9.11	11.33	16.76	25.33
1.37	5.50	6.00	6.51	6.77	7.24	7.62	9.63	12.48	19.15	28.07
0.99	4.85	5.34	5.89	6.24	6.90	7.36	9.11	11.30	16.69	25.28
1.08	5.05	5.54	6.07	6.39	6.98	7.41	9.21	11.58	17.37	26.05
1.14	5.04	5.54	6.09	6.42	7.02	7.43	9.17	11.41	16.93	25.59
1.46	5.71	6.22	6.71	6.92	7.30	7.64	9.69	12.71	19.75	28.80
1.08	4.61	5.09	5.67	6.07	6.85	7.42	9.25	11.40	16.58	25.02
2.02	5.83	6.36	6.90	7.17	7.65	8.11	10.26	13.34	20.36	29.31
1.79	5.83	6.37	6.91	7.16	7.58	7.89	9.81	12.69	19.56	28.57
1.85	5.8	6.32	6.81	7.04	7.49	7.96	10.28	13.58	20.90	29.92
1.32	5.32	5.83	6.37	6.66	7.18	7.54	9.33	11.82	17.96	26.77
1.08	5.03	5.52	6.06	6.38	6.98	7.40	9.22	11.61	17.48	26.18
0.83	4.36	4.85	5.46	5.91	6.75	7.29	8.88	10.60	15.09	23.47
0.69	4.13	4.62	5.24	5.73	6.65	7.24	8.85	10.48	14.74	23.05
0.64	4.03	4.52	5.15	5.66	6.60	7.22	8.81	10.37	14.44	22.70
0.66	3.95	4.44	5.09	5.62	6.60	7.23	8.79	10.27	14.14	22.37
0.63	3.99	4.48	5.12	5.64	6.60	7.22	8.79	10.30	14.28	22.53
0.65	3.98	4.47	5.10	5.62	6.59	7.22	8.80	10.31	14.28	22.53
0.85	4.54	5.03	5.60	6.01	6.78	7.30	9.00	10.98	15.96	24.43
0.77	4.43	4.91	5.50	5.93	6.73	7.27	8.93	10.80	15.59	24.01
0.87	4.71	5.19	5.75	6.12	6.83	7.31	9.06	11.19	16.50	25.05
1.09	5.09	5.59	6.12	6.43	7.01	7.42	9.24	11.67	17.61	26.34
1.14	5.02	5.52	6.07	6.41	7.02	7.43	9.16	11.38	16.87	25.52
1.46	5.13	5.64	6.20	6.55	7.19	7.65	9.48	11.88	17.68	26.32
1.52	5.71	6.22	6.70	6.91	7.32	7.69	9.84	12.95	20.08	29.12

0.91	4.50	4.99	5.59	6.03	6.82	7.33	8.93	10.75	15.45	23.88
0.81	4.39	4.88	5.48	5.92	6.74	7.28	8.90	10.70	15.30	23.70
0.87	4.36	4.85	5.47	5.93	6.78	7.31	8.87	10.55	14.98	23.36
0.69	4.01	4.50	5.14	5.66	6.62	7.24	8.79	10.30	14.24	22.48
0.71	4.05	4.54	5.18	5.69	6.63	7.24	8.80	10.31	14.28	22.54
0.79	4.32	4.81	5.41	5.87	6.71	7.27	8.89	10.63	15.09	23.44
0.67	4.11	4.59	5.22	5.71	6.63	7.23	8.83	10.45	14.64	22.93
0.70	4.15	4.64	5.27	5.76	6.67	7.25	8.83	10.44	14.72	23.05
0.67	4.08	4.56	5.19	5.69	6.62	7.23	8.82	10.41	14.54	22.81
0.68	4.13	4.61	5.23	5.72	6.64	7.24	8.86	10.53	14.83	23.14
0.89	4.62	5.10	5.67	6.06	6.80	7.32	9.09	11.20	16.45	24.96
0.80	4.65	5.13	5.67	6.03	6.75	7.28	9.14	11.37	16.77	25.29
0.88	4.68	5.16	5.73	6.11	6.82	7.31	9.02	11.09	16.29	24.83
1.00	4.91	5.40	5.94	6.28	6.91	7.37	9.17	11.47	17.13	25.76
0.94	4.67	5.16	5.73	6.12	6.85	7.34	9.02	11.03	16.11	24.62
1.07	5.02	5.52	6.05	6.38	6.98	7.40	9.20	11.53	17.27	25.95
1.54	5.57	6.09	6.61	6.88	7.34	7.69	9.58	12.28	18.73	27.62

Table A.69 Scales of Weather Factors (Hamilton)

Temperature	Humidity	Wind	Pressure	Weather Event/Description
2	9	4	5	4
2	7	3	8	3
2	8	4	4	1
4	8	3	5	2
4	6	3	5	2
6	4	2	10	4
7	5	3	2	2
10	3	4	4	1
9	7	4	6	2
9	5	2	6	1
7	4	5	6	1
9	6	1	5	2
10	7	1	4	2
8	6	3	7	2
8	8	4	1	2
6	5	2	6	1
7	3	10	1	2
5	7	2	5	1
2	8	3	9	6
2	5	3	6	3
5	3	10	2	1
1	5	3	10	1
3	10	8	10	4
3	8	3	9	2
2	5	2	6	2
4	9	3	7	3
10	7	3	6	2
9	4	3	5	2
9	6	2	4	3
9	4	3	5	2
10	5	2	4	3
9	6	3	6	3
8	6	3	5	3
8	7	2	5	2
7	7	3	7	1
4	9	4	9	2
1	6	6	7	2
3	8	7	5	2
6	3	3	6	2
7	9	4	7	2
3	2	5	9	1
6	1	3	7	2
6	2	3	7	2
6	4	4	3	3
9	2	3	7	2
10	4	4	5	2
10	4	4	2	2
9	3	6	4	2
8	6	3	4	2
8	3	2	7	2
8	7	3	5	3
6	6	2	4	3
8	7	4	6	1
7	7	3	6	4
5	10	5	6	6

Appendix B: Figures

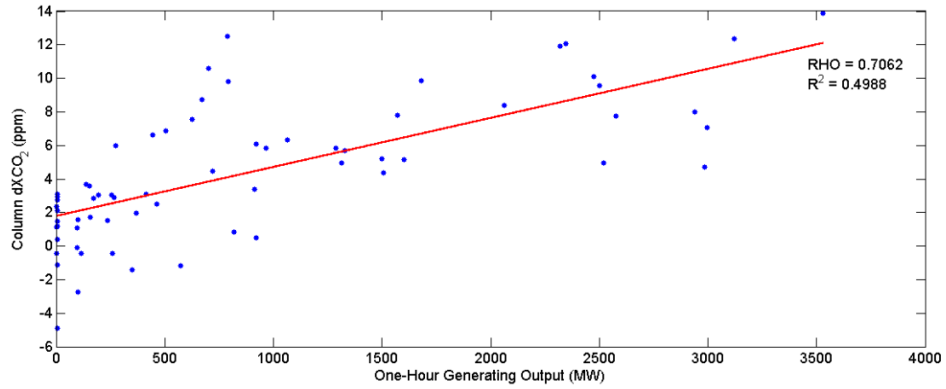


Figure B.1 Linear Regression for Column dXCO₂

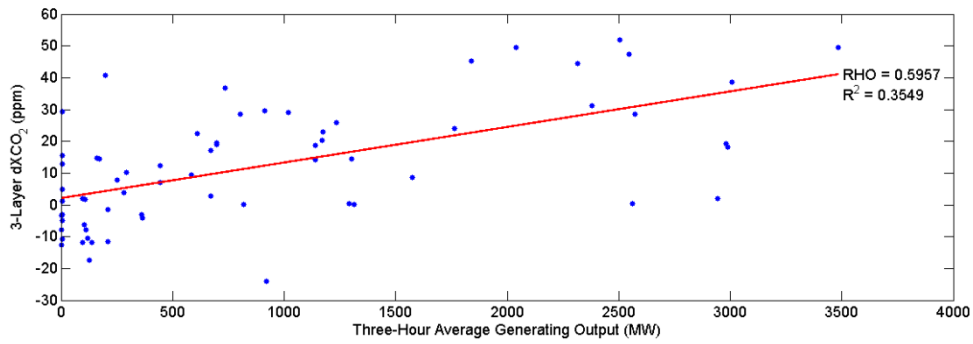


Figure B.2 Linear Regression for 3-Layer Partial Column dXCO₂

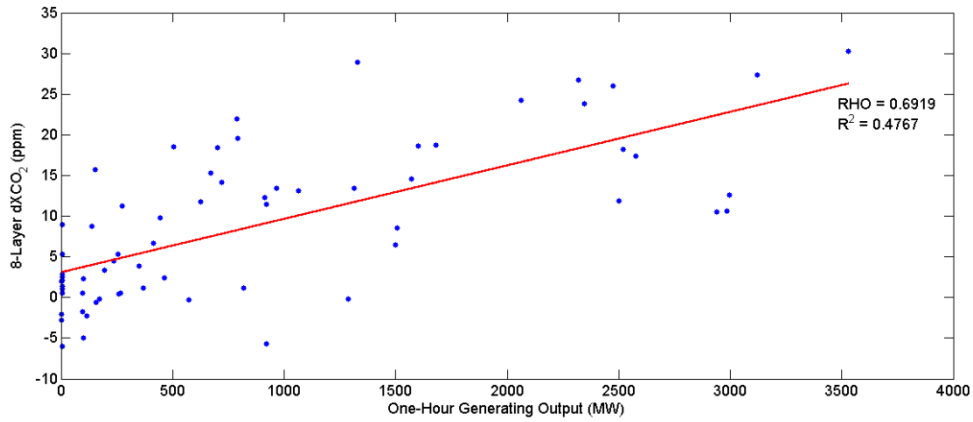


Figure B.3 Linear Regression for 8-Layer Partial Column dXCO₂

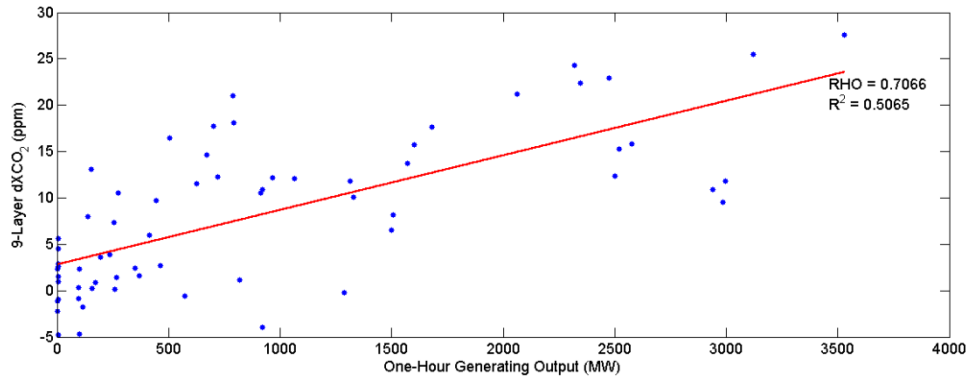


Figure B.4 Linear Regression for 9-Layer Partial Column dXCO₂

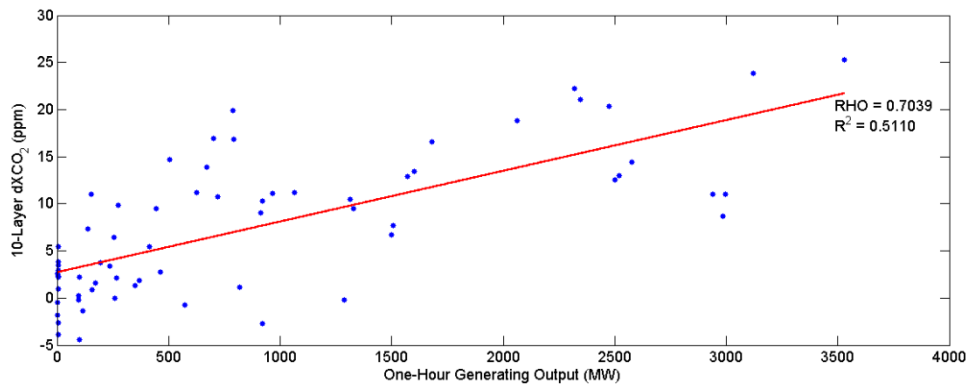


Figure B.5 Linear Regression for 10-Layer Partial Column dXCO₂

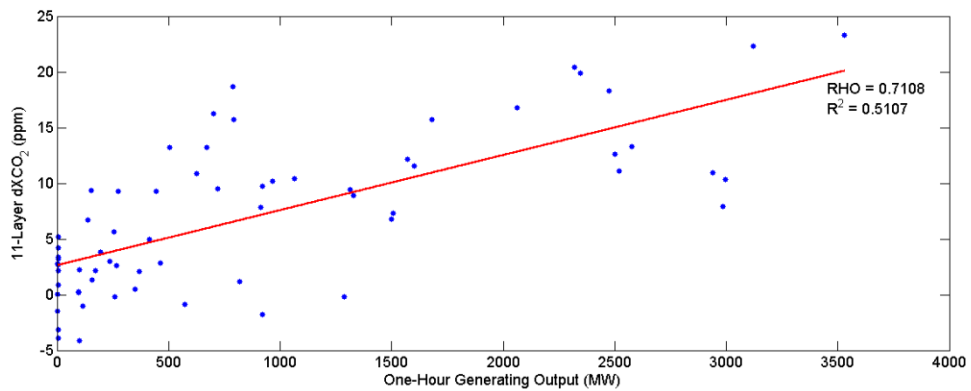


Figure B.6 Linear Regression for 11-Layer Partial Column dXCO₂

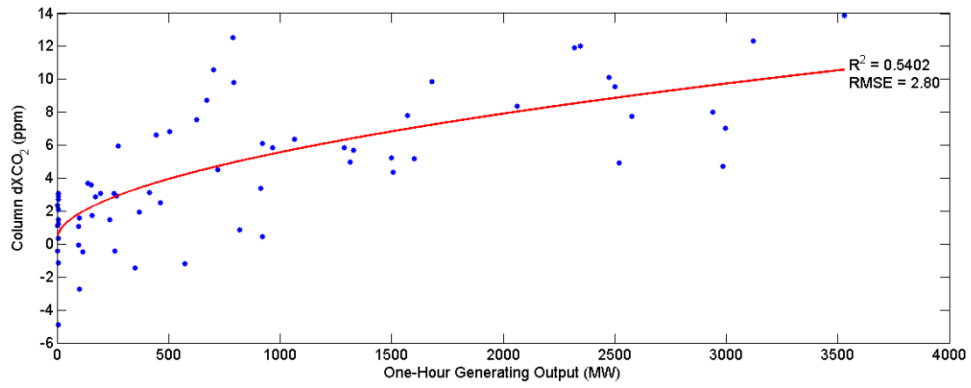


Figure B.7 Power Regression for Column dXCO₂

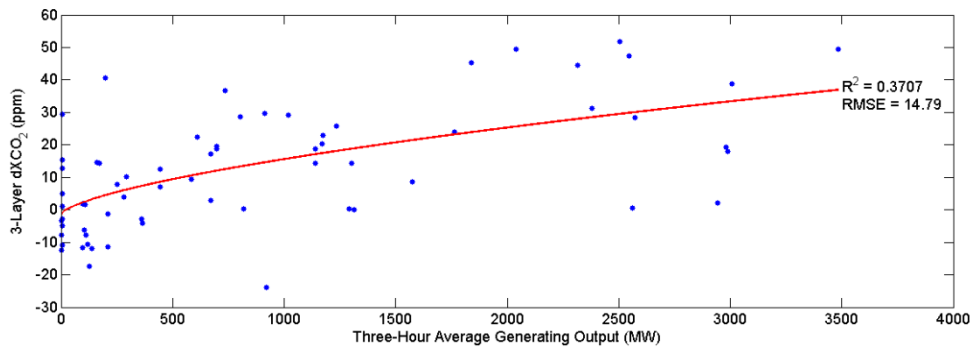


Figure B.8 Power Regression for 3-Layer Partial Column dXCO₂

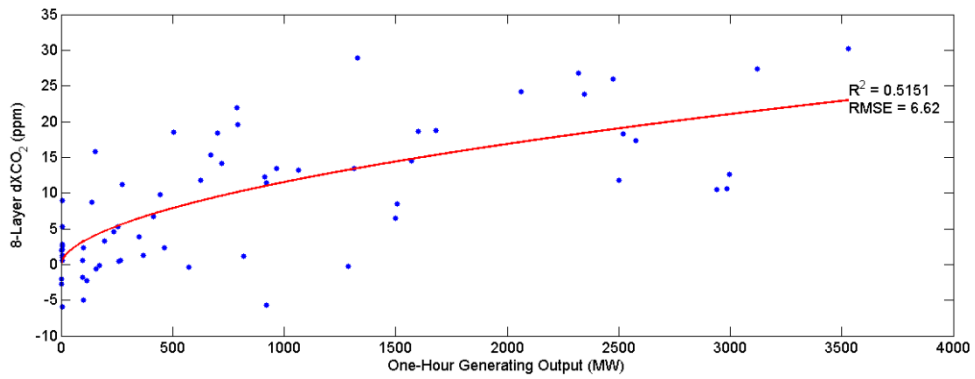


Figure B.9 Power Regression for 8-Layer Partial Column dXCO₂

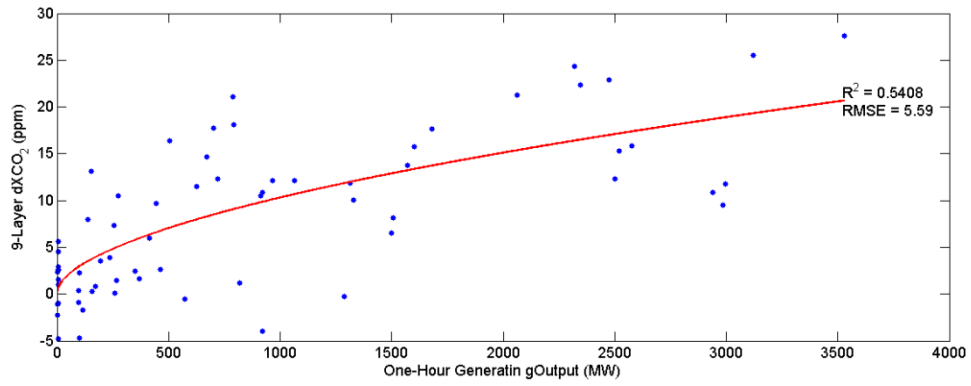


Figure B.10 Power Regression for 9-Layer Partial Column dXCO₂

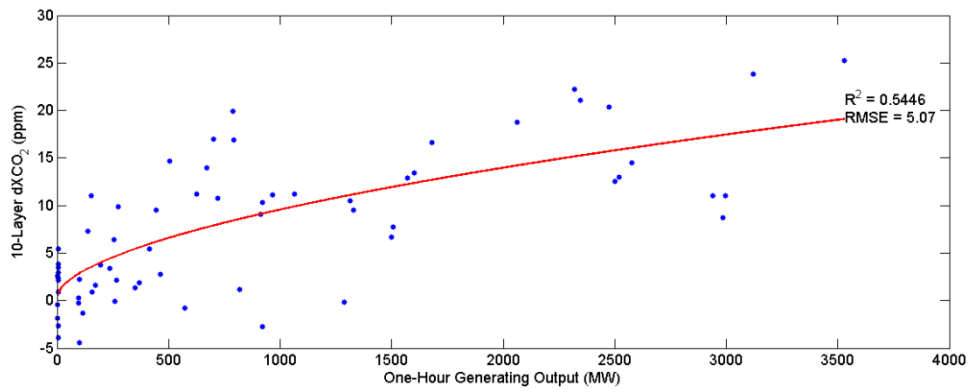


Figure B.11 Power Regression for 10-Layer Partial Column dXCO₂

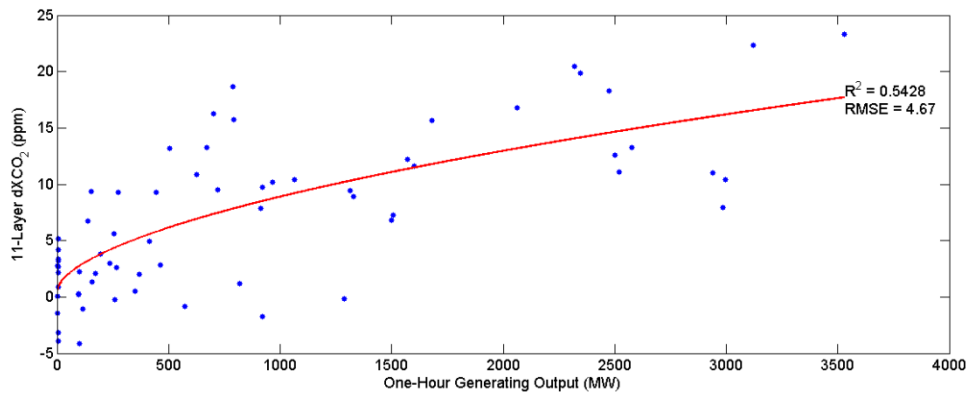


Figure B.12 Power Regression for 11-Layer Partial Column dXCO₂

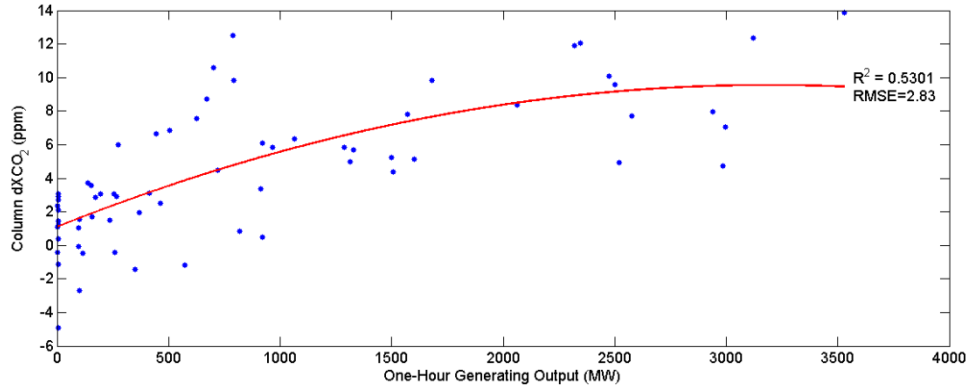


Figure B.13 2-Degree Polynomial Regression for Column dXCO₂

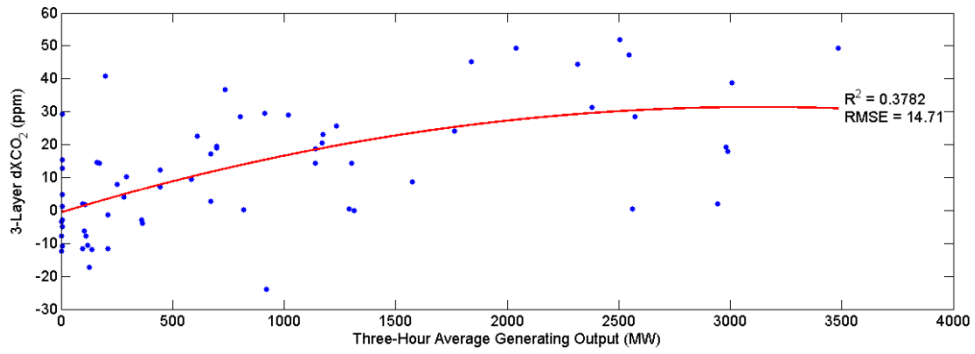


Figure B.14 2-Degree Polynomial Regression for 3-Layer Partial Column dXCO₂

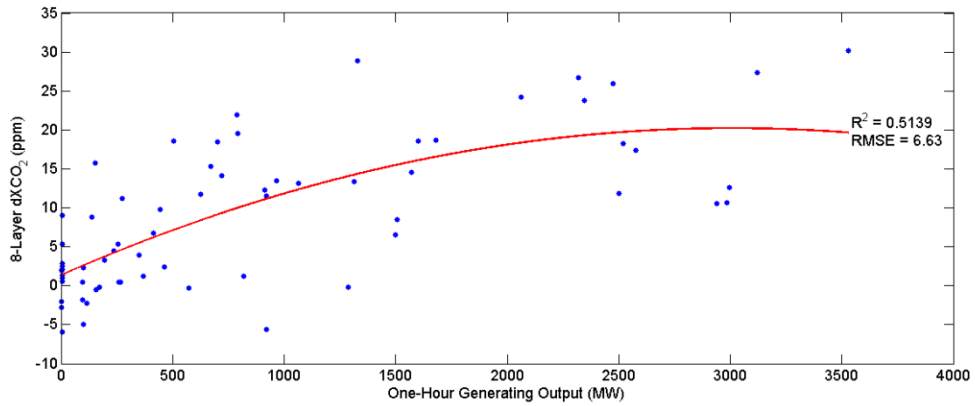


Figure B.15 2-Degree Polynomial Regression for 8-Layer Partial Column dXCO₂

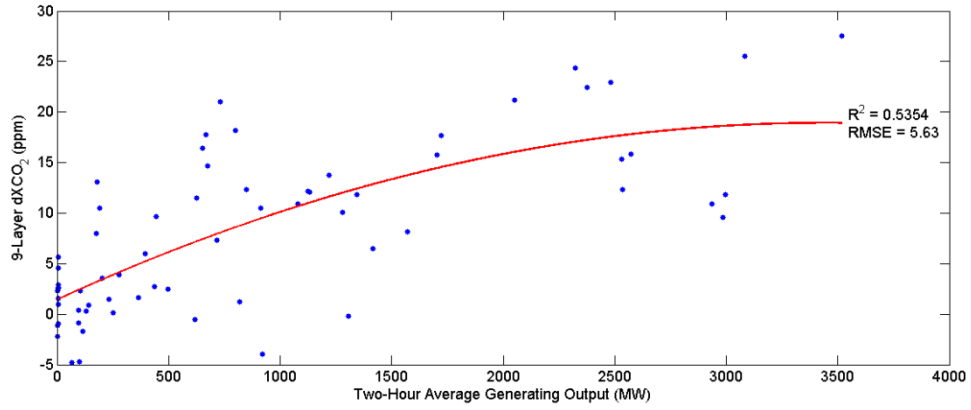


Figure B.16 2-Degree Polynomial Regression for 9-Layer Partial Column dXCO₂

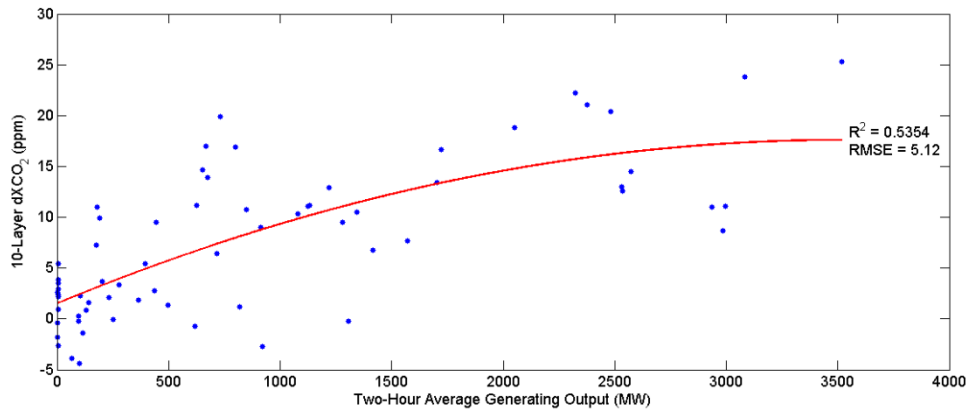


Figure B.17 2-Degree Polynomial Regression for 10-Layer Partial Column dXCO₂

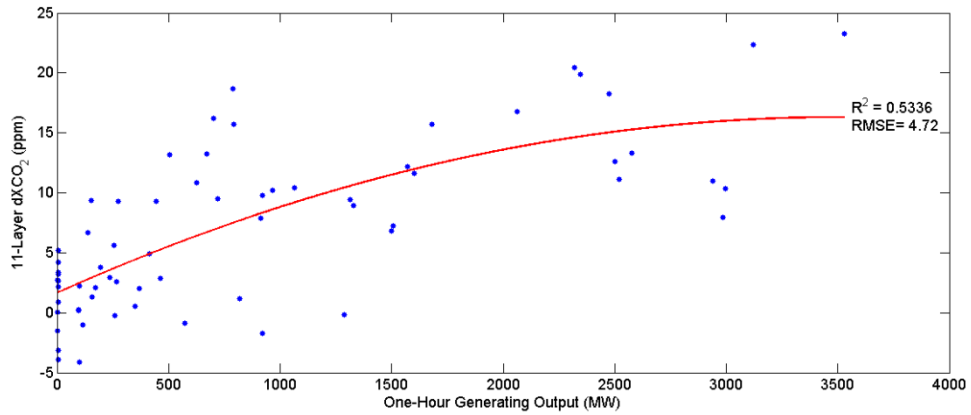


Figure B.18 2-Degree Polynomial Regression for 11-Layer Partial Column dXCO₂

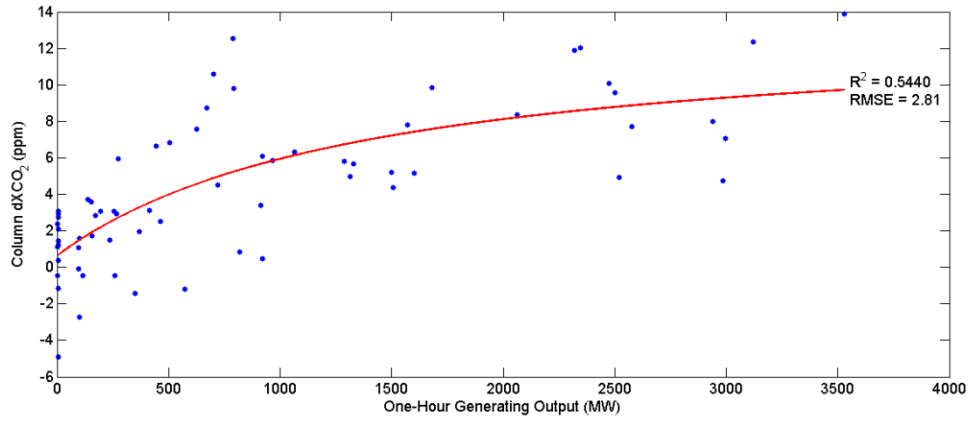


Figure B.19 Rational Regression for Column $dXCO_2$

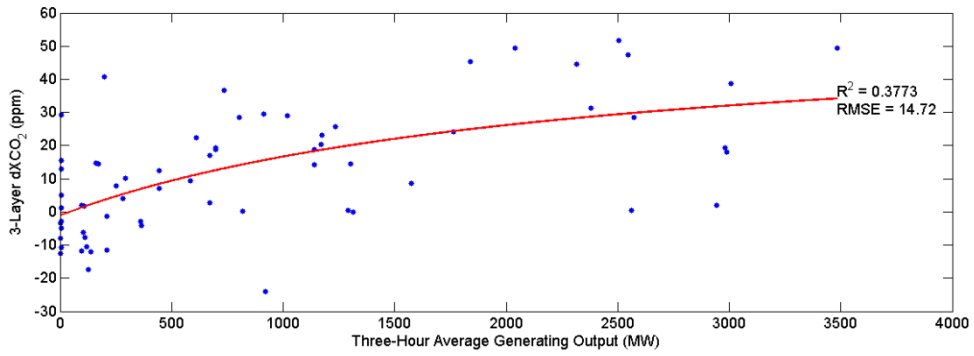


Figure B.20 Rational Regression for 3-Layer Partial Column $dXCO_2$

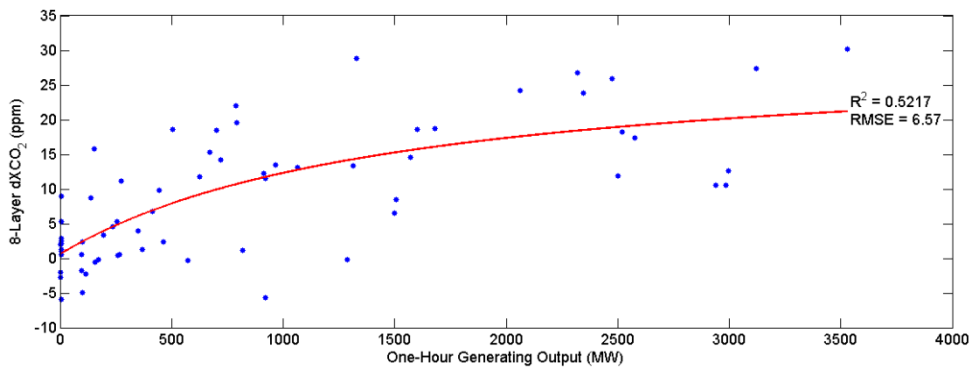


Figure B.21 Rational Regression for 8-Layer Partial Column $dXCO_2$

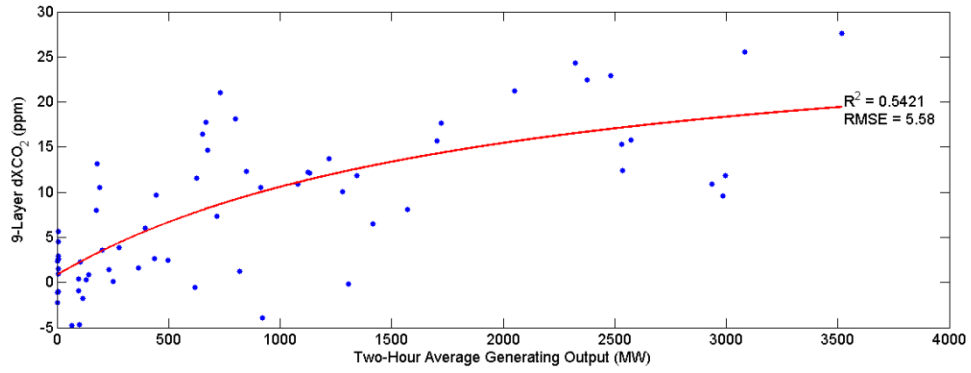


Figure B.22 Rational Regression for 9-Layer Partial Column dXCO₂

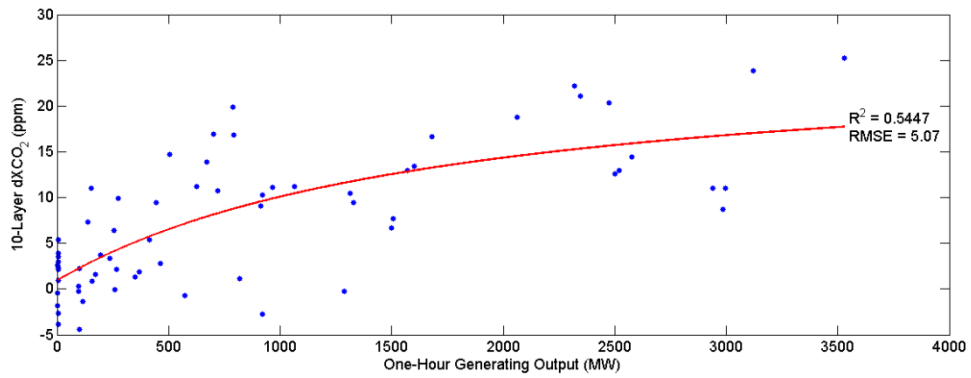


Figure B.23 Rational Regression for 10-Layer Partial Column dXCO₂

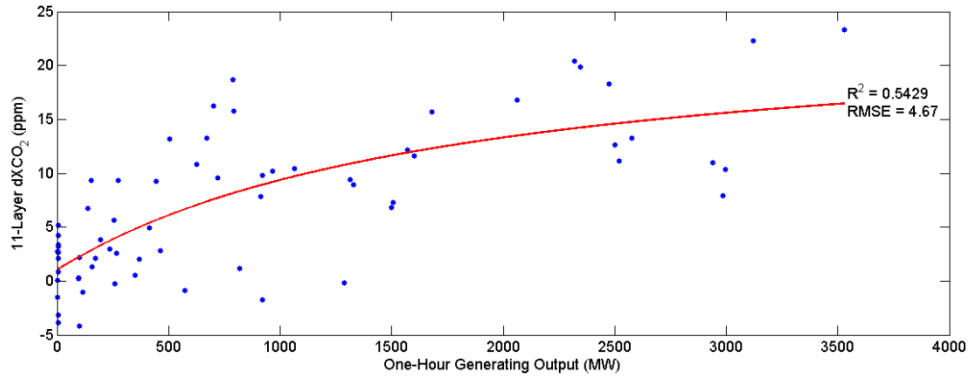


Figure B.24 Rational Regression for 11-Layer Partial Column dXCO₂

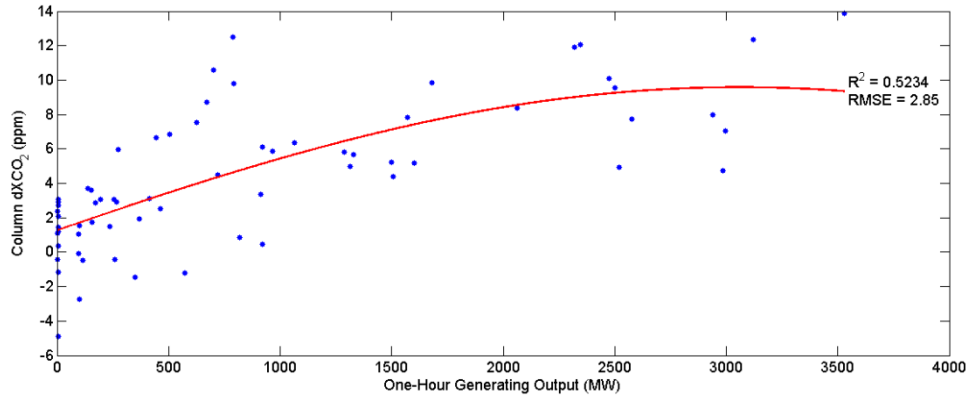


Figure B.25 Sum of Sine Regression for Column dXCO₂

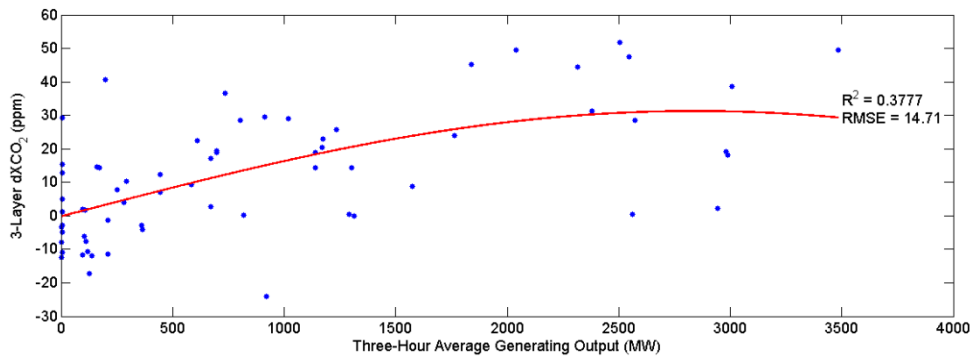


Figure B.26 Sum of Sine Regression for 3-Layer Partial Column dXCO₂

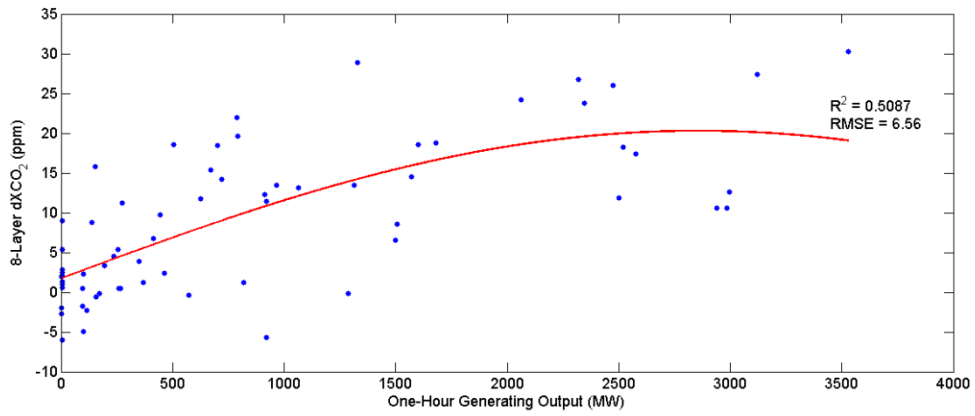


Figure B.27 Sum of Sine Regression for 8-Layer Partial Column dXCO₂

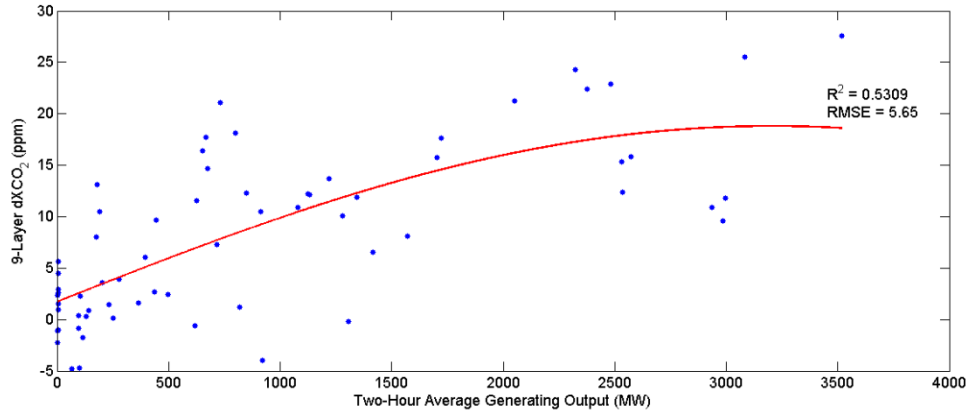


Figure B.28 Sum of Sine Regression for 9-Layer Partial Column dXCO₂

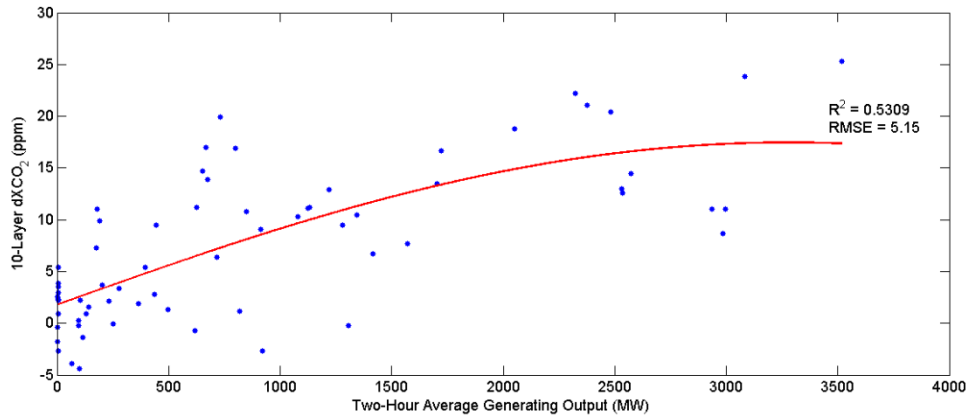


Figure B.29 Sum of Sine Regression for 10-Layer Partial Column dXCO₂

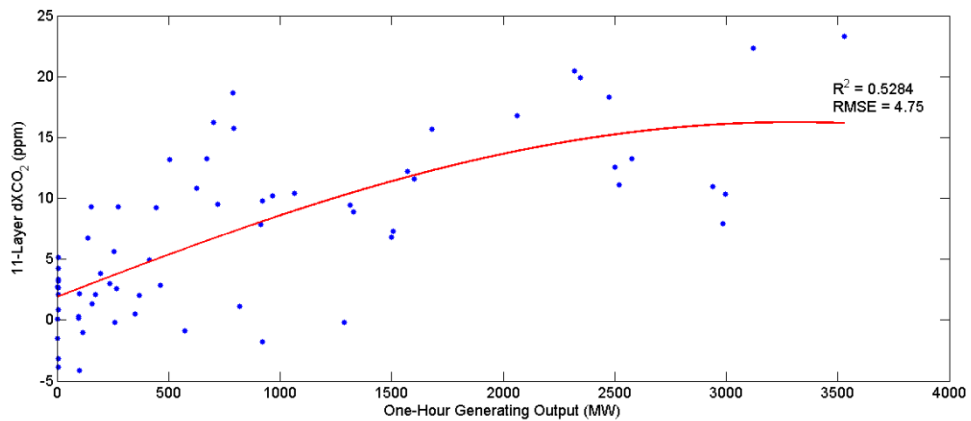


Figure B.30 Sum of Sine Regression for 11-Layer Partial Column dXCO₂

Bibliography

- Ackerman, S. A. (1997) Remote sensing aerosols using satellite infrared observations. *Journal of Geophysical Research: Atmospheres* (1984–2012), 102, 17069-17079.
- Akimoto, K., T. Tomoda, Y. Fujii & K. Yamaji (2004) Assessment of global warming mitigation options with integrated assessment model DNE21. *Energy Economics*, 26, 635-653.
- Aldy, J. E. & W. A. Pizer. 2011. The competitiveness impacts of climate change mitigation policies. National Bureau of Economic Research.
- Andrew, N. R., S. J. Hill, M. Binns, M. H. Bahar, E. V. Ridley, M.-P. Jung, C. Fyfe, M. Yates & M. Khusro (2013) Assessing insect responses to climate change: What are we testing for? Where should we be heading? *PeerJ*, 1, e11.
- Appel, B., Y. Tokiwa, J. Hsu, E. Kothny & E. Hahn (1985) Visibility as related to atmospheric aerosol constituents. *Atmospheric Environment* (1967), 19, 1525-1534.
- Bösch, H., G. Toon, B. Sen, R. Washenfelder, P. Wennberg, M. Buchwitz, R. De Beek, J. Burrows, D. Crisp & M. Christi (2006) Space - based near - infrared CO₂ measurements: Testing the Orbiting Carbon Observatory retrieval algorithm and validation concept using SCIAMACHY observations over Park Falls, Wisconsin. *Journal of Geophysical Research: Atmospheres* (1984–2012), 111.
- Bäumer, D., B. Vogel, S. Versick, R. Rinke, O. Möhler & M. Schnaiter (2008) Relationship of visibility, aerosol optical thickness and aerosol size distribution in an ageing air mass over South-West Germany. *Atmospheric Environment*, 42, 989-998.
- Bahn, O., M. Marcy, K. Vaillancourt & J.-P. Waaub (2013) Electrification of the Canadian road transportation sector: A 2050 outlook with TIMES-Canada. *Energy Policy*, 62, 593-606.
- Baker, D., R. Law, K. Gurney, P. Rayner, P. Peylin, A. Denning, P. Bousquet, L. Bruhwiler, Y. H. Chen & P. Ciais (2006a) TransCom 3 inversion intercomparison: Impact of transport model errors on the interannual variability of regional CO₂ fluxes, 1988–2003. *Global Biogeochemical Cycles*, 20.
- Baker, D. F., S. C. Doney & D. S. Schimel (2006b) Variational data assimilation for atmospheric CO₂. *Tellus B*, 58, 359-365.
- Barkley, M. P., P. S. Monks & R. J. Engelen (2006) Comparison of SCIAMACHY and AIRS CO₂ measurements over North America during the summer and autumn of 2003. *Geophysical Research Letters*, 33.
- Basu, S., S. Guerlet, A. Butz, S. Houweling, O. Hasekamp, I. Aben, P. Krummel, P. Steele, R. Langenfelds & M. Torn (2013) Global CO₂ fluxes estimated from GOSAT retrievals of total column CO₂. *Atmospheric Chemistry and Physics*, 13, 8695-8717.
- Basu, S., M. Krol, A. Butz, C. Clerbaux, Y. Sawa, T. Machida, H. Matsueda, C. Frankenberg, O. Hasekamp & I. Aben (2014a) The seasonal variation of the CO₂ flux over Tropical Asia estimated from GOSAT, CONTRAIL, and IASI. *Geophysical Research Letters*.
- Basu, S., M. Krol, A. Butz, C. Clerbaux, Y. Sawa, T. Machida, H. Matsueda, C. Frankenberg, O. Hasekamp & I. Aben (2014b) The seasonal variation of the CO₂ flux over Tropical Asia estimated from GOSAT, CONTRAIL, and IASI. *Geophysical Research Letters*, 41, 1809-1815.
- Beer, R. (2006) TES on the Aura mission: Scientific objectives, measurements, and analysis overview. *IEEE Transactions on Geoscience and remote sensing*, 44, 1102-1105.

- Belikov, D., S. Maksyutov, T. Miyasaka, T. Saeki, R. Zhuravlev & B. Kiryushov (2011) Mass-conserving tracer transport modelling on a reduced latitude-longitude grid with NIES-TM. *Geoscientific Model Development*, 4, 207-222.
- Bergamaschi, P., C. Frankenberg, J. F. Meirink, M. Krol, M. G. Villani, S. Houweling, F. Dentener, E. J. Dlugokencky, J. B. Miller & L. V. Gatti (2009) Inverse modeling of global and regional CH₄ emissions using SCIAMACHY satellite retrievals. *Journal of Geophysical Research: Atmospheres (1984–2012)*, 114.
- Berrang-Ford, L., J. D. Ford & J. Paterson (2011) Are we adapting to climate change? *Global environmental change*, 21, 25-33.
- Bhutiyani, M., V. Kale & N. Pawar (2010) Climate change and the precipitation variations in the northwestern Himalaya: 1866–2006. *International Journal of Climatology*, 30, 535-548.
- Blyth, W. & N. Lefevre-Marton (2005) Energy Security and Climate Change Policy Interactions—An Assessment Framework. *Oil, Gas & Energy Law Journal (OGEL)*, 3.
- Boesch, H., D. Baker, B. Connor, D. Crisp & C. Miller (2011) Global characterization of CO₂ column retrievals from shortwave-infrared satellite observations of the Orbiting Carbon Observatory-2 mission. *Remote Sensing*, 3, 270-304.
- Bonnor, W. (1956) Boyle's Law and gravitational instability. *Monthly Notices of the Royal Astronomical Society*, 116, 351.
- Bovensmann, H., M. Buchwitz, J. Burrows, M. Reuter, T. Krings, K. Gerilowski, O. Schneising, J. Heymann, A. Tretner & J. Erzinger (2010) A remote sensing technique for global monitoring of power plant CO₂ emissions from space and related applications. *Atmospheric Measurement Techniques*, 3, 781-811.
- Bovensmann, H., J. Burrows, M. Buchwitz, J. Frerick, S. Nož, V. Rozanov, K. Chance & A. Goede (1999) SCIAMACHY: Mission objectives and measurement modes. *Journal of the Atmospheric Sciences*, 56, 127-150.
- Bramstedt, K. (2008) Calculation of SCIAMACHY m-factors. *Tech. Note IFE-SCIA-TN-2007-01-CalcmFactor*.
- Bramstedt, K., S. Nož, H. Bovensmann, J. P. Burrows, C. Lerot, L. Tilstra, G. Lichtenberg, A. Dehn & T. Fehr. 2009. SCIAMACHY monitoring factors: Observation and end-to-end correction of instrument performance degradation. In *Proceedings of the 2009 Atmospheric Science Conference*.
- Bril, A., S. Oshchepkov, T. Yokota & G. Inoue (2007) Parameterization of aerosol and cirrus cloud effects on reflected sunlight spectra measured from space: application of the equivalence theorem. *Applied optics*, 46, 2460-2470.
- Bruhwieler, L., A. Michalak, W. Peters, D. Baker & P. Tans (2005) An improved Kalman Smoother for atmospheric inversions. *Atmospheric Chemistry and Physics*, 5, 2691-2702.
- Buchwitz, M., R. d. Beek, K. Bramstedt, S. Nož, H. Bovensmann & J. Burrows (2004) Global carbon monoxide as retrieved from SCIAMACHY by WFM-DOAS. *Atmospheric Chemistry and Physics Discussions*, 4, 2805-2837.
- Buchwitz, M., R. d. Beek, J. Burrows, H. Bovensmann, T. Warneke, J. Notholt, J. Meirink, A. Goede, P. Bergamaschi & S. Körner (2005) Atmospheric methane and carbon dioxide from SCIAMACHY satellite data: initial comparison with chemistry and transport models. *Atmospheric Chemistry and Physics*, 5, 941-962.
- Buchwitz, M., H. Bovensmann, M. Reuter, O. Schneising, T. Krings, K. Gerilowski & J. P. Burrows. 2010. Passive satellite remote sensing of carbon dioxide and methane: SCIAMACHY, GOSAT, CarbonSat. In *EGU General Assembly Conference Abstracts*, 6556.
- Buchwitz, M. & J. P. Burrows. 2003. Retrieval of CH₄, CO, and CO₂ total column amounts from SCIAMACHY near-infrared nadir spectra: Retrieval algorithm and first results. In *Proceedings of SPIE*, 375-388.

- Buchwitz, M., R. De Beek, S. Nož, J. Burrows, H. Bovensmann, O. Schneising, I. Khlystova, M. Bruns, H. Bremer & P. Bergamaschi (2006) Atmospheric carbon gases retrieved from SCIAMACHY by WFM-DOAS: version 0.5 CO and CH₄ and impact of calibration improvements on CO₂ retrieval. *Atmospheric Chemistry & Physics*, 6.
- Buchwitz, M., V. V. Rozanov & J. P. Burrows (2000) A near - infrared optimized DOAS method for the fast global retrieval of atmospheric CH₄, CO, CO₂, H₂O, and N₂O total column amounts from SCIAMACHY Envisat - 1 nadir radiances. *Journal of Geophysical Research: Atmospheres (1984 - 2012)*, 105, 15231-15245.
- Burdick, D. S., M. H. Stone & A. J. Stenner (2006) The combined gas law and a Rasch reading law. *Rasch Measurement Transactions*, 20, 1059-60.
- Butz, A., S. Guerlet, O. Hasekamp, D. Schepers, A. Galli, I. Aben, C. Frankenberg, J. M. Hartmann, H. Tran & A. Kuze (2011) Toward accurate CO₂ and CH₄ observations from GOSAT. *Geophysical Research Letters*, 38.
- Butz, A., O. Hasekamp, C. Frankenberg, J. Vidot & I. Aben (2010) CH₄ retrievals from space - based solar backscatter measurements: Performance evaluation against simulated aerosol and cirrus loaded scenes. *Journal of Geophysical Research: Atmospheres (1984-2012)*, 115.
- Butz, A., O. P. Hasekamp, C. Frankenberg & I. Aben (2009) Retrievals of atmospheric CO₂ from simulated space-borne measurements of backscattered near-infrared sunlight: accounting for aerosol effects. *Applied optics*, 48, 3322-3336.
- Byckling, K., H. Boesch, R. Parker, A. Webb, P. Palmer, L. Feng & A. Fraser. 2013. Constraining Carbon Surface Fluxes with GOSAT Column Observations of CO₂ and CH₄. In *EGU General Assembly Conference Abstracts*, 8615.
- Byrnes, J. S. 2009. *Unexploded Ordnance Detection and Mitigation*. Springer.
- Caldicott, H. 2013. *Nuclear power is not the answer*. The New Press.
- Chédin, A., A. Hollingsworth, N. A. Scott, S. Serrar, C. Crevoisier & R. Armante (2002a) Annual and seasonal variations of atmospheric CO₂, N₂O and CO concentrations retrieved from NOAA/TOVS satellite observations. *Geophysical Research Letters*, 29, 110-1-110-4.
- Chédin, A., R. Saunders, A. Hollingsworth, N. Scott, M. Matricardi, J. Etcheto, C. Clerbaux, R. Armante & C. Crevoisier (2003a) The feasibility of monitoring CO₂ from high - resolution infrared sounders. *Journal of Geophysical Research: Atmospheres (1984 - 2012)*, 108.
- Chédin, A., S. Serrar, R. Armante, N. A. Scott & A. Hollingsworth (2002b) Signatures of annual and seasonal variations of CO₂ and other greenhouse gases from comparisons between NOAA TOVS observations and radiation model simulations. *Journal of Climate*, 15, 95-116.
- Chédin, A., S. Serrar, A. Hollingsworth, R. Armante & N. Scott (2003b) Detecting annual and seasonal variations of CO₂, CO and N₂O from a multi-year collocated satellite-radiosonde data-set using the new Rapid Radiance Reconstruction (3R-N) model. *Journal of Quantitative Spectroscopy and Radiative Transfer*, 77, 285-299.
- Chédin, A., S. Serrar, N. Scott, C. Crevoisier & R. Armante (2003c) First global measurement of midtropospheric CO₂ from NOAA polar satellites: Tropical zone. *Journal of Geophysical Research: Atmospheres (1984-2012)*, 108.
- Chédin, A., S. Serrar, N. Scott, C. Pierangelo & P. Ciais (2005) Impact of tropical biomass burning emissions on the diurnal cycle of upper tropospheric CO₂ retrieved from NOAA 10 satellite observations. *Journal of Geophysical Research: Atmospheres (1984-2012)*, 110.

- Chahine, M., L. Chen, P. Dimotakis, X. Jiang, Q. Li, E. T. Olsen, T. Pagano, J. Randerson & Y. L. Yung (2008) Satellite remote sounding of mid - tropospheric CO₂. *Geophysical Research Letters*, 35.
- Chan, D., C. W. Yuen, K. Higuchi, A. Shashkov, J. Liu, J. Chen & D. Worthy (2004) On the CO₂ exchange between the atmosphere and the biosphere: the role of synoptic and mesoscale processes. *Tellus B*, 56, 194-212.
- Change, C. (2007) The physical science basis. *Contribution of Working*.
- Chevallier, F., F. M. Br éon & P. J. Rayner (2007) Contribution of the Orbiting Carbon Observatory to the estimation of CO₂ sources and sinks: Theoretical study in a variational data assimilation framework. *Journal of Geophysical Research: Atmospheres* (1984–2012), 112.
- Chevallier, F., N. M. Deutscher, T. Conway, P. Ciais, L. Ciattaglia, S. Dohe, M. Fröhlich, A. Gomez - Pelaez, D. Griffith & F. Hase (2011) Global CO₂ fluxes inferred from surface air - sample measurements and from TCCON retrievals of the CO₂ total column. *Geophysical Research Letters*, 38.
- Chevallier, F., R. J. Engelen & P. Peylin (2005) The contribution of AIRS data to the estimation of CO₂ sources and sinks. *Geophysical Research Letters*, 32.
- Chow, F. K., P. W. Granvold & C. M. Oldenburg (2009) Modeling the effects of topography and wind on atmospheric dispersion of CO₂ surface leakage at geologic carbon sequestration sites. *Energy Procedia*, 1, 1925-1932.
- Church, J. A. & N. J. White (2011) Sea-level rise from the late 19th to the early 21st century. *Surveys in Geophysics*, 32, 585-602.
- Ciais, P., P. Rayner, F. Chevallier, P. Bousquet, M. Logan, P. Peylin & M. Ramonet. 2011. Atmospheric inversions for estimating CO₂ fluxes: methods and perspectives. In *Greenhouse Gas Inventories*, 69-92. Springer.
- Clerbaux, C., A. Boynard, L. Clarisse, M. George, J. Hadji-Lazaro, H. Herbin, D. Hurtmans, M. Pommier, A. Razavi & S. Turquety (2009) Monitoring of atmospheric composition using the thermal infrared IASI/MetOp sounder. *Atmospheric Chemistry and Physics*, 9, 6041-6054.
- Cogan, A., H. Boesch, R. Parker, L. Feng, P. Palmer, J. F. Blavier, N. M. Deutscher, R. Macatangay, J. Notholt & C. Roehl (2012) Atmospheric carbon dioxide retrieved from the Greenhouse gases Observing SATellite (GOSAT): Comparison with ground - based TCCON observations and GEOS - Chem model calculations. *Journal of Geophysical Research: Atmospheres* (1984 - 2012), 117.
- Connor, B. J., H. Boesch, G. Toon, B. Sen, C. Miller & D. Crisp (2008) Orbiting Carbon Observatory: Inverse method and prospective error analysis. *Journal of Geophysical Research: Atmospheres* (1984–2012), 113.
- Corbin, K., A. Denning, E. Lokupitiya, A. Schuh, N. Miles, K. Davis, S. Richardson & I. Baker (2010) Assessing the impact of crops on regional CO₂ fluxes and atmospheric concentrations. *Tellus B*, 62, 521-532.
- Corner, A., D. Venables, A. Spence, W. Poortinga, C. Demski & N. Pidgeon (2011) Nuclear power, climate change and energy security: Exploring British public attitudes. *Energy Policy*, 39, 4823-4833.
- Corner, A., L. Whitmarsh & D. Xenias (2012) Uncertainty, scepticism and attitudes towards climate change: biased assimilation and attitude polarisation. *Climatic change*, 114, 463-478.
- Crevoisier, C., A. Ch édin, H. Matsueda, T. Machida, R. Armante & N. Scott (2009) First year of upper tropospheric integrated content of CO₂ from IASI hyperspectral infrared observations. *Atmospheric Chemistry and Physics*, 9, 4797-4810.

- Crevoisier, C., S. Heilliette, A. Chélin, S. Serrar, R. Armante & N. Scott (2004) Midtropospheric CO₂ concentration retrieval from AIRS observations in the tropics. *Geophysical Research Letters*, 31.
- Crisp, D., H. Bösch, L. Brown, R. Castano, M. Christi, B. Connor, C. Frankenberg, J. McDuffie, C. Miller & V. Natraj (2010) OCO (Orbiting Carbon Observatory)-2 Level 2 Full Physics Retrieval Algorithm Theoretical Basis. *Internet: http://disc.sci.gsfc.nasa.gov/acdisc/documentation/OCO-2_L2_FP_ATBD_v1_rev4_Nov10.pdf*.
- Crisp, D., B. Fisher, C. O'Dell, C. Frankenberg, R. Basilio, H. Bosch, L. Brown, R. Castano, B. Connor & N. Deutscher (2012) The ACOS CO₂ retrieval algorithm-Part II: Global XCO₂ data characterization.
- Crosland, M. P. (1961) The origins of Gay-Lussac's law of combining volumes of gases. *Annals of science*, 17, 1-26.
- Deardorff, J. W. (1972) Parameterization of the planetary boundary layer for use in general circulation models 1. *Monthly Weather Review*, 100, 93-106.
- den Elzen, M., M. Meinshausen & D. van Vuuren (2007) Multi-gas emission envelopes to meet greenhouse gas concentration targets: costs versus certainty of limiting temperature increase. *Global environmental change*, 17, 260-280.
- Denning, A. S., D. A. Randall, G. J. Collatz & P. J. Sellers (1996) Simulations of terrestrial carbon metabolism and atmospheric CO₂ in a general circulation model. *Tellus B*, 48, 543-567.
- Deutscher, N., D. Griffith, G. Bryant, P. Wennberg, G. Toon, R. Washenfelder, G. Keppel-Aleks, D. Wunch, Y. Yavin & N. Allen (2010) Total column CO₂ measurements at Darwin, Australia—site description and calibration against in situ aircraft profiles. *Atmospheric Measurement Techniques*, 3, 947-958.
- Dolman, A., J. Noilhan, P. Durand, C. Sarrat, A. Brut, B. Piguet, A. Butet, N. Jarosz, Y. Brunet & D. Loustau (2006) The CarboEurope Regional Experiment Strategy. *Bulletin of the American Meteorological Society*, 87.
- Dore, M. H. (2005) Climate change and changes in global precipitation patterns: what do we know? *Environment international*, 31, 1167-1181.
- Dubowski, K. M. & N. A. Essary (1996) Vapor-alcohol control tests with compressed ethanol-gas mixtures: Scientific basis and actual performance. *Journal of analytical toxicology*, 20, 484-491.
- Dunlap, R. E. & A. M. McCright (2011) Organized climate change denial. *The Oxford handbook of climate change and society*, 144-160.
- Duren, R. M. & C. E. Miller (2012) Measuring the carbon emissions of megacities. *Nature Climate Change*, 2, 560-562.
- Durran, D. R. & J. B. Klemp (1982) On the effects of moisture on the Brunt-Väisälä frequency. *Journal of the Atmospheric Sciences*, 39, 2152-2158.
- Dzubay, T. G., R. K. Stevens, C. W. Lewis, D. H. Hern, W. J. Courtney, J. W. Tesch & M. A. Mason (1982) Visibility and aerosol composition in Houston, Texas. *Environmental Science & Technology*, 16, 514-525.
- Edenhofer, O., R. Pichs-Madruga & Y. Sokona. 2012. *Renewable energy sources and climate change mitigation: Special report of the intergovernmental panel on climate change*. Cambridge University Press.
- EIA, U. (2011) Canada energy data, statistics and analysis—Oil, gas, electricity, coal. *Country Analysis Briefs: Canada*.
- Eidels-Dubovoi, S. (2002) Aerosol impacts on visible light extinction in the atmosphere of Mexico City. *Science of the total environment*, 287, 213-220.

- Elansky, N., M. Lokoshchenko, I. Belikov, A. Skorokhod & R. Shumskii (2007) Variability of trace gases in the atmospheric surface layer from observations in the city of Moscow. *Izvestiya, Atmospheric and Oceanic Physics*, 43, 219-231.
- Ellerman, A. D. & B. K. Buchner (2007) The European Union emissions trading scheme: origins, allocation, and early results. *Review of environmental economics and policy*, 1, 66-87.
- Enting, I., C. Trudinger & R. Francey (1995) A synthesis inversion of the concentration and $\delta^{13}\text{C}$ of atmospheric CO_2 . *Tellus B*, 47, 35-52.
- Euskirchen, E., M. S. Bret-Harte, G. Scott, C. Edgar & G. R. Shaver (2012) Seasonal patterns of carbon dioxide and water fluxes in three representative tundra ecosystems in northern Alaska. *Ecosphere*, 3, art4.
- Evans, K. M. 2005. *The environment: a revolution in attitudes*. Information Plus.
- Fan, S., M. Gloor, J. Mahlman, S. Pacala, J. Sarmiento, T. Takahashi & P. Tans (1998) A large terrestrial carbon sink in North America implied by atmospheric and oceanic carbon dioxide data and models. *Science*, 282, 442-446.
- Fang, S., L. Zhou, P. Tans, P. Ciais, M. Steinbacher, L. Xu & T. Luan (2014) In situ measurement of atmospheric CO_2 at the four WMO/GAW stations in China. *Atmospheric Chemistry and Physics*, 14, 2541-2554.
- Feng, L., P. I. Palmer, Y. Yang, R. M. Yantosca, S. R. Kawa, J.-D. Paris, H. Matsueda & T. Machida (2011) Evaluating a 3-D transport model of atmospheric CO_2 using ground-based, aircraft, and space-borne data. *Atmospheric Chemistry and Physics*, 11, 2789-2803.
- Flaounas, E., S. Bastin & S. Janicot (2011) Regional climate modelling of the 2006 West African monsoon: sensitivity to convection and planetary boundary layer parameterisation using WRF. *Climate Dynamics*, 36, 1083-1105.
- Frankenberg, C., P. Bergamaschi, A. Butz, S. Houweling, J. F. Meirink, J. Notholt, A. K. Petersen, H. Schrijver, T. Warneke & I. Aben (2008) Tropical methane emissions: A revised view from SCIAMACHY onboard ENVISAT. *Geophysical Research Letters*, 35.
- Frankenberg, C., J. B. Fisher, J. Worden, G. Badgley, S. S. Saatchi, J. E. Lee, G. C. Toon, A. Butz, M. Jung & A. Kuze (2011) New global observations of the terrestrial carbon cycle from GOSAT: Patterns of plant fluorescence with gross primary productivity. *Geophysical Research Letters*, 38.
- Frankenberg, C., U. Platt & T. Wagner (2005) Iterative maximum a posteriori (IMAP)-DOAS for retrieval of strongly absorbing trace gases: Model studies for CH_4 and CO_2 retrieval from near infrared spectra of SCIAMACHY onboard ENVISAT. *Atmospheric Chemistry and Physics*, 5, 9-22.
- Fraser, A., P. Palmer, L. Feng, R. Parker, H. Boesch, A. Cogan, G. Team & A. Team. 2011. Estimating regional CO_2 and CH_4 fluxes using GOSAT XCO_2 and XCH_4 observations. In *AGU Fall Meeting Abstracts*, 0230.
- Fraser, R. S., O. P. Bahethi & A. Al-Abbas (1977) The effect of the atmosphere on the classification of satellite observations to identify surface features. *Remote Sensing of Environment*, 6, 229-249.
- Fraser, R. S. & Y. J. Kaufman (1985) The relative importance of aerosol scattering and absorption in remote sensing. *Geoscience and Remote Sensing, IEEE Transactions on*, 625-633.
- Friedman, M. (1974) Explanation and scientific understanding. *Journal of Philosophy*, 71, 5-19.
- Fung, I., C. Tucker & K. Prentice (1987) Application of Advanced Very High Resolution Radiometer vegetation index to study atmosphere - biosphere exchange of CO_2 . *Journal of Geophysical Research: Atmospheres (1984 - 2012)*, 92, 2999-3015.
- Geels, C., J. Christensen, L. Frohn & J. Brandt (2002) Simulating spatiotemporal variations of atmospheric CO_2 using a nested hemispheric model. *Physics and Chemistry of the Earth, Parts A/B/C*, 27, 1495-1505.

- Geels, C., S. Doney, R. Dargaville, J. Brandt & J. Christensen (2004) Investigating the sources of synoptic variability in atmospheric CO₂ measurements over the Northern Hemisphere continents: a regional model study. *Tellus B*, 56, 35-50.
- Geels, C., M. Gloor, P. Ciais, P. Bousquet, P. Peylin, A. Vermeulen, R. Dargaville, T. Aalto, J. Brandt & J. Christensen (2007) Comparing atmospheric transport models for future regional inversions over Europe—Part 1: mapping the atmospheric CO₂ signals. *Atmospheric Chemistry and Physics*, 7, 3461-3479.
- Gibert, F., M. Schmidt, J. Cuesta, P. Ciais, M. Ramonet, I. Xueref, E. Larmanou & P. H. Flamant (2007) Retrieval of average CO₂ fluxes by combining in situ CO₂ measurements and backscatter lidar information. *Journal of Geophysical Research: Atmospheres* (1984–2012), 112.
- Gloor, M., P. Bakwin, D. Hurst, L. Lock, R. Draxler & P. Tans (2001) What is the concentration footprint of a tall tower? *Journal of Geophysical Research: Atmospheres* (1984–2012), 106, 17831-17840.
- Gordon, H. R., D. K. Clark, J. W. Brown, O. B. Brown, R. H. Evans & W. W. Broenkow (1983) Phytoplankton pigment concentrations in the Middle Atlantic Bight: Comparison of ship determinations and CZCS estimates. *Applied optics*, 22, 20-36.
- Gordon, I. E., L. S. Rothman, R. R. Gamache, D. Jacquemart, C. Boone, P. F. Bernath, M. W. Shephard, J. S. Delamere & S. A. Clough (2007) Current updates of the water-vapor line list in HITRAN: A new “Diet” for air-broadened half-widths. *Journal of Quantitative Spectroscopy and Radiative Transfer*, 108, 389-402.
- Goudie, A. S. 2013. *The human impact on the natural environment: past, present, and future*. John Wiley & Sons.
- Gourdji, S. M., K. L. Mueller, K. Schaefer & A. M. Michalak (2008) Global monthly averaged CO₂ fluxes recovered using a geostatistical inverse modeling approach: 2. Results including auxiliary environmental data. *Journal of Geophysical Research: Atmospheres* (1984–2012), 113.
- Gregory, J., N. White, J. Church, M. Bierkens, J. Box, M. van den Broeke, J. Cogley, X. Fettweis, E. Hanna & P. Huybrechts (2013) Twentieth-Century Global-Mean Sea Level Rise: Is the Whole Greater than the Sum of the Parts? *Journal of Climate*, 26.
- Grubb, M., J. Edmonds, P. Ten Brink & M. Morrison (1993) The costs of limiting fossil-fuel CO₂ emissions: a survey and analysis. *Annual Review of Energy and the environment*, 18, 397-478.
- Gurney, K. R., R. M. Law, A. S. Denning, P. J. Rayner, D. Baker, P. Bousquet, L. Bruhwiler, Y.-H. Chen, P. Ciais & S. Fan (2002) Towards robust regional estimates of CO₂ sources and sinks using atmospheric transport models. *Nature*, 415, 626-630.
- Hand, J., S. Kreidenweis, D. Eli Sherman, J. Collett Jr, S. Hering, D. Day & W. Malm (2002) Aerosol size distributions and visibility estimates during the Big Bend regional aerosol and visibility observational (BRAVO) study. *Atmospheric Environment*, 36, 5043-5055.
- Hansen, J., M. Sato & R. Ruedy (2012) Perception of climate change. *Proceedings of the National Academy of Sciences*, 109, E2415-E2423.
- Haszpra, L., Z. Barcza, D. Hidy, I. Szilágyi, E. Dlugokencky & P. Tans (2008) Trends and temporal variations of major greenhouse gases at a rural site in Central Europe. *Atmospheric Environment*, 42, 8707-8716.
- Heino, P. & R. Kakko (1998) Risk assessment modelling and visualisation. *Safety Science*, 30, 71-77.
- Heymann, J., H. Bovensmann, M. Buchwitz, J. Burrows, N. Deutscher, J. Notholt, M. Rettinger, M. Reuter, O. Schneising & R. Sussmann (2012a) SCIAMACHY WFM-DOAS XCO₂: reduction of scattering related errors. *Atmospheric Measurement Techniques*, 5, 2375-2390.

- Heymann, J., O. Schneising, M. Buchwitz, M. Reuter, H. Bovensmann & J. Burrows. 2012b. SCIAMACHY WFM-DOAS XCO₂: Improvements and comparison with FTS measurements. In *EGU General Assembly Conference Abstracts*, 328.
- Heymann, J., O. Schneising, M. Reuter, M. Buchwitz, V. Rozanov, H. Bovensmann & J. Burrows (2012c) SCIAMACHY WFM-DOAS XCO₂: comparison with CarbonTracker XCO₂ focusing on aerosols and thin clouds.
- Hoberg, G. & I. H. Rowlands. 2012. Green Energy Politics in Canada: Comparing Electricity Policies in BC and Ontario. In *APSA 2012 Annual Meeting Paper*.
- Hofman, K. & X. Li (2009) Canada's energy perspectives and policies for sustainable development. *Applied Energy*, 86, 407-415.
- Hohmeyer, O. 1988. *Social costs of energy consumption*. Springer.
- Holburn, G. L. (2012) Assessing and managing regulatory risk in renewable energy: Contrasts between Canada and the United States. *Energy Policy*, 45, 654-665.
- Hoogeveen, R. W., R. T. Jongma, P. J. Tol, A. Gloudemans, I. Aben, J. de Vries, H. Visser, E. Boslooper, M. Dobber & P. F. Levelt. 2007. Breadboarding activities of the TROPOMI-SWIR module. In *Remote Sensing*, 67441T-67441T-8. International Society for Optics and Photonics.
- Horvath, H. (1993) Atmospheric light absorption—A review. *Atmospheric Environment. Part A. General Topics*, 27, 293-317.
- Houghton, J. T. 1996. *Climate change 1995: The science of climate change: contribution of working group I to the second assessment report of the Intergovernmental Panel on Climate Change*. Cambridge University Press.
- Houghton, J. T., Y. Ding, D. J. Griggs, M. Noguer, P. J. van der LINDEN, X. Dai, K. Maskell & C. Johnson. 2001. *Climate change 2001: the scientific basis*. Cambridge university press Cambridge.
- Houghton, R. A. & G. M. Woodwell (1989) Global climate change. *Scientific American*, 260, 36-40.
- Houweling, S., I. Aben, F.-M. Breon, F. Chevallier, N. Deutscher, R. Engelen, C. Gerbig, D. Griffith, K. Hungershofer & R. Macatangay (2010) The importance of transport model uncertainties for the estimation of CO₂ sources and sinks using satellite measurements. *Atmospheric Chemistry and Physics*, 10, 9981-9992.
- Houweling, S., S. Basu, F. Chevallier, L. Feng, S. Maksyutov, P. Palmer, P. Peylin, Z. Poussi & H. Takagi. 2012. Global CO₂ fluxes from GOSAT: First results from an inter-comparison of inverse models. In *EGU General Assembly Conference Abstracts*, 12978.
- Houweling, S., F.-M. Breon, I. Aben, C. Rödenbeck, M. Gloor, M. Heimann & P. Ciais (2004) Inverse modeling of CO₂ sources and sinks using satellite data: A synthetic inter-comparison of measurement techniques and their performance as a function of space and time. *Atmospheric Chemistry and Physics*, 4, 523-538.
- Houweling, S., W. Hartmann, I. Aben, H. Schrijver, J. Skidmore, G.-J. Roelofs & F.-M. Breon (2005) Evidence of systematic errors in SCIAMACHY-observed CO₂ due to aerosols. *Atmospheric Chemistry and Physics*, 5, 3003-3013.
- Hu, X.-M., J. W. Nielsen-Gammon & F. Zhang (2010) Evaluation of Three Planetary Boundary Layer Schemes in the WRF Model. *Journal of Applied Meteorology & Climatology*, 49.
- Imasu, R., G. Inoue, H. Kondo, Y. Niwa, H. Matsueda, T. Machida, Y. Matsumi, M. Kawasaki, T. Nakayama & Y. Hayashi. 2010. GOSAT specific observation targeting urban CO₂ emissions. In *AGU Fall Meeting Abstracts*, 0281.
- Inoue, M., I. Morino, O. Uchino, Y. Miyamoto, Y. Yoshida, T. Yokota, T. Machida, Y. Sawa, H. Matsueda & C. Sweeney (2013) Validation of XCO₂ derived from SWIR spectra of GOSAT TANSO-FTS with aircraft measurement data. *Atmospheric Chemistry and Physics*, 13, 9771-9788.

- Iraci, L., M. Johnson, E. Yates, T. Tanaka, C. Sweeney, J. Tadic, M. Roby, A. Andrews & J. Lopez. 2013. Assessing Day-to Day Variability in the Vertical Distribution of Methane, Carbon Dioxide, and Ozone over Railroad Valley, NV. In *AGU Fall Meeting Abstracts*, 0082.
- Isogai, K., G. Cook & R. Anderson (2002) Reconstructing the history of ^{14}C discharges from Sellafield: Part 1—atmospheric discharges. *Journal of environmental radioactivity*, 59, 207-222.
- Jaccard, M., N. Melton & J. Nyboer (2011) Institutions and processes for scaling up renewables: Run-of-river hydropower in British Columbia. *Energy Policy*, 39, 4042-4050.
- Jarvis, P., J. Massheder, S. Hale, J. Moncrieff, M. Rayment & S. Scott (1997) Seasonal variation of carbon dioxide, water vapor, and energy exchanges of a boreal black spruce forest. *Journal of Geophysical Research: Atmospheres (1984–2012)*, 102, 28953-28966.
- Jean-Baptiste, P. & R. Ducroux (2003) Energy policy and climate change. *Energy Policy*, 31, 155-166.
- Jones, N. (2013) Troubling milestone for CO₂. *Nature Geoscience*, 6, 589-589.
- Jones, P., K. Trenberth, P. Ambenje, R. Bojariu, D. Easterling, T. Klein, D. Parker, J. Renwick, M. Rusticucci & B. Soden (2007) Observations: surface and atmospheric climate change. In *Climate Change 2007: The Physical Science Basis. Contribution of Working Group I to the Fourth Assessment Report of the Intergovernmental Panel on Climate Change*, 235-336.
- Jovanovic, M., N. Afgan & V. Bakic (2010) An analytical method for the measurement of energy system sustainability in urban areas. *Energy*, 35, 3909-3920.
- Kaminski, T., M. Heimann & R. Giering (1999) A coarse grid three - dimensional global inverse model of the atmospheric transport: 2. Inversion of the transport of CO₂ in the 1980s. *Journal of Geophysical Research: Atmospheres (1984–2012)*, 104, 18555-18581.
- Kaminski, T., P. J. Rayner, M. Heimann & I. G. Enting (2001) On aggregation errors in atmospheric transport inversions. *Journal of Geophysical Research: Atmospheres (1984–2012)*, 106, 4703-4715.
- Karl, T. R. & K. E. Trenberth (2003) Modern global climate change. *Science*, 302, 1719-1723.
- Karstens, U., M. Gloor, M. Heimann & C. Rödenbeck (2006) Insights from simulations with high - resolution transport and process models on sampling of the atmosphere for constraining midlatitude land carbon sinks. *Journal of Geophysical Research: Atmospheres (1984 - 2012)*, 111.
- Kaufman, Y., D. Tanré, L. A. Remer, E. Vermote, A. Chu & B. Holben (1997) Operational remote sensing of tropospheric aerosol over land from EOS moderate resolution imaging spectroradiometer. *Journal of Geophysical Research: Atmospheres (1984–2012)*, 102, 17051-17067.
- Kaufman, Y. J. (1989) The atmospheric effect on remote sensing and its correction. *Theory and applications of optical remote sensing*, 336-428.
- Keeling, C. D., R. B. Bacastow, A. Carter, S. C. Piper, T. P. Whorf, M. Heimann, W. G. Mook & H. Roeloffzen (1989) A three-dimensional model of atmospheric CO₂ transport based on observed winds: 1. Analysis of observational data. *Geophysical Monograph Series*, 55, 165-236.
- Kern, F. & A. Smith (2008) Restructuring energy systems for sustainability? Energy transition policy in the Netherlands. *Energy Policy*, 36, 4093-4103.
- Kim, S. & B. E. Dale (2005) Environmental aspects of ethanol derived from no-tilled corn grain: nonrenewable energy consumption and greenhouse gas emissions. *Biomass and Bioenergy*, 28, 475-489.
- Kort, E. A., C. Frankenberg, C. E. Miller & T. Oda (2012) Space - based observations of megacity carbon dioxide. *Geophysical Research Letters*, 39.

- Kretschmer, R., C. Gerbig, U. Karstens, G. Biavati, A. Vermeulen, F. Vogel, S. Hammer & K. Totsche (2014) Impact of optimized mixing heights on simulated regional atmospheric transport of CO₂. *Atmospheric Chemistry and Physics Discussions*, 14, 4627-4685.
- Kulawik, S., D. Jones, R. Nassar, F. Irion, J. Worden, K. Bowman, T. Machida, H. Matsueda, Y. Sawa & S. Biraud (2010) Characterization of Tropospheric Emission Spectrometer (TES) CO₂ for carbon cycle science. *Atmospheric Chemistry and Physics*, 10, 5601-5623.
- Kulawik, S., J. Worden, S. Wofsy, S. Biraud, R. Nassar, D. Jones & E. Olsen (2012) Comparison of improved Aura Tropospheric Emission Spectrometer (TES) CO₂ with HIPPO and SGP aircraft profile measurements. *Atmospheric Chemistry and Physics Discussions*, 12, 6283-6329.
- Lac, C., R. Donnelly, V. Masson, S. Pal, S. Riette, S. Donier, S. Queguiner, G. Tanguy, L. Ammoura & I. Xueref-Remy (2013) CO₂ dispersion modelling over Paris region within the CO₂-MEGAPARIS project. *Atmospheric Chemistry & Physics*, 13.
- Lambert, J.-C., A. Piters, A. Richter, S. Mieruch, H. Bovensmann, M. Buchwitz & A. Friker. 2011. Validation. In *SCIAMACHY-Exploring the Changing Earth's Atmosphere*, 147-173. Springer.
- Langmann, B. (2000) Numerical modelling of regional scale transport and photochemistry directly together with meteorological processes. *Atmospheric Environment*, 34, 3585-3598.
- Law, R., W. Peters & C. Rödenbeck (2006) Protocol for TransCom continuous data experiment. *Purdue Climate Change Res. Cent. Tech. Rep.*
- Law, R., W. Peters, C. Rödenbeck, C. Aulagnier, I. Baker, D. Bergmann, P. Bousquet, J. Brandt, L. Bruhwiler & P. Cameron - Smith (2008) TransCom model simulations of hourly atmospheric CO₂: Experimental overview and diurnal cycle results for 2002. *Global Biogeochemical Cycles*, 22.
- Law, R., P. Rayner, A. Denning, D. Erickson, I. Fung, M. Heimann, S. Piper, M. Ramonet, S. Taguchi & J. Taylor (1996) Variations in modeled atmospheric transport of carbon dioxide and the consequences for CO₂ inversions. *Global Biogeochemical Cycles*, 10, 783-796.
- Leiserowitz, A. (2006) Climate change risk perception and policy preferences: the role of affect, imagery, and values. *Climatic change*, 77, 45-72.
- Leventidou, E., P. Zanis, D. Balis, E. Giannakaki, I. Pytharoulis & V. Amiridis (2013) Factors affecting the comparisons of planetary boundary layer height retrievals from CALIPSO, ECMWF and radiosondes over Thessaloniki, Greece. *Atmospheric Environment*, 74, 360-366.
- Levitan, O., J. Dinamarca, G. Hochman & P. G. Falkowski (2014) Diatoms: a fossil fuel of the future. *Trends in biotechnology*, 32, 117-124.
- Lichtenberg, G., Q. Kleipool, J. Krijger, G. v. Soest, R. v. Hees, L. Tilstra, J. Acarreta, I. Aben, B. Ahlers & H. Bovensmann (2006) SCIAMACHY Level 1 data: calibration concept and in-flight calibration. *Atmospheric Chemistry and Physics*, 6, 5347-5367.
- Lin, J. C., D. Brunner & C. Gerbig (2011) Studying atmospheric transport through Lagrangian models. *Eos, Transactions American Geophysical Union*, 92, 177-178.
- Lu, L., A. S. Denning, M. A. da Silva - Dias, P. da Silva - Dias, M. Longo, S. R. Freitas & S. Saatchi (2005) Mesoscale circulations and atmospheric CO₂ variations in the Tapajós Region, Pará Brazil. *Journal of Geophysical Research: Atmospheres (1984-2012)*, 110.
- Mabee, W. E., J. Mannion & T. Carpenter (2012) Comparing the feed-in tariff incentives for renewable electricity in Ontario and Germany. *Energy Policy*, 40, 480-489.
- Machida, T., H. Matsueda, Y. Sawa, Y. Nakagawa, K. Hirokuni, N. Kondo, K. Goto, T. Nakazawa, K. Ishikawa & T. Ogawa (2008) Worldwide Measurements of Atmospheric

- CO₂ and Other Trace Gas Species Using Commercial Airlines. *Journal of Atmospheric & Oceanic Technology*, 25.
- Maksyutov, S., P. K. Patra, R. Onishi, T. Saeki & T. Nakazawa (2008) NIES/FRCGC global atmospheric tracer transport model: Description, validation, and surface sources and sinks inversion. *J. Earth Simulator*, 9, 3-18.
- Maksyutov, S., H. Takagi, V. Valsala, M. Saito, T. Oda, T. Saeki, D. Belikov, R. Saito, A. Ito & Y. Yoshida (2013) Regional CO₂ flux estimates for 2009-2010 based on GOSAT and ground-based CO₂ observations. *Atmospheric Chemistry & Physics*, 13.
- Marvão Pereira, A. & R. M. Marvão Pereira (2010) Is fuel-switching a no-regrets environmental policy? VAR evidence on carbon dioxide emissions, energy consumption and economic performance in Portugal. *Energy Economics*, 32, 227-242.
- Matsueda, H., H. Y. Inoue & M. Ishii (2002) Aircraft observation of carbon dioxide at 8–13 km altitude over the western Pacific from 1993 to 1999. *Tellus B*, 54, 1-21.
- Matthews, H. D. & K. Caldeira (2008) Stabilizing climate requires near - zero emissions. *Geophysical Research Letters*, 35.
- Mattoo, A., A. Subramanian, D. Van Der Mensbrugge & J. He (2009) Reconciling climate change and trade policy.
- Maurellis, A. & J. Tennyson (2003) The climatic effects of water vapour. *Physics World*, May.
- McCright, A. M. & R. E. Dunlap (2000) Challenging global warming as a social problem: An analysis of the conservative movement's counter-claims. *Social Problems*, 499-522.
- Meehl, G. A., A. Hu, C. Tebaldi, J. M. Arblaster, W. M. Washington, H. Teng, B. M. Sanderson, T. Ault, W. G. Strand & J. B. White III (2012) Relative outcomes of climate change mitigation related to global temperature versus sea-level rise. *Nature Climate Change*, 2, 576-580.
- Michalak, A. M., A. Hirsch, L. Bruhwiler, K. R. Gurney, W. Peters & P. P. Tans (2005) Maximum likelihood estimation of covariance parameters for Bayesian atmospheric trace gas surface flux inversions. *Journal of Geophysical Research: Atmospheres (1984–2012)*, 110.
- Min, S.-K., X. Zhang, F. W. Zwiers & G. C. Hegerl (2011) Human contribution to more-intense precipitation extremes. *Nature*, 470, 378-381.
- Mitigation, C. C. (2011) IPCC special report on renewable energy sources and climate change mitigation.
- Moeng, C.-H. (1984) A large-eddy-simulation model for the study of planetary boundary-layer turbulence. *Journal of the Atmospheric Sciences*, 41, 2052-2062.
- Moeng, C.-H. & P. P. Sullivan (1994) A comparison of shear-and buoyancy-driven planetary boundary layer flows. *Journal of the Atmospheric Sciences*, 51, 999-1022.
- Monin, A. & A. Obukhov (1954) Basic laws of turbulent mixing in the surface layer of the atmosphere. *Contrib. Geophys. Inst. Acad. Sci. USSR*, 151, 163-187.
- Montzka, S., E. Dlugokencky & J. Butler (2011) Non-CO₂ greenhouse gases and climate change. *Nature*, 476, 43-50.
- Morino, I., O. Uchino, M. Inoue, Y. Yoshida, T. Yokota, P. Wennberg, G. Toon, D. Wunch, C. Roehl & J. Notholt (2011) Preliminary validation of column-averaged volume mixing ratios of carbon dioxide and methane retrieved from GOSAT short-wavelength infrared spectra. *Atmospheric Measurement Techniques*, 4, 1061-1076.
- Nakicenovic, N. & R. Swart (2000) Special report on emissions scenarios. *Special Report on Emissions Scenarios, Edited by Nebojsa Nakicenovic and Robert Swart, pp. 612. ISBN 0521804930. Cambridge, UK: Cambridge University Press, July 2000., 1.*
- Natraj, V., R. J. Spurr, H. Boesch, Y. Jiang & Y. L. Yung (2007) Evaluation of errors from neglecting polarization in the forward modeling of O₂ A band measurements from space, with relevance to CO₂ column retrieval from

- polarization-sensitive instruments. *Journal of Quantitative Spectroscopy and Radiative Transfer*, 103, 245-259.
- Newman, S., Y. Wong, H. Lee, K. Li, X. Xu, J. Campbell & Y. Yung. 2013. Natural Variabilities and Trends in CO₂ from the Los Angeles Megacity Measured Over 15 Years. In *AGU Fall Meeting Abstracts*, 03.
- Nicholls, M. E., A. S. Denning, L. Prihodko, P. L. Vidale, I. Baker, K. Davis & P. Bakwin (2004) A multiple - scale simulation of variations in atmospheric carbon dioxide using a coupled biosphere - atmospheric model. *Journal of Geophysical Research: Atmospheres (1984–2012)*, 109.
- Nishimura, K. (2012) Grassroots action for renewable energy: how did Ontario succeed in the implementation of a feed-in tariff system? *Energy, Sustainability and Society*, 2, 1-11.
- NOAA, U. & U. A. Force. 1976. US standard atmosphere, 1976. NOAA-S/T.
- Noh, Y., W. Cheon, S. Hong & S. Raasch (2003) Improvement of the K-profile model for the planetary boundary layer based on large eddy simulation data. *Boundary-layer meteorology*, 107, 401-427.
- Norman, J., H. L. MacLean & C. A. Kennedy (2006) Comparing high and low residential density: life-cycle analysis of energy use and greenhouse gas emissions. *Journal of Urban Planning and Development*, 132, 10-21.
- Nurrenbern, S. C. & M. Pickering (1987) Concept learning versus problem solving: Is there a difference? *Journal of Chemical Education*, 64, 508.
- O'Dell, C., B. Connor, H. Bösch, D. O'Brien, C. Frankenberg, R. Castano, M. Christi, D. Eldering, B. Fisher & M. Gunson (2012) The ACOS CO₂ retrieval algorithm—Part 1: Description and validation against synthetic observations. *Atmospheric Measurement Techniques*, 5, 99-121.
- O'Dell, C., I. Polonsky, C. Frankenberg, D. Crisp, A. Eldering, M. Gunson, D. Wunch, P. Wennberg & F. Chevallier. 2013. Analysis of four years of GOSAT data through the ACOS B3. 4 Retrieval Algorithm. In *AGU Fall Meeting Abstracts*, 05.
- Olsen, E. T., M. Chahine, L. Chen, X. Jiang, T. S. Pagano & Y. L. Yung. 2011. Validation of the AIRS mid-tropospheric CO₂ retrieved by the Vanishing Partial Derivative Method. Preparation.
- Oreskes, N. (2004) The scientific consensus on climate change. *Science*, 306, 1686-1686.
- Oreskes, N. & E. M. Conway (2010) Merchants of doubt. *New York: Bloomsbury*.
- Oshchepkov, S., A. Bril & T. Yokota (2008) PPDF - based method to account for atmospheric light scattering in observations of carbon dioxide from space. *Journal of Geophysical Research: Atmospheres (1984 - 2012)*, 113.
- Oshchepkov, S., A. Bril & T. Yokota (2009) An improved photon path length probability density function - based radiative transfer model for space - based observation of greenhouse gases. *Journal of Geophysical Research: Atmospheres (1984 - 2012)*, 114.
- Oshchepkov, S., A. Bril, T. Yokota, I. Morino, Y. Yoshida, T. Matsunaga, D. Belikov, D. Wunch, P. Wennberg & G. Toon (2012) Effects of atmospheric light scattering on spectroscopic observations of greenhouse gases from space: Validation of PPDF - based CO₂ retrievals from GOSAT. *Journal of Geophysical Research: Atmospheres (1984 - 2012)*, 117.
- Oshchepkov, S., A. Bril, T. Yokota, P. O. Wennberg, N. M. Deutscher, D. Wunch, G. C. Toon, Y. Yoshida, C. W. O'Dell & D. Crisp (2013) Effects of atmospheric light scattering on spectroscopic observations of greenhouse gases from space. Part 2: Algorithm intercomparison in the GOSAT data processing for CO₂ retrievals over TCCON sites. *Journal of Geophysical Research: Atmospheres*, 118, 1493-1512.
- Osterman, G., E. Martinez, A. Elderling & C. Avis. 2011. ACOS Level 2 Standard Product Data User's Guide, v2. 9.

- Ou, X., X. Zhang, S. Chang & Q. Guo (2009) Energy consumption and GHG emissions of six biofuel pathways by LCA in (the) People's Republic of China. *Applied Energy*, 86, S197-S208.
- Pérez-Landa, G., P. Ciais, G. Gangoiti, J. Palau, A. Carrara, B. Gioli, F. Miglietta, M. Schumacher, M. Millán & M. Sanz (2007) Mesoscale circulations over complex terrain in the Valencia coastal region, Spain—Part 2: Modeling CO₂ transport using idealized surface fluxes. *Atmospheric Chemistry and Physics*, 7, 1851-1868.
- Pérez, I., M. Sánchez, M. García & B. d. Torre. 2009a. Boundary layer structure and stability classification validated with CO₂ concentrations over the Northern Spanish Plateau. In *Annales Geophysicae*, 339-349. Copernicus GmbH.
- Pérez, I. A., M. L. Sánchez, M. García & B. de Torre (2009b) A classification of CO₂ concentrations based on a binary meteorological six variable system. *Agricultural and forest meteorology*, 149, 1686-1692.
- Pérez, I. A., M. L. Sánchez & M. Á. García (2012) CO₂ dilution in the lower atmosphere from temperature and wind speed profiles. *Theoretical and Applied Climatology*, 107, 247-253.
- Pagano, T. S., H. Nguyen, E. Olsen, A. Ruzmaikin & X. Jiang (2012) Correlations of the seasonal variability of AIRS mid-tropospheric CO₂ with MODIS derived Gross Primary Productivity (GPP).
- Pagano, T. S. & E. T. Olsen (2012) Large scale variability of mid-tropospheric carbon dioxide as observed by the Atmospheric Infrared Sounder (AIRS) On The NASA EOS Aqua platform.
- Pal, R. (2014) Has the Appellate Body's Decision in Canada—Renewable Energy/Canada—Feed-in Tariff Program Opened the Door for Production Subsidies? *Journal of International Economic Law*, 17, 125-137.
- Parker, P., I. H. Rowlands & D. Scott (2003) Innovations to reduce residential energy use and carbon emissions: an integrated approach. *The Canadian Geographer/Le Géographe canadien*, 47, 169-184.
- Patra, P., R. Law, W. Peters, C. Rödenbeck, M. Takigawa, C. Aulagnier, I. Baker, D. Bergmann, P. Bousquet & J. Brandt (2008) TransCom model simulations of hourly atmospheric CO₂: Analysis of synoptic - scale variations for the period 2002 - 2003. *Global Biogeochemical Cycles*, 22.
- Patra, P. K., S. Maksyutov, Y. Sasano, H. Nakajima, G. Inoue & T. Nakazawa (2003) An evaluation of CO₂ observations with Solar Occultation FTS for Inclined - Orbit Satellite sensor for surface source inversion. *Journal of Geophysical Research: Atmospheres (1984 - 2012)*, 108.
- Patterson, M. G. (1996) What is energy efficiency?: Concepts, indicators and methodological issues. *Energy Policy*, 24, 377-390.
- Pernigotti, D., A. M. Rossa, M. E. Ferrario, M. Sansone & A. Benassi (2007) Influence of ABL stability on the diurnal cycle of PM₁₀ concentration: illustration of the potential of the new Veneto network of MW-radiometers and SODAR. *Meteorologische Zeitschrift*, 16, 505-511.
- Pielke, R. A. (2005) Land use and climate change. *Science*, 310, 1625-1626.
- Planning, O. R. C. o. E. P. 1980. *The Report of the Royal Commission on Electric Power Planning*. Royal Commission on Electric Power Planning.
- Plattner, G.-K., R. Knutti, F. Joos, T. Stocker, W. Von Bloh, V. Brovkin, D. Cameron, E. Driesschaert, S. Dutkiewicz & M. Eby (2008) Long-Term Climate Commitments Projected with Climate—Carbon Cycle Models. *Journal of Climate*, 21.
- Poortinga, W. 2012. Attitudes toward nuclear power as a solution to climate change. In *INTERNATIONAL JOURNAL OF PSYCHOLOGY*, 352-352. PSYCHOLOGY PRESS 27 CHURCH RD, HOVE BN3 2FA, EAST SUSSEX, ENGLAND.

- Poortinga, W., A. Spence, L. Whitmarsh, S. Capstick & N. F. Pidgeon (2011) Uncertain climate: An investigation into public scepticism about anthropogenic climate change. *Global environmental change*, 21, 1015-1024.
- Prentice, I., G. Farquhar, M. Fasham, M. Goulden, M. Heimann, V. Jaramillo, H. Kheshgi, C. LeQuéré & R. Scholes & D. W. Wallace (2001) The carbon cycle and atmospheric carbon dioxide.
- Ray, E. A., F. L. Moore, J. W. Elkins, G. S. Dutton, D. W. Fahey, H. Vömel, S. J. Oltmans & K. H. Rosenlof (1999) Transport into the Northern Hemisphere lowermost stratosphere revealed by in situ tracer measurements. *Journal of Geophysical Research: Atmospheres (1984–2012)*, 104, 26565-26580.
- Rayner, P., I. Enting, R. Francey & R. Langenfelds (1999) Reconstructing the recent carbon cycle from atmospheric CO₂, δ¹³C and O₂/N₂ observations*. *Tellus B*, 51, 213-232.
- Rayner, P. & D. O'Brien (2001) The utility of remotely sensed CO₂ concentration data in surface source inversions. *Geophysical Research Letters*, 28, 175-178.
- Retalis, A., D. G. Hadjimitsis, S. Michaelides, F. Tymvios, N. Chrysoulakis, C. R. Clayton & K. Themistocleous (2010) Comparison of aerosol optical thickness with in situ visibility data over Cyprus. *Natural Hazards & Earth System Sciences*, 10.
- Reuter, M., M. Buchwitz, O. Schneising, J. Heymann, H. Bovensmann & J. Burrows (2010) A method for improved SCIAMACHY CO₂ retrieval in the presence of optically thin clouds. *Atmospheric Measurement Techniques*, 3, 209-232.
- Richter, A., J. P. Burrows, H. Nüß, C. Granier & U. Niemeier (2005) Increase in tropospheric nitrogen dioxide over China observed from space. *Nature*, 437, 129-132.
- Roosevelt, P. F. D. (2008) National Weather Service. *Disasters, Accidents, and Crises in American History: A Reference Guide to the Nation's Most Catastrophic Events*, 1969.
- Rothman, L., R. Gamache, A. Goldman, L. Brown, R. Toth, H. Pickett, R. Poynter, J.-M. Flaud, C. Camy-Peyret & A. Barbe (1987) The HITRAN database: 1986 edition. *Applied optics*, 26, 4058-4097.
- Rothman, L. S., I. E. Gordon, A. Barbe, D. C. Benner, P. F. Bernath, M. Birk, V. Boudon, L. R. Brown, A. Campargue & J.-P. Champion (2009) The HITRAN 2008 molecular spectroscopic database. *Journal of Quantitative Spectroscopy and Radiative Transfer*, 110, 533-572.
- Roussel-Debet, S., G. Gontier, F. Siclet & M. Fournier (2006) Distribution of carbon 14 in the terrestrial environment close to French nuclear power plants. *Journal of environmental radioactivity*, 87, 246-259.
- Rubin, E. S., A. B. Rao & C. Chen (2004) Comparative assessments of fossil fuel power plants with CO₂ capture and storage.
- Saitoh, N., R. Imasu, Y. Ota & Y. Niwa (2009) CO₂ retrieval algorithm for the thermal infrared spectra of the Greenhouse Gases Observing Satellite: Potential of retrieving CO₂ vertical profile from high - resolution FTS sensor. *Journal of Geophysical Research: Atmospheres (1984–2012)*, 114.
- Sakuma, F., C. J. Bruegge, D. Rider, D. Brown, S. Geier, S. Kawakami & A. Kuze (2010) OCO/GOSAT preflight cross-calibration experiment. *Geoscience and Remote Sensing, IEEE Transactions on*, 48, 585-599.
- Sarrat, C., J. Noilhan, A. Dolman, C. Gerbig, R. Ahmadov, L. Tolk, A. Meesters, R. Hutjes, H. Ter Maat & G. Pérez-Landa (2007) Atmospheric CO₂ modeling at the regional scale: an intercomparison of 5 meso-scale atmospheric models. *Biogeosciences Discussions*, 4.
- Sato, K., S. Mito, T. Horie, H. Ohkuma, H. Saito, J. Watanabe & T. Yoshimura (2011) Monitoring and simulation studies for assessing macro-and meso-scale migration of CO₂ sequestered in an onshore aquifer: Experiences from the Nagaoka pilot site, Japan. *International Journal of Greenhouse Gas Control*, 5, 125-137.

- Schmidt, H., C. Derognat, R. Vautard & M. Beekmann (2001) A comparison of simulated and observed ozone mixing ratios for the summer of 1998 in Western Europe. *Atmospheric Environment*, 35, 6277-6297.
- Schneider, D. R., M. Kirac & A. Hublin (2013) GHG reduction potential in waste management in Croatia. *Management of Environmental Quality: An International Journal*, 24, 738-754.
- Schneising, O., P. Bergamaschi, H. Bovensmann, M. Buchwitz, J. Burrows, N. Deutscher, D. Griffith, J. Heymann, R. Macatangay & J. Messerschmidt (2012a) Atmospheric greenhouse gases retrieved from SCIAMACHY: comparison to ground-based FTS measurements and model results. *Atmospheric Chemistry and Physics*, 12, 1527-1540.
- Schneising, O., M. Buchwitz, J. Heymann, M. Reuter, H. Bovensmann & J. Burrows. 2012b. Improved carbon dioxide and methane retrieved from SCIAMACHY onboard ENVISAT: Validation and land-atmosphere related applications. In *EGU General Assembly Conference Abstracts*, 4991.
- Schneising, O., M. Buchwitz, M. Reuter, J. Heymann, H. Bovensmann & J. Burrows (2011) Long-term analysis of carbon dioxide and methane column-averaged mole fractions retrieved from SCIAMACHY. *Atmospheric Chemistry and Physics*, 11, 2863-2880.
- Schneising, O., J. Heymann, M. Buchwitz, M. Reuter, H. Bovensmann & J. P. Burrows. 2013. Anthropogenic carbon dioxide source regions observed from space. In *EGU General Assembly Conference Abstracts*, 4752.
- Schuh, A. E., T. Lauvaux, T. O. West, A. S. Denning, K. J. Davis, N. Miles, S. Richardson, M. Uliasz, E. Lokupitiya & D. Cooley (2013) Evaluating atmospheric CO₂ inversions at multiple scales over a highly inventoried agricultural landscape. *Global change biology*, 19, 1424-1439.
- Scott Denning, A., M. Nicholls, L. Prihodko, I. Baker, P. L. Vidale, K. Davis & P. Bakwin (2003) Simulated variations in atmospheric CO₂ over a Wisconsin forest using a coupled ecosystem-atmosphere model. *Global change biology*, 9, 1241-1250.
- Seidel, D. J., Y. Zhang, A. Beljaars, J. C. Golaz, A. R. Jacobson & B. Medeiros (2012) Climatology of the planetary boundary layer over the continental United States and Europe. *Journal of Geophysical Research: Atmospheres (1984-2012)*, 117.
- Semenza, J. C., D. E. Hall, D. J. Wilson, B. D. Bontempo, D. J. Sailor & L. A. George (2008) Public perception of climate change: voluntary mitigation and barriers to behavior change. *American journal of preventive medicine*, 35, 479-487.
- Sims, R. E., H.-H. Rogner & K. Gregory (2003) Carbon emission and mitigation cost comparisons between fossil fuel, nuclear and renewable energy resources for electricity generation. *Energy Policy*, 31, 1315-1326.
- Smith, W., H. Woolf, C. Hayden, D. Wark & L. McMillin (1979) TIROS-N operational vertical sounder. *Bulletin of the American Meteorological Society*, 60, 1177-1187.
- Solomon, S. 2007. *Climate change 2007-the physical science basis: Working group I contribution to the fourth assessment report of the IPCC*. Cambridge University Press.
- Solomon, S., R. T. Pierrehumbert, D. Matthews, J. S. Daniel & P. Friedlingstein. 2013. Atmospheric composition, irreversible climate change, and mitigation policy. In *Climate Science for Serving Society*, 415-436. Springer.
- Solomon, S., G.-K. Plattner, R. Knutti & P. Friedlingstein (2009) Irreversible climate change due to carbon dioxide emissions. *Proceedings of the National Academy of Sciences*, 106, 1704-1709.
- Soytas, U., R. Sari & B. T. Ewing (2007) Energy consumption, income, and carbon emissions in the United States. *Ecological Economics*, 62, 482-489.
- Spurr, R. & M. Christi (2007) Linearization of the interaction principle: Analytic Jacobians in the "Radiant" model. *Journal of Quantitative Spectroscopy and Radiative Transfer*, 103, 431-446.

- St Denis, G. & P. Parker (2009) Community energy planning in Canada: The role of renewable energy. *Renewable and Sustainable Energy Reviews*, 13, 2088-2095.
- Steinke, J. M. & A. Shepherd (1988) Comparison of Mie theory and the light scattering of red blood cells. *Applied optics*, 27, 4027-4033.
- Stocker, T., D. Qin, G. Plattner, M. Tignor, S. Allen, J. Boschung, A. Nauels, Y. Xia, V. Bex & P. Midgley. 2013a. Climate change 2013: the physical science basis. Contribution of working Group I to the fifth assessment report of the intergovernmental panel on climate change. Cambridge: Cambridge University Press) at press.
- Stocker, T., D. Qin, G. Plattner, M. Tignor, S. Allen, J. Boschung, A. Nauels, Y. Xia, V. Bex & P. Midgley. 2013b. IPCC, 2013: Climate Change 2013: The Physical Science Basis. Contribution of Working Group I to the Fifth Assessment Report of the Intergovernmental Panel on Climate Change. Cambridge Univ Press, Cambridge, United Kingdom and New York, NY, USA.
- Stohl, A. (1998) Computation, accuracy and applications of trajectories—A review and bibliography. *Atmospheric Environment*, 32, 947-966.
- Stohl, A., S. Eckhardt, C. Forster, P. James & N. Spichtinger (2002) On the pathways and timescales of intercontinental air pollution transport. *Journal of Geophysical Research: Atmospheres (1984–2012)*, 107, ACH 6-1-ACH 6-17.
- Stokes, L. C. (2013) The politics of renewable energy policies: The case of feed-in tariffs in Ontario, Canada. *Energy Policy*, 56, 490-500.
- Stoll-Kleemann, S., T. O’Riordan & C. C. Jaeger (2001) The psychology of denial concerning climate mitigation measures: evidence from Swiss focus groups. *Global environmental change*, 11, 107-117.
- Streimikiene, D., T. Baležentis & L. Baležentienė (2013) Comparative assessment of road transport technologies. *Renewable and Sustainable Energy Reviews*, 20, 611-618.
- Streimikiene, D. & S. Girdzijauskas (2009) Assessment of post-Kyoto climate change mitigation regimes impact on sustainable development. *Renewable and Sustainable Energy Reviews*, 13, 129-141.
- Stubbe, P. (1972) Vertical neutral gas motions and deviations from the barometric law in the lower thermosphere. *Planetary and Space Science*, 20, 209-215.
- Suter, J. F. & M. R. Shammin (2013) Returns to residential energy efficiency and conservation measures: A field experiment. *Energy Policy*, 59, 551-561.
- Sutherland, R. J. (1991) Market barriers to energy-efficiency investments. *The Energy Journal*, 12, 15-34.
- Syri, S., A. Lehtilä, T. Ekholm, I. Savolainen, H. Holttinen & E. Peltola (2008) Global energy and emissions scenarios for effective climate change mitigation—Deterministic and stochastic scenarios with the TIAM model. *International Journal of Greenhouse Gas Control*, 2, 274-285.
- Takagi, H., R. Andres, D. Belikov, A. Bril, H. Boesch, A. Butz, S. Guerlet, S. Houweling, S. Maksyutov & I. Morino. 2013. Influence of differences in latest GOSAT XCO₂ products on surface CO₂ flux estimation. In *EGU General Assembly Conference Abstracts*, 6869.
- Takahashi, T., S. C. Sutherland, C. Sweeney, A. Poisson, N. Metzl, B. Tilbrook, N. Bates, R. Wanninkhof, R. A. Feely & C. Sabine (2002) Global sea-air CO₂ flux based on climatological surface ocean CO₂, and seasonal biological and temperature effects. *Deep Sea Research Part II: Topical Studies in Oceanography*, 49, 1601-1622.
- Takata, M., K. Fukushima, M. Kawai, N. Nagao, C. Niwa, T. Yoshida & T. Toda (2013) The choice of biological waste treatment method for biological waste treatment methods for urban areas in Japan—An environmental perspective. *Renewable and Sustainable Energy Reviews*, 23, 557-567.

- Tan, K., H. Lim & M. MatJafri. 2012. Carbon dioxide distribution over Peninsular Malaysia from Scanning Imaging Absorption Spectrometer for Atmospheric Cartography (SCIAMACHY). In *Computer and Communication Engineering (ICCCE), 2012 International Conference on*, 354-357. IEEE.
- Tans, P. P., I. Y. Fung & T. Takahashi. 1990. *Observational constraints on the global atmospheric CO2 budget*.
- Tarantola, A. 2005. *Inverse problem theory and methods for model parameter estimation*. siam.
- Taylor, J. (1989) A stochastic Lagrangian atmospheric transport model to determine global CO2 sources and sinks—a preliminary discussion. *Tellus B*, 41, 272-285.
- Team, C. W. (2008) Synthesis Report. *Climate Change 2007. Working Groups I, II and III to the Fourth Assessment*.
- Tegen, I. & A. A. Lacis (1996) Modeling of particle size distribution and its influence on the radiative properties of mineral dust aerosol. *Journal of Geophysical Research: Atmospheres (1984–2012)*, 101, 19237-19244.
- Toon, G., J.-F. Blavier, R. Washenfelder, D. Wunch, G. Keppel-Aleks, P. Wennberg, B. Connor, V. Sherlock, D. Griffith & N. Deutscher. 2009. Total column carbon observing network (TCCON). In *Fourier Transform Spectroscopy*, JMA3. Optical Society of America.
- Trenberth, K. E. (2011) Changes in precipitation with climate change. *Climate Research*, 47, 123.
- Tsai, Y. I. & M. T. Cheng (1999) Visibility and aerosol chemical compositions near the coastal area in central Taiwan. *Science of the total environment*, 231, 37-51.
- Uchino, O., I. Morino, Y. Yoshida, N. Kikuchi, M. Inoue, K. Nakamae, T. Yokota, D. Wunch, P. Wennberg & G. Toon. 2012. Advanced validation of the GOSAT-observed CO2 and CH4 at TCCON and prioritized observation sites. In *EGU General Assembly Conference Abstracts*, 1463.
- Velasco, V., M. Buchwitz, H. Bovensmann, M. Reuter, O. Schneising, J. Heymann, T. Krings, K. Gerilowski & J. P. Burrows (2011) Towards space based verification of CO2 emissions from strong localized sources: fossil fuel power plant emissions as seen by a CarbonSat constellation.
- Vermeulen, A., G. Pieterse, A. Hensen, W. Van Den Bulk & J. Erisman (2006) COMET: a Lagrangian transport model for greenhouse gas emission estimation—forward model technique and performance for methane. *Atmospheric Chemistry and Physics Discussions*, 6, 8727-8779.
- Vitousek, P. M., H. A. Mooney, J. Lubchenco & J. M. Melillo (1997) Human domination of Earth's ecosystems. *Science*, 277, 494-499.
- Vourlitis, G., W. Oechel, S. Hastings & M. Jenkins (1993) A system for measuring in situ CO2 and CH4 flux in unmanaged ecosystems: an arctic example. *Functional Ecology*, 369-379.
- Waggoner, A. P., R. E. Weiss, N. C. Ahlquist, D. S. Covert, S. Will & R. J. Charlson (1981) Optical characteristics of atmospheric aerosols. *Atmospheric Environment (1967)*, 15, 1891-1909.
- Walther, G.-R., E. Post, P. Convey, A. Menzel, C. Parmesan, T. J. Beebee, J.-M. Fromentin, O. Hoegh-Guldberg & F. Bairlein (2002) Ecological responses to recent climate change. *Nature*, 416, 389-395.
- Wang, C., R. Shi, C. Zhou, C. Liu & W. Gao. 2011. Comparison of SCIAMACHY and AIRS CO2 measurements over China from 2003 to 2005. In *SPIE Optical Engineering+ Applications*, 81560N-81560N-9. International Society for Optics and Photonics.
- Wang, J. W., A. S. Denning, L. Lu, I. T. Baker, K. D. Corbin & K. J. Davis (2007) Observations and simulations of synoptic, regional, and local variations in atmospheric CO2. *Journal of Geophysical Research: Atmospheres (1984–2012)*, 112.

- Wang, W., Q. Shao, T. Yang, S. Peng, W. Xing, F. Sun & Y. Luo (2013) Quantitative assessment of the impact of climate variability and human activities on runoff changes: a case study in four catchments of the Haihe River Basin, China. *Hydrological Processes*, 27, 1158-1174.
- Watson, R. T. 2000. *Land use, land-use change, and forestry: a special report of the intergovernmental panel on climate change*. Cambridge University Press.
- Webster, C. R. & R. D. May (1987) Simultaneous in situ measurements and diurnal variations of NO, NO₂, O₃, jNO₂, CH₄, H₂O, and CO₂ in the 40 - to 26 - km region using an open path tunable diode laser spectrometer. *Journal of Geophysical Research: Atmospheres (1984–2012)*, 92, 11931-11950.
- Whitmarsh, L. (2011) Scepticism and uncertainty about climate change: dimensions, determinants and change over time. *Global environmental change*, 21, 690-700.
- Wigley, T. M., R. Richels & J. A. Edmonds (1996) Economic and environmental choices in the stabilization of atmospheric CO₂ concentrations.
- Williams, I., W. Riley, M. Torn, J. Berry & S. Biraud (2011) Using boundary layer equilibrium to reduce uncertainties in transport models and CO₂ flux inversions. *Atmospheric Chemistry and Physics*, 11, 9631-9641.
- Williams, I., W. Riley, M. Torn, S. Biraud & M. Fischer (2013) Biases in regional carbon budgets from covariation of surface fluxes and weather in transport model inversions. *Atmospheric Chemistry and Physics Discussions*, 13, 19051-19083.
- Worden, H. M., K. W. Bowman, J. R. Worden, A. Eldering & R. Beer (2008) Satellite measurements of the clear-sky greenhouse effect from tropospheric ozone. *Nature Geoscience*, 1, 305-308.
- Wunch, D., G. C. Toon, J.-F. L. Blavier, R. A. Washenfelder, J. Notholt, B. J. Connor, D. W. Griffith, V. Sherlock & P. O. Wennberg (2011a) The total carbon column observing network. *Philosophical Transactions of the Royal Society A: Mathematical, Physical and Engineering Sciences*, 369, 2087-2112.
- Wunch, D., G. C. Toon, P. O. Wennberg, S. C. Wofsy, B. B. Stephens, M. L. Fischer, O. Uchino, J. B. Abshire, P. Bernath & S. C. Biraud (2010) Calibration of the Total Carbon Column Observing Network using aircraft profile data. *Atmospheric Measurement Techniques*, 3, 1351-1362.
- Wunch, D., P. Wennberg, G. Toon, B. Connor, B. Fisher, G. Osterman, C. Frankenberg, L. Mandrake, C. O'Dell & P. Ahonen (2011b) A method for evaluating bias in global measurements of CO₂ total columns from space. *Atmospheric Chemistry and Physics*, 11, 12317-12337.
- Yadav, S. K. & G. C. Mishra (2013) Global Energy Demand Consequences Versus Greenhouse Gases Emission. *International Journal of Engineering*, 6, 781-788.
- Yokota, T., Y. Yoshida, N. Eguchi, Y. Ota, T. Tanaka, H. Watanabe & S. Maksyutov (2009) Global concentrations of CO₂ and CH₄ retrieved from GOSAT: First preliminary results. *Sola*, 5, 160-163.
- Yoshida, Y., N. Kikuchi, I. Morino, O. Uchino, S. Oshchepkov, A. Bril, T. Saeki, N. Schutgens, G. Toon & D. Wunch (2013) Improvement of the retrieval algorithm for GOSAT SWIR XCO₂ and XCH₄ and their validation using TCCON data. *Atmospheric Measurement Techniques Discussions*, 6.
- Yoshida, Y., N. Kikuchi & T. Yokota (2012) On-orbit radiometric calibration of SWIR bands of TANSO-FTS onboard GOSAT. *Atmospheric Measurement Techniques Discussions*, 5, 4711-4734.
- Yoshida, Y., Y. Ota, N. Eguchi, N. Kikuchi, K. Nobuta, H. Tran, I. Morino & T. Yokota (2011) Retrieval algorithm for CO₂ and CH₄ column abundances from short-wavelength

- infrared spectral observations by the Greenhouse gases observing satellite. *Atmospheric Measurement Techniques*, 4, 717-734.
- Yumimoto, K. & T. Takemura (2013) The SPRINTARS version 3.80/4D-Var data assimilation system: development and inversion experiments based on the observing system simulation experiment framework. *Geoscientific Model Development*, 6.
- Zahedi, G., S. Azizi, A. Bahadori, A. Elkamel & S. R. Wan Alwi (2013) Electricity demand estimation using an adaptive neuro-fuzzy network: a case study from the Ontario province–Canada. *Energy*, 49, 323-328.
- Zhang, Z. 1998. *The economics of energy policy in China: implications for global climate change*. E. Elgar Pub.
- Zhang, Z., H. Jiang, J. Liu, X. Zhang, C. Huang, X. Lu, J. Jin & G. Zhou (2014) An analysis of the global spatial variability of column-averaged CO₂ from SCIAMACHY and its implications for CO₂ sources and sinks. *International Journal of Remote Sensing*, 35, 2047-2066.
- Zhou, N., M. D. Levine & L. Price (2010) Overview of current energy-efficiency policies in China. *Energy Policy*, 38, 6439-6452.
- Zilitinkevich, S., I. Esau & A. Baklanov (2007) Further comments on the equilibrium height of neutral and stable planetary boundary layers. *Quarterly Journal of the Royal Meteorological Society*, 133, 265-271.